

Hygrothermal modelling as a top-down design tool for mesoporous desiccants

Fernando Sarce Thomann

Thesis submitted to the University of Nottingham for the degree of Doctor of Philosophy

December 2015

ABSTRACT

When considering targeted regulation of transient response to changes in relative humidity within closed environments, selection of a material's suitability requires fundamental understanding of its hygrothermal functional properties as well as the morphology of mesoporous materials. The overall aim of this research was to develop a top-down design technique using hygrothermal modelling simulations that enabled the design of mesoporous desiccants materials. This technique was used to inform the specification of optimized hygrothermal properties with the intention to enhance regulation of any relative humidity buffering application within closed environments. In order to accomplish this, a series numerical simulations using as a template pre-existing mesoporous desiccants properties data were performed. It was found that the linear portion of the hypothetically-created water vapour isotherms correlated with the rate of decline in adsorption/ desorption. This was found to be highly sensitive to the moisture content gradient, Δw between the upper and the lower relative humidity limits of the water vapour adsorption isotherm. The stages of the kinetics of water vapour adsorption found consistent agreement with the moisture content gradient and the exchange rates for moisture loads. This assisted the design process for newly created mesoporous solids (MCM-41 and SBA-15) when informing the optimized hygrothermal properties with respect to targeted relative humidity buffering applications. The latter enabled the quantification of the relative effect on energy efficiency (latent heat) when assisting an HVAC system as a dehumidifier. The major implication of this research was the novel theoretical insight that enabled a top-down predictive design using hygrothermal numerical modelling. This allowed functional properties optimization for mesoporous solids with respect to specific targeted closed environments, by informing material's preparation *via* enhanced modulation of 'ideal' pore geometry.

ACKNOWLEDGEMENTS

First of all, as a believer, I wish to gratefully give thanks and honour to God for this beautiful opportunity that He gave to me, for all the strength and support, patience and wisdom given to carry out this whole process to a successful end.

I wish to offer grateful thanks to one particular person, my current friend and supervisor Dr Matthew R. Hall. Thanks Matthew for all the passion shown from the beginning of this project, for the encouragement and perseverance given and the hard work that you bestowed on me. For all the knowledge and wisdom given, and for your endless guidance and support. Thanks for every single conversation and for our many hours of discussion, but above all, for showing me everything in the humblest way with simplicity in a joyful environment, and always with a smile on your face.

In addition, I offer special acknowledgment to the continuing support and funding of this research to my sponsors CONICYT, through the 'Programa de Formación de Capital Humano Avanzado, BECAS CHILE' – Ministerio de Educación, Gobierno de Chile.

I also would like to thank Dr Andrew Patman, Dr Keith Dinsdale in Wolfson, Mike Langford, Andrew Maddison and Nigel Rook in NCG for all the assistance and technical support provided. I am also grateful to Rich Blakemore, Mick Winfield and Jon Watson in NTEC for their support. Special thanks to James Grenfell for his support and collaboration. Additionally, I wish to offer grateful thanks to Dr Robert Mokaya for the time spent together and the insights given into this research, to Wantana Sangchoom and Lee Stevens for all the support and collaboration given.

I would also like to thank my fantastic colleagues and friends, Mohammed Mahmood, Konstantinos Giannoukos, Vasileios Matziaris, and Piotr Osinski for our great time spent together, discussions and joyful moments, their cultural exchange and friendship throughout this research. Special thanks to Sean Casey for all the experience transmitted and the support given, advice and friendship.

I wish to gratefully thank my extended family here in Nottingham, to Tim and Jensine Kitchen for their endless support and love given towards us, for opening their doors as a family through Clare and Gordon Clow, and for the continuing friendship and prayers. Thank you so much. We love you so much!

To my parents, I give special thanks to Juan Sarce and Evelyn Thomann, for their prayers and love, for their belief in me shown from the start of my career. Thank you so much.

At last but not least, to my beloved ones, Sofia and Valentina, and to my extraordinary wife Annesi, for her tireless patience and support and for all the moments of prayer together as a couple. Thanks for all your dedication and perseverance without which, this project might not have been possible.

Te amo con todo mi ser…you are '*my unforgettable*'

DECLARATION

I can declare that, except when explicit reference to other people is given, the contents of this thesis is solely attributed to my own personal work realized within the facilities of The University of Nottingham, Faculty of Engineering during the period between May 2012 and November 2015. Hereby, I also can declare that this thesis has not been submitted to any other University nor other educational institution with the purpose to obtain a Degree, Diploma or other qualifications.

Fernando Sarce Thomann

December 2015

PUBLICATIONS

Journal articles

THOMANN, F. S., HALL, M. R., MOKAYA, R. & STEVENS, L. A. 2015. Hygrothermal simulation-informed design of mesoporous desiccants for optimised energy efficiency of mixed mode air conditioning systems. *Journal of Materials Chemistry A*, 3, 17290-17303.

THOMANN, F. S., HALL, M. R., SANGCHOOM, W. & MOKAYA, R. 2015. A hygrothermal modelling approach to water vapour sorption isotherm design for mesoporous humidity buffers. *Microporous and Mesoporous Materials*, 211, 113-123.

Conference papers

Sarce F, Hall MR, Casey SP. *Multi-layered hygroscopic wall assemblies for humidity buffering and improved energy efficiency in a Passivhaus standard building*. CMM2013 20th International Conference on Computer Methods in Mechanics, 27th – 31st August, Poznań, Poland (2013).

Casey SP, Hall MR, Sarce F, Tsang SCE, Khan AM. *Physical and numerical predicted results for the hygric properties of desiccant materials*. CMM2013 20th International Conference on Computer Methods in Mechanics, 27th – 31st August, Poznań, Poland (2013).

LIST OF FIGURES

Figure 1.1 – Schematic representation of the moisture storage function, *w* within capillary-active porous materials. 2

Figure 1.2 – Methodological scheme for the top-down design tool. 9

Figure 2.1 – Schematic cross-section of a porous solid showing the different types of pores.. 18

Figure 2.2 – Water distribution arrangements.. 19

Figure 2.3 – a) Tightly adsorbed bonded water ~ 2 nm, b) loosely bonded adsorbed water ~ 2-6 nm, c) viscous or capillary water.. 20

Figure 2.4 – Schematic representation of a water vapour adsorption isotherm for a hygroscopic capillary-active material.. 22

Figure 2.5 – Schematic representation of an interconnected porous material and the moisture transport mechanisms during a) dry and b) wet winter.. 23

Figure 2.6 – Representation of a pore structure where a) Knudsen and b) Fickian water vapour diffusion are presented. 27

Figure 2.7 – Fickian diffusion in the presence of multilayer adsorption. 28

Figure 2.8 – Schematic representation of surface diffusion in different pore sizes 30

Figure 2.9 – Capillary system and liquid-gas interface in the capillary tube. . 31

Figure 2.10 – The Kelvin capillary condensation. 32

Figure 2.11 – Flow chart for hygrothermal simulations. 35

Figure 2.12 – Weather data input for WUFI+. 38

Figure 2.13 – Internal loads calculator. 39

Figure 2.14 – Flow chart that shows the coupled heat and moisture transport equations for WUFI computer based program. 45

Figure 2.15 – Schematic representation of nitrogen physisorption starting from monolayer formation to multilayer and capillary condensation.. 48

Figure 2.16 – Adsorption isotherm classification and hysteresis loops. 50

Figure 2.17 – Schematic representation of the Langmuir adsorption model based on the fractional loading. 52

Figure 2.18 – a) Kelvin radius r_p in a cylindrical closed pore, b) Kelvin radius r_K and the introduced statistical thickness, t in a cylindrical open pore, and c) desorption process from a cylindrical open pore using the Kelvin radius r_K. .. 59

Figure 2.19 – Simplified conceptual scheme-model of water vapour adsorption/ desorption isotherm pore filling stages for a mesoporous material. 62

Figure 2.20 – Simplified conceptual scheme-model of the kinetics of water vapour adsorption/ desorption for a three-cycle time-response pore filling stages representation. 65

Figure 2.21 – Schematic representatiion of Foster's delayed condensation phase due to meniscus formation. 67

Figure 2.22 – Schematic representation of McBain's bell jar model and the pore-blocking (ink-bottle) effect for hysteresis 68

Figure 2.23 – Hysteresis loops. Adapted from (Rouquerol *et al.,* 1994). 71

Figure 2.24 – Water adsorption (black filled squares)/ desorption (black empty squares) isotherms in a 10 Å silica slit pore and water adsorption (red filled diamonds)/ desorption (red empty diamonds) isotherms in a 20 Å silica slit pore at T = 300 K (P0 = 4400 Pa). 74

Figure 2.25 – Typical molecular configurations for water confinement at 300 K and under different pressures in silica nanopores. (a) 10 Å and (b) 20 Å. 76

Figure 2.26 – a) Water molecules in the vicinity of a surface (Silica – high silanol groups density), b) density profileamorphous silica slit pore at T = 300 K (P0 = 4400 Pa); where, origin of the *z*-axis is the hydrogen positions on the silica surfaces.. 77

Figure 2.27 – Schematic representation of molecular condensation in nanopores; where adsorption process corresponds to letters a), b), and c), and desorption to letters d), e), and f) 80

Figure 2.28 – Hierarchical wetting model and molecular condensation in heterogeneous multilayer nanopores with different sections (a) and (b) 81

Figure 3.1 – a) Schematic representation of the experimental setup, b) Climatic Chamber – TAS Series 3, c) touchscreen graphical programmer interface, and d) mass change recordings using the VIBRA HT Series electronic weighing balance. 87

Figure 3.2 – Close environment representation for the numerical simulations 89

Figure 3.3 – Humidity buffering decay representation when the fluctuation of $\varphi(t)$ exceeds the upper limit (φ_{max}) at N number of cycles. 90

Figure 3.4 – Moisture loads schedule as a function of time (*t*), where a) corresponds to the 4 h cycle and b) to the 24 h cycle. 91

Figure 3.5 – Schematic representation of an 'optimum' hypothetical water vapour isotherm where the maximum Δw is defined between the upper ($\varphi_{i,U}$) and lower ($\varphi_{i,L}$) limits. 93

Figure 3.6 – Schematic representation of a hypothetical water vapour isotherm design. a) Initial adjustments in the *x–y* axis values. b) Further modifications in the *x–y* axis values for new candidates with modal pore diameter and pore volume variations derived from first candidate. 95

Figure 3.7 – a) Hypothetical water vapour isotherm candidates and, b) corresponding PSD derived from Kelvin equation 97

Figure 3.8 – Second set of isotherm candidates. a) Proportionally reduced water vapour isotherms derived from candidate A_3. b) Corresponding modal pore diameter derived from Kelvin's equation 99

Figure 3.9 – Volumetric method diagram of physisorption measurements. 106

Figure 3.10 – a) Schematic representation of the DVS Advantage Advantage-2 series. Adapted images are under authorization from Surface Measurements Systems Ltd., London, UK. b) The DVS unit inside the Laboratory within the Nottingham Transportation Engineering Centre, Faculty of Civil Engineering, University of Nottingham. c) Special forceps used for hanging samples within the sample chamber. 111

Figure 3.11 – Water vapour isotherm example from the ACS, using the gravimetric DVS from Surface Measurements Systems Ltd, UK. The example corresponds to the MCM-41@165 desiccant. 113

Figure 3.12 – Schematic diagram of adsorption/ desorption between pre-defined $\Delta\varphi$ cycles ($\Delta\varphi$ = 0.2 – 0.3; 0.3 – 0.5, 0.5 – 0.7; and 0.7 – 0.95), where t = 2 h. 115

Figure 3.13 – Water vapour sorption isotherms for all desiccant candidates. References are provided for the following desiccants candidates: MIL-101, PS-C16-R, KIT-1 and FSM-16, Aerogel 118

Figure 3.14 – Close environment representation for the numerical simulations. 119

Figure 3.15 – Moisture loads schedule as a function of time (*t*), which corresponds to the 24 h cycle for the parametric assessment (refer to Table 3.5) of all desiccant materials as depicted in Table 3.4. 121

Figure 4.1 – Water vapour adsorption isotherms for MS-3.3 and 8.3. 127

Figure 4.2 – Relative humidity buffering for the 4h cycle and number of cycles, N = 60. 129

Figure 4.3 – Relative humidity buffering for the 24h cycle and number of cycles, N = 11. 130

Figure 4.4 – Relative humidity buffering results for all the new hypothetically-created isotherms candidates (A_1 – A_6) for the 4h cycle and number of cycles, N = 60. 132

Figure 4.5 – Relative humidity buffering results for all the new hypothetically-created isotherms candidates (A_1 – A_6) for the 4h cycle and number of cycles, N = 11. 133

Figure 4.6 – Water vapour isotherm candidates A_1-A_6 showing the portion of the isotherm for potential relative humidity buffering between $\varphi_{i,U} - \varphi_{i,L.}$ 135

Figure 4.7 – Relative humidity buffering results from the proportionally reduced water vapour isotherms derived from candidate A_3; where the number of cycles, N = 60 136

Figure 4.8 – Relative humidity buffering results from the proportionally reduced water vapour isotherms derived from candidate A_3; where the number of cycles, N = 11. 137

Figure 4.9 – Correlation between Δw and relative humidity buffering decay. a) Water uptake at Δw range. b) $\Delta w/t$ linear correlation..... 139

Figure 4.10 – Isotherm candidates for different $\varphi_{i,U} - \varphi_{i,L}$ limits. a) Water vapour sorption isotherms. b) Corresponding modal pore diameter derived from Kelvin's equation. c) $\Delta w/t$ linear correlation..... 140

Figure 4.11 – Permissible volumetric moisture loads at constant φ = 0.5..... 141

Figure 4.12 – Permissible volumetric moisture loads at constant ACH = 0.35 and different φ_e 142

Figure 4.13 – Conceptual model for expanded hygrothermal applications within a psychrometric chart and under non-isothermal conditions. 147

Figure 4.14 – Conceptual model for hygrothermal buffering through enhanced heat transfer and storage for hypothetically designed absorbents 149

Figure 5.1 – Nitrogen adsorption isotherms 154

Figure 5.2 – PSD for all materials. a) Incremental pore volume BJH from the adsorption branch. b) Relative volume (%) BJH from the adsorption branch. 158

Figure 5.3 – Water vapour adsorption/ desorption isotherms..... 159

Figure 5.4 – Comparison between moisture content (g/g) at different φ ranges, for the kinetics of water vapour adsorption/ desorption for a three-cycle time-response DVS test. 163

Figure 5.5 – Water vapour sorption/desorption kinetics comparison between experimental DVS and numerical simulations for MCM-41@150–180, and SBA-15 6 nm 167

Figure 5.6 – Water vapour adsorption/ desorption kinetics comparison between experimental DVS and numerical simulations for MCM-41@150–180, and SBA-15 6 nm. 168

Figure 5.7 – Water vapour adsorption/ desorption kinetics comparison between experimental DVS and numerical simulations for SBA-15 6 nm 169

Figure 6.1 – Kinetics of continuous water vapour adsorption (against time) at the corresponding three stages (refer to Figure 6.1) for all desiccant candidates when achieving EMC_{100} 179

Figure 6.2 – a) Water vapour sorption isotherm portions within the three stages *a*-*b*, *b*-*c*, and *c*-*d*. b) Corresponding kinetics of water adsorption at different EMC stages *a*-*b*, *b*-*c*, and *c*-*d* that shows EMC in the segments 1, 2 and 3. 180

Figure 6.3 – Cumulative water vapour uptake for all desiccant candidates 183

Figure 6.4 – a) Linear correlation between *w* and the and the water vapour being exchanged (against time). b) Relationship between total *w* and the time taken to achieve EMC_{100} 187

Figure 6.5 – Relative humidity buffering results for all desiccant candidates within the following operating ranges: a) φ = 0.4 – 0.5; b) φ = 0.5 – 0.6; c) φ = 0.6 – 0.7; d) φ = 0.7 – 0.8. The red-dotted lines correspond to the maximum and minimum relative humidity limits. 189

Figure 6.6 – a) Water vapour uptake capacity at different Δw for all desiccant candidates. b) Time taken for desiccant failure when the fluctuation of $\varphi(t)$ exceeds the φ_{max} limit; where Δw = 40 – 50; 50 – 60; 60 – 70; 70 – 80; and 80 – 90. This also correspond to the threshold when the materials reaches failure at the number of cycles, N = 12 190

Figure 6.7 – Dehumidification ratio performed by the HVAC system and the desiccant candidates according to the operating φ ranges a) 0.4 – 0.5; b) 0.6 – 0.7; and c) 0.7 – 0.8. 192

Figure 6.8 – Comparison between the resultant indoor $\varphi(t)$ and the material's $\varphi(t)$ at different operating ranges for desiccant materials MIL-101, FSM-16 and MCM-41@165. 194

Figure 6.9 – Correlation between moisture sorption capacity and the latent heat used for air dehumidification from the HVAC system at the corresponding operating ranges (φ = 0.4 – 0.5; 0.5 – 0.6; 0.6 – 0.7; 0.7 – 0.8; 0.8 – 0.9) 196

Figure 6.10 – Latent heat of dehumidification comparison among all desiccant from the HVAC system at the corresponding operating ranges (φ = 0.4 – 0.5; 0.5 – 0.6; 0.6 – 0.7; 0.7 – 0.8; 0.8 – 0.9)..... 197

Figure 6.11 – a) Total energy used for air dehumidification for all desiccant candidates. In the case of materials MIL-101 and PS-C16-R, a cooling demand is represented by the hatched box above the values. b) Non-linear correlation between total moisture storage, *w* and total latent heat for air dehumidification. 199

Figure 6.12 – Schematic representation of desiccant's regeneration..... 201

LIST OF TABLES

Table 3.1 – Hygrothermal functional properties for mesoporous silicas 89

Table 3.2 – First set of isotherm candidates (A_1–A_6) within the specified $\varphi_{i,L}$ – $\varphi_{i,U}$ range. * Derived from Kelvin's equation. 98

Table 3.3 – Parameters for the numerical model setup when assessing infiltration and ventilation sensitivity analysis for the standardization process. 102

Table 3.4 – Moisture storage function for all desiccant materials. References are provided for the following materials: MIL-101 (Henninger *et al.*, 2012), PS-C16-R (Naono *et al.*, 2000), KIT-1 and FSM-16. 119

Table 3.5 – Parameters for the numerical model setup when performing the parametric assessment for humidity buffering under five pairs of operational limits (φ_{min}–φ_{max}) 0.4 – 0.5; 0.5 – 0.6; 0.6 – 0.7; 0.7 –0.8; and 0.8 – 0.9. 122

Table 4.1 – Water vapour adsorption with respect to the relative humidity ranges (φ = 0 – 0.3; 0.3 – 0.7; and 0.7 – ~1), and corresponding moisture content, *w*. 128

Table 5.1 – Adsorption/ desorption lower and upper P/P_0 ranges for SBA-15 and MCM-41 materials, when using nitrogen as an adsorbate. 155

Table 5.2 – Textural properties summary for MCM-41, SBA-15 and MS desiccant materials 156

Table 5.3 – Stages for water vapour adsorption in the ranges $\varphi_{a\text{-}b}$, $\varphi_{b\text{-}c}$, and $\varphi_{c\text{-}d}$ and the corresponding moisture storage, Δw for same φ ranges 160

Table 5.4 – a) Desorption percolation threshold ($\varphi_{,P}$) and b) lower closer point ($\varphi_{,L}$) for SBA-15 and MCM-41 materials using water vapour as an adsorbate. c) Onset of capillary condensation ($P/P_{0(L)}$) for SBA-15 and MCM-41 materials, when using nitrogen as an adsorbate. 162

Table 5.5 – Moisture storage capacity at different Δw (kg/m^3) for all desiccant materials. 164

Table 5.6 – Average difference (%) between experimental and numerical *w* data for all desiccants materials, when modelling the kinetics of water vapour adsorption/ desorption for the three-cycle time-response test 171

Table 6.1 – Moisture storage (Δw gradient) for the specific portions of the isotherm *a-b*, *b-c*, and *c-d*. 181

Table 6.2 – Capillary transport coefficient of suction (D_{ws}) contribution at each portion of the isotherm. 185

LIST OF ACRONYMS

3D	Three Dimensional
ACH	Air Changes per Hour
ACS	Advantage Control Software
BET	Brunauer–Emmett–Teller
BJH	Barrett–Joyner–Halenda
BSI	British Standards Institution
DVS	Dynamic Vapour Sorption
EMC	Equilibrium Moisture Content
FSM	Folded Sheets Mechanism
HVAC	Heating Ventilation and Air Conditioning
IUPAC	International Union of Pure and Applied Chemistry
KIT	Korea Advanced Institute of Science and Technology
MCM	Mobil Crystalline Material
MIL	Materials of Institute Lavoisier
MOF	Metal–Organic Frameworks
MS	Mesoporous Silica
PCM	Phase Change Materials
SBA	Santa Barbara Amorphous type material
S_{BET}	BET Specific Surface Area
SSA	Specific Surface Area
WUFI	Wärme Und Feuchte Instationär

NOMENCLATURE

A	liquid water absorption rate	$kg/m^2s^{0.5}$
°C	celsius degrees	-
C_p	constant pressure specific heat capacity	J/(kg K)
C_v	mass concentration of water vapour	kg/m^3
D	diffusion coefficient for water vapour in still air	m^2/s
D_{ws}	capillary transport coefficient of suction	m^2/s
D_p	mean pore diameter	nm
d	thickness	m
D_φ	liquid conduction coefficient	kg/m s
G	water flow rate	kg/s
g_w	liquid flux density	kg/m^2 s
H	enthalpy	J
h_v	latent heat of phase change	J/kg
N	number of cycles	-
n	bulk porosity	m^3/m^3
P_0	standard atmospheric pressure (barometric)	Pa
P/P_0	partial pressure	-
P_a	total air pressure	Pa
p_v/p_0	partial pressure of water vapour	Pa
p_{vsat}	saturation vapour pressure	Pa
p_{vsat}^*	saturation vapour pressure above a flat water surface	Pa
r	radius	m
r_c	critical radius	m
S	entropy	J/K
S_d	vapour diffusion thickness	-
t	time	s
T	thermodynamic temperature	K
T_c	critical temperature	K
T_{cc}	critical capillary temperature	K
T_{ch}	hysteresis critical temperature	K
T_{db}	dry bulb temperature	°C
U	internal energy	J

V	volume	m^3
V_m	molar volume	cm^3/mol
V_m	micropore volume	cm^3/g
V_p	total pore volume	cm^3/g
W	water vapour permeance	$kg/(m^2 s Pa)$
w	moisture content	kg/m^3
$w=(f)$	water vapour sorption isotherm	kg/m^3
W_f	free water saturation (also termed capillary saturation)	kg/m^3

Greek letters

δ_{air}	water vapour permeability in air	kg/(m s Pa)
δ	water vapour permeability of a material	kg/(m s Pa)
ρ_b	bulk density	kg/m^3
γ	surface tension	N/m
λ	dry state thermal conductivity	W/(m K)
$\lambda(w)$	moisture-dependant thermal conductivity	W/(m K)
μ	chemical potential	-
μ	water vapour diffusion resistance factor	-
φ	relative humidity (decimal)	-
Ψ	capillary potential	Pa
ω	local interaction energy	-
ω_{ml}	volumetric moisture loads	$(g/h/m^3)$
Φ	interaction potential	-

Suffixes

i	interior
e	exterior
L	lower limit
U	upper limit
max	maximum
min	minimum

TABLE OF CONTENTS

ABSTRACT i
ACKNOWLEDGEMENTS ii
DECLARATION iv
PUBLICATIONS v
LIST OF FIGURES vi
LIST OF TABLES xii
LIST OF ACRONYMS xiii
NOMENCLATURE xiv
TABLE OF CONTENTS xvi

CHAPTER 1 Introduction 1

1.1 Overview 1
1.2 Research overall aim 8
1.3 Research objectives 10
1.4 Research limitations 11
1.5 The thesis structure 11

CHAPTER 2 Scientific Background 15

2.1 Introduction 15
2.2 Porous solids materials 16
2.2.1.1 Porosity and pore size 16
2.2.1.2 Pore morphology 17
2.3 Moisture storage, transport and distribution 19
2.3.1 Moisture storage 21
2.3.1.1 Moisture regions 21
2.4 Moisture transport mechanisms 23
2.4.1 Water vapour diffusion 24
2.4.1.1 Fick's law – mass fraction diffusivity 25
2.4.1.2 Partial and saturated vapour pressure 25
2.4.1.3 Knudsen and Fickian diffusion 27
2.4.2 Liquid transport 29
2.4.2.1 Surface diffusion 29
2.4.3 Capillary condensation 30
2.4.3.1 Kelvin's equation of capillary condensation 32
2.5 Hygrothermal numerical simulations 34
2.5.1 WUFI validation 36
2.5.2 Input data for hygrothermal simulations in WUFI+ 37
2.5.2.1 Boundary conditions and climate data 37
2.5.2.2 Moisture storage function 39
2.5.2.3 Liquid transport coefficients 39
2.5.2.4 Water vapour diffusion 40
2.5.2.5 Moisture-dependent thermal conductivity 42
2.5.2.6 Combined heat and moisture transport equations 43
2.6 Gas adsorption 46
2.6.1 Physical adsorption 46

2.6.2 Classification and definition of isotherms 49
2.6.3 Surface area measurements 51
2.6.3.1 The Langmuir adsorption isotherm 51
2.6.3.2 The BET theory 54
2.6.3.3 The *t*-method and α_s method 55
2.6.4 Pore size distribution and pore volume 57
2.6.4.1 The BJH method 57
2.7 Water vapour adsorption 60
2.7.1 Water vapour adsorption/ desorption isotherm 61
2.7.2 Kinetics of water vapour adsorption/ desorption 64
2.7.3 Hysteresis phenomena 66
2.7.3.1 Hysteresis loops 70
2.8 Molecular dynamic simulations of water under confinement 73
2.8.1.1 Water molecule behaviour in nanopores 74
2.8.1.2 Hysteresis in nanopores 77
2.8.1.2.1 Unstable equilibrium 78
2.8.1.2.2 Molecular condensation and hysteresis 79
2.9 Summary 82

CHAPTER 3 Methods 83

3.1 Overview 83
3.2 Hygrothermal functional properties characterization 85
3.2.1 Water vapour adsorption/ desorption isotherms 85
3.3 Hygrothermal modelling technique for the design of water vapour isotherms 88
3.3.1 Preliminary humidity buffering capacity simulations 88
3.3.2 Design process of water vapour isotherms 92
3.3.3 Isotherm candidates 96
3.3.4 Sensitivity analysis for new isotherm candidates 100
3.3.5 Standardization and parametric studies 101
3.4 Synthesis and characterization of mesoporous desiccants 103
3.4.1 Nitrogen physisorption 106
3.4.1.1 Pore volume and pore size distribution 108
3.4.1.2 Specific surface area determination 109
3.4.2 Water vapour isotherms using dynamic vapour sorption 110
3.5 Physical modelling for water vapour adsorption/ desorption kinetics comparison 113
3.5.1 Climatic chamber 114
3.5.2 Dynamic vapour sorption (DVS) 115
3.5.3 Hygrothermal model validation 116
3.6 3D Numerical simulations for optimized water vapour isotherms 117
3.6.1 Sensitivity analysis for continuous moisture loads 118
3.6.2 Humidity buffering 121
3.6.3 Dehumidification loads and energy consumption 122
3.7 Summary 124

CHAPTER 4 Hygrothermal design approach for ideal water vapour isotherms 126

4.1 Overview..... 126
4.2 Water vapour isotherm characterization for pre-existing MS materials... 127
4.3 Numerical simulations for the development of hygrothermal modelling technique..... 128
4.3.1 Preliminary sensitivity analysis for pre-existing MS materials 128
4.3.2 Sensitivity analysis for new isotherm candidates 131
4.3.3 Sensitivity analysis for isotherms with pore volume reduced .. 135
4.4 Standardization process for humidity buffering 141
4.4.1 Volumetric moisture load analysis 141
4.4.2 Ventilation sensitivity analysis on volumetric moisture loads . 142
4.5 Discussion..... 143
4.6 Future work..... 146
4.6.1 Conceptual model for adsorption/ heat transfer..... 146
4.7 Summary..... 150

CHAPTER 5 Mesoporous desiccant characterization and water vapour adsorption/ desorption kinetics 152

5.1 Overview..... 152
5.2 Nitrogen Physisorption 153
5.2.1 Nitrogen adsorption/ desorption isotherms..... 153
5.2.2 Specific surface area and pore size distribution 156
5.3 Hygrothermal functional properties characterization 159
5.3.1 Water adsorption isotherm..... 159
5.4 Kinetics of water adsorption/ desorption comparison 162
5.5 Experimental results and model validation..... 166
5.5.1 Dynamic vapour sorption (DVS)..... 166
5.6 Discussion..... 172
5.7 Summary..... 174

CHAPTER 6 Mesoporous desiccant optimization for energy efficiency of mixed mode HVAC systems..... 177

6.1 Overview..... 177
6.2 Sensitivity analysis 178
6.2.1 Continuous moisture loads 178
6.2.2 Water vapour adsorption kinetics 182
6.2.3 Sensitivity analysis for specific relative humidity buffering scenarios 188
6.3 Air dehumidification and energy consumption 191
6.3.1 Dehumidification loads..... 191
6.3.2 Energy consumption for air dehumidification..... 195
6.4 Future work..... 200
6.4.1 Material’s regeneration for re-use within specific operating ranges 200
6.5 Discussion..... 202

6.6 Summary 204

CHAPTER 7 Discussion 208
CHAPTER 8 Conclusions 212

8.1 Concluding remarks 212
8.2 Recommendations for further research .....

REFERENCES 219

CHAPTER 1 Introduction

1.1 Overview

In order to maintain suitable levels of indoor air quality and energy efficiency it is important to control the psychrometric variables within well-defined operational upper and lower limits inside 'closed environments'; *e.g*. buildings, laboratories, cars, aircraft, *etc*. According to the International Energy Agency, the building sector represents between 20 – 40% of the final energy consumption for developed countries (IEA, 2016). Within the same sector, the energy consumption for heating, ventilation and air conditioning (HVAC) represents 50% of the total (Pérez-Lombard *et al.*, 2008). This has been accounted for a large use of fossil fuels and associated greenhouse gas emissions (Freire *et al.*, 2008; Davis and Caldeira, 2010). Since the early 1960's, hygrothermics has been dedicated to the investigation of the coupled phenomena between heat and moisture (liquid and vapour phases) that occurs within porous solid materials as a result of adsorption and diffusion. Hygroscopic materials are those with the ability to adsorb and store moisture at the pore surface and network, until equilibrium with the ambient relative humidity (φ) is reached (Künzel, 1995; Krus, 1996). A desirable behaviour for hygroscopic materials is the simultaneous buffering of fluctuations in energy (heat) and mass (water vapour) concentration with respect to partial or equilibrium moisture content (Hall, 2010). This occurs during transient exchange of heat, air, and moisture between the material and the air inside a closed environment (*e.g*. a room or vehicle interior) with respect to the exterior psychrometric conditions (Hens, 2012).

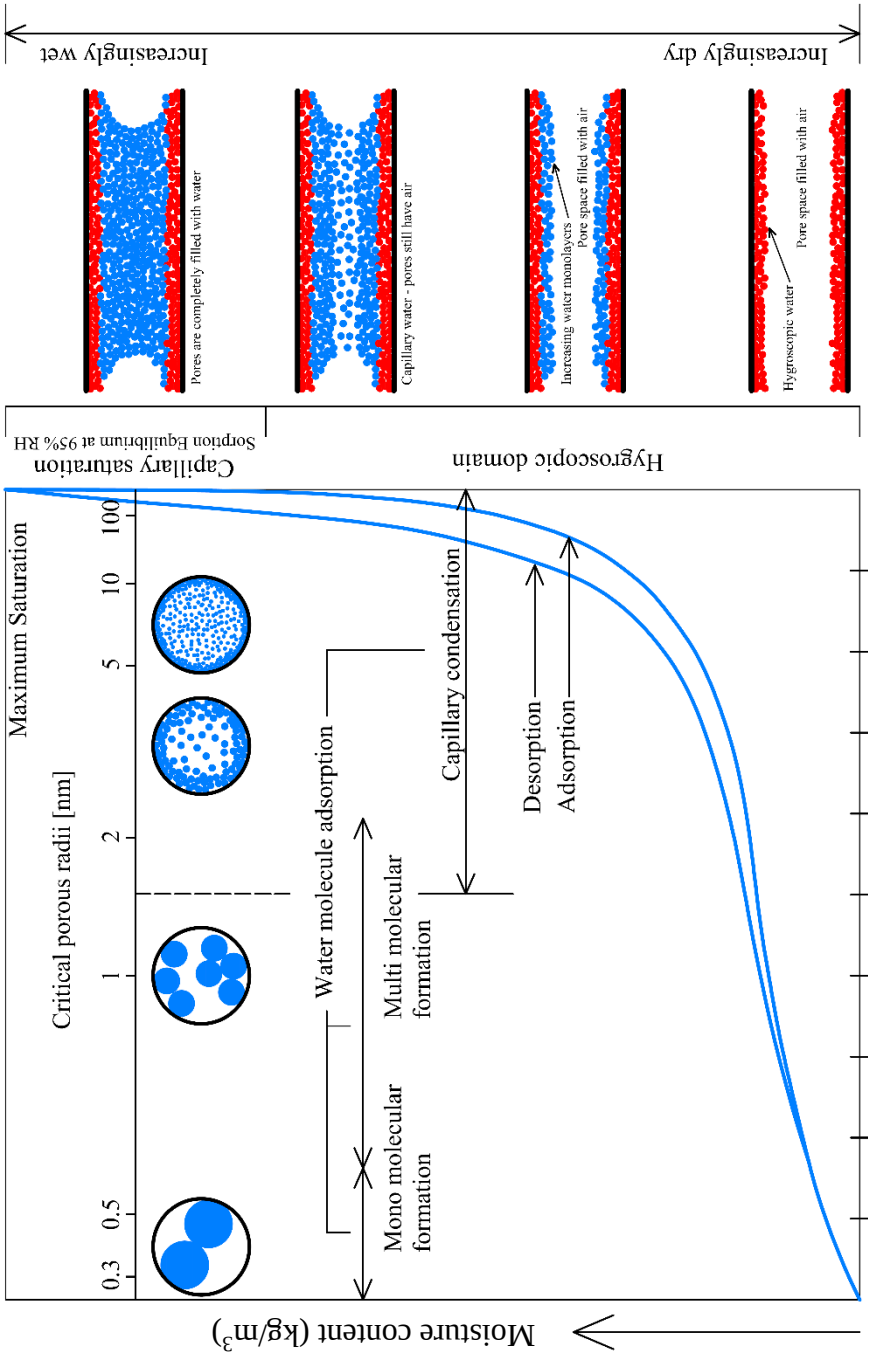


Figure 1.1 – Schematic representation of the moisture storage function, *w* within capillary-active porous materials. Adapted from (Künzel, 1995; Hall, 2010).

As Figure 1.1 shows, the moisture storage function, w defines the non-linear relationship between the adsorbed water (mass in kg) and the relative humidity, φ; known as sorption isotherm when performed at constant temperature. This behaviour is largely attributable to the corresponding hygrothermal functional properties of the material, and can be represented by the following list of bulk-scale transport and storage phenomena:

- Heat storage, c_p in J/kg K of the dry building material with moisture content dependency, $c_p = f(w)$.
- Bulk density, ρ_b in kg/m^3.
- Bulk porosity, n in m^3/m^3.
- Heat transport by thermal conduction, λ in W/m K with moisture-dependent thermal conductivity $\lambda = f(w)$.
- Moisture storage function, w by vapour sorption and capillary forces, where $w = f(\varphi)$ in kg/m^3.
- Water vapour diffusion resistance, μ with moisture-dependent diffusivity $\mu = f(\varphi)$.
- Water diffusivity, D_w due to capillary transport with moisture-dependency $D_w = f(w)$.

Figure 1.1 also shows the dependency of n on w, which is controlled by total pore volume (maximum saturation), whereas the thermal conductivity, $\lambda = f(w)$ can be described as dependent on the moisture content. The stored energy can be described as the summation of the corresponding c_p for both the surface of porous materials (adsorbent) and the water vapour (adsorbate). Furthermore, significant heat transfer can occur due to the heat of adsorption released during adsorption, and from the evaporation/ condensation phase of the adsorbate

during transport and diffusion. The Fickian diffusion resistance of water vapour, μ found in the hygroscopic domain is highly dependent on the relative humidity, φ which is the result of the pore restriction due to capillary condensation; *i.e*. liquid water transport dominates over water vapour diffusion. Water diffusivity, D_w in the capillary domain is strongly dependent on the moisture content, w by the variation of the suction potential; *i.e*. when w is high (capillary saturation) there is lower motivation force for liquid transport (Künzel, 1995; Hall, 2010).

A significant amount of literature has been published in regard to the assessment of hygroscopic materials with respect to passive moisture control within closed environments (Cerolini *et al.*, 2009; Osanyintola and Simonson, 2006; Ramos *et al.*, 2010). Primarily, due to the great importance concerning the occupants' perception of indoor air quality (Steeman *et al.*, 2010a; Osanyintola and Simonson, 2006; Steeman *et al.*, 2009a; Woloszyn *et al.*, 2009), occupants' health due to mould formation (dos Santos *et al.*, 2009; Nik *et al.*, 2012; Sedlbauer, 2002; Krus and Sedlbauer, 2005), and building damage and durability (Abuku *et al.*, 2009; Steeman *et al.*, 2009b; Sedlbauer *et al.*, 2001; Sedlbauer, 2001). The NORDTEST project (Rode *et al.*, 2005) suggested a set of experimental procedures in order to assess the moisture buffering performance in transient quasi equilibrium conditions; *i.e*. not assuming equilibrium moisture content. Hence, the indication of moisture uptake/ release by the material under repeated cycles of relative humidity variations between two given levels could be determined; also known as Moisture Buffering Value (MBV). Previous studies have shown the evaluation of the MBV respect to dynamic moisture loads (Zhang *et al.*, 2012), maximum accumulated moisture buffering (Yang *et al.*, 2012), and sorption isotherm hysteresis effect (Kwiatkowski *et al.*, 2011).

Additionally, experimental and benchmark procedures have been developed to investigate the role of hygroscopic materials on the performance of buildings for indoor climate regulation (Van Belleghem *et al.*, 2011), and largely for validation of numerical computational heat and moisture transport models (Steeman *et al.*, 2010b; Desta *et al.*, 2011; Korjenic and Bednar, 2012). However, all these investigations have followed a bottom-up approach where various pre-existing materials have mostly been experimentally assessed with the intention of determining their moisture buffering performance. This research will instead focus on a top-down approach where the ideal material properties are first determined (and aided by numerical simulations), and then a new desiccant material is synthesised that possesses these properties. The material property that mainly controls the humidity buffering behaviour of a desiccant is the moisture storage function, *i.e*. water vapour adsorption/ desorption isotherms (Casey *et al.*, 2012).

The morphology of the mesoporous desiccants, such as MCM-41, as a material template for pore network optimization has been widely recognized for its exceptional features of fine-tunability. This material has previously attracted the attention from many researchers for investigations in catalysis (Maschmeyer *et al.*, 1995; Blasco *et al.*, 1995), synthesis of different pore sizes (Selvam *et al.*, 2001; Corma *et al.*, 1997; Grün *et al.*, 1999), new methods for determining pore size distribution (PSD) (Storck *et al.*, 1998; Ravikovitch *et al.*, 1997; Kruk *et al.*, 1997b), and drug delivery rate of ibuprofen (Horcajada *et al.*, 2004; Munoz *et al.*, 2003; Vallet-Regi *et al.*, 2001). It has been found that these MCM-41 materials, working in the desiccant industry, exhibited enhanced water vapour adsorption properties compared with traditional silica-based materials, as a result

of the highly ordered pore structure and surface areas (Collier *et al.*, 1986). In the last two decades, the study of desiccants as dehumidifiers has attracted the interest of many researchers in the air conditioning (AC) industry (Kinsara *et al.*, 1996; Srivastava and Eames, 1998; Dai *et al.*, 2001), primarily motivated for the reduction of the 'energy penalties' caused by mechanical air dehumidification (Daou *et al.*, 2006; La *et al.*, 2010; Zhang and Niu, 2002). In this regard, desiccant material performance has been assessed with respect to the target application and the isotherm characteristics (Belding *et al.*, 1996; Chung and Lee, 2009).

Ongoing research, with respect to the improvement of water vapour adsorption (*i.e.*, high surface areas and pore volume), has directed the attention in the preparation of the metal-organic frameworks (MOFs). Great interest of this material has appeared in applications such as: i) heating and cooling (Henninger *et al.*, 2009), ii) dehumidifiers (Seo *et al.*, 2012), iii) heat pumps (Henninger *et al.*, 2012), iv) heat transformation (Zheng *et al.*, 2014), and v) gas storage (Jasuja *et al.*, 2012; Farha *et al.*, 2010). These MOFs have shown large adsorption capacity, exceptional pore tunability, high surface areas and pore volume controlled by varying the organic ligands and metal sub-units (Canivet *et al.*, 2014; Küsgens *et al.*, 2009; Ehrenmann *et al.*, 2011). Furukawa *et al.*, (2014) found that their MOF materials (measured at 25° C) exhibited outstanding adsorption/ desorption performance, reporting large water vapour adsorption capacity (735 – 850 cm^3/g) and pore volume (0.88 cm^3/g). Furthermore, several investigations in water vapour adsorption/ desorption properties have been conducted on Materials of Institute Lavoisier (MIL) frameworks. Particularly, with the intention of using the low-temperature residual heat from industrial

processes in thermally-driven adsorption chillers or heat pumps (Khutia *et al.*, 2013; Akiyama *et al.*, 2012), and in energy-efficiency dehumidification systems (Seo *et al.*, 2012). These materials presented even greater values for water vapour adsorption (1.06 – 1.7 cm^3/g – measured at 20° C) and large pore volume (1.4 – 1.58 cm^3/g), having low regeneration temperature (30 °C), and rapid-response rates for adsorption/ desorption cycles. Conversely, hygrothermics not only has to consider full adsorption capacity (*i.e*. large pore volumes under isothermal physisorption) independent of isotherm shape, but also the temperature dependency of heat and moisture diffusion and storage, along with the moisture dependency of heat storage and thermal conductivity.

In recent work conducted by Casey *et al*., (2013b) and Hall *et al*., (2012), two significant principles were recognized with respect to hygrothermal behaviour of mesoporous solids: (1) adjustments of the hygrothermal functional properties from one mesoporous can be duplicated in order to predict the behaviour of another, and (2) an empirical logarithmic correlation between mesopore diameter and the kinetics of water vapour adsorption/ desorption when performing relative humidity buffering applications in closed environments. However, the correlations between the hygrothermal functional properties, and the structure of the pore network (pore morphology, physisorption, and hysteresis) are still under debate and have not been fully quantified nor fundamentally understood. This, when considering the material's suitability for regulation of transient response to changes in relative humidity for specific buffering applications within closed environments. Consequently, enhanced moisture buffering performance from hygroscopic materials can then be intelligently designed. This, by hypothetical manipulation of the morphology of

the pore network (*e.g.* pore volume, pore size distribution, and water vapour isotherm), could eventually assist the optimization of the hygrothermal functional properties respect to relative humidity buffering applications.

1.2 Research overall aim

In this research, a top-down design tool using hygrothermal modelling simulations will be developed to enable the design of desiccant materials. Some of the major advantages in using hygrothermal simulations to inform material synthesis are: i) no associated costs for synthesis of the materials, ii) no experimental set-up costs, iii) no laboratory work and use of equipment, iv) reduced time scale, and v) feasibility for redesign and repeatability. In general terms, this top-down approach will use a design-centred strategy which follows: i) the hypothetical design of a material and application using existing hygrothermal properties data, ii) the material synthesis process, and iii) optimization and further applications of the technique.

The aim of this research is therefore to develop a hygrothermal modelling technique that assists top-down predictive design of hypothetically-created water vapour adsorption isotherms. This will be based on pre-existing mesoporous hygrothermal functional properties, optimized to suit any relative humidity buffering applications within closed environments. A methodological scheme is presented in Figure 1.2, where three main stages that constitute the top-down design tool using hygrothermal modelling simulations are proposed. It is intended that each number within the methodology (1 to 5) comply and matches with the research objectives outlined below in Section 1.3, correspondingly. Similarly, each stage represents the work presented in Chapters 4, 5 and 6.

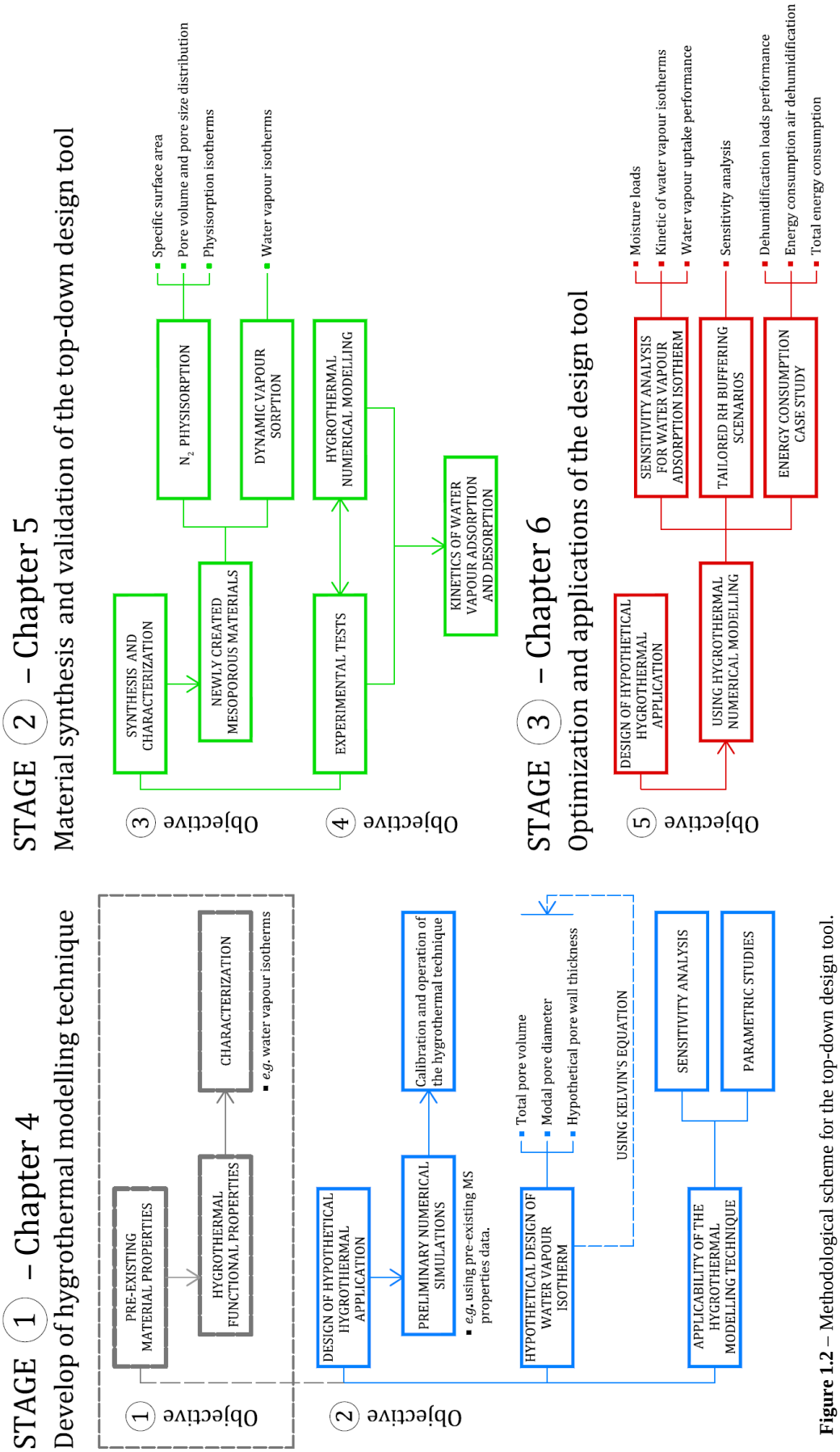


Figure 1.2 – Methodological scheme for the top-down design tool.

1.3 Research objectives

1. To determine through experimental characterization the hygrothermal functional properties of pre-existing mesoporous silica (MS) materials.
2. To develop a top-down technique based on numerical modelling simulations that assists the design of hypothetical water vapour isotherms, using as a template the pre-existing MS materials by performing sensitivity and parametric simulations.
3. To inform the design of optimized hygrothermal functional properties *via* experimental re-creation of MS through synthesis and modulation of their textural properties respect to specific relative humidity buffering applications.
4. To accomplish experimental validation against the numerical simulation data of the top-down technique. This, by performing a series of physical modelling under specific operational relative humidity scenarios and assessing the kinetics of water vapour adsorption/ desorption for the pre-existing and newly created MS materials.
5. To determine the 'optimized' water vapour adsorption isotherm, when working as dehumidifiers, and its suitability for regulating specific relative humidity buffering applications in terms of operational energy used. This, by performing numerical simulations, based on an energy consumption case scenario, to enable the relative effect on energy efficiency of the desiccant's when assisting a hypothetical mixed mode HVAC system.

1.4 Research limitations

Some limitations have been set due to time restriction of the whole research. The main objective of this research was to develop a hygrothermal modelling technique to assists and inform the design of 'ideal' water vapour adsorption isotherms. Consequently, this research does not focus on the creation of numerical modelling code packages, which may be included in hygrothermal numerical modelling. Instead, this research gives an approach that enables hygrothermal functional properties to be assessed respect to specific relative humidity buffering scenarios for operational suitability and optimization of ideal behaviour, when considering the 'hypothetically-created' water vapour adsorption isotherms. In this regard, experimental and sensitivity analysis for the kinetics of water vapour adsorption/ desorption, when considering the coupled phenomena of adsorption time-response (kinetics) and realistic scanning curves associated with the hysteresis loops within the isotherms are not included in this research.

1.5 The thesis structure

This thesis is divided into 8 Chapters, which will emphasis in the issue raised above with respect to the design of hypothetical desiccant materials based on a top-down design technique using numerical simulations. A summary of each Chapter is presented below:

Chapter 1:

Introduction. State of the problem, aim and objectives for this research.

Chapter 2:

Chapter 2 explains the scientific background associated to hygrothermal phenomena. This includes the underling concepts for moisture storage, transport and distribution mechanism within hygroscopic materials. This will be followed by detailed explanation of how the selected hygrothermal numerical modelling package operates; *i.e*. governing equations. Gas adsorption theory as well as description and classification of physisorption isotherms (*e.g*. nitrogen and water vapour) will then be presented. Finally, the hysteresis phenomena in water vapour isotherms will be briefly discussed and an overview of the implications for hygrothermics will be given.

Chapter 3:

Chapter 3 provides the description of some relevant principles and theories behind the experimental and numerical techniques used. Detail procedures will subsequently follow each of the stages (1 to 3) shown in Figure 1.2, which also correspond to objectives 1 to 5 previously outlined in Section 1.3.

Chapter 4:

Chapter 4 provides the description of the top-down design tool which is summarised in Stage 1 from Figure 1.2. Here, the description of the hygrothermal modelling technique is presented, as well as how this is used for the design of hypothetical desiccant materials. This Chapter is aimed to meet objective numbers 1 and 2 previously outlined in Sections 1.3.

Chapter 5:

Chapter 5 shows the results of the characterization for the pre-existing and new material made, which is in Stage 2 from Figure 1.2. Nitrogen and water vapour physisorption, as well as the corresponding textural properties of the pore structure are presented. The kinetics of water vapour adsorption/ desorption comparison (experimental and numerical simulation data) is then presented for the validation of the top-down design tool. This Chapter is aimed to meet objective numbers 3 and 4 previously outlined in Sections 1.3.

Chapter 6:

Chapter 6 further explore the applicability of the top-down design technique developed in Chapter 4, based on hygrothermal numerical simulations, which is in Stage 3 from Figure 1.2. The top-down technique will then be used to inform the design of optimized mesoporous desiccant for an energy-consumption case study, by assessing their suitability for regulating specific psychrometric requirements of closed environments when assisting a mixed mode HVAC system. This Chapter is aimed to meet objective number 6 previously outlined in Sections 1.3.

Chapter 7:

Chapter 7 will present the discussion section which provides a global evaluation and the theoretical implications of the results provided with respect to the implementation of the proposed top-down design technique.

Chapter 8:

Chapter 8 presents the concluding remarks respect to the overall aim and objectives outlined in Chapter 1, which also correspond to the three stages of the methodological scheme presented in Figure 1.2. Additionally, recommendations for further research given by the author are also provided here.

CHAPTER 2 Scientific Background

2.1 Introduction

Transient adsorption/ desorption phenomena are the result of complex interaction between gas molecules (adsorbate) and the surfaces of porous materials (adsorbent). These interactions are governed by physical, thermodynamic, and chemical variables such as: temperature, pressure, chemical bonding and pore network morphology. Desired water vapour adsorption/ desorption properties for hygrothermal materials might be found in the ability to exchange heat (enthalpy) and moisture (mass transport) with the environment (Hall and Hoff, 2012; Hall, 2010). A great number of building scientists have investigated such phenomena, where partial saturation in porous materials (through fluxes, heat/ mass exchange and liquid transport) has been related to areas such as: thermal comfort (Steeman *et al.*, 2010a; Osanyintola and Simonson, 2006), energy consumption (Casey *et al.*, 2013a; Hall *et al.*, 2013), building materials damage (Abuku *et al.*, 2009; Sedlbauer *et al.*, 2001) and development of new materials (Carrasco-Marín *et al.*, 1997; Hutson and Yang, 1997). The aim of this chapter is to introduce hygrothermal phenomena and numerical simulations from three main perspective areas:

i) The structure and morphology of porous solid materials.

ii) Moisture storage, transport and distribution mechanisms.

iii) Water vapour adsorption (gas adsorption theory) and the hysteresis phenomena within hygroscopic materials.

2.2 Porous solids materials

The term ‘hygroscopic’ is referred to the ability of a material to attract and hold water molecules (chemically) by adsorption processes from the environment through the open pore network (Hall and Hoff, 2012). Generally, porous materials are described as a complex matrix of interconnected voids which can allow a fluid (air, water vapour or liquid) to enter and eventually pass through all space available within it. In a porous structure, water vapour molecules will be driven by the attractive forces on the material’s surface, pressure/ temperature differences, and pore size, which will define different stages of water distribution and moisture transport. However, some restrictions can be found in the fluid path, inner surface roughness of the material, and the path length of the interconnected voids; *e.g*. tortuosity. A hygroscopic material candidate will be then described as above regarding to a specific moisture content equilibrium with the relative humidity (φ) of the ambient air and its respective pore space potential to adsorb/ desorb moisture (Hall and Hoff, 2012; Hall, 2010).

2.2.1.1 Porosity and pore size

Porosity of a material is the term used to denote how much void space is presented in a bulk material volume by the volume that occupies for it. In other words, the ratio of the void (volume/bulk) volume of the material (Rouquerol *et al.*, 1994). The resistance found within the material to fluid flow, is controlled by geometry and interconnection of the pore network commonly called permeability, δ. Porosity can be found as open and close or as connected and disconnected. The available space for water/ gas flow interaction with

environmental conditions and the void space will be called ‘connected’, whereas non-available as ‘isolated or disconnected porosity’ (Hall and Hoff, 2012). Those features are responsible for the main physical interactions between solid surfaces, liquid and gases (Rouquerol *et al.*, 1994); which is the great importance for water molecules on hygroscopic material. On the other hand, pore size definition has become into a controversial debate, since highly irregular shapes and variable interconnections leads to an insufficient definition. However, in terms of ‘the size’, the International Union of Pure and Applied Chemistry (IUPAC) (Rouquerol *et al.*, 1994) has provided a scale in order to classify the aforementioned with respect to their pore-width, instead of their radius:

- Micropores have widths smaller than 2 nm.
- Mesopores have widths between 2 nm and 50 nm.
- Macropores have widths greater than 50 nm.

2.2.1.2 Pore morphology

In general terms, pore morphology that contains cavities would be rather interconnected or not by channels/ interstices (Rouquerol *et al.*, 1994; Hall and Hoff, 2012), where some porous materials are completely formless. All these pores can be classified with respect to their availability for entry by external fluid. As Figure 2.1 shows, closed pores seen in region (a) may influence macroscopic properties such as: (1) bulk density, (2) mechanical strength, and (3) thermal conductivity. However, they are inactive in processes of adsorption and fluid flow (Hall and Hoff, 2012). Interconnected pores, will be those with continuum communication to the external surface of the body, such as: (b), (c),

(d), (e), and (f). Special attention is given for regions (b) and (f), which may have only one open side, since these would participate in adsorption/ desorption hysteresis and in pore-blocking effect; later described in Section 2.7.3. Similarly, the type of pores in region (b) and (f), would lead to a delayed desorption phase due to the so called 'ink-bottled phenomena'. Ultimately, this phenomenon would last until the pressure difference between the air-liquid interface and the small pore neck is sufficiently high. Eventually, this would enable spontaneous desorption, and hence affecting the reversibility of the isotherm leading to the well-known hysteresis loops (Branton *et al.*, 1995; Rouquerol *et al.*, 1998).

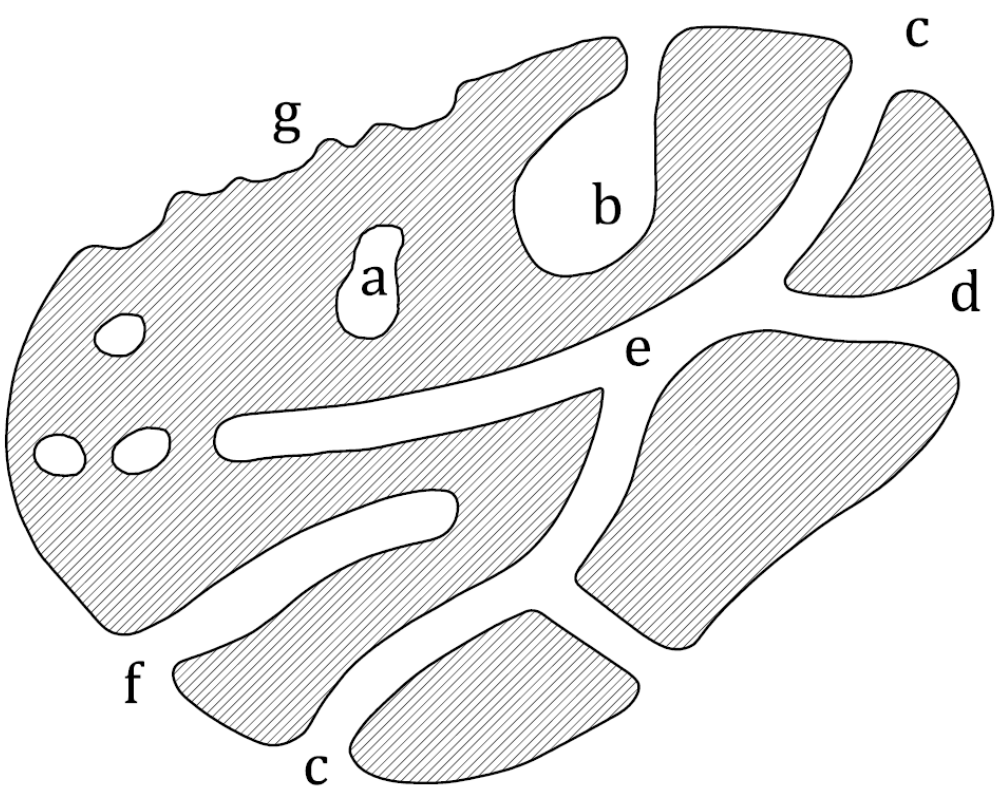


Figure 2.1 – Schematic cross-section of a porous solid showing the different types of pores. Adapted from (Rouquerol *et al.*, 1994).

2.3 Moisture storage, transport and distribution

Water vapour adsorption depends in how water molecules are arranged and attracted by electrical force interactions with the surfaces such as: i) hydrogen bonding, ii) surface-dipole attraction and, iii) capillary condensation. As Regalado (2006) and Mitchel (2005) explain, the increment on adsorbed water layers will reduce the attractive forces with distance the surface of the adsorbent, similarly with increasing the pore radius. As Figure 2.2a shows, water molecules (dipole-dipole) are tightly adsorbed into the pore wall surface (negative net electrically charged) in an extremely well-arranged monolayer. This definition is related to the 'adsorbed water' or 'hygroscopic water'. A non-hygroscopic material will be termed hydrophobic, where water molecules are not being adsorbed and only can be founded on dew point state (Künzel, 1995).

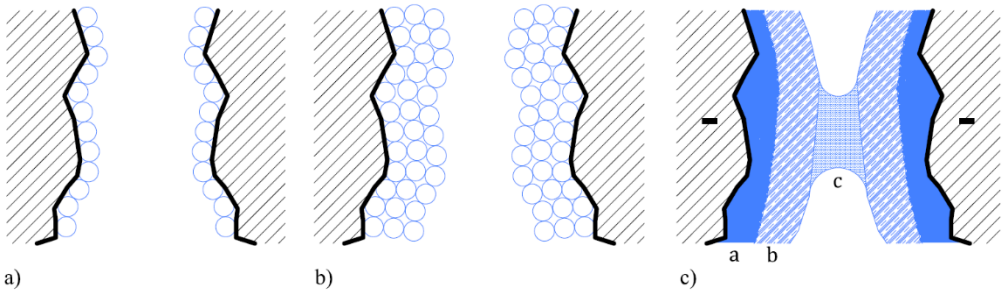


Figure 2.2 – Water distribution arrangements. Adapted from (Saarenketo, 1998).

The next layers are defined as multilayer (Figure 2.2b) and viscous or capillary water (Figure 2.2c). These layers (~ 2-6 nm) are less bonded, which represents the slightly diffusive and loosely bound water. A closer approach of the multilayer formation can be seen on Figure 2.3b, where water molecules are in direct contact with tightly adsorbed water (governed only by colloidal forces). The loosely bounded water is seen in Figure 2.2c and Figure 2.3c, which is

characterized by the presence of menisci formation. Here, surface tension is developed by water intermolecular forces of adhesion rather than of adsorption (controlled by surface tension and colloidal forces). The last layer is also known as ‘free water’, also termed as ‘gravitational water’, which is very loosely attracted by the adsorbent surface. The later, can be driven independently by gravity forces (Saarenketo, 1998). Water molecules with high dipolar momentum, leads to great attractive electrostatics interactions among them, but also with cations, ions and surfaces being charged. This is why in Figure 2.3 water molecules are well arranged on the surface, where a large amount of energy (heat of adsorption) has been released as a result of the adsorption monolayer wetting process. Conversely, loosely and viscous water molecules (Figure 2.3b-c) do not control those interactions, but rather, participate in hydrogen bond configurations for bulk water state. In other words, bulk water properties govern their intermolecular interaction, rather than with the charged surface of the adsorbent (Saarenketo, 1998).

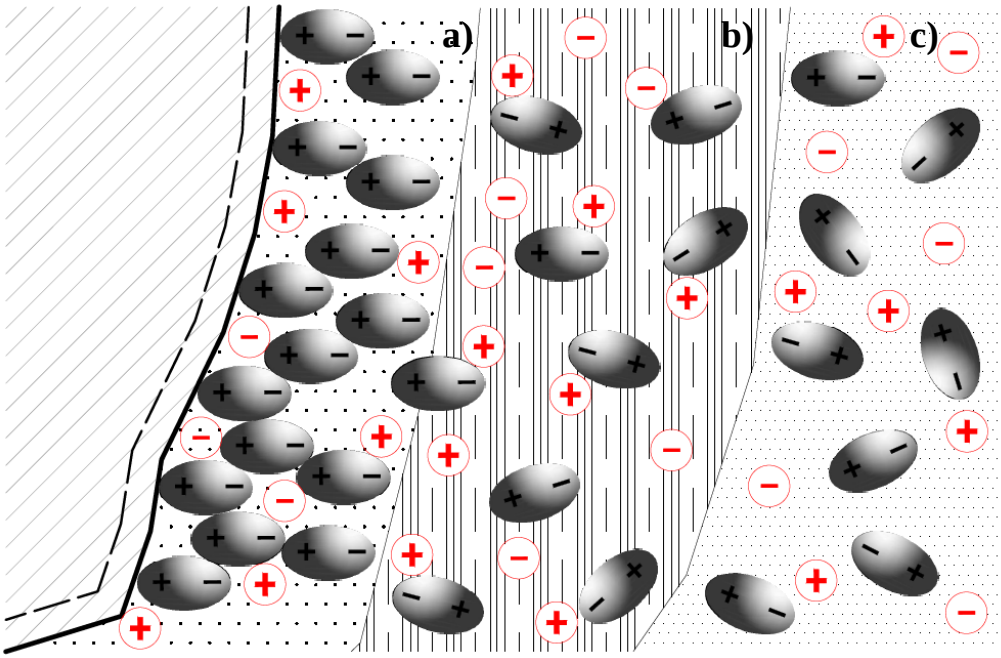


Figure 2.3 – a) Tightly adsorbed bonded water ~ 2 nm, b) loosely bonded adsorbed water ~ 2-6 nm, c) viscous or capillary water. Adapted from (Saarenketo, 1998).

2.3.1 Moisture storage

Moisture storage in hygroscopic materials is a complex phenomenon where chemical, physical, and pore morphology define the relationship between water adsorption and diffusion (Hall and Hoff, 2012). Moisture within hygroscopic materials is the term used for the presence of water molecules in vapour, liquid, and solid state. For simplicity, in terms of the driven potentials (relative humidity or partial pressure), it has been defined as the sum of all of them to a unique value known as total moisture content, *w*. This has been proposed by Künzel (1995), since water vapour diffusion, liquid transport and surface diffusion are independently active at the same time until a state of full water saturation is presented.

2.3.1.1 Moisture regions

The ability to store moisture within hygroscopic materials with respect to specific environmental conditions, such as relative humidity and liquid contact, is known as the moisture storage capacity, *w*. This has been classified in three main moisture regions, as a function of moisture conditions: (1) sorption or hygroscopic region, (2) capillary water region, and (3) supersaturated region. As shown in Figure 2.4, this non-linear relationship represents the moisture adsorbed by the three water distribution layers, explained on previous Section 2.3 and Figure 2.3. The sorption region (1) is usually dependent on environmental moisture equilibrium from φ = 0 to 0.95 (Künzel, 1995). Generally, for a given pore radii, this is dependent of water multilayers formation in the micropore and mesopore range; *i.e.* up to ~ 50 nm (Hall, 2010). Capillary

condensation phenomenon for critical pore radii (~ 10 nm at φ = 0.5) can simultaneously occur in the micropore/ mesopore range; later explained as surface diffusion (Hall and Allinson, 2009a). Additionally, the micropore volume would define the hygroscopic water domain on small pores. The capillary region (2) is usually referred to when the capillary/ viscous water domain is present and equilibrium is reached up to free saturation, W_f (or capillary saturation). In this area, multilayer of water molecules, air entrapped and menisci formation (see Figure 2.2c) reduces capillary potential, ψ for liquid transport; large pores become filled with water at φ = ~ 0.99 at the expense of small ones. As Künzel (1995) explains, above 10^{-7} m pore radii, moisture content rises steeply as the macropore structures becomes filled with water; φ > 0.95. In the supersaturated region (3), all pores are filled with water (φ = ~ 1) and there

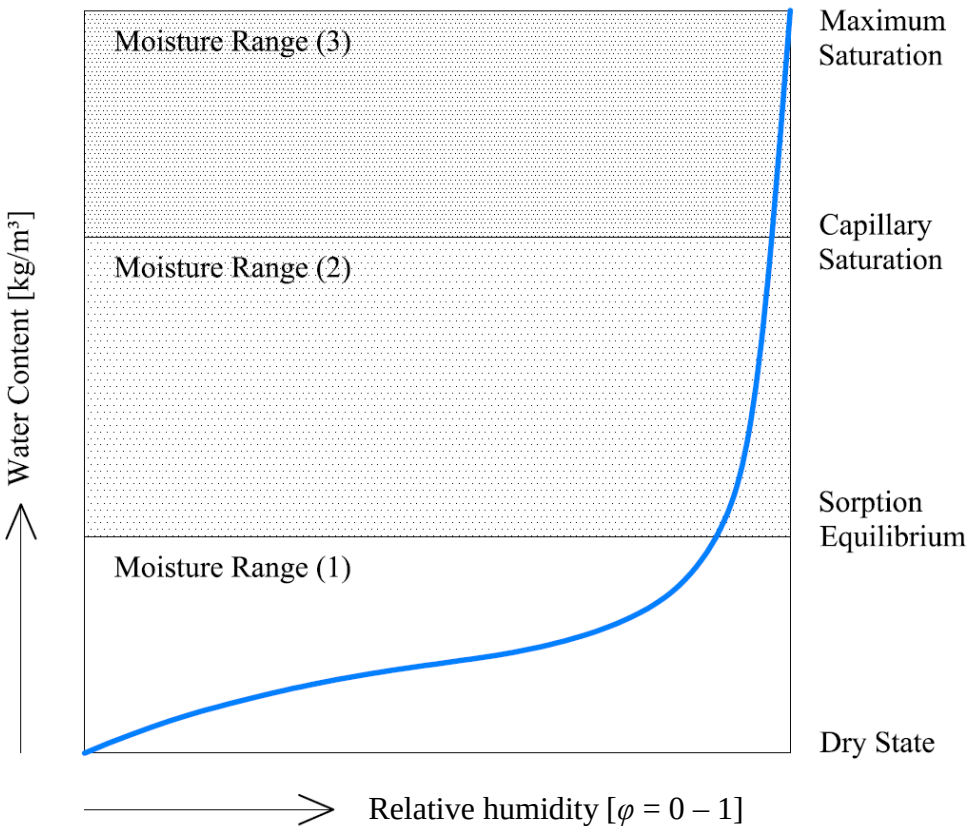


Figure 2.4 – Schematic representation of a water vapour adsorption isotherm for a hygroscopic capillary-active material. Adapted from (Künzel, 1995).

is no longer moisture equilibrium and capillary potential, ψ under natural conditions. The supersaturated state can be only achieved once trapped air-bubbles are dissolved/ discharged under external forces by applying pressure (Künzel, 1995; Krus, 1996; Hall, 2010; Hall and Hoff, 2012).

2.4 Moisture transport mechanisms

There are two main types of moisture transport mechanisms in hygroscopic materials: (1) water vapour diffusion and (2) liquid transport by capillary condensation. In principle, both mechanisms are governed by moisture gradients, also referred as vapour pressure gradients. However, liquid transport can also be present in small pores due to relative humidity gradients; also referred to as surface diffusion (Section 2.4.2.1). Figure 2.5 shows that water vapour diffusion can independently be driven from liquid transport.

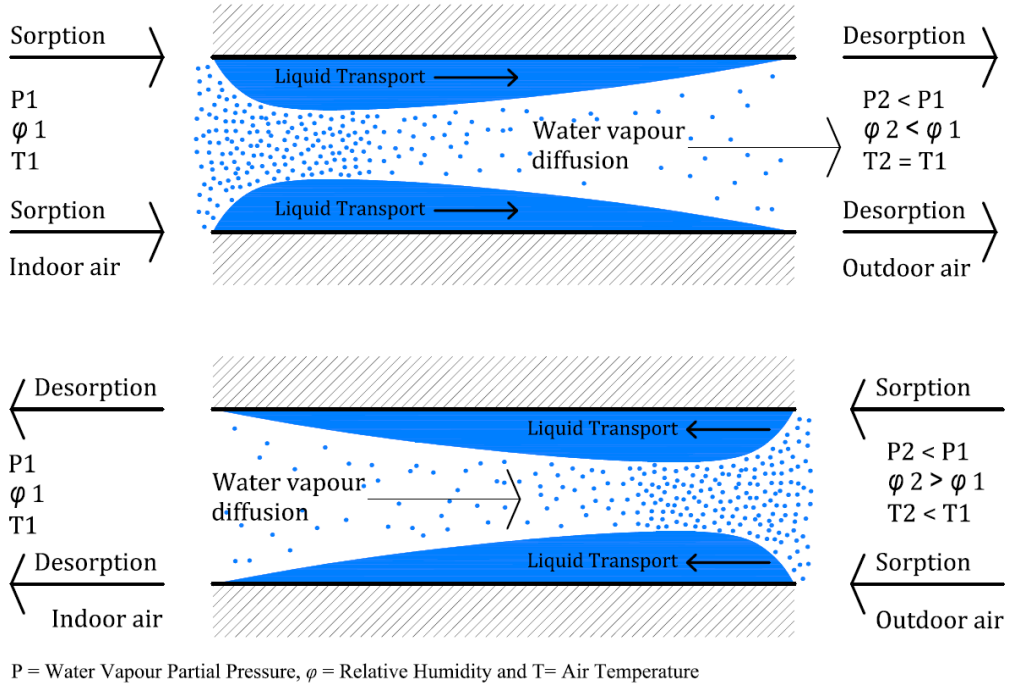


Figure 2.5 – Schematic representation of an interconnected porous material and the moisture transport mechanisms during a) dry and b) wet winter. Adapted from (Krus, 1996).

Here, a schematic representation of an interconnected porous material with defined indoor/ outdoor boundary conditions is presented; a dry winter (Figure 2.5a) and a wet winter (Figure 2.5b). As a consequence of moisture mass concentration, liquid transport, will tend to be accumulated as a sorbate film which becomes thicker as relative humidity increases (Krus, 1996; Künzel, 1995).

2.4.1 Water vapour diffusion

Water vapour diffusion has the driving potential from total pressure, *P* temperature and mass transport. The term diffusion, referring to Fick's first law of diffusion, is defined as the diffusive mass flux rate which is proportional to the mixture mass density, $\rho = \rho_A + \rho_B$, as well as by its gradient mass concentration, $m_A = \rho_A / \rho$; it is commonly expressed in kg/s m^2 (Incropera *et al.*, 2007). As previously seen in Figure 2.5a (dry winter), water vapour molecules will tend to diffuse from the higher (indoor) to the lower mass concentration (outdoor). Here the pressure gradient along with the open space and mass concentration is governing water molecules diffusion throughout. In the case of the wet winter (Figure 2.5b), water vapour diffusion becomes more unstable as temperature gradients are dominant from the warmest side (left side of Figure 2.5b) and mass concentration from the coldest side. Consequently, a counter flow of water vapour diffusion from the outdoor can also occur, since evaporation of liquid water is activated by temperature gradients; *i.e.* diffusion flux in reverse direction. Additionally, liquid transport from the outdoor to the indoor can be also be triggered as high mass concentration is developed by surface diffusion (Krus, 1996; Künzel, 1995).

2.4.1.1 Fick's law – mass fraction diffusivity

Mass diffusivity is an important transport property of matter (Incropera *et al.*, 2007), where the rate of migration is expressed by its flux (J). The flux is the quantity of that migration passing through a given area, A in a time interval, *t* divided by A and the time duration of that interval Δ*t* (Atkins and De Paula, 2010). It is also referring as the proportionality of the flux of matter to the concentration gradient as the Fick's first law of diffusion states; where J = -D (dN/dz), where the constant D is known as the 'diffusion coefficient'. Because of the mass concentration variations, this law implies that diffusion will be faster when it varies steeply, whereas it will be slow when concentration distribution is nearly uniform. In the same logic, it is expected spontaneous dynamic tendency of molecules for their movement to occur, in which combining with its chemical potential can be interpreted as an effective force per mole molecules, called 'thermodynamic force' (Atkins and De Paula, 2010).

2.4.1.2 Partial and saturated vapour pressure

Differing from the theoretical ideal gas (monatomic gas), air can be treated as a mixture of gases. Where total gas pressure, *P* will be related to the sum of individual partial pressures; *i.e*. the pressure of individual gas components in the air mixture (Chang and Overby, 2003). Dalton's law states that: '*the total pressure of a mixture of gases is just the sum of the pressures that each gas would exert if it were present alone*'. When water vapour molecules and dry air are mixed together, both partial pressures can be expressed as total pressure, P_T, (Hall, 2010; Hens, 2012) as Equation 2.1 shows:

$$P_T = P_A + P_B, where\ P_A = \frac{n_A RT}{V}\ and\ P_B = \frac{n_B RT}{V}$$

Equation 2.1 – Total pressure from Dalton's law. From (Chang and Overby, 2003).

Where P_T = total pressure, P_A and P_B = partial pressure *A* and *B*, *n* = the total number of moles of gases present, *R* = the proportional constant, 'the Gas Constant', and *T* = absolute temperature (°K). In terms of air relative humidity, φ partial vapour pressure (p_v) is defined as a proportion of the vapour saturation pressure p_{vsat} in thermodynamic equilibrium. Vapour pressure will increase as temperature does, and hence, for a particular air temperature, there would be an equilibrium vapour pressure between the liquid and solid (non-vapour phases). This is expressed as the maximum vapour concentration pressure, known as 'vapour pressure saturation', p_{vsat}; where further vaporization is not physically possible without changing the temperature (Hens, 2012). At low vapour pressure it can be expected less water vapour molecule interactions to the point of aggregation or condensation phase. By increasing pressure and temperature, kinetic energy gives to water vapour molecules the potential to move and collide with each another, and also to escape from the aggregate state. At this point, the evaporation phase would corresponds with the saturation pressure, p_{vsat} when is equal to the atmospheric pressure (760 mm Hg) at 100°C. On the other hand, as mass concentration and kinetic energy increases on the air-vapour mixture, the Fick's first law can be related with the flux migration and the gradient direction. This eventually results in a higher water vapour diffusive transport rate. In terms of vapour concentration, water vapour would modify the air mass depending on its relative humidity; which is equal to the ratio of partial and saturated pressure. Therefore, the maximum vapour saturation pressure p_{vsat} and concentration (in

thermodynamic equilibrium) of the air-vapour mixture would be highly dependent on temperature (Hens, 2012).

2.4.1.3 Knudsen and Fickian diffusion

Water vapour fluxes can be restricted through porous materials, by the pore morphology of the pore path (*e.g*. tortuosity). This may cause an impediment for water vapour fluxes to access the cross-section of the pore affecting gas adsorption (Hall and Hoff, 2012). Fick's diffusion (Figure 2.6a) is applicable for pores larger than 10^{-6} m; also known as macropore diffusion. Below this pore size, water vapour molecules collisions will be higher with the pore surface rather than among molecules. Brownian motion is therefore applicable for Fickian diffusion, since molecules in random movement, are not dependent on their previous motion governed by kinetic energies (Hall, 2010). However, Fickian diffusion (empty light-blue circles in Figure 2.7) can be restricted within the pores, due to the increment of adsorbed water vapour layers. As sketched in Figure 2.7, multilayer adsorption would eventually fill all the pore space.

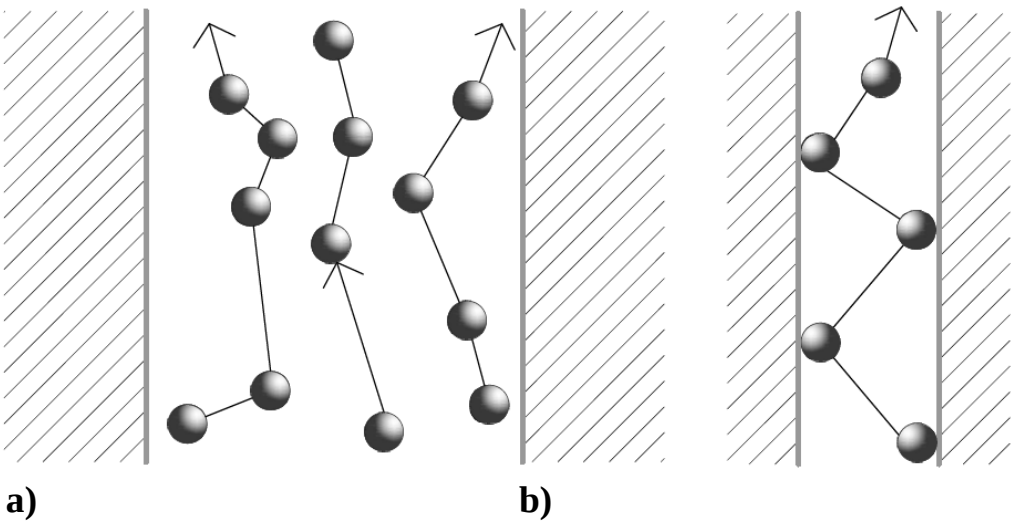


Figure 2.6 – Representation of a pore structure where a) Knudsen and b) Fickian water vapour diffusion are presented.

The latter, would lead to capillary condensation and causing increased diffusion resistance (Ruthven, 1984); normally termed as the water vapour diffusion resistant factor, μ (Künzel, 1995). When water vapour concentration arises in small pores, the resistance for water vapour to flow increases. Here, molecular diffusion will be the dominant transport mechanism, as the travelled distance between molecular collisions and the pore wall is reduced. However, at low vapour pressure, the mean free path of the molecule would be greater. Here, water molecules collision would occur more frequently with the pore wall; process known as Knudsen diffusion, which refers to Figure 2.6b (Ruthven, 1984). This process is taking place on small or micropores less than $5x10^{-9}$ m (Krus, 1996; Künzel, 1995), where water vapour molecules would greatly interact with the surface of the pore structure. It can be suggested that reducing the kinetic energy on small pore size (as Knudsen diffusion) would eventually increase adsorption process and clustering of water molecules. Here, micropore diffusivity would be dependent on the chemical potential gradient, instead of the concentration one, leading to constant surface intermolecular attractive forces on the adsorbent surface (Ruthven, 1984).

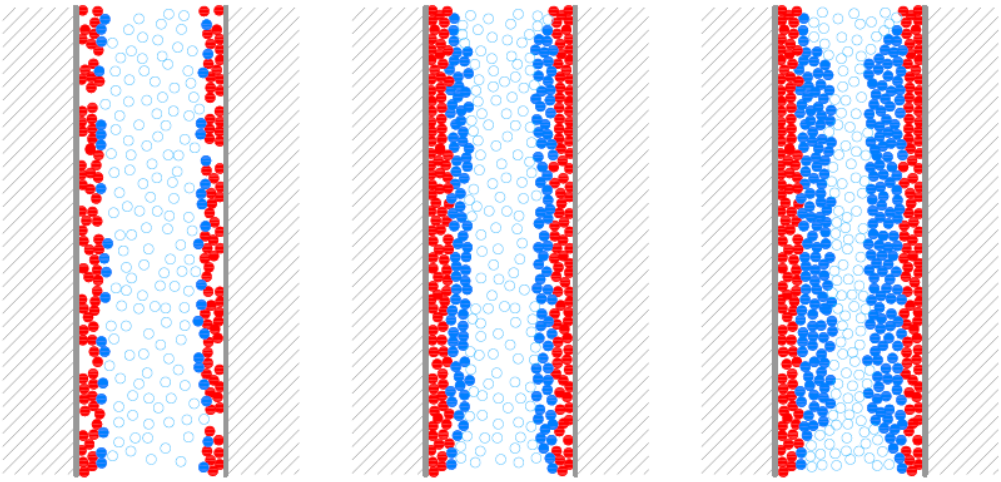


Figure 2.7 – Fickian diffusion in the presence of multilayer adsorption.

2.4.2 Liquid transport

Water vapour diffusion and liquid transport can simultaneously be driven in porous materials. However, as mass concentration arises, water vapour diffusion fluxes can no longer be expected. Unlike water vapour diffusion driven by vapour pressure, liquid transport is governed by relative humidity gradients (Krus, 1996; Künzel, 1995).

2.4.2.1 Surface diffusion

Moisture liquid transport is already occurring on small pore size or micro-capillaries. This process is known as ‘surface diffusion’ in an adsorbed layer. After increasing diffusion mass concentration on micropores (once water molecules have been adsorbed by intermolecular surface energies), surface diffusion would slowly arise through the pore structure by surface tension. This can also be enhanced by increasing temperature, which would lower the surface tension and viscosity of water molecules, and enabling them to flow in these micropores (Krus, 1996; Künzel, 1995). This type of liquid moisture transport is actually occurring at the moisture region (1) in Figure 2.4, where adsorption process through vapour diffusion (Fickian and Knudsen) is being incremented layer by layer. Surface diffusion would require special determination by experimental work, since adsorption of water vapour in this region (small pore size) leads to a combined effect from both capillary condensation and surface diffusion. It is advised that surface diffusion together with capillary condensation is included independently of vapour diffusion (Künzel, 1995). As Figure 2.8 shows, liquid transport (surface diffusion) on very small pore space

can be obstructed by adsorbed water molecules at very low relative humidity levels. This typology of molecular condensation will be later explained in more detail in Section 2.7. On the other hand, increasing mass concentration and achieving critical pore size (refer to Figure 2.8), will eventually lead to capillary condensation.

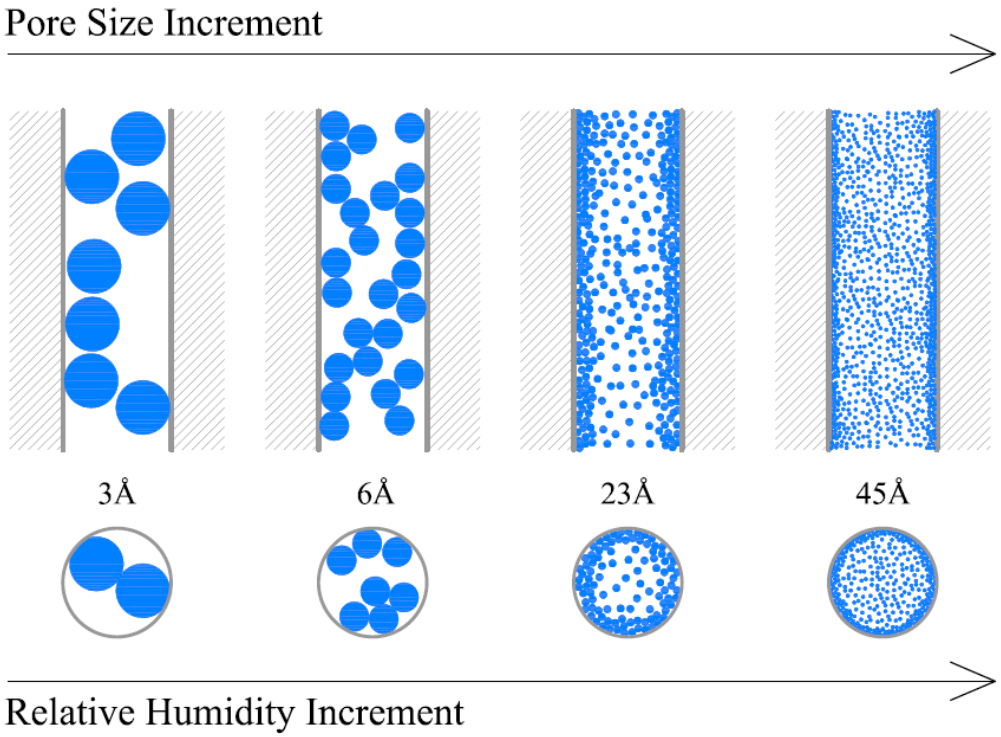


Figure 2.8 – Schematic representation of surface diffusion in different pore sizes.

2.4.3 Capillary condensation

Capillary condensation is responsible for liquid transport through the pore network, which is occurring in the capillary region (2) seen in Figure 2.4, where $\varphi > 0.95$ in the moisture storage diagram. Tensional stress on water molecules is on continuous movement, and it is driven by surface tension (intermolecular attractive forces) and pressure differences in the air-water interface (refer to Figure 2.9).

Capillary condensation has its origin on the capillary water domain, which is founded at high moisture content and large pore size. Surface energetics play an important role on capillary action determined by the affinity between the contact angle and the surface in contact with the air-liquid interface. However, water molecules can still spread over the capillary if the surface energy of the solid (σ_{SA}) in contact with the air, minus the solid in contact with water (σ_{SL}), is higher than the liquid in air (σ_{LA}); thus, $\sigma_{SA} - \sigma_{SL} > \sigma_{LA}$ = water can distribute through the capillary (Hall and Hoff, 2012). On the other hand, Laplace's law states that, there is a pressure dependency on surface tension as a result of the hydrostatic equilibrium between curved air-water interfaces (refer to Figure 2.9). It also provides the relationship between the height h and the radius r for its rising movement from: $h = 2\gamma/\rho g r$; the lower the radius, the higher the height of the water column (Hall and Hoff, 2012).

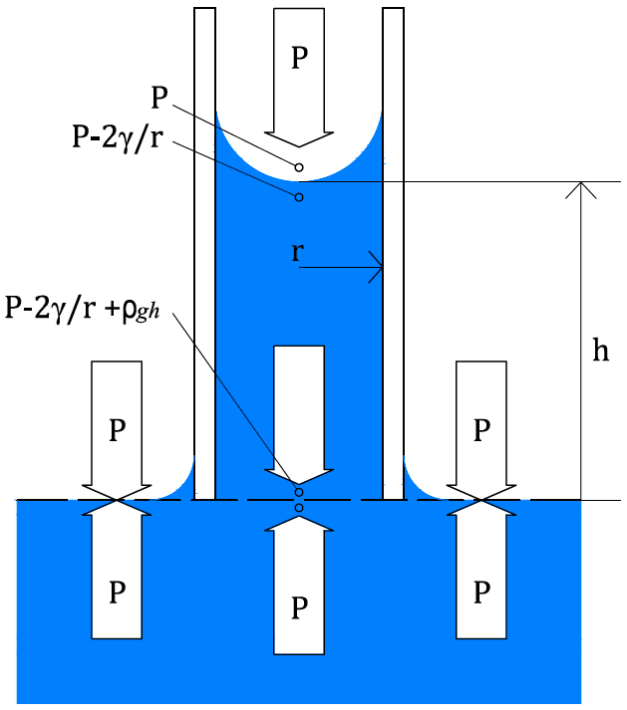


Figure 2.9 – Capillary system and liquid-gas interface in the capillary tube. Adapted from (Spangler and Handy, 1982; Atkins and De Paula, 2010).

2.4.3.1 Kelvin's equation of capillary condensation

Kelvin's equation is associated with gas condensing or evaporating within confined pores with respect to the pressure difference at the liquid-vapour interface. This implies that there is a mechanical equilibrium between the gas pressure above the meniscus curvature, P_a with respect to the pressure within the mass of water P_1 (refer to Figure 2.10). Conversely, when a spherical liquid-gas interface of radius, r and surface tension, γ is presented, the pressure P_1 within the mass of water is lower than the outside gas pressure P_a. This pressure difference relates to a phenomenon between the saturation vapour pressure, p_{vsat} within the mass of water to that of a flat surface, p_{vsat}*. Consequently, the water vapour having a pressure lower than p_{vsat} can condense within the pore, which is termed as the capillary condensation.

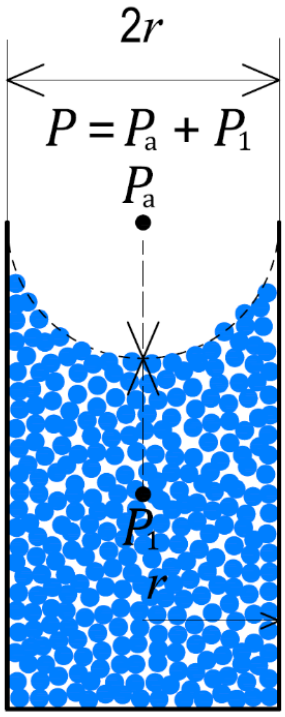


Figure 2.10 – The Kelvin capillary condensation.

The mathematical expression that applies to capillary condensation and vapour pressure is obtained from the Kelvin's Equation:

$$p_{vsat} = p_{vsat}^{*} e^{2\gamma Vm / rRT}$$

Equation 2.2 – Kelvin's equation. From **(**Hall, 2010**).**

Where p_{vsat} is the saturation vapour pressure of water held inside a pore of radius r, p_{vsat}* saturation vapour pressure above a flat surface, V_m molar volume of water (~18 ml at STP) and R, the gas constant (Hall, 2010). The so called, critical pore radii (r_c), is found by rearranging the Kelvin's equation by assuming $p_v = p_{vsat}$**.** This can lead to the specific relative humidity value for capillary condensation and the specific pore radii r, by following the expression from Hall (2009a).

$$\varphi = \frac{p_v}{p_{vsat}} = \exp\left(\frac{2\gamma}{r} \frac{1}{R_{vap}\rho_w T} \right)$$

Equation 2.3 – Relative humidity derived from critical pore radii when Kelvin condensation occurs - Kelvin's Equation Rearrangement taken from (Hall and Allinson, 2009a).

Where R_{vap}, is the gas constant for water vapour (J/kg K) and ρ_w is the density of liquid water (kg/m^3). Wider pores require higher relative humidity for capillary condensation to occur (Hall, 2010; Hens, 2012). Conversely, increasing pore size will lead to a more flat menisci surface and more tensile stress on the menisci (Hens, 2012).

2.5 Hygrothermal numerical simulations

The simultaneous heat and moisture transport phenomena – the study of hygrothermics – has become a transdisciplinary theme worldwide, which considers the limitation of the exchange of heat, air and moisture within an enclosed volume of air in which psychrometric condition are isolated. A number of worldwide validated computer codes and advanced hygrothermal numerical models have been developed for the understanding of hygrothermics, aiming to match the requirements of controlled 'closed environments' (Trechsel, 2001). Over the past 15+ years, hygrothermal numerical packages have been validated against experimental data, and addressed as part of the Annex 41 project (Woloszyn and Rode, 2008), which include (but not limited to) DELPHIN, HAM, MATCH, MOIST, TCCD2, and WUFI (Trechsel, 2001; Hall, 2010). These numerical packages are frequently used to simulate bulk-scale hygrothermal behaviour and to represent reliable input data for numerical model validations for heat and moisture transport/ storage (Pavlík and Černý, 2008; Kalamees and Vinha, 2003). The significance of the hygrothermal numerical modelling tools, is the predictive capacity for transient response of combined heat, air and moisture between an interior air zone and the adjacent hygroscopic material. Primarily, when considering the migration of moisture through water vapour diffusion and liquid transport, and the normal flows of heat (conduction, convection and radiation). Currently, all hygrothermal numerical models are required to accurately represent (as a minimum) the following bulk-scale transport and storage phenomena (BSI, 2007; Hall, 2010):

- Heat storage of the dry building material and of the contained moisture

- Heat transport by thermal conduction with moisture-dependent thermal conductivity
- Latent heat transport by vapour diffusion with phase change (vapour evaporation/ condensation)
- Moisture storage by vapour sorption and capillary forces
- Water vapour transport by vapour diffusion
- Liquid transport by surface diffusion and capillary conduction

A schematic diagram is provided in Figure 2.11, where the execution flow chart for hygrothermal numerical simulations is presented according to the prEN 15026; updated in 2007 (BSI, 2007).

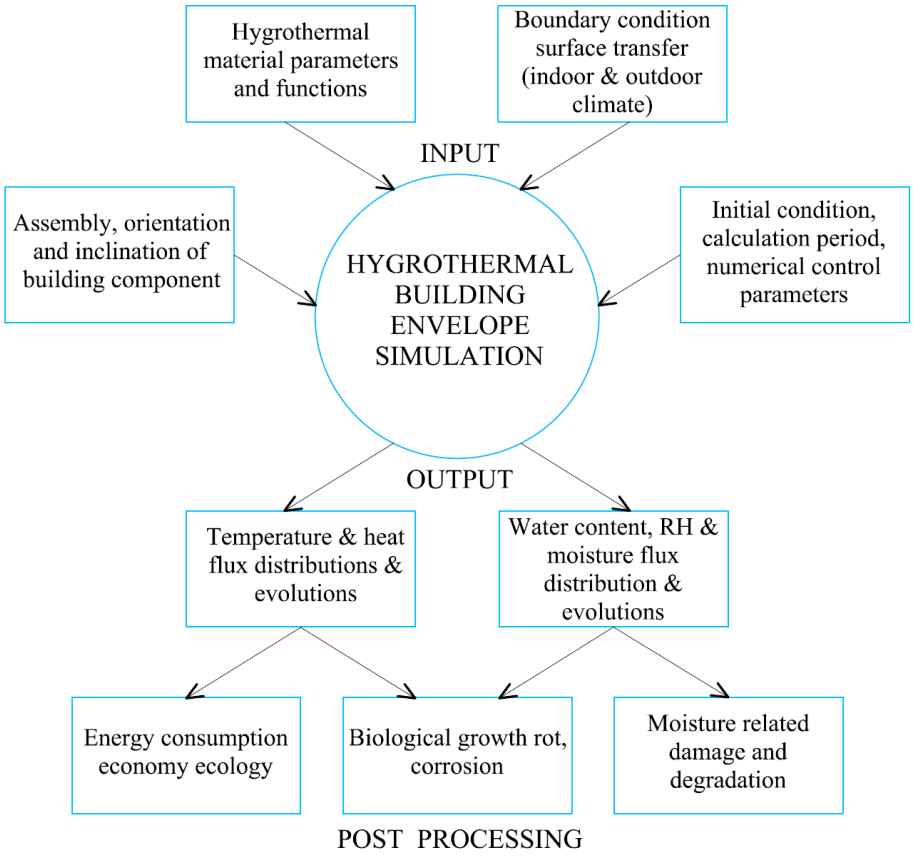


Figure 2.11 – Flow chart for hygrothermal simulations according to the prEN 15026, 2004. Adapted from (Hall, 2010).

2.5.1 WUFI validation

Extensive validation against experimental data have been conducted for the WUFI hygrothermal models. This include full evaluation of WUFI+ against a selection of standards such as: VDI 6020, ANSI/ASHARAE Standard 140-2007, within the framework of the IEA ECBCS Annex 41 (Antretter *et al.*, 2011). As a design tool for building envelope and architects, WUFI 1D was validated against the moisture behaviour of natural stone façade (Karagiozis *et al.*, 2001), for determination of energy patterns of latent heat loads and indoor air comfort and hygiene (Künzel *et al.*, 2005), and for moisture and heat transfer between two different rooms (test and reference room) (Holm *et al.*, 2003). WUFI was also validated and compared for practical applications with other numerical simulations respect to the influence of uncertainties of initial hygrothermal conditions within the components for realistic analysis. This was performed when drying an autoclave aerated concrete (AAC) in a flat and sealed roof (Holm and Kuenzel, 2002). WUFI+ was also validated against field experimental data when considering a room constructed by stabilised rammed earth (SRE), in which an unheated and unoccupied room was tested during 10 months for temperature and relative humidity variations (Allinson and Hall, 2010). The influence of the time averaging of the exterior wind-driven rain loads was examined for determination of local climate effect on the performance of envelopes (Karagiozis *et al.*, 2003). WUFI has also been simulated and validated against microbial growth for external insulations systems when condensation occurred due to low resistance in insulated buildings (Krus *et al.*, 2013), and in exterior finishes (Künzel *et al.*). For this research, the Wärme und Feuchte Instationär (WUFI) hygrothermal numerical model, WUFI+ v2.5.3 (Fraunhofer,

Germany), was used to perform all numerical modelling simulations based on the extensive peer review presented and availability (Karagiozis, 2001; Karagiozis *et al.*, 2001; Kuenzel *et al.*, 2001).

2.5.2 Input data for hygrothermal simulations in WUFI+

The prediction of hygrothermal performance requires important information regarding to the 'closed environment' (*e.g.* geometry, boundary conditions and material's hygrothermal properties). The initial set of data needed for the numerical simulation is provided here with respect to the building component:

- Proper mesh size for the numerical grid.
- Thermal and hygric parameters, and material functional properties; *i.e.* which include (but not limited to) bulk density, porosity, specific heat capacity, moisture-dependant thermal conductivity, and moisture-dependant water vapour diffusion resistance factor.
- The climatic boundary conditions (inside/ outside) complemented by the time increments respect to the climatic data.
- The transitional (*e.g.* heat and moisture transfer coefficients, and the short wave absorptivity) or symmetrical conditions for the boundaries of the building components.

2.5.2.1 Boundary conditions and climate data

Generally, the boundary conditions for hygrothermal simulations imply two defined exterior and interior conditions between elements. These conditions are

often regarded as critical to its accuracy for the mathematical model. WUFI+ not only considers the evolution of temperature and moisture distribution within the material based on the transport equations (refer to Equation 2.12 and Equation 2.13), but also its interaction with the surroundings (*e.g.* exterior and interior ambient air). Therefore, the resultant heat and moisture fluxes through the surfaces, as well as the direction and magnitude would strongly depend on the initial condition of the component with its surroundings. Figure 2.12 shows the exterior climate data used in WUFI+, which is typically based on hourly meteorological parameters such as: exterior air temperature and relative humidity. Other exterior climate data includes: vertical rain load on the exterior surface (L/m^2h), vertical solar radiation (W/m^2) incident on the exterior surface, and barometric pressure (Pa). If preferred, the interior climate data (ambient air within the 'closed environment') can be also introduced as hourly data of temperature and relative humidity.

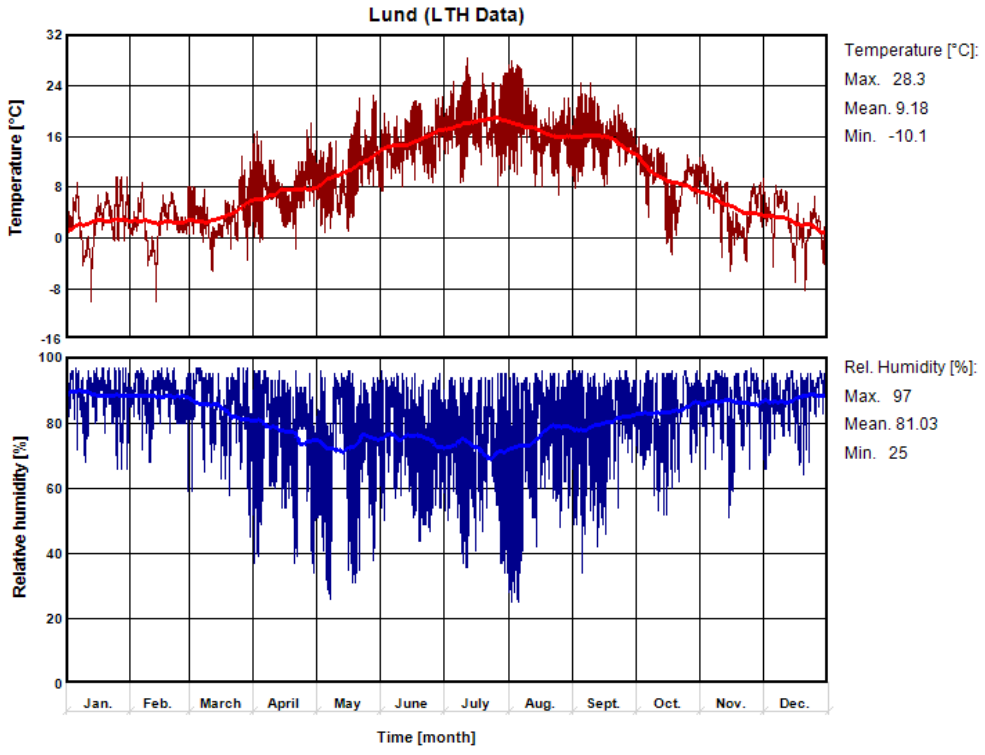


Figure 2.12 – Weather data input for WUFI+. (Fraunhofer)

In the case of interior loads and occupancy, WUFI+ offers an internal loads calculator for human activities (metabolic rate – refers to) or an hourly load schedule which includes: convective and radiant heat, moisture loads rates, and CO_2 production.

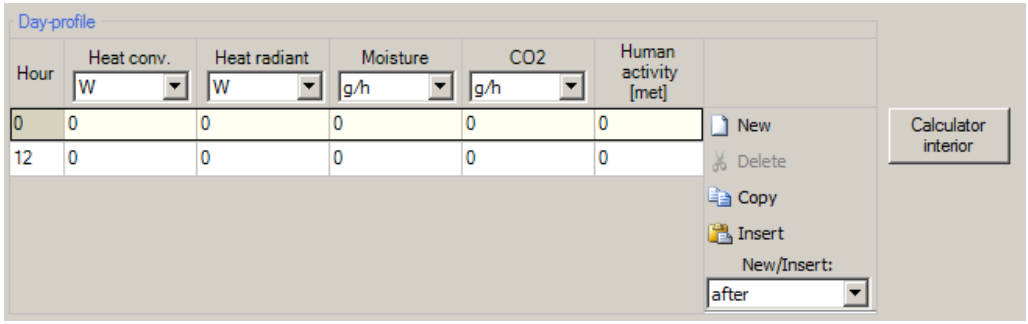


Figure 2.13 – Internal loads calculator. (Fraunhofer)

2.5.2.2 Moisture storage function

The moisture storage function is one of several hygrothermal properties where $w = f(\varphi)$ defines the non-linear relationship between the mass of adsorbed water and the ratio of vapour pressure to saturation vapour pressure, known as the sorption isotherm when at constant temperature. The inputs for the moisture storage function, *w*, are assigned with respect to the relative humidity, which assumes that equilibrium moisture content has also been reached.

2.5.2.3 Liquid transport coefficients

The main transport mechanism within hygroscopic materials is the liquid transport through capillary condensation. WUFI+ assumes that such process can be described as a diffusion phenomenon, following that:

$$g_w = -D_\varphi \nabla_\varphi$$

Equation 2.4 – Liquid transport coefficient

where,

g_w	= liquid flux density	(kg/m^2 s)
D_φ	= liquid conduction coefficient	(kg/m s)
φ	= relative humidity	(-)

Additionally, WUFI+ uses as a standard parameter for capillary suction that is the water absorption coefficient, *A*; *i.e*. when a hygroscopic material is in contact with liquid water. Combined with the capillary transport coefficient, D_{ws} (capillary uptake when a surface is fully wetted), the suction process can be estimated as follows:

$$D_{ws}(w) = 3.8(A/W_f)^2 1000^{w/W_f - 1}$$

Equation 2.5 – Capillary transport coefficient

where,

$D_{ws}(w)$	= capillary transport coefficient for the suction process	(m^2/s)
A	= water absorption coefficient	(kg/m^{2}s$^{0.5}$)
w	= moisture content	(kg/m^3)
W_f	= free water saturation also called capillary saturation	(kg/m^3)

2.5.2.4 Water vapour diffusion

As previously described in Section 2.4.1, diffusion of water vapour in air (refer to Equation 2.6) can be restricted by the pore morphology (*i.e*. tortuosity) and by the increment of adsorbed water vapour layers. In the same logic, WUFI+ introduces the water vapour diffusion resistant factor, μ (Equation 2.8), which is the ratio of water vapour permeability of air, δ_{air} (Equation 2.7) to that within the material δ (Equation 2.9); *i.e*. moisture transport *via* Fickian diffusion.

$$g_v = -\delta_{air} \nabla p_v$$

Equation 2.6 – Water vapour diffusion in air

$$\delta_{air} = 2x10^{-7} T^{0.81} / P_0$$

Equation 2.7 – Water vapour permeability in air

$$\mu = \frac{\delta_{air}}{\delta}$$

Equation 2.8 – Water vapour diffusion resistant factor

where,

g_v = water vapour flux density (kg/m^2 s)

δ_{air} = water vapour permeability in air [kg/(m s Pa)]

δ = water vapour permeability of a material [kg/(m s Pa)]

p_v = water vapour partial pressure (Pa)

P_0 = ambient atmospheric pressure (Pa)

In practical terms, the product between the water vapour permeance, *W* and the thickness of the material, *d*, is used to estimate δ.

$$\delta = Wd$$

Equation 2.9 – Water vapour permeability of the material

Correspondingly, the water vapour permeance, *W* (Equation 2.10) can be estimated by the water flow rate, *G* (experimentally given by $\Delta m/t$), which is divided by the product of difference in water vapour pressure, Δp_v (between the two opposed surfaces) and the expose surface area, A. Procedures for the experimental estimations can be found in the BS ISO 12572 (ISO, 2001).

$$W = \frac{G}{A\Delta p_v}$$

Equation 2.10 – Water vapour permeance

2.5.2.5 Moisture-dependent thermal conductivity

Thermal conduction (dry state) is defined as the heat transfer which occurs between molecules in close contact each other. The rate of heat transfer (per unit time) by conduction is proportional to the temperature gradient, and is limited by the thermal conductivity coefficient, λ (W/m K), under steady conditions and for one dimension (Hall, 2010). In hygroscopic materials, WUFI+ recognizes the moisture-dependency in thermal conductivity as an isolated contribution to heat transport by the effect of localized water within the material. This means that when increasing the moisture content, *w* there is a gradual occupation of the void spaces (water with higher λ than air) by capillary water. The latter results in inter-particle menisci formation (Hall and Allinson, 2009b), which increases the heat flow within the material, and so the thermal conductivity. However, further heat transport is also considered by condensation and evaporation (sensible and latent heat, respectively), which cannot be solely described by the thermal conductivity equations. The following equation from Künzel (1995) describes the moisture-dependent thermal conductivity for hygroscopic materials:

$$\lambda(w) = \lambda(1 + b \cdot w / \rho_s)$$

Equation 2.11 – moisture-dependent thermal conductivity

where,

λ = thermal conductivity of the dry material (W/m K)

ρ_s = bulk density of dry material (kg/m^3)

b = thermal conductivity supplement (%/M)

The supplement term *b*, indicates the percentage in which thermal conductivity increases per mass percent of the moisture content, *w*.

2.5.2.6 Combined heat and moisture transport equations

The governing equations for the combined heat and mass transfer for vapour diffusion and liquid transport, as well as the thermal transport are solved with the following equations:

$$\frac{dw}{d\varphi} \cdot \frac{\partial \varphi}{\partial t} = \nabla \cdot \left(D_w \nabla \varphi + \delta_p \nabla (\varphi \cdot p_{sat}) \right)$$

Equation 2.12 – Moisture balance

$$\frac{dH}{dT} \cdot \frac{\partial T}{\partial t} = \nabla \cdot (\lambda \nabla T) + h_v \nabla \cdot \left(\delta_p \nabla (\varphi \cdot p_{sat}) \right)$$

Equation 2.13 – Heat balance

The moisture storage function, which is proportional to the derivative of the water vapour isotherm ($\partial w/\partial \varphi$), is presented in the LHS of Equation 2.12. The divergence of liquid and vapour flow are described on the RHS of Equation 2.12, which accounts for the transport term. There is a strong temperature-dependency (saturation pressure $p_{vsat} \sim \exp(T)$) for water vapour pressure ($p_v = \varphi \cdot p_{vsat}$), which is the driving potential for vapour fluxes, whilst capillary forces govern liquid flow as a function of φ; *i.e.* from Kelvin condensation.

The divergence of vapour flow multiplied by the specific heat of evaporation is represented in the RHS of Equation 2.13, which denotes the latent heat term of the energy balance. The sensible heat flow is represented by the divergence of heat conduction. The storage term of the energy equation is represented in the LHS of Equation 2.13 – described as the derivative of total enthalpy – contains the heat capacity of the dry material plus the enthalpy of absorbed water which depends on its state; *i.e*. solid, liquid or gaseous phase (Künzel *et al.*, 2005; Karagiozis, 2001; Kuenzel *et al.*, 2001; Künzel, 1995). A schematic diagram is

provided in Figure 2.14, where it is explained the most important steps in solving the coupled heat and moisture transport equations (Equation 2.12 and Equation 2.13). After the setting of the inputs data and parameters (*e.g.* steady-state of initial distributions of moisture and temperature – refer to the list provided in Section 2.5.2), the transient calculations of the coupled phenomena are performed. This, until the criterion (length of time increments with respect to the mesh size) is reached, the heat and moisture transport equations are solved and convergence is executed. In simple terms, this occurs when the termination criteria for each numerical iteration is reached. In the case of estimations of relative humidity between two successive iteration steps, WUFI+ will calculate the maximum change variable until the iteration falls below one thousandth of one percent in relative humidity. Similarly, when the temperature gradient is estimated, WUFI+ will calculate the maximum change variable until the iteration falls below one thousandth of one degree centigrade. This will finally determine the accuracy of the numerical model with respect to the time and structure (mesh size) of the boundary conditions, for the expected temperature and moisture transients in the material.

On the other hand, the results from the hygrothermal simulation consist of heat and moisture fluxes, complemented by cross-sectional gradients of temperature, relative humidity and moisture content. This can also be visualized within specific limits or points respect to a time slot or temporal variations within the building component. Additionally, all outputs can be saved in text (txt.) and Excel files documents for further analysis in order to detect inconsistencies, and for comparison with suitable experimental data if desired (Künzel, 1995; Hall, 2010).

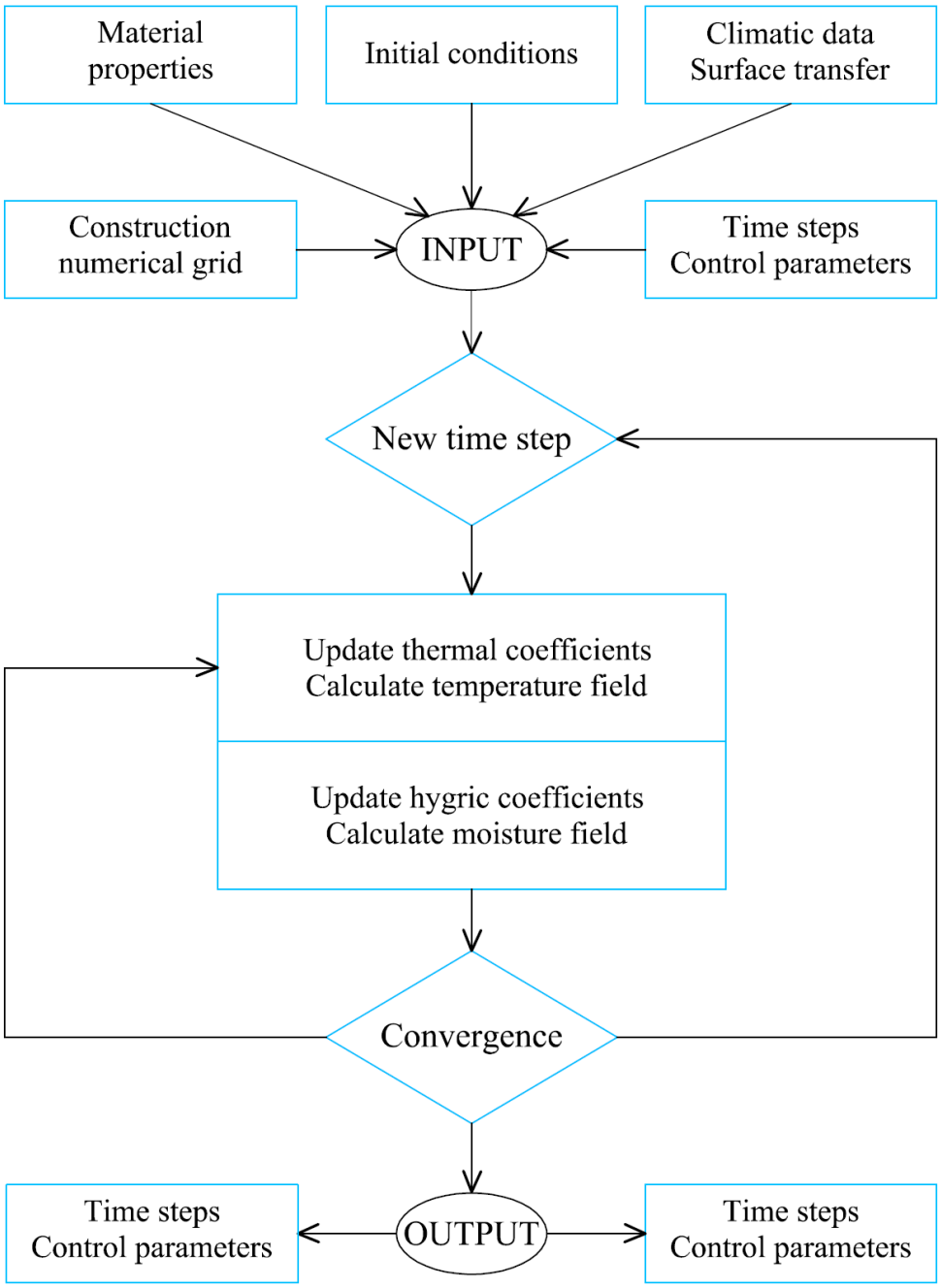


Figure 2.14 – Flow chart that shows the coupled heat and moisture transport equations for WUFI computer based program. Adapted from (Künzel, 1995).

2.6 Gas adsorption

Adsorption has been widely recognized as a technique for the investigation of porous materials; *e.g*. in determining specific surface areas (SSA) and pore size distribution (PSD). In general terms, the process of 'gas adsorption' takes place when a solid surface (adsorbent) interacts with a gas/ liquid (adsorbate), and as a result, enrichment of the adsorbate is developed on the adsorbent's surface. This enrichment would be, for example, dependent on the surface availability; *i.e*. adsorbent sites.

2.6.1 Physical adsorption

It is important to distinguish the differences between physical adsorption, known as 'physisorption' (refer to Figure 2.15), and chemisorption. The former one, refers to the adhering of gas molecules which involves relatively weak intermolecular forces (*i.e*., van der Waals) into a surface at a pressure that is lower than the vapour pressure. Chemisorption, on the other hand, involves the formation of a chemical bonding between the adsorbent and the adsorbate, which is irreversible (Ruthven, 1984; Rouquerol *et al.*, 1998). Some of the differentiating features between both adsorption processes are listed below:

a) Physisorption is a more general phenomenon which involves low heat of adsorption and low degree of specificity, whereas chemisorption depend on the reactivity of both adsorbent and adsorbate with high heat of adsorption.

b) Multilayer formation occurs at high relative pressures for physisorption, whereas for chemisorption the reaction activity is at the level of a confined monolayer at the adsorbent surface.

c) The adsorption interactions (intermolecular attractive/ repulsive forces, when both adsorbent-adsorbate and adsorbate-adsorbate interaction are presented) are non-specific for physisorption, whereas in chemisorption are highly specific.

d) Physisorption does not involve changes in the identity of the molecule when desorption is developed, whereas in chemisorption the identity of the molecule is transformed (reaction) and not recovered at the desorption phase.

e) Physisorption is always exothermic which does not greatly exceed the energy at the condensation phase, whereas the energy of chemisorption are generally same order of magnitude comparable to a chemical reaction.

The relationship between the amount of gas adsorbed, n^a by unit mass, m^s of an adsorbent and the equilibrium pressure, P represents the adsorption isotherm at constant known temperature. According to Rouquerol *et al.*, (1998), this can be written by the following expression:

$$\frac{n^a}{m^s} = f(P)_T$$

Equation 2.14 – The adsorption isotherm as a function of the equilibrium pressure at constant *T*. From (Rouquerol *et al.*, 1998).

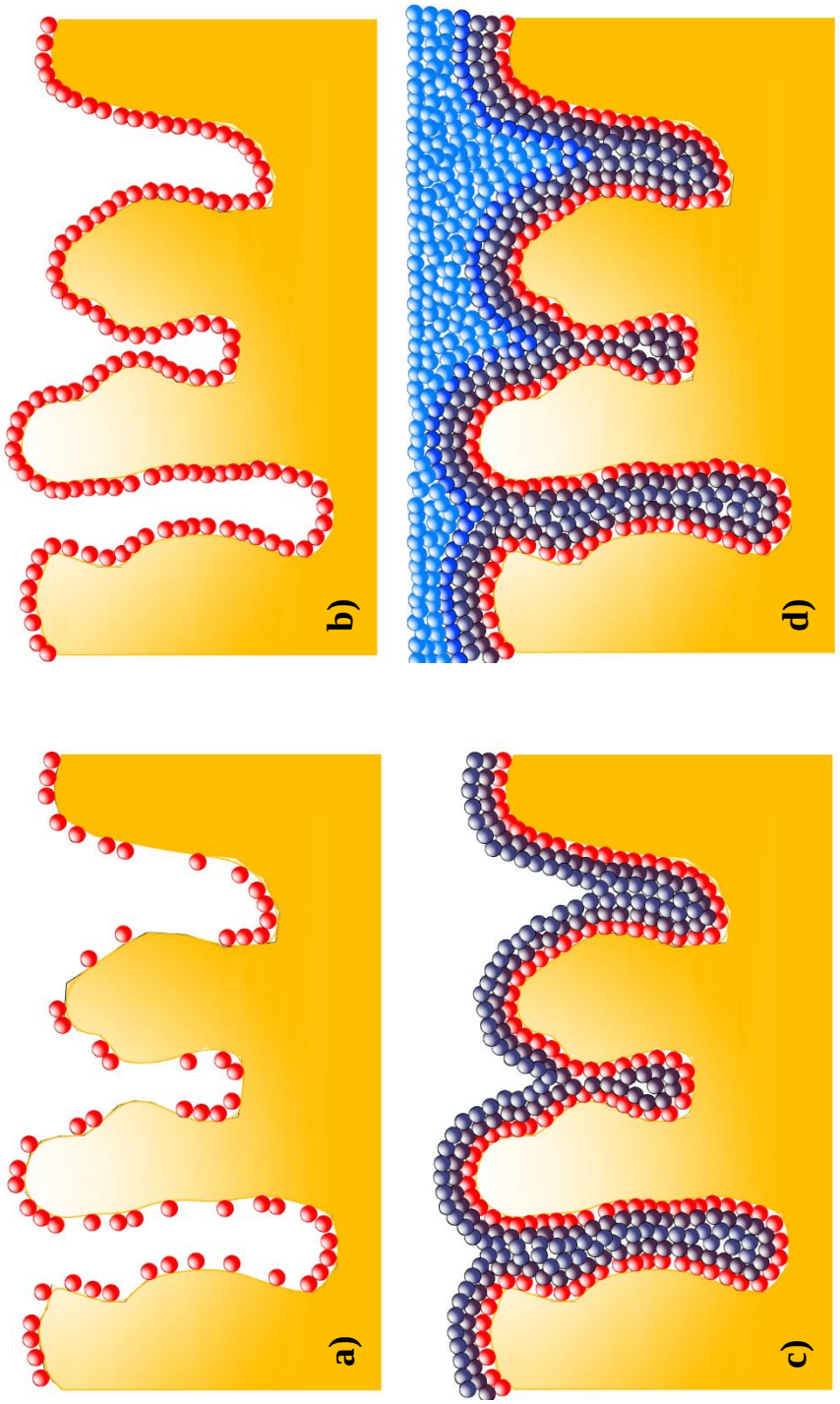


Figure 2.15 – Schematic representation of nitrogen physisorption starting from monolayer formation to multilayer and capillary condensation. Adapted from (Micromeritics, 2015).

Thus, the adsorbed gas is a function of the equilibrium pressure, *P*, and dependent on the temperature, *T*, of the system and from the nature of the gas-solid system. Figure 2.15 shows a schematic representation of the physisorption process, where: a) represents the beginning of adsorbed molecules (gas) on isolated sites of the adsorbent at very low pressure, where the first interactions between the solid and neighbours molecules begins, b) is the completion of a well-packed monolayer as a result of an extended coverage from gas molecules on the surface caused by van der Waals forces which is enhanced as the fractional coverage increases, c) is the formation of multilayer coverage where small pores are filled with the adsorbate as pressure increased, whilst molecules may act as an extension of the adsorbent surface for attraction of additional gas molecules by van der Waals forces, and d) further increment in pressure would eventually induce the complete coverage on the adsorbent and fill of all the pores, a process known as multilayer adsorption (Rouquerol *et al.*, 1998).

2.6.2 Classification and definition of isotherms

The IUPAC has classified and defined a group of six adsorption/ desorption isotherms, as it is shown in Figure 2.16. The term adsorption, for convenience, has been adopted when gas molecules penetrate the surface and enter to the structure of a bulk solid. The process involved here, 'adsorption', will be the dynamic enrichment of the components which participate in that process as an interfacial layer. The opposite process is called 'desorption', as a counterpart of adsorption decrement. They are used adjectivally to denote direction on the experimental adsorption determination, *i.e.* adsorption/ desorption curve. Adsorption isotherm will be then the successive amount gas adsorbed at constant

temperature to the corresponding equilibrium volume in cm^3/g (S.T.P.) as a function of relative equilibrium pressure, P/P_0 (Pierotti and Rouquerol, 1985). As Figure 2.16 shows, there is a group of six types of adsorption isotherms, in which four of them (I, II, III, and VI) may not present any kind of hysteresis (reversibility process). In the case of Type I isotherm, a characteristic micropore filling is observed at the low relative pressure range, where a distinctive plateau suggests that all pores have been filled with the adsorbate. Types II represents a typical non-porous material, where a concave shape is found until the common point B with Type IV; where monolayer adsorption has been complete and the onset for multilayer adsorption is about to begin.

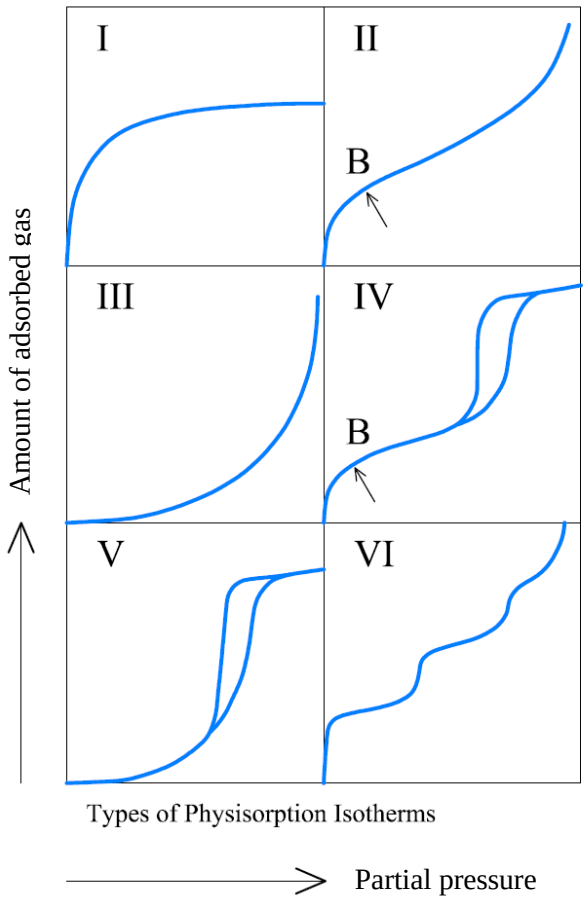


Figure 2.16 – Adsorption isotherm classification and hysteresis loops. Adapted from (Rouquerol *et al.*, 1994).

Unlike Type II isotherms, Type IV differs by having a steep step of gas adsorption within the mesopore region. This is mainly due to capillary condensation, where a distinctive plateau is observed at the top, representing complete pore filling. Additionally, it presents a characteristic hysteresis loop associated to capillary condensation on the mesopore region when desorption is performed (Pierotti and Rouquerol, 1985; Rouquerol *et al.*, 1998). Type III and V isotherms are characterized to have low adsorption affinity or weak adsorbate–adsorbent interactions (Branton *et al.*, 1997; Branton *et al.*, 1995). In the case of the Type V isotherm, a classic 'S-shaped' isotherm is developed, which exhibits a hysteresis loop associated to the pore filling/ empting mechanisms (Inagaki *et al.*, 1996; Nalaparaju *et al.*, 2010). Type VI is associated to different stages of multilayer formation at specific relative pressure ranges, which can suggest the presence of a hierarchical pore structure.

2.6.3 Surface area measurements

2.6.3.1 The Langmuir adsorption isotherm

From a classical model approach for monolayer adsorption based on the kinetic theory, the Langmuir model provided the basis for the development of the Brunauer–Emmett–Teller (BET) theory. The Langmuir model was originally developed to represent chemisorption. The model assumed an adsorbent surface as an array of N^s sites for equivalent and independent adsorption (adsorption sites), where the fraction occupied by N^a molecules was $\theta = N^a/N^s$ (refer to Figure 2.17). It also assumed that there is no interaction between adsorbed molecules on the adsorption sites, and that each site can hold one molecule.

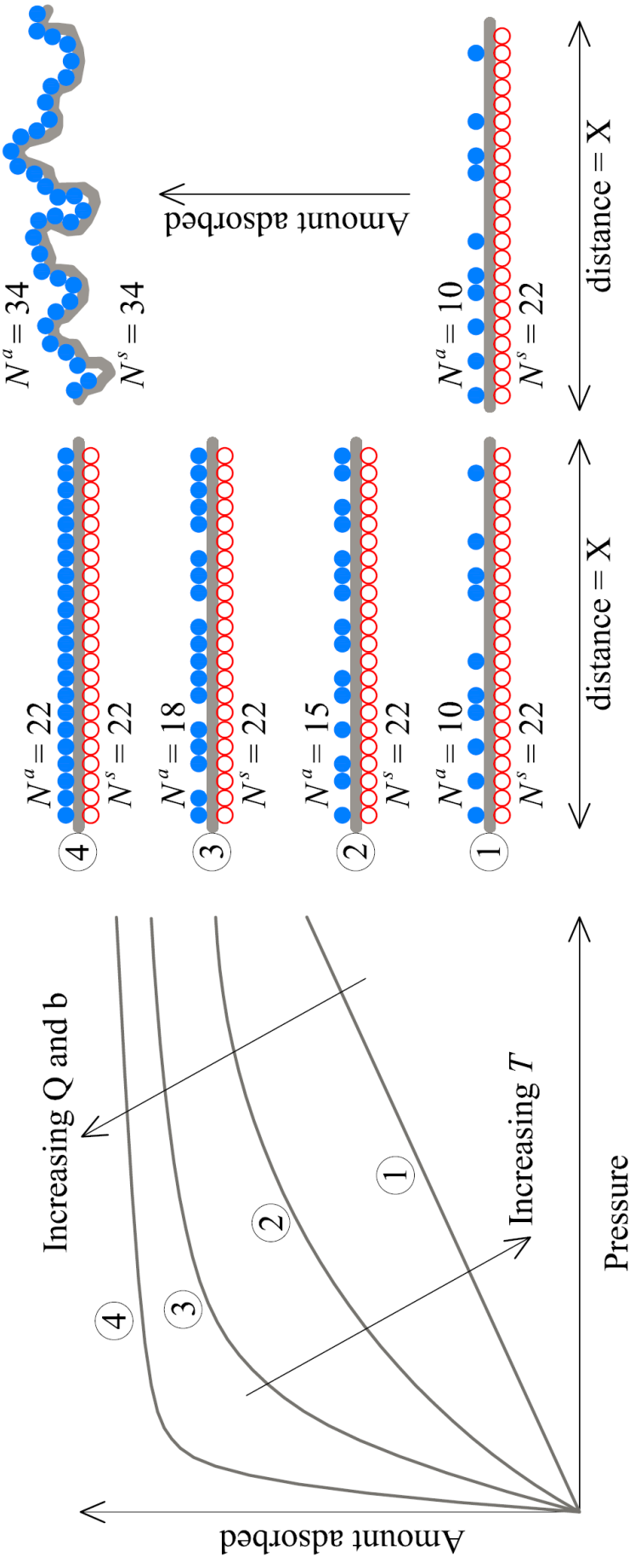


Figure 2.17 – Schematic representation of the Langmuir adsorption model based on the fractional loading.

The following mathematical expression represents the well-known Langmuir adsorption isotherm, in terms of fractional loading:

$$\theta = \frac{bP}{1+bP} \qquad b = \frac{\alpha \exp(Q/R_g T)}{k_{d\infty}\sqrt{2\pi M R_g T}}$$

Equation 2.15 – The Langmuir adsorption isotherm equation, and the affinity coefficient *b*.

Where Q represents the heat of adsorption and *b*, is the parameter known as the affinity constant or Langmuir constant. The Langmuir adsorption isotherm equation (refer to Equation 2.15) indicates that the amount adsorbed linearly increases with pressure until it is sufficiently high that the adsorbent reaches the saturation capacity. Figure 2.17 schematically represents the Langmuir adsorption process where the number of sites, $N^s = 22$ (red circles). The reduction in the adsorbed molecules, $N^a = 10$, as in the case of isotherm 1 in Figure 2.17, indicates the temperature dependency due to the increment of the kinetic energy on the molecules; *i.e*. molecules can easily evaporates from the adsorbent. If the affinity coefficient *b* increases, then the number of sites occupied, N^a would also increase (N^a = 15, 18, 22 for isotherm 2, 3, and 4 seen in Figure 2.17 respectively). This is due to stronger molecule affinity with the adsorbent. On the other hand, if Q increases (isotherm 4), then the number of sites occupied would also increase due to higher energy barriers that molecules need to overcome in order to return to the gas phase. However, the linearity of this method can only applies for adsorbents over a limited pressure ranges. For example, as Figure 2.17 schematically shows, increasing the surface roughness would require a higher number molecules, N^a (N^a = 34) as the number of adsorption sites, N^s also increases. This, by assuming the same pressure in the

system, would definitely require a higher amount of adsorbed gas molecules into the adsorbent, therefore suggesting a discontinuous isotherm instead of a linear (Ruthven, 1984; Rouquerol *et al.*, 1998; Do, 1998).

2.6.3.2 The BET theory

Expanded work from the Langmuir monolayer mechanism of adsorption was performed by Brunauer–Emmett–Teller, the BET theory, which denotes a Type II isotherm. This method included a multilayer adsorption of well-packed molecules towards infinite number of adsorbed layers. This model does not account for the adsorbent-adsorbate and adsorbate-adsorbate interactions, which are comparable in order of magnitude in the physisorption process. It also requires that a molecule is adsorbed in a specific site, which contributes for the adsorption of subsequent layers. The BET method also assumes that the subsequent adsorbed layers, in direct contact with the first monolayer, behave like a saturated liquid. The monolayer capacity, n_m can be obtained from the BET method which assumes the validity of Kelvin's equation (refer to Section 2.4.3.1); in the most general form, the surface area of a material is given by:

$$\frac{P/P_0}{n\ (1-P/P_0)} = \frac{1}{n_m C} + \frac{C-1}{n_m C}\frac{P}{P_0}$$

Equation 2.16 – General expression for surface area determination using the BET model. From (Sing *et al.*, 1985).

Where n is the amount adsorbed, n_m is the monolayer capacity and C is the empirical constant that relates to the heat of adsorption of the gas when in contact with the solid surface. The constant C, is usually assumed to be exponentially

related to E_1; *i.e*. average heat of adsorption from the less active part of the adsorbent's surface, and to the net heat of adsorption $E_1 - E_L$.

$$C \approx \exp\left(\frac{E_1 - E_L}{RT}\right)$$

Equation 2.17 – The constant C, from the BET equation. From (Sing *et al.*, 1985).

The 'linear transformed BET equation', is the basis for the BET plot for experimental data between $(P/P_0)/[n(1 - P/P_0)]$ and P/P_0, where the a straight line with the slope, $s = (C - 1)/n_m C$ and intercept $i = 1/n_m C$. The linear BET plots over an approximate range $P/P_0 = 0.05 - 0.35$. However, it is suggested by Rouquerol *et al*., (1998) that in order to obtain the best linear fit, it is necessary to adjust it by statistical analysis for a corresponding portion of the isotherm which considers Point B; *i.e*. inflection point for the onset of capillary condensation.

2.6.3.3 The *t*-method and α_s method

An alternative method to estimate the SSA, based on a reduced portion of an adsorption isotherm, is the *t*-method. This method uses the universal multilayer thickness curve, known as the *t*-curve, which is given by the following relation:

$$t = \frac{n}{n_m} d'$$

Equation 2.18 – The *t*-curve equation. From (Rouquerol *et al.*, 1998).

Where, *d'* is the effective thickness of a monolayer which assumes that both the adsorbed and bulk absolute densities are identical to the bulk liquid adsorbate at the operational temperature. The effective thickness is usually denotes for well-packed nitrogen molecules, as an average molecular thickness, *t* where $d' = 0.354n/n_m$. From the *t*-curve equation, a converted multilayer thickness, *t* can be obtained as a function of pressure, *P* assuming a flat surface, compared to a referenced non-porous material at the same pressure. This method assumes that the reference material is without any micro or mesopores, where the effects of curvature (*i.e.* capillary condensation) can be neglected (Rouquerol *et al.*, 1998). The linear plot between the experimental data and the standard *t*-curve, derives in a linear region which determines the SSA (denoted as $a(t)$) from the slope, $s_t = n/t$ according to the following equation:

$$a(t) = \frac{M}{\rho} x\left(\frac{n}{t}\right)$$

Equation 2.19 – Specific surface derived from the *t*-curve. From (Rouquerol *et al.*, 1998).

The α_s method, on the other hand, simplified the *t*-method by avoiding the estimation of n_m, and converting it into an standard amount adsorbed at a pre-defined relative pressure, P/P_{0s} usually taken at $P/P_{0s} = 0.4$. Derived empirically, the slope (α_s-curve; *i.e.* α_s versus P/P_0) of the standard and experimental isotherms is 'ideally' proportional to the ratios of surface areas, $a(S)/a_{ref}$. Any ascending deviation from the α_s-curve, is assumed to be as a result of the onset of capillary condensation within the mesopore region of the isotherm.

2.6.4 Pore size distribution and pore volume

Since the discovery of the well-defined mesoporous sieves, named collectively as the M41S group, the MCM-41 has been widely recognized as a template material for determining surface area and pore size distribution, and mainly for the development of the gas adsorption theory (Rouquerol *et al.*, 1998). Some of the exceptional features of the MCM-41 are: (1) hexagonal array of tuneable cylindrical pores (ranging between 1.5 to 10 nm), (2) easy preparation, (3) the surface properties for anchoring organic/ inorganic species for chemical bonding, and (4) surface modification (Kruk *et al.*, 1997a).

2.6.4.1 The BJH method

Further investigations, from the classical PSD estimations based on the Kelvin's equation, were implemented by the Barret–Joyner–Halenda (BJH) method in 1951. This method included the formation of an adsorbed film on the pore walls as part of the adsorption process. The pore radii from the Kelvin's equations (r_p) was then corrected and a statistical film thickness, t introduced, where the actual pore radii became, $r_p = r_K + t$ as it is shown below in Equation 2.20:

$$r_p = \frac{-2\gamma V_m}{RT \ln(P/P_0)} + t$$

Equation 2.20 – The Kelvin equation, where the radius r_K (nm) is used for mesoporous size calculations when assuming cylindrical pore geometry. From (Rouquerol et al., 1994).

γ = the surface tension of nitrogen at its boiling point.

V_m = the molar volume of liquid nitrogen (34.7 cm^3/mol).

R = gas constant (8.314 J/(mol K)).

T = boiling point of nitrogen.

P/P_0 = partial pressure of nitrogen.

r_K = the Kelvin radius of the pore.

By substituting surface tension, γ and the molar volume of nitrogen, V_m at 77.35 K, the Kelvin's equation can be rewritten as to the radius, r_K:

$$r_K = \frac{0.415}{RT \ln(P/P_0)} + t$$

Equation 2.21 – Rewritten of the Kelvin's equation for estimation of radius r_K (nm). From (Rouquerol et al., 1994).

Assuming that all pores are filled with liquid and that the relative pressure is closed to unity (*i.e.* closer to true thermodynamic equilibrium, P/P_0 = 0.99), the desorption branch of the isotherm can be selected to then relate the amount of the adsorbate lost by sequential desorbed steps. This would eventually estimate the average size of the pore that has been emptied within the relative pressure intervals. Figure 2.18a shows a representation of the Kelvin's radius, r_p in the 'ideal' and simplified condition for cylindrical pore filling mechanism (closed end), with the formation of a hemispherical meniscus. Pore condensation in this case, would be the continuous progression from multilayer adsorption to capillary condensation, and can be estimated by Equation 2.20 (Ruthven, 1984; Rouquerol *et al.*, 1998). However, in order to account for the statistical layer thickness, t in the adsorption process, Figure 2.18b shows pore condensation assuming a new pore radius, r_K (also known as the Kelvin's core) that can be estimated from Equation 2.21. This condition is for a cylindrical pore filling mechanism (open end), with the formation of a cylindrical meniscus.

Conversely, the layer thickness, *t* gradually becomes thinner with the successive decreases in pressure, *P* (Figure 2.18c). Assuming the universal molecular thickness, for nitrogen found by Halsey (Equation 2.22) and Harkins–Jura (Equation 2.23), the statistical thickness, *t* can be estimated as follow:

$$t = 3.54\left[\frac{5}{\ln(\frac{P_0}{P})}\right]^{\frac{1}{3}}$$

Equation 2.22 – Halsey equation that describe the statistical thickness, *t* for nitrogen.

$$t = \left[\frac{13.99}{\log_{10}(\frac{P_0}{P}) + 0.034}\right]^{\frac{1}{2}}$$

Equation 2.23 – Harkins–Jura equation that describe the statistical thickness, *t* for nitrogen.

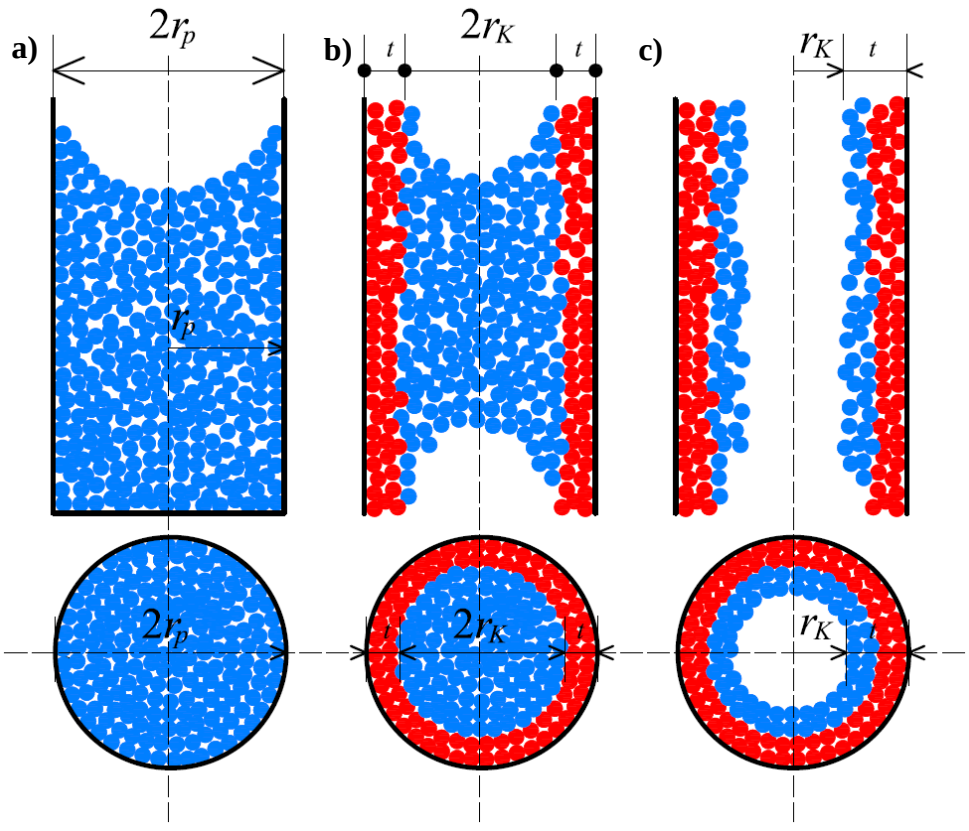


Figure 2.18 – a) Kelvin radius r_p in a cylindrical closed pore, b) Kelvin radius r_K and the introduced statistical thickness, *t* in a cylindrical open pore, and c) desorption process from a cylindrical open pore using the Kelvin radius r_K.

The method proposed by Barrett, Joyner and Halenda still remains as one of the most widely used for mesopore analysis from nitrogen isotherm. However, even though nitrogen gas adsorption techniques and methods are well established, the accuracy and reliability it is still yet a difficult debate on the evaluation of the pore analysis data results. This is mainly attributable to pore geometry analysis of the second level: (1) pore shape, (2) surface roughness, (3) surface fractal dimension, and (4) structural correlation and (5) surface heterogeneities. It is has been suggested by Sing and Jaroniec *et al*., (2004; 1999), that further and more rigorous analysis is needed in order to accurately model typological features for disordered pore-network.

2.7 Water vapour adsorption

The widely known gravimetric method, described in BS EN ISO 12571:2000 (2007), at equilibrium moisture content (EMC) has been used by many authors in order to determine water vapour adsorption/ desorption isotherms (Yu and Zhang, 2012a; Yu and Zhang, 2012b; Kwiatkowski *et al.*, 2011; Kwiatkowski *et al.*, 2009). Saturated salt-in-water solutions and corresponding relative humidity levels have been also used to produce the correlating moisture content, *w* at constant temperature. More recent techniques determined by gravimetric dynamic vapour sorption (DVS) have been used in order to better predict hygrothermal and kinetic responses on high-performance desiccants (Hall *et al.*, 2012; Casey *et al.*, 2012). The latter, with the advantage of minimizing the testing desiccator arrays at different salt-in-water solutions (Osanyintola and Simonson, 2006; Ramos *et al.*, 2010) in order to produce the adsorption isotherm.

2.7.1 Water vapour adsorption/ desorption isotherm

A simplified model that represents the pore filling stages of water vapour (adsorption/ desorption) and hysteresis loop is presented in Figure 2.19; where points *a-b-c-d* represent adsorption and *d-c'-b'-a* desorption. Between points *a–b*, water vapour is adsorbed within the micropore region, which assumes the formation of a tightly adsorbed uniform monolayer. It is widely accepted (Branton *et al.*, 1995; Branton *et al.*, 1997; Nalaparaju *et al.*, 2010; Inagaki *et al.*, 1996) that this apparent low pore filling is due to a low adsorption affinity (weak adsorbent–adsorbate interactions) resulting in the classic 'S-shaped' Type V isotherm with the IUPAC classification (Rouquerol *et al.*, 1998).

Previous studies in activated carbons have reported (Do and Do, 2000; Do *et al.*, 2009) that water molecules can be adsorbed around functional groups (*e.g.* -OH or -COOH) at very low vapour pressure. However, Ohba *et al.*, (2004) proposed in his model for activated carbons, that water adsorption at low vapour pressure is even possible in hydrophobic surfaces. This is due to self-stabilized water cluster formation, which can then serve as active sites (hydrogen bonding) for further water adsorption. Metastable formation and bridging of the clusters in an inhomogeneous adsorbed layer can result in packaging of clusters that only occupy a fraction of the micropore volume. The latter, may explain the reason why in the low pressure range the micropore volume does not always correlate (smaller) with that calculated from nitrogen adsorption. Consequently, as vapour pressure increases, growth of the water cluster results in a homogenous adsorption phase (Do *et al.*, 2009). This can be seen in Figure 2.19 as the onset for capillary condensation between point *b–c*; clusters of water molecules have already started to aggregate forming a condensed phase.

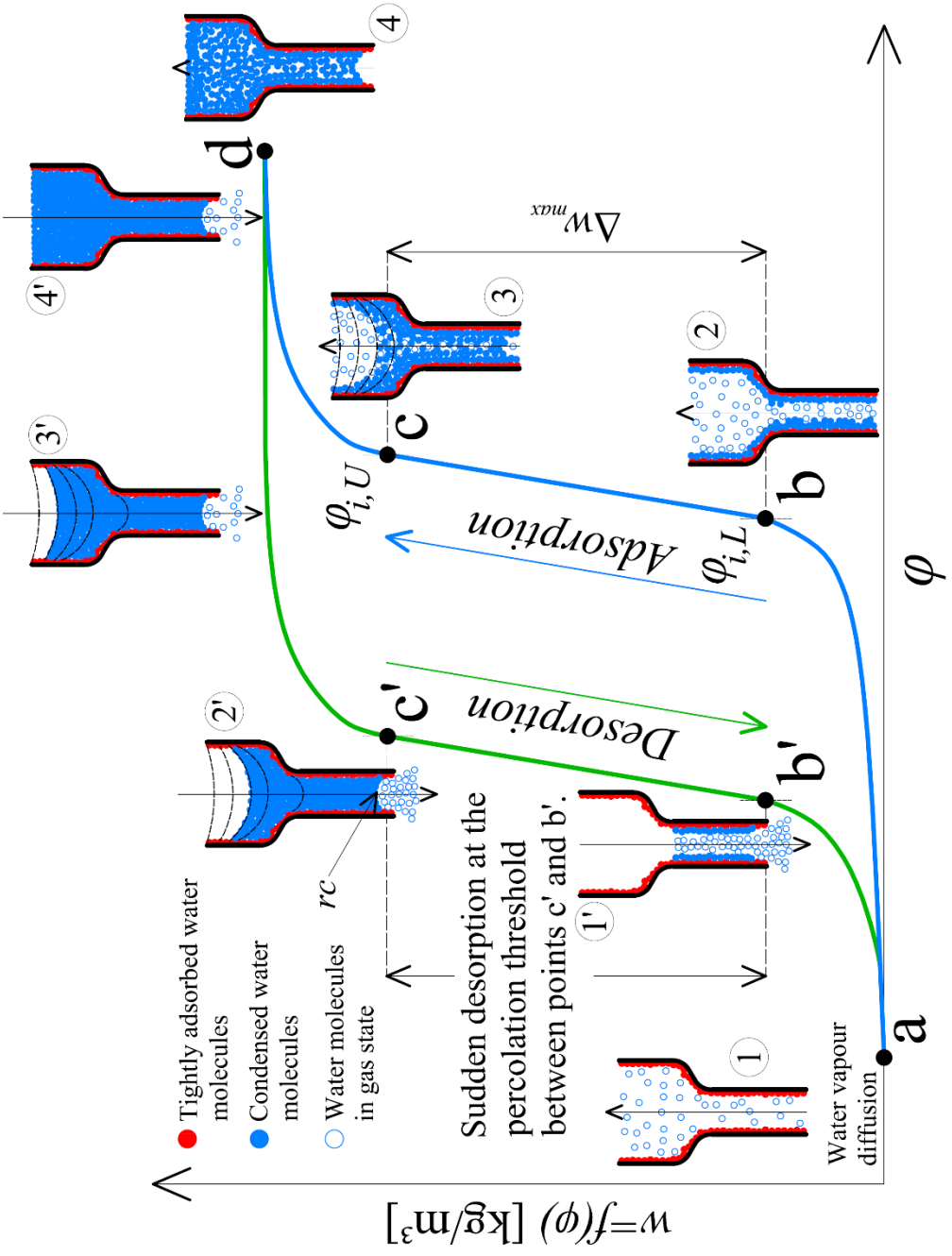


Figure 2.19 – Simplified conceptual scheme-model of water vapour adsorption/ desorption isotherm pore filling stages for a mesoporous material, where points *a-d* correspond to adsorption and points *d-a* to desorption within a hypothetical Type H2 hysteresis loop.

Horikawa *et al.*, (2011) extended the work proposed from Do (2000) for prediction of water vapour adsorption in mesoporous carbons. Horikawa proposed that further water adsorption is due to the contribution of larger self-stabilized water cluster formation within the mesopore range, which are about 3-6 times the maximum size for entering micropores. Recent studies were conducted by Thanh (2011) aiming to describe how water adsorption is performed within hydrophobic carbons. They concluded that a critical factor for adsorption in mesopores is the formation of large and stabilized water clusters at the window between large and small pores. They found that there was a critical window size that induced spontaneous filling from the micropore to the empty mesopore, which is not observed in weak polar gases like nitrogen.

Further studies from Horikawa (2013) suggested that the rate of water cluster formation is temperature-dependent, which has an effect on water vapour uptake. It was observed that the adsorption branch shifted to a higher vapour pressure range whilst reducing temperature. This means that at lower temperature, a greater reduction in pressure is needed for cluster formation in order to facilitate adsorption. In the case of mesopores, higher temperature enables the formation of bigger clusters to enter in the mesopore region. This is caused by progressive accumulation of clusters as the pore size is increased; *i.e*. onset for capillary condensation. In the same logic, this could also suggest a delayed condensation phase with respect to temperature, with implications for total water vapour uptake. Likewise, Figure 2.19 shows that the greatest Δw_{max} (steepest gradient over $\varphi_{i,L}$ and $\varphi_{i,U}$) correspond to the greatest water vapour uptake. After point *c*, menisci formation may be presented at this high water vapour pressure stage until point *d* (capillary saturation) is reached; *i.e.* where the capillary potential,

ψ is reduced. Here, air entrapped (bubbles) are still mixed with condensed water within the pore space, and external pressure is needed in order to achieve φ = ~ 1. Once all pores are filled with condense water at point *d*, and vapour pressure is lowered, the desorption process begins. As indicated in Figure 2.19 (numbers 4'–2'), wider pores have been filled with a homogeneous condensed water phase; *i.e*. stabilization of the hydrogen bonding. Once the major water vapour desorption has been performed (after point *b*'), the residual desorption step will follow until both desorption/ adsorption curves join together. This would define the 'lower closer point' where the water phases (gas-liquid-like and condensate) enter metastable equilibrium (Rouquerol *et al.*, 1998).

2.7.2 Kinetics of water vapour adsorption/ desorption

A conceptual model that represents the kinetics of water vapour adsorption/ desorption is shown in Figure 2.20. A hypothetical water vapour adsorption/ desorption Type V isotherm with a characteristic Type H2 hysteresis loop and corresponding scanning curves are represented in Figure 2.20. Figure 2.20b shows a schematic representation of the pore-blocking effect within a hypothetical three-cycle time-response test. The operative range is defined between the $\Delta\varphi_{0.7\text{-}0.95}$ range, where adsorption is denoted with points 1–1a, 2–2a, and 3–3a, and desorption with points 1b–1c, 2b–2c and 3b–3c between same $\Delta\varphi_{0.7\text{-}0.95}$ range. In the first adsorption cycle ($\Delta\varphi$ = 0.7 → 0.95) in points 1–1a, equilibrium moisture content (EMC) has not been achieved, *e.g*. EMC_{95}. Here the adsorption occurred through vapour diffusion and capillary condensation towards φ = 0.95; *i.e.* where clusters of water molecules spontaneously aggregate, but equilibrium moisture content have not achieved within the pores.

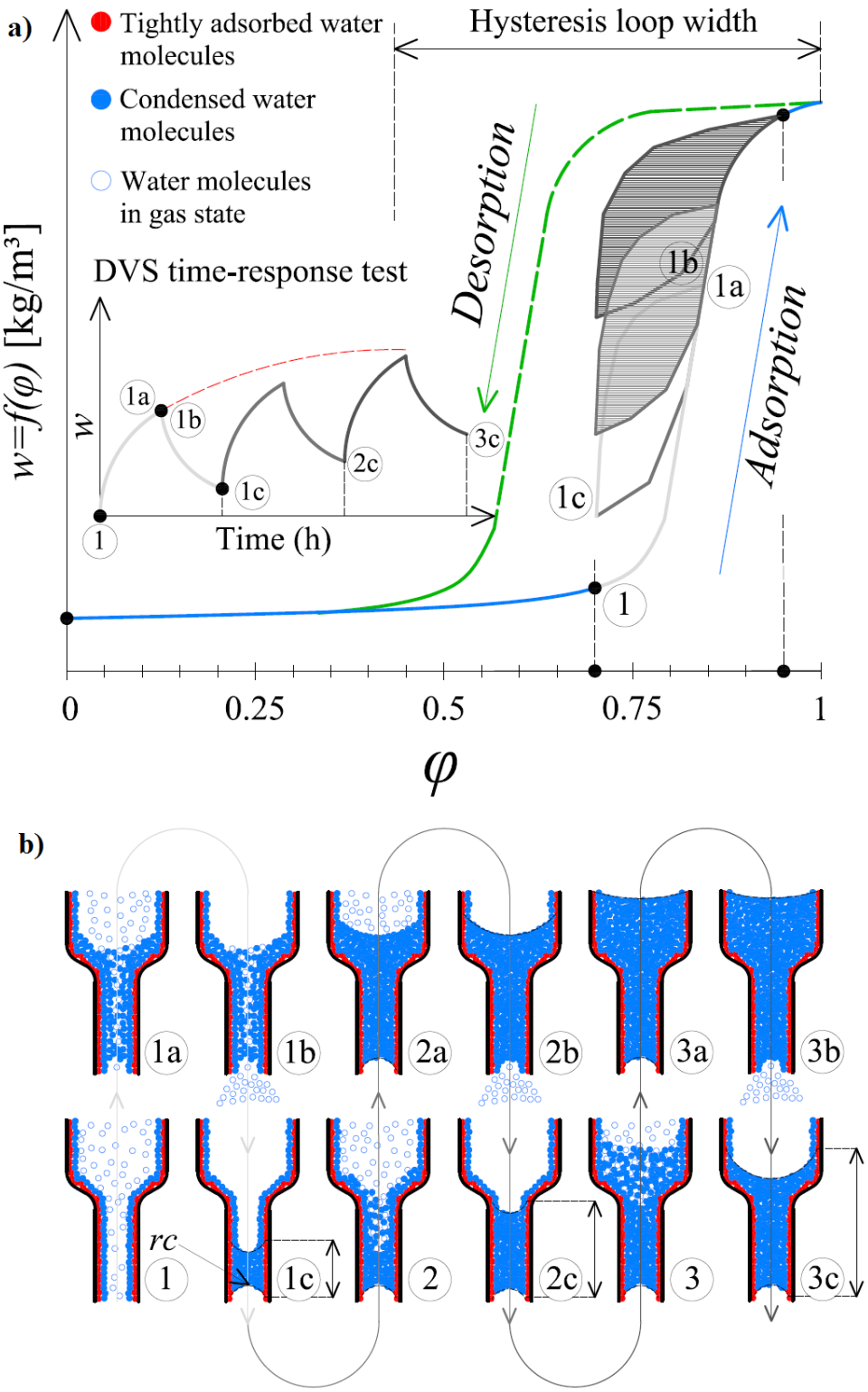


Figure 2.20 – Simplified conceptual scheme-model of the kinetics of water vapour adsorption/ desorption for a three-cycle time-response pore filling stages representation. a) Hypothetical water vapour adsorption/ desorption Type V isotherm with a typical Type H2 hysteresis loop and corresponding scanning curves for the three-cycle time-response test. b) Schematic representation for the pore-blocking effect within the three-cycle time-response test. Points 1–1a, 2–2a, and 3–3a denote adsorption cycles between a specific $\Delta\varphi_{0.7\text{-}0.95}$ range. Points 1b–1c, 2b–2c, and 3b–3c denote desorption between same $\Delta\varphi$ range.

At the first desorption stage ($\Delta\varphi$ = 0.95 → 0.7) in Point 1b–1c, the confined water (liquid-like) exhibits a pore-blocking effect due to dissimilarities in pore size, and as a result the vapour pressure is not enough to enable full reversibility of the cycle at the pore neck, r_c. At point 1c, a meniscus has been formed with a significant amount of retained water, resulting in an increased moisture content, *w* within the materials at the apparent EMC_{70} (hysteresis); *i.e.* the first scanning curve has been generated. Similarly, the process of desorption in points 2b–2c and 3b–3c follow same pattern as previously described. It can be seen that three different scanning curves (grey dashed areas seen in Figure 2.20a) have been generated within the hysteresis loop, resulting in a monotonous increase of the moisture content, *w* (points 2c and 3c of Figure 2.20b). This eventually would result in (for total reversibility to occur) a critical vapour pressure at the pore neck, r_c and would have to be enough to enable full desorption of the condensed water. It can be suggested that the scanning curves follow the same trend of the Type H2 hysteresis loop, indicating strong dependency with the differences in pore size within an interconnected pore structure at the $\Delta\varphi_{0.7\text{-}0.95}$ range.

2.7.3 Hysteresis phenomena

As previously shown in Figure 2.19 and Figure 2.20, the desorption branch exhibits a pronounced 'hysteresis', implying that a pressure drop should be sufficiently enough to allows desorption at the pore neck (r_c in point c'). General description of the hysteresis phenomena have been deeply studied for many years, and yet not fully understood. From classical theory approach, this is, by assuming capillary condensation from the Kelvin's equation, Zsigmondy (1911 – (Rouquerol *et al.*, 1998) suggested that hysteresis has its origin from the

difference in contact angles of the adsorbate, which differs from the adsorption (not-wet, because of impurities) and desorption (totally wet, displacement of impurities) process. Foster (1932), suggested that during adsorption process, multilayer formation was increased from the pore wall (making it thicker – refer to Figure 2.21) in pores with open ends. In this scenario, adsorptive forces become weaker as multilayer adsorption proceeds and the centre of the capillary become smaller. As a result of these forces, a defined hemispherical meniscus formation was meant to propagate as an adsorbed film. The delay in condensation (and meniscus formation) occurs because of the instability of the liquid due to differences in capillary sizes. Foster concluded that desorption must be at thermodynamic equilibrium, and that the lack of reversibility (hysteresis) is due to the delayed process for menisci formation during the process of adsorption (Foster, 1932).

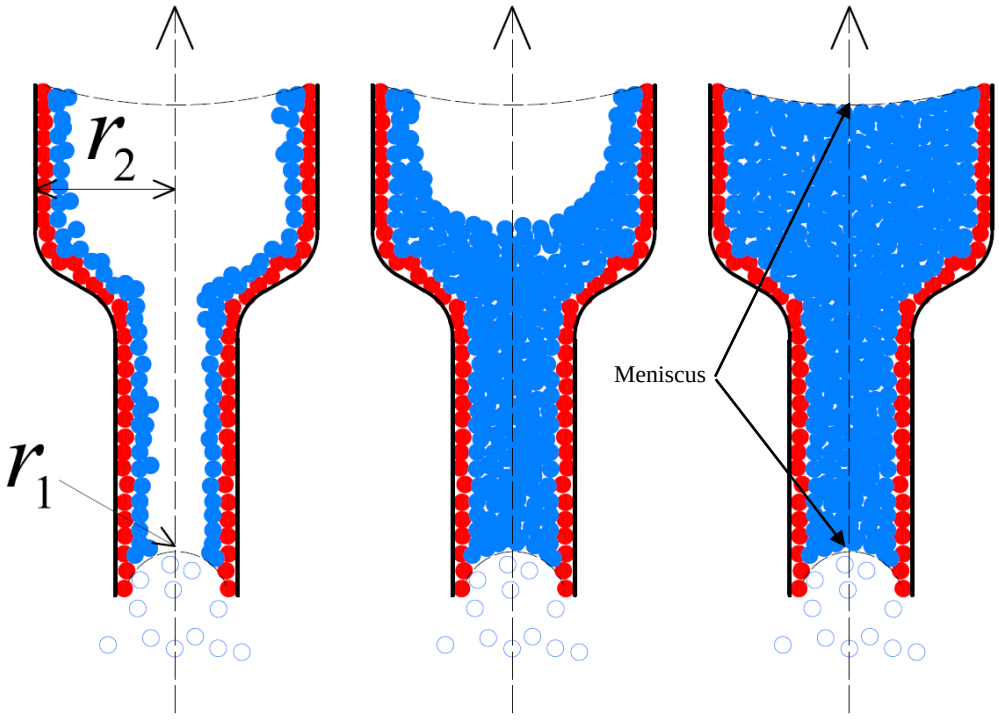


Figure 2.21 – Schematic representatiion of Foster's delayed condensation phase due to meniscus formation.

McBain (1935) presented an alternative mechanism for the understanding of hysteresis phenomena by considering the 'Jamin effect' due to microscopic bubbles formation within the desorption process, and when cavities of different sizes are presented. He also coined the concept of pore-blocking – or commonly termed as the 'ink-bottle effect as represented in Figure 2.22. He suggested that evaporation from the ink-bottle is obstructed by the pore constrictions, which can be only performed after the narrower neck (r_1 in Figure 2.22) is empty. In other words, hysteresis phenomena occur due to the high differences in vapour pressure between the wider (r_2) and smaller neck (r_1) during the desorption process (McBain, 1935). Cohan (1938) supplemented the theory from Zsigmondy (1911) and the work from Foster (1932) of discontinuous isotherms due to the presence of menisci formation.

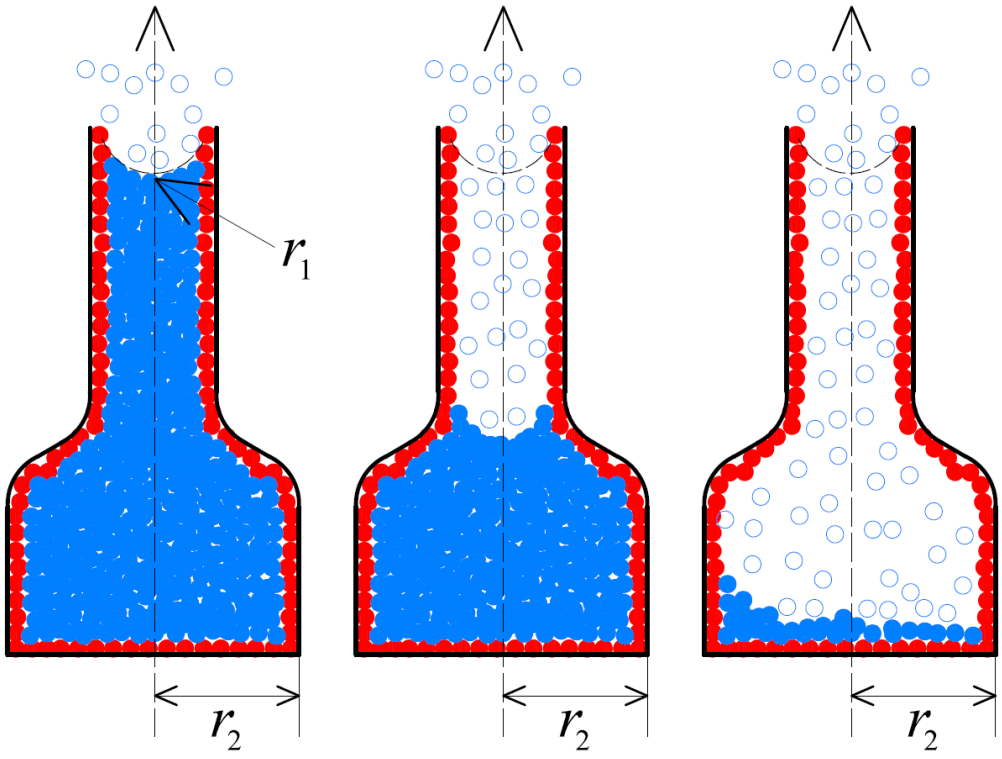


Figure 2.22 – Schematic representation of McBain's bell jar model and the pore-blocking (ink-bottle) effect for hysteresis.

He also suggested that hysteresis can be fully eliminated when complete wetting has occurred for a closed capillary. This by assuming that all gases and impurities are eliminated, and being reversible (hysteresis) at the lower end of the isotherm, even when no chemical adsorption occurs. Further studies in hysteresis phenomena using the quantum thermodynamic theory, were conducted by Saam and Cole (1975). Here, the concept of instability, metastability and stability of the adsorbed film (and also multilayer formation) was associated to the competition between surface energies (adsorption) and van der Waals forces (capillary forces for multilayer adsorption and pore condensation). The spontaneous formation of a meniscus during adsorption was as a result of an unstable critical film, T_c, whereas a residual thickness film, T_m, was related to the desorption process at lower vapour pressure, thus different size in the Kelvin radius, r_K (Rouquerol *et al.*, 1998). This difference of a metastable thickness over the range of multilayer adsorption, and consequently for the estimation of PSD, was further developed by Everett (1979) by introducing the distortion of the Kelvin radius, r_K, and its dependency in the chemical potential (potential energy, ϵ); this, by assuming the presence of surface forces that modified the interface of the meniscus curvature.

Broadbent and Hammersley (1957) introduced the 'percolation and diffusion theory', by illustrating a pore network model as a lattice with linear intersections (sites), connected with segments (bonds). In a square lattice, a bond can sequentially be connected with neighbours bonds, which allows a fluid to pass through using a simplified state, 'empty' or 'open'. This was mainly determined by a network coordination number and the size distribution of the corresponding neck, under favourable thermodynamic conditions for vaporization when direct

pore connection was with the vapour phase (Rouquerol *et al.*, 1998; Berkowitz and Ewing, 1998). This brought great attention to researchers in the porous media area, and has been closely connected with micropore/ mesopore network models (Liu *et al.*, 1993; Liu *et al.*, 1992; Seaton, 1991; Mason, 1988), capillary condensation and hysteresis (Guyer and McCall, 1996; Yanuka, 1989), pore size distribution determination (Wall and Brown, 1981; Zhdanov *et al.*, 1987), three-dimensional models for geometrical-topological network system (Kikkinides *et al.*, 2003), computer simulations for fluid transport in porous media (Ferreiro-Rangel *et al.*, 2012), and practical applications for calculating pore network connectivity and PSD from scanning curves (Cimino *et al.*, 2013).

2.7.3.1 Hysteresis loops

Figure 2.23 shows the classification from the IUPAC (1994) of the hysteresis loops. According to the IUPAC, Type H1 loops are commonly associated with a narrow distribution of uniform pores, which indicate overall reversibility with very steep and parallel adsorption and desorption branches. In this research, hysteresis loops H1 and H2 will be analysed. Type H2 loops exhibit a prolonged and delayed desorption phase which is attributed to the complexity of interconnected pores of different sizes (Rouquerol *et al.*, 1998; Seaton, 1991). It has been controversial for many years, the implications of the hysteresis phenomena for material's characterization in the building physics field; *i.e*. hygrothermics. The uncertainties regarding to this phenomena, carried out for the precision of material's functional properties, has been lead to the acknowledgement of critical information for material's characterization.

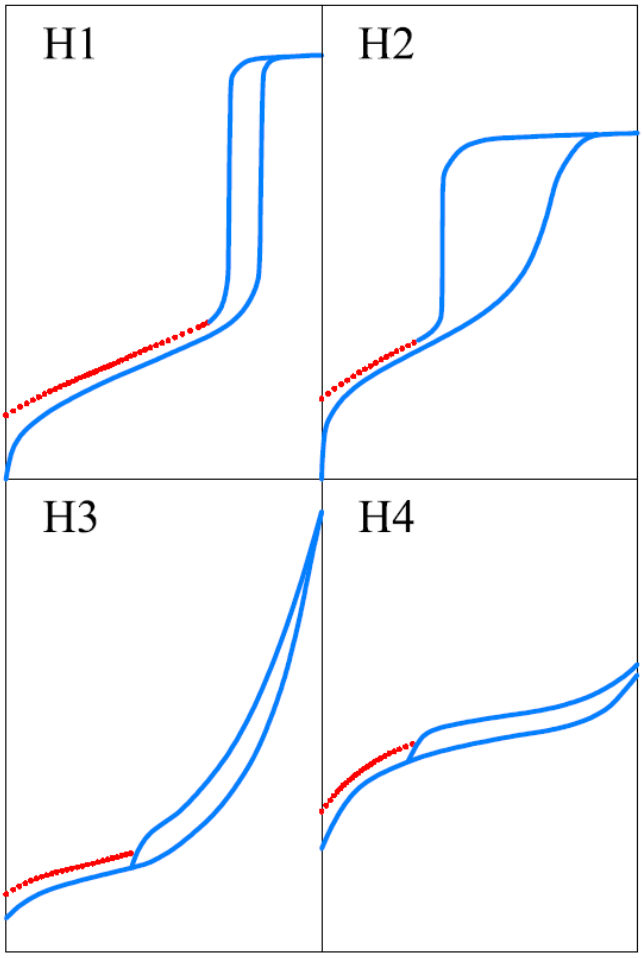


Figure 2.23 – Hysteresis loops. Adapted from (Rouquerol *et al.*, 1994).

According to Yu *et al*., (2012a), (1) moisture content regarding to water regions, (2) capillary moisture potential and (3) moisture content differential, are important for material's characterization. Since moisture content, *w* is not linear and its time-dependency is attributed to water redistribution, they suggested that: increasing moisture content will be entirely dependent on (a) air removal rate and (b) for hysteresis phenomena. In this regards, two kinds of hysteresis were identified: (1) derived from pore structure network and (2) for air entrapped on adsorption/ desorption. Simplification on material's characterization and physical modelling was advised in order to normalize pore structure approach to the free water capillary saturation on hysteresis phenomena. Kwiatkowski *et al.*,

(2009) recognized that water vapour permeability and adsorption isotherms have significant influence on hygrothermal behaviour. He suggested that, hysteresis should be needed to taking into account to avoid overestimation for moisture buffering properties. For this reason, high errors were found on desorption measurements due to uncertainties on the full understanding of materials micro-structural properties; *e.g*., pore-size distribution, which will eventually enhance numerical modelling.

Concerning to capillary condensation and equilibrium moisture content (EMC), Kwiatkowski *et al.*, (2009) explained that, to reach EMC before condensation occur, it is necessary to better understand pore-features and adsorption hysteresis. Furthermore, Yu *et al*., (2012b) stated that apart from traditional geometrical characterization (mean pore-size distribution), it is important to analyse methods that estimates measurements in moisture fixation and transport characteristics. This, in terms of adsorption/ desorption isotherms for capillary moisture content; where the concept of capillary hysteresis can be better understood. The results provided from the porous material designed by Yu *et al*., (2012b), (especially for those that achieved high water vapour adsorption rates) shown significant differences on the moisture content rates. This was mainly attributed to (1) geometrical characterization and (2) the two kind of hysteresis mentioned in their previous work from Yu *et al*., (2012a). They concluded that by using their capillary saturation method (according to the degree of capillary saturation) instead of moisture content, *w* the effect in capillary hysteresis may be applied as a simplified methods for material's characterization.

2.8 Molecular dynamic simulations of water under confinement

With the aid of Molecular Dynamic (MD) simulations, hysteresis has been approached by analysing pore structure and the thermodynamics associated, (Bonnaud *et al.*, 2010; Coasne *et al.*, 2008b; Coasne *et al.*, 2008a), establishing significant insights within hygroscopic materials. Within the microscopic scale, this phenomena has been also analysed (Bazant and Bažant, 2012; Bažant and Bazant, 2012; Coasne *et al.*, 2008b; Coasne *et al.*, 2008a; Bonnaud *et al.*, 2010) as a far-reaching transport dilemma. Since transport of water molecules (gas and liquid) may be altered as a result of pore morphology and surface chemistry in the vicinity of adsorbent interface; *i.e*. gas-liquid-solid (Giovambattista *et al.*, 2012; Soler-Illia and Azzaroni, 2011).

Additionally, molecular simulations has explored this phenomenon through atomistic models such as, Grand Canonical Monte Carlo (GCMC) technique. These procedures have enabled simulations of water molecules for (1) adsorption, (2) desorption, and (3) aggregation in complex and simple pore morphologies/ topologies (Bonnaud *et al.*, 2010). These have been largely performed in desiccant materials such as amorphous silica nanopores by (Bonnaud *et al.*, 2010; Coasne *et al.*, 2008a; Coasne *et al.*, 2008b; Shirono and Daiguji, 2007; Lerbret *et al.*, 2011; Milischuk and Ladanyi, 2011; Limmer and Chandler, 2012), in carbon nanotubes (Striolo *et al.*, 2005; Khademi and Sahimi, 2011), and in calcium-silicates-hydrate (Manzano *et al.*, 2012; Shahsavari *et al.*, 2010), to only name a few. In the interest of this research, this section will introduce to some water molecules behaviour (dynamics) in nanopores upon confinement. Adsorption behaviour and density profiles (thermodynamics) as well water molecules diffusivity will also be deal in this section. Surface

chemistry of amorphous silica nanopores and solid-liquid interfacial tension will be then briefly discussed. In addition, hysteresis on nanopores and critical factors for unstable water molecule behaviour (theory of sorption hysteresis) will be the end of this section.

2.8.1.1 Water molecule behaviour in nanopores

Particular to water molecules is the van der Waals type of intermolecular attractions; *i.e*. hydrogen bond. This particular intermolecular dipole-dipole interaction among water molecules is responsible for the nature of water; *e.g*. surface tension and capillary action. Experiments in two cylindrical hydroxylated silicas (nanopore structures at 10Å and 20Å diameter seen in Figure 2.24) were carried out by Bonnaud *et al*., (2010) for water molecules behaviour in the vicinity of the pore surface.

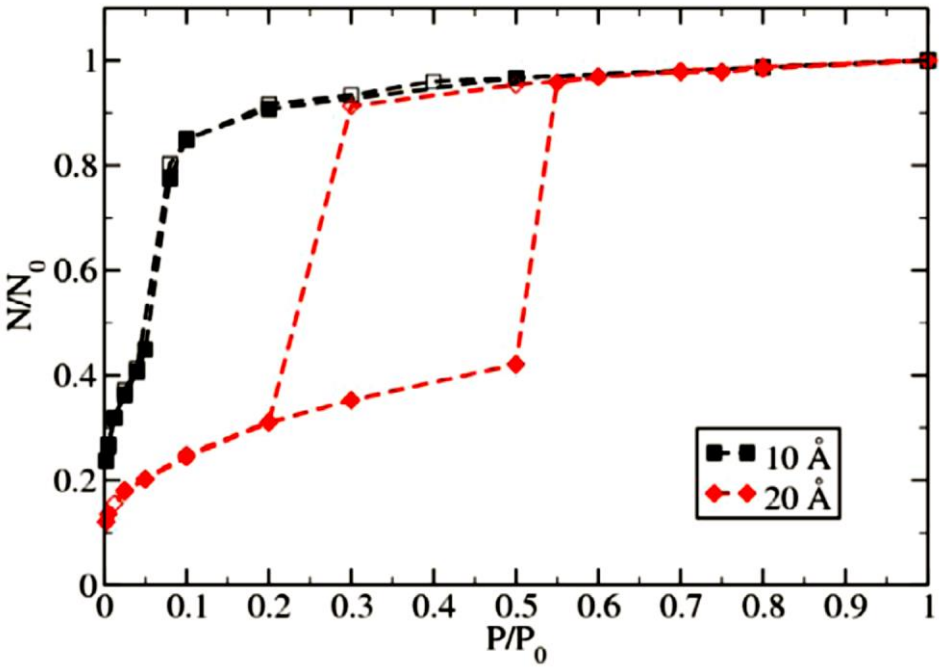


Figure 2.24 – Water adsorption (black filled squares)/ desorption (black empty squares) isotherms in a 10 °A silica slit pore and water adsorption (red filled diamonds)/ desorption (red empty diamonds) isotherms in a 20 °A silica slit pore at T = 300 K (P0 = 4400 Pa) – Image from (Bonnaud *et al.*, 2010).

They found that the monolayer adsorption at low vapour pressure was presented for the two systems until sudden jump to capillary condensation occurred. However, when desorption was performed (see Figure 2.24), a Type H2 hysteresis loop occurred for the 20Å nanopore material. They suggested that the appearance of hysteresis was associated to a 'critical temperature', T_{ch}. Above it, capillary condensation becomes reversible; *i.e*. as T_{ch} increase, the pore size would also need to increase in order to satisfy reversibility. In addition to that phenomenon, a 'critical capillary temperature', T_{cc}' (above it the isotherm becomes reversible) implied that T_{cc} should be located above T_{ch}; since full reversibility was performed at 300 K in the 10Å sample.

Furthermore, Coasne *et al*., (2008a) came to the conclusion that capillary condensation temperature also is independent of the pore shape and surface heterogeneities. This was mainly due to the highly hydrophilic behaviour of water molecules that can also be described as a large density of polar groups (silanol groups) on the silica nanopore. At low vapour pressure and small pore size (see Figure 2.25a), pores become saturated before 0.50 P/P_0, whereas for case b) there is no sign of pore saturation. On the other hand, the studies conducted by Bonnaud *et al*., (2010) suggested that, water molecules tend to be gathered as an H-down orientation; *i.e*., hydrogen atom is perpendicular to the surface. This also imply that above 8Å from the surface, water molecules recover their bulk (liquid) behaviour and also the isosteric heat of adsorption (Q_{st}) to the order of 55 kJ mol $^{-1}$; *i.e.*, cohesive forces govern over adhesive at the surface. The peak density of hydrogen and oxygen atoms described in two different studies (Shirono and Daiguji, 2007) and (Bonnaud *et al.*, 2010), reveals that for

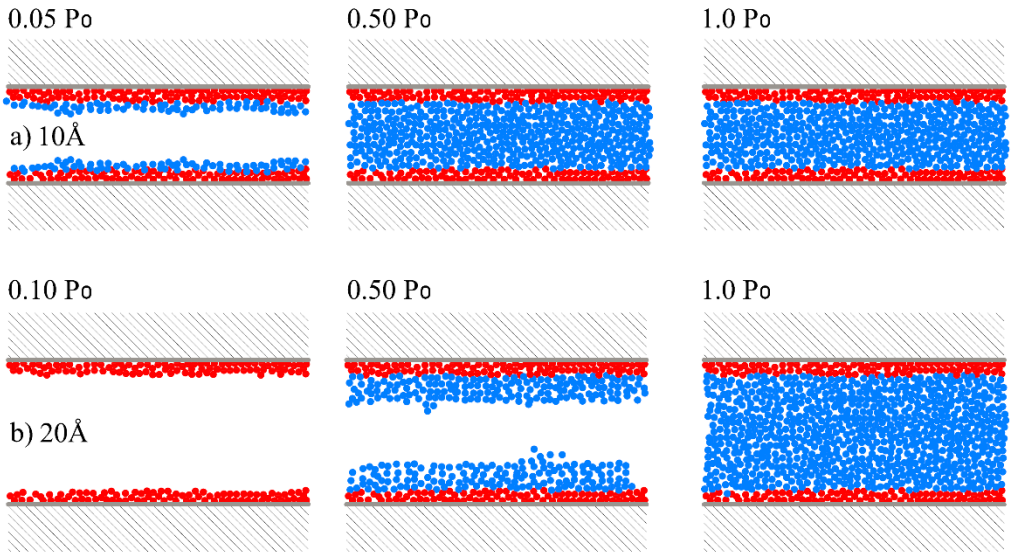


Figure 2.25 – Typical molecular configurations for water confinement at 300 K and under different pressures in silica nanopores. (a) 10 Å and (b) 20 Å – Adapted from (Bonnaud *et al.*, 2010).

nanopore widths of ~ 10Å, high hydroxylated surfaces are responsible for the great adsorption of water molecules and their configuration. As a result, the peak density of hydrogen atoms is at -0.25Å below the surface (Figure 2.26b bottom), whereas for oxygen atoms is at 0.75 Å (Figure 2.26b top). This suggests, that the H-down orientation describes a sub-monolayer adsorption as can be seen on Figure 2.26a. For pores greater than 20 Å, this behaviour remains the same at lower adsorbed amounts (μmol m^2). As a result, water molecules recover their bulk liquid behaviour, since less attraction from the pore surface is presented and intermolecular interactions among them govern their activity. Additionally, the pair correlation function also describe this peak connection, as the nearest oxygen atoms would eventually be at the same distance (~2.9 Å) from the first peak described in Figure 2.26b. This showed that upon confinement intermolecular distances do not change. Angle orientation of water molecules also is affected by the surface chemistry. As stated above, it not only describes the density of water molecules near the surface but also the specific angle, which eventually would enable more hydrogen bond formation.

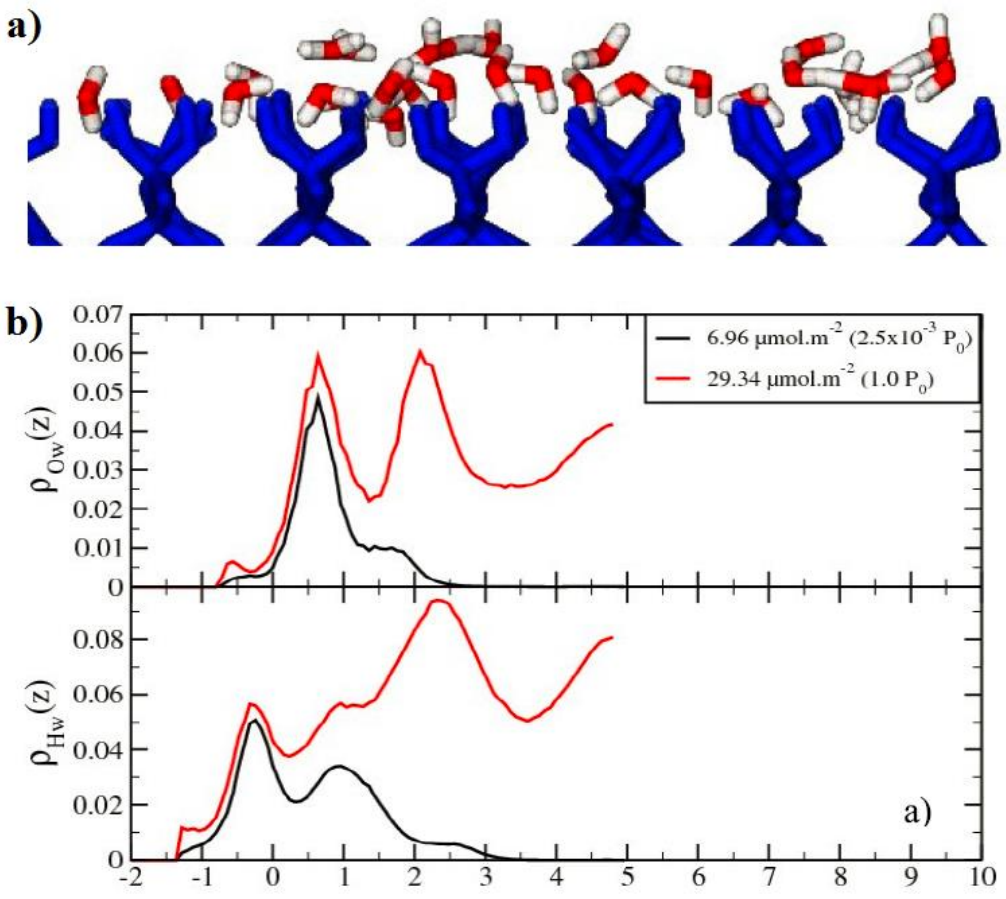


Figure 2.26 – a) Water molecules in the vicinity of a surface (Silica – high silanol groups density), b) density profileamorphous silica slit pore at T = 300 K (P0 = 4400 Pa); where, origin of the *z*-axis is the hydrogen positions on the silica surfaces. Images taken from (Bonnaud *et al.*, 2010).

This behaviour was also found for the two systems analysed by Bonnaud *et al.* (2010). They found that at lower pressure, water molecules behave similarly. The perpendicular orientation with the H-down is clearly identify in the adsorbed monolayer, whereas the second one is near the 2.5Å; which confirms the peak of H atoms that are seen at the bottom of Figure 2.26b.

2.8.1.2 Hysteresis in nanopores

Recent studies were conducted by Bažant and Bazant (2012; 2012), from a discrete (discontinuous) molecular forces approach within nanopores. They

showed that adsorption/ desorption hysteresis in nanopores is due to the non-uniqueness (disjoining pressure) that exist between the pore width differences and intermolecular (van de Waals interaction) forces. They introduced the theory of adsorption hysteresis through two main mechanisms: (1) snap-through instabilities and (2) molecular condensation. The aim of this section is to introduce some molecular dynamics for water molecules on nanopores, supported by these two theories series as a background.

2.8.1.2.1 Unstable equilibrium

According to Bažant (2012), adsorption hysteresis may occur even if the pore morphology is completely smooth or if the pore structure does not change. The adsorptive film is not unique, and this also can contribute to the adsorption history, and then for the hysteresis phenomena. Pore width also contribute to it by generating disjoining oscillations in transverse pressure from tensile (+) to compressive (-) stress as the number of monolayer adsorbed increase. These nano-oscillations were also found in Yang *et al*., (2011) on their molecular simulations for nitrogen, where roughness of the surface was the main precursor of them. They said that the chemical potential, 'μ' can be altered in the vicinity of the filling front on the nanopores, where tension/ compression is acting. This misfit in pressure differences would eventually be reduced as the number of monolayers increase across the nanopores (~ 3 nm), lowering the attraction forces with the surface and enabling cohesive forces among them. On the other hand, unstable transition phases from the adsorbate must dynamically snap-through from one point to another after dissipating the energy in the system; the so called 'snap-through instability'. They concluded that this instability would

cause hysteresis as a result of misfits on chemical potential, μ. In the case of pore geometry dissimilarities, the phenomenon increases as the repulsion and attractive forces enhance the snap-through instabilities in the system.

2.8.1.2.2 Molecular condensation and hysteresis

The density of the adsorbate film, as seen in previous Section 2.8.1.2.1, is non-unique or 'heterogeneous'. This means that water in liquid or gas state is under constant dissociation from the action of orthogonal attractive forces. However, lateral interactions can be more important and may lead into more general hysteresis even in perfect geometries (Bažant and Bazant, 2012). The second part of the theory from Bazant (2012) presents the instability of adsorption/ desorption process as shown in Figure 2.27. Molecular condensation at low vapour pressure, referred as the phase separation of adsorbed molecules, is history dependent. This can occurs by the sudden instability activation of metastable state of water molecules under confinement. As Figure 2.27a-c shows, adsorption process become thermodynamically unstable and separates into a stable local low density phase (b), to then activate into a stable homogeneous density of adsorbate (c). When desorption begins, the phenomenon is in reverse from (d) destabilization and coalescence state to form a dense part (e), which results in a stable low density state (f). This would eventually lead into a hysteresis process due to a delayed phase separation and diffusional chemical potential, μ. Attractive lateral forces at low temperature may lead to a stable high-density (liquid-like), and stable low-density (vapour-like).

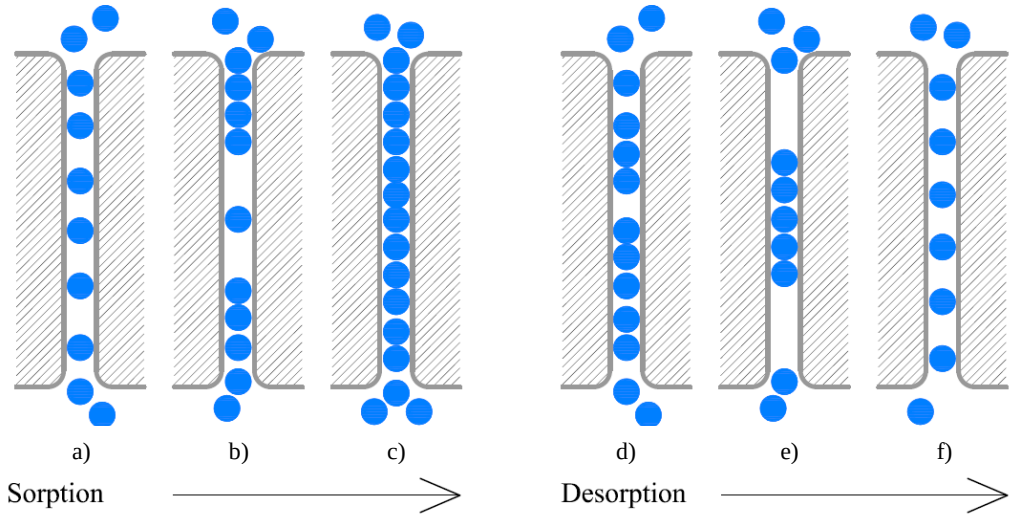


Figure 2.27 – Schematic representation of molecular condensation in nanopores; where adsorption process corresponds to letters a), b), and c), and desorption to letters d), e), and f). Adapted from (Bazant and Bažant, 2012).

Similarly, as previously depicted in Section 2.8.1.1, there is a critical temperature (T_{cc}) in which adsorption hysteresis disappears. At higher temperature, molecular condensation is thermodynamically unfavourable, and hysteresis no longer appears. Enhanced hysteresis can also be as a consequence of pore space reduction and morphology heterogeneities, which results in fewer sites for nucleation. On the other hand, in the adsorption process, water molecules can be hindered by the screening effect of other molecules (cations/ anions). Based on van der Waals forces, surface forces would decay as distance from the pore surface is increased. As a result, local interaction energy (ω), which depends on position, would also be affected by reaching values near the bulk water behaviour (refer also to Figure 2.3). This also can be explained by the adsorption model seen in Section 2.8.1.1 and on Figure 2.26, where molecular adsorption assumes a first strong monolayer which decay quickly as distance from the surface is increased. Eventually small cluster of water molecules will coarsen within the nanopores to minimize the gradient energy similarly to surface tension phenomenon.

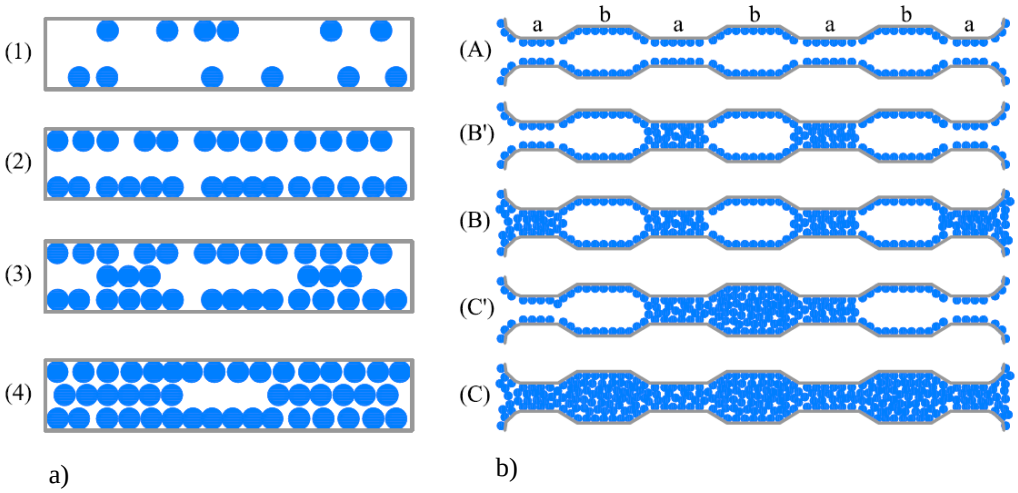


Figure 2.28 – Hierarchical wetting model and molecular condensation in heterogeneous multilayer nanopores with different sections (a) and (b) – From (Bazant and Bažant, 2012).

As Figure 2.28a shows, there were suggested two types of hysteresis, one which is found at low vapour pressure (1) with low-density and the other at high-density (2) in the monolayer. The latter, due to pore-spanning cluster of molecules or voids (cavities) represented as nano-bubbles or, as in the case of region (3) and (4) as droplets at high density and pressure. It can be suggested that, for droplet phase separation, the critical temperature T_{cc} in the bulk nanopores should be higher than for the first monolayer being adsorbed. Interfacial tension on the adsorption process, which is the sum of lateral interaction and surface chemistry, is explained in Figure 2.28b as follow. As a result of locally metastable state of water molecules, phase separation can occur anywhere that achieves that state. Pore type (b) has lower adsorption energy and larger interaction energy (ω – as a result of greater water molecules number), whereas small pore (a) would have great adsorption energy.

2.9 Summary

This chapter provided underlying theory associated to the terminology and classification of porous solid materials in order to approach the definitions that support the studies of hygrothermics in terms of moisture storage, transport and distribution. This was followed by the introduction of hygrothermal modelling simulation tools for simultaneous heat and moisture transport phenomena. The basic principles and theory was also presented, as well as the description of the hygrothermal simulation tool used in this research (WUFI+), and the applicability of the model in the hygrothermics field. Consecutively, the theory of gas adsorption and the implications of adsorbent-adsorbate interactions for the determination of textural properties of porous solid materials was presented. Similarly, water vapour adsorption was introduced with the purpose to associate physisorption theory with hysteresis phenomena and capillary condensation, and the implications that these have for hygrothermal material's characterization. Finally, the hysteresis phenomena and molecular condensation for water vapour was introduced, by the presentation of some molecular dynamic studies within nanopores.

CHAPTER 3 Methods

3.1 Overview

This Chapter provides the description of the experimental and numerical techniques used for the implementation of the top-down design strategy for mesoporous desiccants based on the following hypothesis, where:

1. N may have a direct correlation between the pore volume and a specific portion of the isotherm.
2. For any φ buffering application the maximum theoretical pore volume should occur within the linear portion of the isotherm between the $\varphi_{i,L} - \varphi_{i,U}$ limits, in order to maintain the fluctuation $\varphi(t)$ between the φ_{max} and φ_{min} limits of any given scenario.

The methodology was therefore designed to test these hypothesis and consisted of three distinctive stages as previously shown in Figure 1.2 and the objectives set in Section 1.3.

Stage 1. Development of the hygrothermal modelling technique, which corresponds to objectives 1 & 2. This comprises Sections 3.2 and 3.3 and includes the characterization (water vapour isotherm) of the pre-existing MS materials (MS-3.3 and 8.3), and the development of the hygrothermal numerical modelling-based design tool. Preliminary numerical simulations were included aimed to calibrate the top-down technique for water vapour isotherm design using the pre-existing MS properties data. This was followed by a range of relative humidity buffering simulations and parametric studies to provide

sensitivity analysis for the hypothetically-designed ‘ideal’ isotherms and for further applicability of the design tool.

Stage 2. Material synthesis process of the new created MS materials (SBA-15 & MCM-41), which corresponds to objectives 3 & 4. This comprises Sections 3.4 to 3.5 and include the synthesis and characterization of the MS materials using nitrogen physisorption and dynamic vapour sorption techniques. Additionally, validation of the hygrothermal numerical modelling technique is presented by comparing the experimental and numerical data for the kinetics of water vapour adsorption/ desorption.

Stage 3. Optimization and application of the hygrothermal numerical technique based on an energy consumption case scenario, which corresponds to objective 5. This comprises Section 3.6 and include a series of relative humidity buffering simulations, with the aim of informing the specification of ‘ideal’ water vapour isotherms. Sensitivity analysis was conducted between selected desiccant materials gathered from literature and the ones synthesised in this study, and aimed to assess the kinetics of continuous moisture loads and their performance for water vapour exchange. This was followed by humidity buffering simulations in a series of closed environments (*i.e.* specific operating φ limits), with the aim to assess material suitability for specific relative humidity applications. Additional simulations were conducted with the aim to assess the dehumidification performance of the desiccants, and to estimate the relative effect on energy efficiency when assisting a mixed mode HVAC system.

3.2 Hygrothermal functional properties characterization

This section describes the characterization methods for the determination of the water vapour adsorption/ desorption isotherms (or 'moisture storage function') under isothermal conditions. This aimed to comply with objective 1 as outlined in Section 1.3. As discussed in Section 2.3.1, the moisture storage is defined as a unique value referred as total moisture content, *w*. WUFI+ uses this as an important input for the numerical estimations, assuming that equilibrium moisture content has been reached. From this WUFI+ can interpolate it across the material by solving the moisture transport equations (refer to equations 2.12 and 2.13).

3.2.1 Water vapour adsorption/ desorption isotherms

A climatic chamber is a self-contained humidity system with precise air-cooled cascade refrigeration system that incorporates an integrated heater. In this research, a climatic chamber (TAS Series 3 LTCL – 600, Temperature Applied Sciences Ltd, West Sussex, UK) was used to independently control T_{db} and φ to an accuracy of ± 0.3 – 1.0 K and ± 3 %, respectively (refer to Figure 3.1b). This was used for the determination of the water vapour adsorption isotherms for the pre-existing desiccant materials MS-3.3, 8.3, and Silica gel (refer to Section 4.3.1 for results). The climatic chamber incorporates an electronic weighing balance (VIBRA HT Series Tuning-fork frequency sensing, 0.0001g accuracy - Figure 3.1d) connected into a PC using an Eltima RS232 data logging software for continuous measurements recorded in 30 sec time-steps. Prior to the test, all desiccants were outgassed under high-vacuum at 120 °C for 12 h. This was done

in order to achieve the moisture content condition, $w = w_0$, and to ensure that all moisture and volatiles were properly evacuated (in this point, the Micromeritics ASAP 2020 analyser was used). Before placing the samples within the climatic chamber, this was left to fully equilibrate at 23 °C (± 0.5 °C) and at the corresponding φ (*e.g.* φ = 0.2) for 1 h to ensure stability for measurements accuracy (Figure 3.1c). Once the chamber was fully equilibrated, the dry samples (~ 2 g) were rapidly placed (to avoid overexposure before starting the recording) within the petri dish in a uniform ~ 2 mm thick layer. The upper vent was open (1 cm) to allow the airflow inside the balance (refer to Figure 3.1a). Immediately after that, the pre-set targeted relative humidity values were activated from the climatic chamber panel (Figure 3.1c). The relative humidity (set points) were set as: φ = 0.2, 0.3, 0.5, 0.7 and 0.95, along with the change in mass step as a function of time, *t* until equilibrium moisture content (EMC) was reached; *i.e.* $\Delta m < \pm 0.5$ %. Each φ set point at EMC was recorded and plotted with a straight line, in order to produce the adsorption isotherm. All protocols were conducted according to the BS EN ISO 12571:2000.

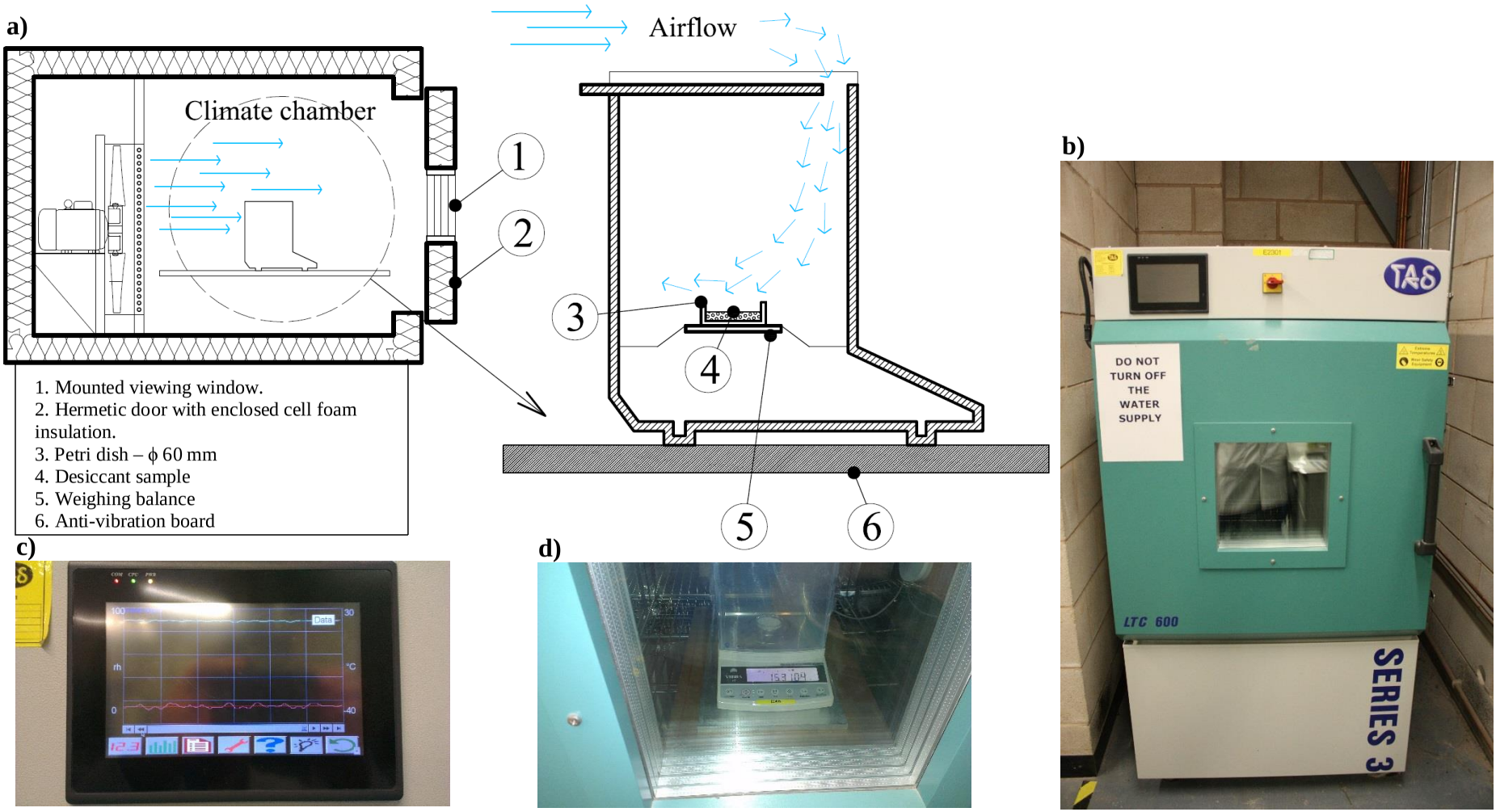


Figure 3.1 – a) Schematic representation of the experimental setup, b) Climatic Chamber – TAS Series 3, c) touchscreen graphical programmer interface, and d) mass change recordings using the VIBRA HT Series electronic weighing balance.

3.3 Hygrothermal modelling technique for the design of water vapour isotherms

3.3.1 Preliminary humidity buffering capacity simulations

A preliminary sensitivity analysis was conducted using the hygrothermal numerical model WUFI+ v2.5.3 (described in Section 2.5), and aimed to comply with objective 2 as outlined in Section 1.3. This consisted of a series of hygrothermal simulations to enable the calibration and operation of the hygrothermal modelling technique for water vapour isotherm design. For this, two different closed environments were simulated, and calibrated by (refer to Figure 3.2) assessing the fluctuation of $\varphi(t)$ within the operational limits (φ_{min} = 0.55 and φ_{max} = 0.7) when performing repeated loop cycling, at N number of cycles. This was done in order to test the hypothesis (refer to Section 3.1) in which N may have a direct correlation between the pore volume and to a specific portion of the isotherm. The φ_{min} value was initially set to represent the median value between the lower and upper φ range (φ = 0.4 – 0.7) within the indoor comfort zone defined by the ASHRAE (Handbook, 2009), at T_{db} = 23 °C. Consequently, the decay for humidity buffering of the materials was defined once the fluctuation of $\varphi(t)$ exceeded the comfort upper limit (φ_{max} = 0.70) at N number of cycles; *i.e.* material failure point (refer to Figure 3.3). In the same logic, two pre-existing MS materials (MS 3.3 and 8.3) and their hygrothermal properties were used as a template, and served as the initial candidates for the calibration process. These were gathered from previous research (Hall *et al.*, 2012), where the hygrothermal properties are found in Table 3.1.

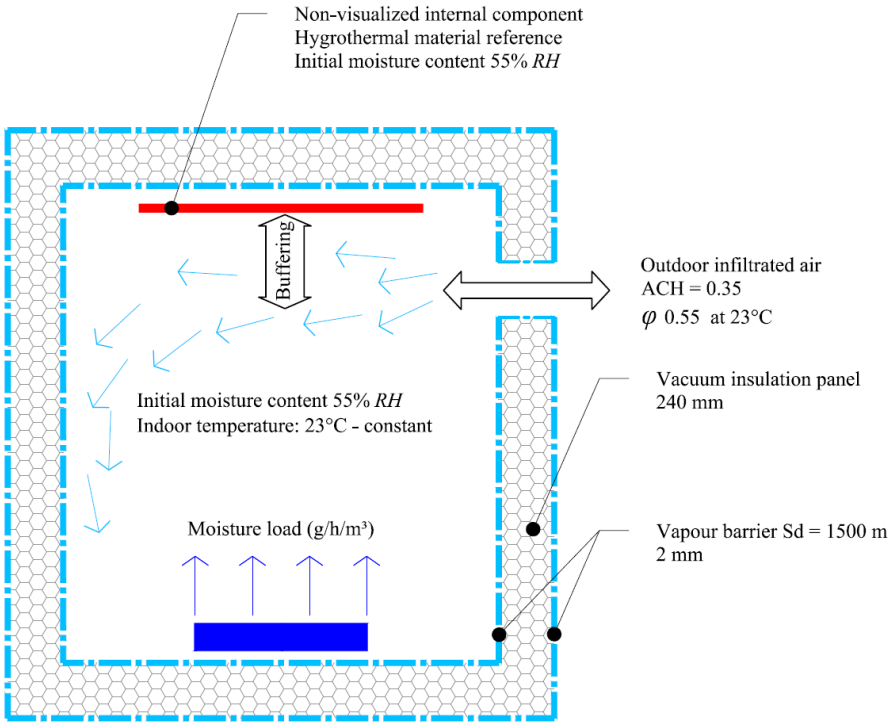


Figure 3.2 – Closed environment representation for the numerical simulations (Thomann *et al.*, 2015b).

Material	n	ϕ_{pore}	ρ_b	C_p	λ	A	μ
	(m^3/m^3)	(nm)	(kg/m^3)	(J/kg K)	(W/m K)	($kg/m^2\ s^{0.5}$)	(-)
MS-3.3[a]	0.76	3.3	501	1011	0.05	2.112	4.54
MS-8.3[a]	0.76	8.3	618	1691	0.05	0.550	10.52

Table 3.1 – Hygrothermal functional properties for mesoporous silicas. [a] Values taken from (Hall *et al.*, 2012; Casey *et al.*, 2012).

The first scenario consisted of successive cycles of 4 h, where a moisture load of 2.5 g/h was applied for 2 h followed by 2 h of no moisture loads (refer to Figure 3.4a). The calibrated moisture load was fixed once the fluctuation of $\varphi(t)$ exceed the comfort upper limit (φ_{max} = 0.70) by φ = 0.05 and stabilised along the total number of cycles, N = 60 (refer to Figure 3.3). Consequently, a 2 mm thick layer of the MS materials was calibrated, with an exposed surface area of 0.12 m^2. Within the hygrothermal modelling (WUFI+), this was represented by a non-visualized internal component.

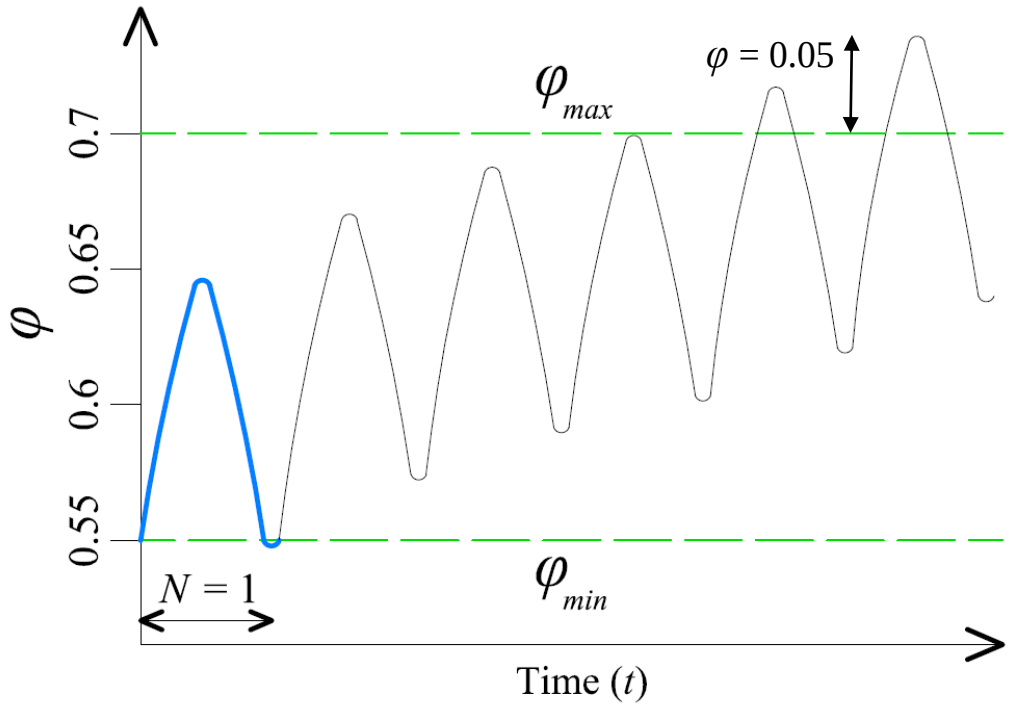


Figure 3.3 – Humidity buffering decay representation when the fluctuation of $\varphi(t)$ exceeds the upper limit (φ_{max}) at N number of cycles.

For both of the scenarios, the same closed environment (refer to Figure 3.2) was used, which comprised in a thermally and hygrically isolated box of volume, V = 1 m^3; minimum internal volume permissible by WUFI+. As Figure 3.2 shows, the test box fabric comprised 2 mm thick water vapour barrier (S_d = 1500 m) and 240 mm thick vacuum insulation panel (λ = 0.001 W/ m K). Similarly, the second scenario consisted of successive cycles of 24 h, where calibrated moisture loads of 4 g/h were applied during the first 8 h, followed by 16 h of no moisture loads generation (refer to Figure 3.4b). The calibration of the moisture load was fixed by the same principle described above, where the total number of cycles, N = 11. The increment of moisture loads applied, compared with previous scenario, were intentionally created in order to represent an 'overloading moisture scenario' with respect to the isolated box of volume, V = 1 m^3, using the same exposed surface area of 0.12 m^2.

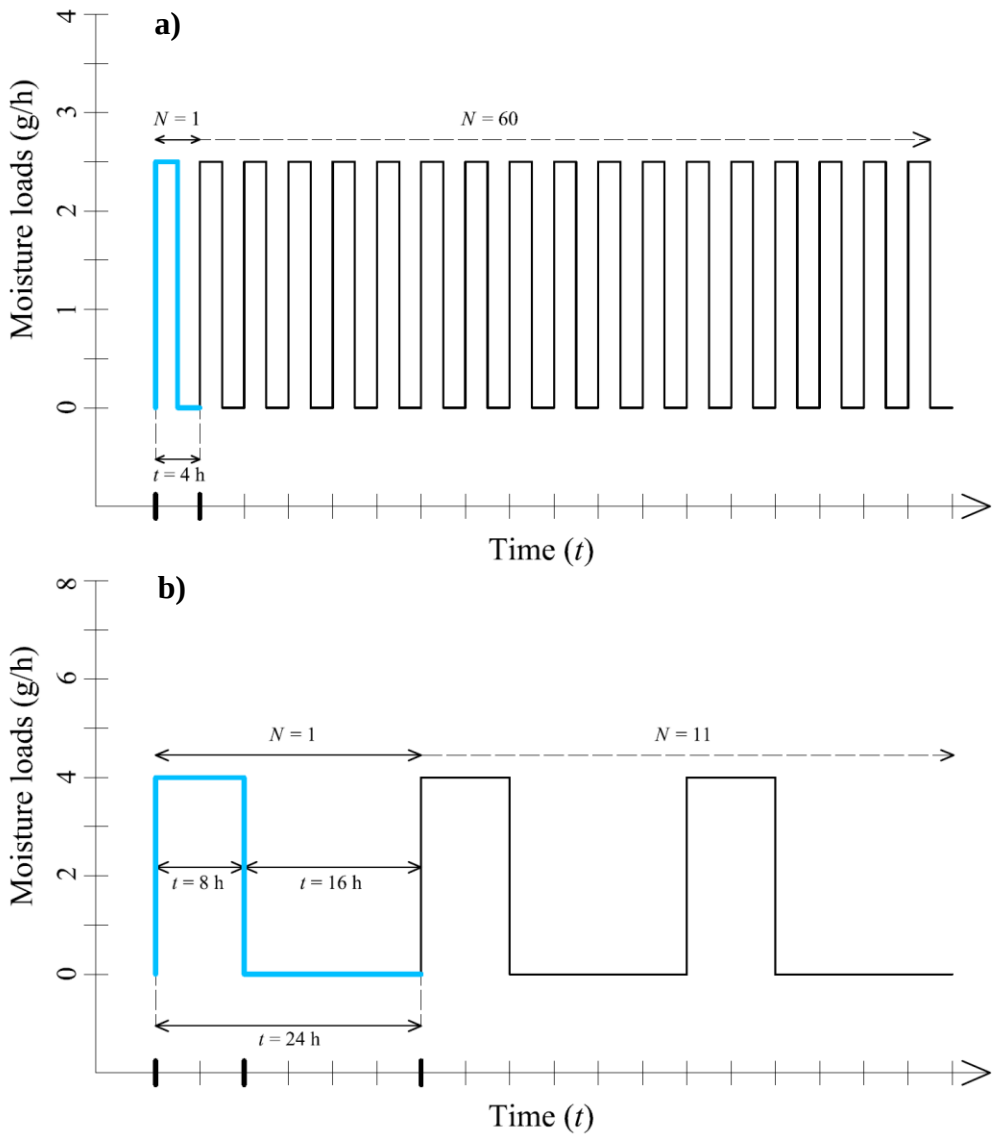


Figure 3.4 – Moisture loads schedule as a function of time (*t*), where a) corresponds to the 4 h cycle and b) to the 24 h cycle.

Additionally, in order to provide an airtight condition of the isolated box, a constant air infiltration rate of 0.35 ACH was set for both closed environments. This was intentionally done in order to test the capacity for humidity buffering of the MS materials under low infiltration rates, with respect to the *N* number of cycles. In addition, this would provide assessment of the humidity buffering performance solely by means of the moisture loads and not from the psychrometric conditions of the outdoor air humidity. In a later stage (refer to Section 3.3.3) a ventilation sensitivity analysis was conducted in order to assess

the effect of the background air infiltration on the interior moisture loads. The simulations were carried out under isothermal conditions, where the initial indoor/ outdoor air humidity was equally set as φ_i = 0.5, φ_e = 0.5, respectively at T_{db} = 23 °C. The initial conditions of each MS material were also set at φ = 0.5, and the derived initial moisture content, w from the water vapour adsorption isotherm was then used by WUFI+; in this research named as w_{50}. The parameters for the numerical model were set to have: (i) increased accuracy and adapted convergence (*i.e.* when termination criteria for each numerical iteration is finished – refer to Section 2.5.2.6), (ii) net volume = 1 m^3, (iii) time step 1 min, (iv) optional climate (φ = 0.5 / 23 °C), (v) inner climate calculated, (vi) initial boundary conditions (φ = 0.5 / 23 °C), (vii) 'fine' mesh grid spacing, and (viii) calculation accuracy of 0.5 % / 0.5 °C for φ and T_{db}, respectively.

3.3.2 Design process of water vapour isotherms

The design process of the water vapour isotherm presented here is part of the development of the hygrothermal modelling technique, aimed to comply with objective 2 from Stage 1 outlined in Section 1.3 – refer also to Figure 1.2. This design process follows the principle (refer to Section 3.3.1) that, when assessing a closed environment in which a calibrated moisture load have set (either fixed, intermittent or variable), the material would fail once the fluctuation of $\varphi(t)$ exceeds the upper limit, φ_{max}. If after subsequent cycles the capacity for moisture storage decays, then after N cycles the fluctuation between φ_{max} and φ_{min} can no longer be maintained and the desiccant must be fully outgassed for re-use. Therefore, an 'optimum isotherm' is the one that can maintain the fluctuation $\varphi(t)$ between the upper/ lower limits (φ_{max} and φ_{min}) of any given scenario. This

follows the hypothesis set in Section 3.1. that, for any φ buffering application in a closed environment scenario the 'optimum isotherm' would have the maximum theoretical pore volume and a steep relative humidity gradient between the upper ($\varphi_{i,U}$) and lower ($\varphi_{i,L}$) limits.

As represented in Figure 3.5, the linear portion of the isotherm between $\varphi_{i,L}$ (1st inflection point; the onset of multilayer physisorption) and $\varphi_{i,U}$ (2nd inflection point; the top knee) would correspond to the available moisture storage capacity, Δw for humidity buffering between φ_{min} and φ_{max} limits. Additionally, this would imply that a range of hypothetical isotherm candidates could be described as a transition from Type I to Type V (inclusive) and designed according to a specific φ buffering application by adapting the steepness of the curve schematically sketched in Figure 3.5.

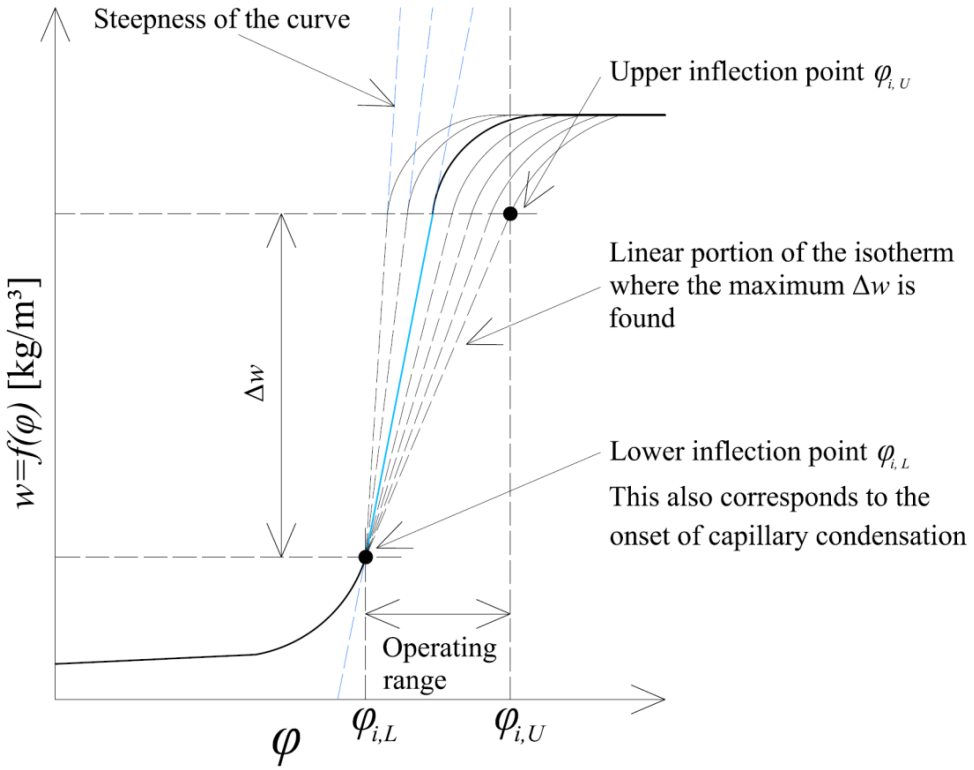


Figure 3.5 – Schematic representation of an 'optimum' hypothetical water vapour isotherm where the maximum Δw is defined between the upper ($\varphi_{i,U}$) and lower ($\varphi_{i,L}$) limits. Adapted from (Thomann *et al.*, 2015b).

The process of generating hypothetical water vapour isotherms initially begins, as Figure 3.6a shows, by adjustments to the *x*–*y* axis values. This would define the first candidate with a corresponding modal pore diameter, a maximum theoretical pore volume (*i.e.* referenced as with an existent material), and the steepness of the *w* gradient (refer to Figure 3.5). Consequently, as Figure 3.6b shows, the modal pore diameter and pore volume variations could be designed by successive adjustments on the *x*–*y* axes by hypothetically altering pore wall thickness. At this stage, the maximum pore volume, *n* could remain unchanged, because of the linear portion of the isotherm between $\varphi_{i,L}$ and $\varphi_{i,U}$ also remain unchanged. This could potentially facilitate extended applications for materials design (*e.g.* where the maximum Δw is required to be unaltered) or if matching of an existent water vapour isotherm at lower pore volume (*e.g.* constant modal pore diameter) is needed.

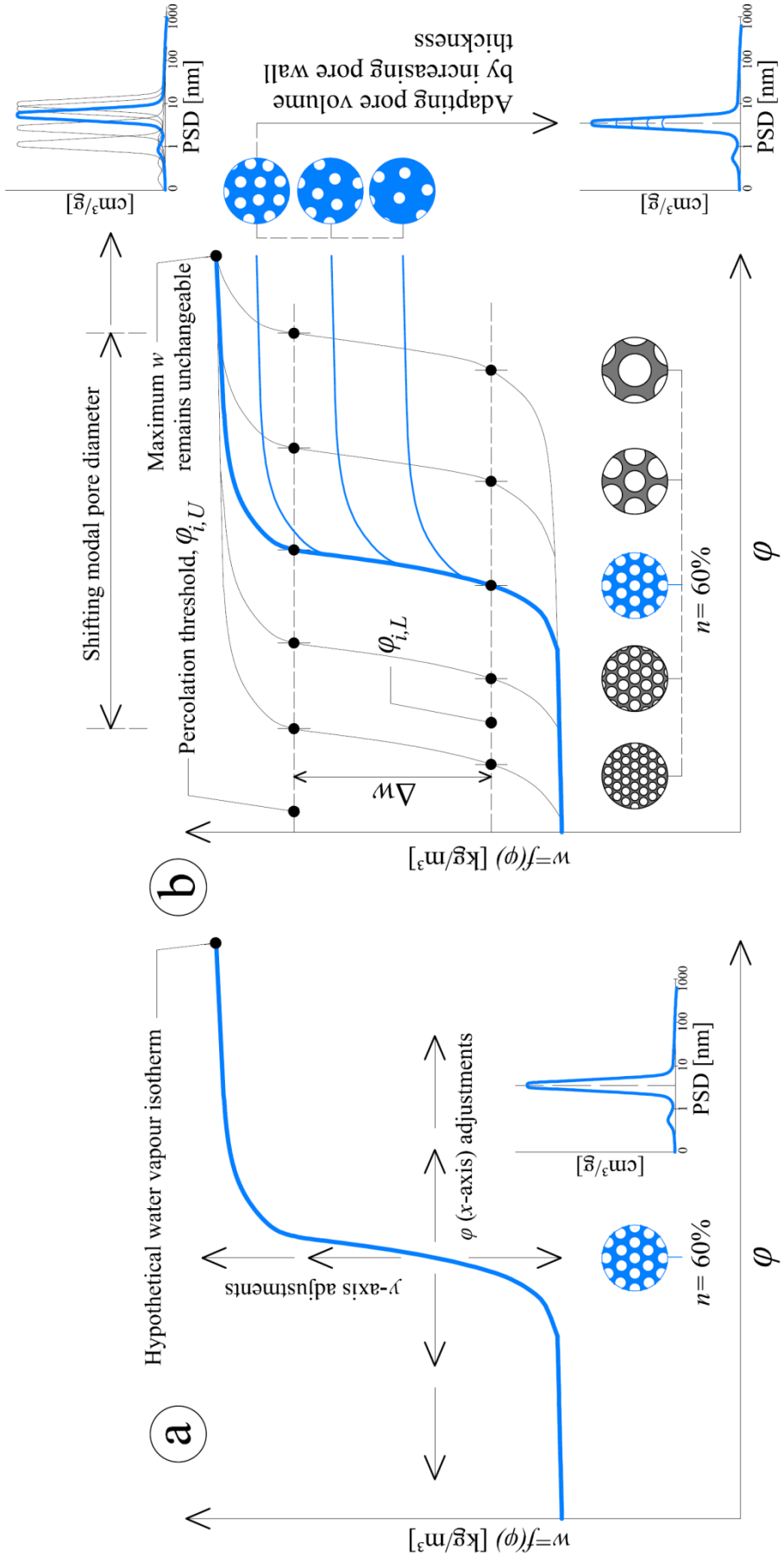


Figure 3.6 – Schematic representation of a hypothetical water vapour isotherm design. a) Initial adjustments in the *x*–*y* axis values. b) Further modifications in the *x*–*y* axis values for new candidates with modal pore diameter and pore volume variations derived from first candidate. Adapted from (Thomann *et al.*, 2015b).

For this research, the following approach was established in order to start with the hypothetical design of a water vapour sorption isotherm:

1. To generate a variety of new isotherm candidates derived from the modification of an existing material, which in this case is referred to the MS-8.3 (Section 3.3.3).
2. To conduct a sensitivity analysis to correlate the effects of the isotherm modification on relative humidity buffering behaviour, which will be able to produce an optimum isotherm for any closed environment scenario (Section 3.3.4).

3.3.3 Isotherm candidates

In order to test the above mentioned hypothesis (refer to Section 3.1), a first set of candidate isotherms were introduced (A_1–A_6). These were derived from the pre-existing MS-8.3, having a moisture content, w = 773.6 kg/m^3, each having identical moisture storage capacity (Δw = 671 kg/m^3) within the specified $\varphi_{i,L}$ – $\varphi_{i,U}$ range seen in

Table 3.2 and Figure 3.7a. Figure 3.7b shows the modal pore diameters and incremental pore volume derived from Kelvin's equation ranging from 2.85 nm to 6.56 nm. These were hypothetically created by altering pore wall thickness such that pore volume remained unaltered (refer to Figure 3.6). The hygrothermal functional properties derived from MS-8.3 were used for all candidates (A_1–A_6). Similarly, the capillary transport coefficient (D_{ws}) used in the hygrothermal numerical model was calculated after producing the water vapour isotherm (Künzel, 1995); refer to Section 2.5.2.3 and Equation 2.5.

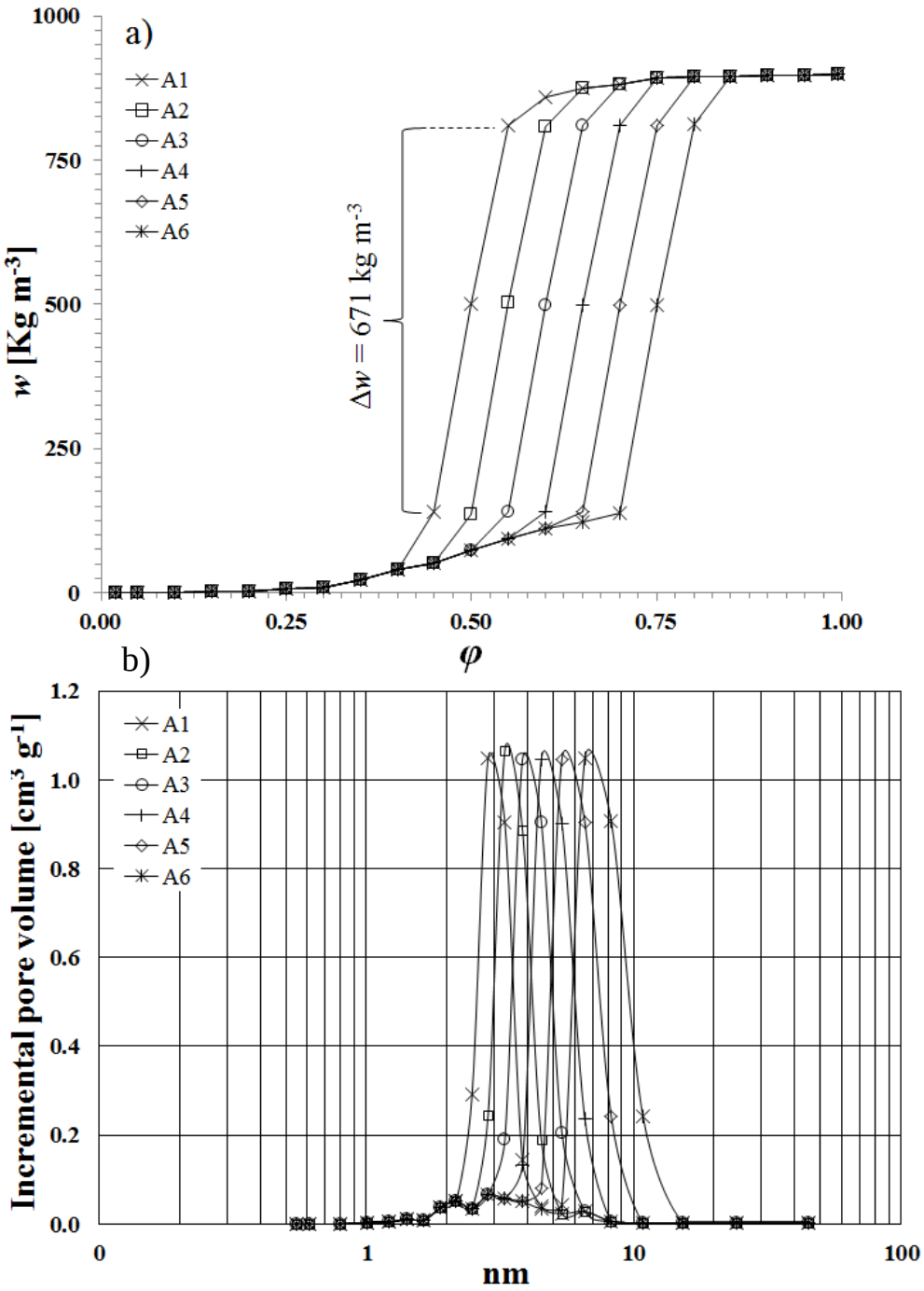


Figure 3.7 – a) Hypothetical water vapour isotherm candidates and, b) corresponding PSD derived from Kelvin equation (Thomann *et al.*, 2015b).

Material	n	ϕ_{pore}	$\Delta w_{45\text{-}55}$	$\Delta w_{50\text{-}60}$	$\Delta w_{55\text{-}65}$	$\Delta w_{60\text{-}70}$	$\Delta w_{65\text{-}75}$	$\Delta w_{70\text{-}80}$
	(m^3/m^3)	(nm^*)			($kg//m^3$)			
A_1	0.9	2.85	**671**	360	63	22	18	12
A_2	0.9	3.29	451	**671**	371	73	18	12
A_3	0.9	3.83	88	425	**671**	383	81	12
A_4	0.9	4.51	42	65	406	**671**	392	84
A_5	0.9	5.38	42	37	45	388	**671**	394
A_6	0.9	6.56	42	37	30	27	376	**671**

Table 3.2 – First set of isotherm candidates (A_1–A_6) within the specified $\varphi_{i,L} - \varphi_{i,U}$ range. * Derived from Kelvin's equation.

A second set of isotherm candidates (B_1–B_4) were introduced by proportionally reducing the total pore volume (*y*–axis adjustment) from 100 % to 60 % (refer to Figure 3.8a). The A_3 candidate isotherm was used as a reference to continue to test the hypothesis for the design of an 'optimum isotherm'. The aim was to determine whether the fluctuation of $\varphi(t)$ for humidity buffering could still proportionally be maintained for the new isotherm candidates (B_1–B_4) with respect to the number of cycles, $N = 60$ before failure. This, by assessing the new isotherms within the same operating limits set at the calibration stage of the hygrothermal modelling technique, *i.e.* $\varphi_{min} = 0.55$ and $\varphi_{max} = 0.70$. Figure 3.8b shows the PSD histogram and the corresponding modal pore diameter derived from the Kelvin equation, hypothetically created by altering total pore volume and wall thicknesses (refer to Figure 3.6b).

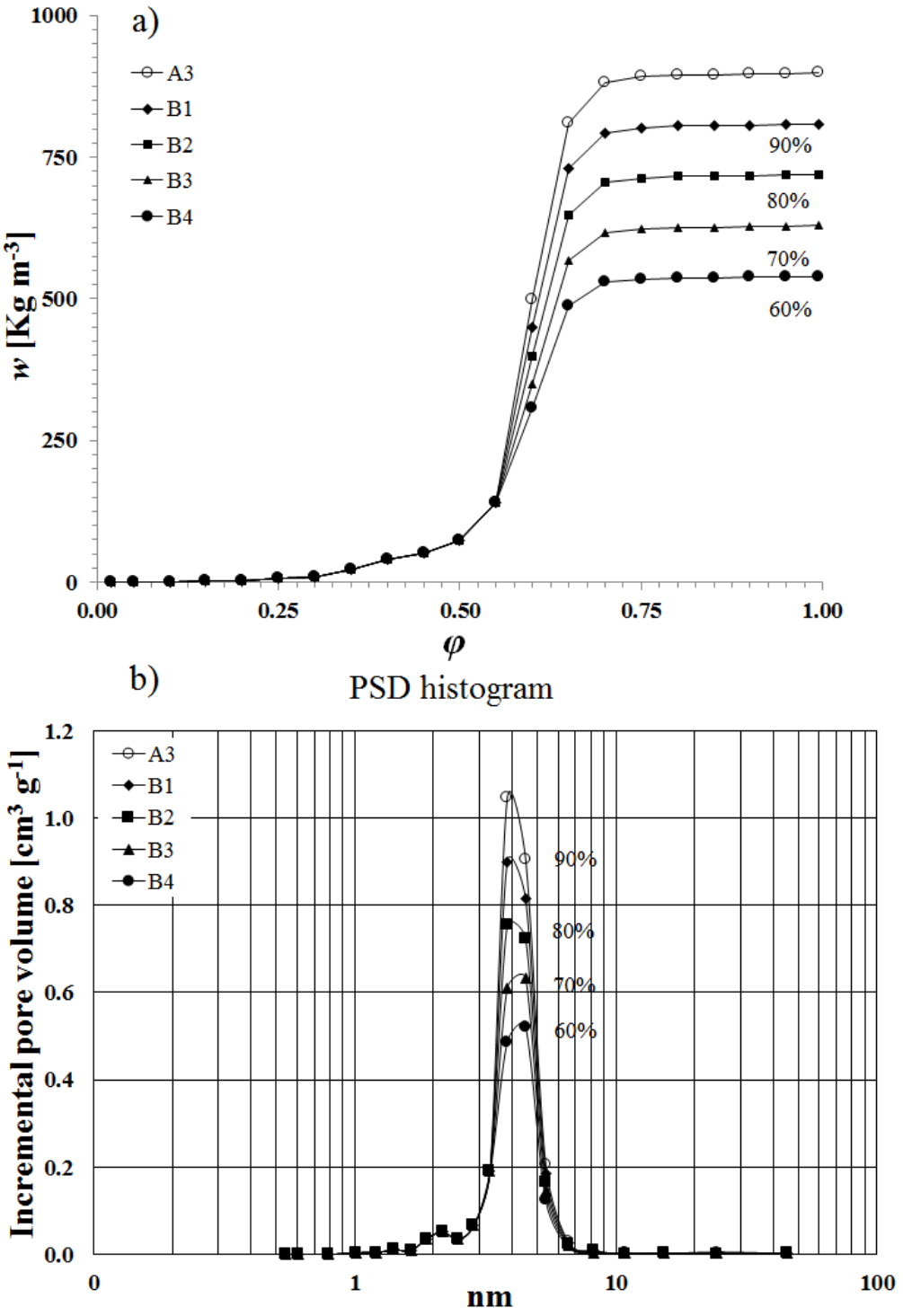


Figure 3.8 – Second set of isotherm candidates. a) Proportionally reduced water vapour isotherms derived from candidate A_3. b) Corresponding modal pore diameter derived from Kelvin's equation (Thomann *et al.*, 2015b).

3.3.4 Sensitivity analysis for new isotherm candidates

A series of numerical simulations were conducted for the hypothetically created isotherms (A_1–A_6) as depicted in the design process in Section 3.3.2. This was aimed to comply with objective 2 as outlined in Section 1.3. All materials introduced were designed according to the storage capacity (Δw = 671 kg/m^3) within the specified upper ($\varphi_{i,U}$) and lower ($\varphi_{i,L}$) limits (refer to Section 3.3.3, Figure 3.7, and Table 3.2). The aim was to determine the 'optimum isotherm' for specific operating φ limits, under the hypothesis already set in Section 3.1.

Further numerical simulations were conducted for the second set of isotherms (B_1–B_4) derived from the isotherm candidate A_3; where the total pore volume was proportionally reduced from 100 % to 60% – refer to Section 3.3.3. All these simulations were conducted using the same closed environment scenario (used in the preliminary simulations – refer to Figure 3.2), and using the same operational limits (φ_{min} = 0.55 and φ_{max} = 0.70). The aim was to show consistency with previous simulations using the calibrated hygrothermal model (refer to Section 3.3.1), and with the isotherm design process (and humidity buffering comparison) under identical scenarios. In the same logic, for both new sets of isotherms, same number of cycles (N = 60) were set, and consisted in successive cycles of 4 h using a moisture load of 2.5 g/h during the first 2 h, followed by 2 h of no moisture loads generation (refer to Figure 3.4a). The parameters and settings for the closed environment within the numerical model, as well as the initial conditions for each designed isotherm were exactly the same as depicted in previous Section 3.3.1.

3.3.5 Standardization and parametric studies

The next series of hygrothermal simulations followed a standardization process to determine the permissible moisture loads capacity per unit mass (kg), where the hypothetical isotherm designed (A_3 – refer to Figure 3.7) was selected. The aim was to allow analysis of the quantity of material required whilst producing humidity buffering control within the specified operational limits (φ_{min} and φ_{max}), before the fluctuation of $\varphi(t)$ exceeds the upper limit, φ_{max}. This was done within the scope of objective 2 from Stage 1, previously outlined in Section 1.3.

Within the hygrothermal modelling, this was assessed by introducing a volumetric moisture load (ω_{ml} – g/h/m^3) using same closed environment as with previous simulations; *i.e.* isolated box of volume, V = 1 m^3 – refer to Figure 3.2. These moisture loads were progressively added in successive cycles of 4 h (2 h of moisture loads followed by 2 h of no moisture loads) until the fluctuation of $\varphi(t)$ exceeded the maximum upper limit (φ_{max} = 0.70), and when completing the total number of cycles,(N = 60). This enabled the standardization process of volumetric moisture loads (ω_{ml}) in 1m^3 at N = 60. The theoretical isotherm A_3 was selected as a reference for the standardization process with an assumed exposed surface area of 0.12 m^2 (equivalent to 0.15 kg/m^3). The latter was estimated by using the bulk density (ρ_b = 618 kg/m^3) and a 2 mm thick layer of MS-8.3 material (refer to Table 3.1). Again, within the hygrothermal model this was represented by a non-visualized internal component. Further simulations were then conducted, using same procedure described above, across a new set of exposed surface areas, as presented in Table 3.3; *e.g.* 0.2024 m^2 – equivalent to 0.25 kg. Hence, these simulations enabled to construct the curve of volumetric moisture loads (g/h/m^3) that a specific quantity of material (kg) can cope before

the fluctuation of $\varphi(t)$ exceeds the operational limits (where: φ_{min} = 0.55 and φ_{max} = 0.70). The error bars of the produced curve (refer to Section 4.4 and Figure 4.11and Figure 4.12) would not be visible in some cases, since the accuracy of it was within 3 %. The initial parameters set for the hygrothermal modelling were the same used for the closed environment referred in Section 3.3.1. For the above described simulations, the initial infiltration rate was set as 0.35 ACH, and the initial indoor/ outdoor air humidity was equally set as φ_i = 0.5 and φ_e = 0.5, respectively. This was performed under isothermal conditions at T_{db} = 23 °C, where the initial moisture content, w was set at φ = 0.5 (*i.e.* w_{50}).

Infiltration rates sensitivity analysis				Ventilation sensitivity analysis			
Exposed surface area	Mass	ACH	φ_e	Area/volume ratio	Mass	ACH	φ_e
(m^2)	(kg)	(-)	(-)	(m^2)	(kg)	(-)	(-)
0.0405	0.05	0.25	0.5	0.0405	0.05	0.35	0.2
0.0810	0.1	0.5		0.0810	0.1		0.3
0.1214	0.15	0.7		0.1214	0.15		0.4
0.1619	0.2			0.1619	0.2		0.6
0.2024	0.25			0.2024	0.25		0.7
0.2429	0.3			0.2429	0.3		
0.2283	0.35			0.2283	0.35		
0.3239	0.4			0.3239	0.4		
0.3643	0.45			0.3643	0.45		

Table 3.3 – Parameters for the numerical model setup when assessing infiltration and ventilation sensitivity analysis for the standardization process.

After the first curve of total moisture loads was plotted and assessed (Table 3.3), a ventilation sensitivity analysis was conducted for three different ACH values: 0.25, 0.5 and 0.7. The aim was to assess how the air infiltration rate (at constant

outdoor air humidity, φ_e = 0.5 and T_{db} = 23 °C) affected the humidity buffering capability for isotherm A_3.

In order to determine the effect of φ_e in diluting/ intensifying the interior moisture load, a new set of five new different φ_e values were added (φ_e = 0.2, 0.3, 0.4, 0.6 and 0.7) as Table 3.3 shows. In this scenario, a constant air infiltration rate was set as 0.35 ACH, and the initial indoor air humidity was set as φ_i = 0.5. The same initial conditions and number of cycles were used for both parametric studies, in order to show consistency with previous simulations, where the moisture loads were also progressively added until the fluctuation of $\varphi(t)$ exceeded the upper limit, φ_{max}. Again, this was performed under isothermal conditions at T_{db} = 23 °C, where the initial moisture content, w was set at φ = 0.5 (w_{50}).

3.4 Synthesis and characterization of mesoporous desiccants

The synthesis and characterization of the new MS desiccants (SBA-15 and MCM-41) aimed to meet objective 3 (Stage 2), as outlined in Section 1.3 – also refer to Figure 1.2. The description of the desiccants' preparation is provided below, and also can be found in previous publications from the author Thomann *et al*., (2015a; 2015b).

The synthesis of SBA-15 (6 nm pore size) was performed following instructions from the author within the scope of the collaborative research, and prepared by Dr Lee Stevens at the Department of Chemical and Environmental Engineering, Faculty of Engineering, University of Nottingham. This was conducted in a similar manner to Zhao *et al*., (1998) with the same batch of SBA-15 used throughout the study. Typically, a Pluronic surfactant 123 (P123, triblock

copolymer (EO)20(PO)70(EO)20, 80.0 g) was dissolved, applying vigorous stirring at 35 °C, in an aqueous hydrochloric acid (1.33M, 3000 ml). Once the dissolution was completed, tetraethoxyorthosilicate was added (TEOS, 182 ml) dropwise, and for 24 h the mixture was stirred at 35 °C. The solution was then transferred to a Teflon lined autoclave and statically heated at 85 °C for 48 h. Before heating in a furnace (at 600°C for 6 h), the resulting white solid product was recovered and separated by filtration, following a dried period of 2 h in an oven at 105 °C. After calcination, a white solid powder without residual organic templates yielded the final mesoporous solid.

In a similar manner, the synthesis of the SBA-15 (10 nm pore size) followed same procedure as depicted by Zhao *et al*., (1998) with the same batch of SBA-15 used throughout the study. Similarly to SBA-15 6 nm, a Pluronic surfactant 123 (P123, triblock copolymer (EO)20(PO)70(EO)20, 4.0 g) was used and dissolved, by applying vigorous stirring at 35 °C in an aqueous hydrochloric acid (1.33M, 75 ml) in addition with mesitylene (2 ml). Subsequently, once the dissolution was completed, tetraethoxyorthosilicate was added (TEOS, 4.55 ml) dropwise, and for 24 h the mixture was stirred at 35 °C. The solution was then transferred and placed into a Teflon lined autoclave and statically heated at 120 °C for 24 h. Before heating in a furnace (at 600°C for 6 h), the resulting white solid product was recovered and separated by filtration, following a dried period of 2 h in an oven at 105 °C. After calcination, a white solid powder without residual organic templates yielded the final mesoporous solid.

The description of the MCM-41 desiccants' preparation (MCM-41@150, 165, and 180) provided here can be also found in Thomann *et al*., (2015b). The

synthesis of all MCM-41 was performed following instructions from the author within the scope of the collaborative research, and prepared by the PhD student Wantana Sangchoom, under the supervision of Dr Robert Mokaya, at the School of Chemistry, Faculty of Science, University of Nottingham.

The synthesis of the three pure MCM-41 samples was conducted from fumed silica as the silica source, using as a structure directing agent (or template) cetyltrimethylammonium bromide (CTAB), tetramethylammonium hydroxide (TMAOH) and water. Typically, TMAOH (1.9 g) and CTAB (4.6 g) were dissolved in 34.1 g of distilled water by applying vigorous stirring at 35 °C. This was followed, by adding 3.0 g of fumed silica to the current solution by applying stirring for 1 h to then obtain a homogeneous gel of molar composition SiO_2:0.25CTAB:0.2TMAOH:40H_2O.

After this, the gel was left to age for 20 h at room temperature. The aged gel mixtures were then transferred to a Teflon-lined autoclave and statically heated at 150 or 180 °C for 48 h. Before the calcination process, the resulting solid product was recovered and separated by filtration, washed with water and dried in air at room temperature; this yielded the as-synthesized sample. In the calcination process, the surfactant templates within the as-synthesized sample were removed in a furnace (heating ramp rate of 5 °C/min) at 550 °C for 6 h. After all samples were calcined, the MCM-41 desiccants were designated according to their synthesis (crystallisation) temperature, *i.e.* MCM-41@150 or 180.

3.4.1 Nitrogen physisorption

As previously described in Section 2.6.1, physisorption is the result of molecular attractive and repulsive interactions caused by van der Waals forces (*i.e*. between the adsorbent-adsorbate) that approaches the adsorbent surface, which at higher P/P_0 induce spontaneous formation of multilayer coverage on the adsorbent and fill of all the pores. The volumetric method determines (at constant temperature) the accessible internal/ external surface of the pore structure by the intrusion of an adsorbent gas (in this case N_2 at ~ 77 K). The amount adsorbed is measured point-by-point by admitting successive known volumes of nitrogen and measuring the equilibrium pressure, *P*, to then obtain the adsorption isotherm for the specific relative pressure P/P_0 achieved. Procedures and techniques were in accordance with BSI 4359-1: 1996; where (1) is the sample, (2) dewar vessel with liquid nitrogen, (3) vacuum-generating system, (4) manometer, and (5) calibrated volume (refer to Figure 3.9).

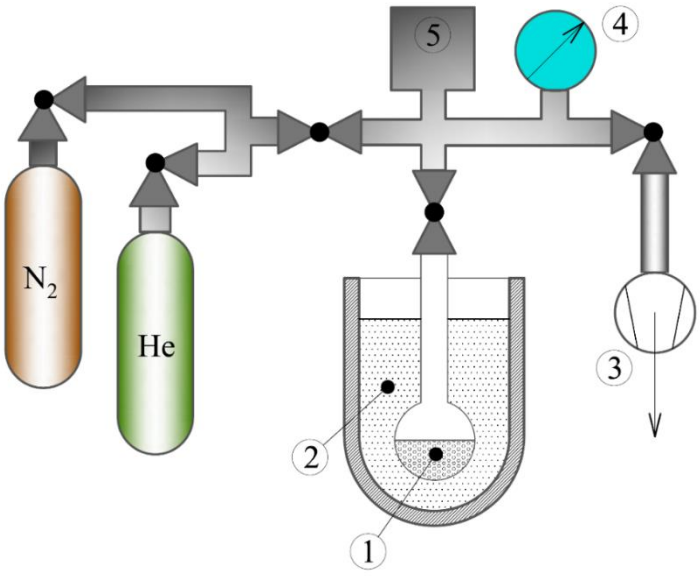


Figure 3.9 – Volumetric method diagram of physisorption measurements. Adapted from BSI 4359-1: 1996.

Nitrogen physisorption for all SBA-15 desiccants was performed by Dr Lee Stevens and assisted by the author at the Department of Chemical and Environmental Engineering, Faculty of Engineering, University of Nottingham, using a Micromeritics ASAP 2020 analyser. All samples (approximately 0.2 g) were outgassed prior to analysis under high vacuum at 120 °C for 15 h in order to ensure that all moisture and volatiles were properly evacuated prior the test. The initial mass (M_0) of each SBA-15 samples was weighed and recorded using an electronic balance (VIBRA HT Series Tuning-fork frequency sensing, 0.0001g accuracy). The samples were then transferred to the instrument station (N_2 bath vessel), following automatic immersion in liquid nitrogen at -196 °C. The volumetric measurement method was used, where a set of relative pressure increments (adsorption/ desorption branches) were systematically programmed to increase until condensation pressure was reached. Measurements of the gas adsorbed were automatically recorded and calculated, allowing equilibration with the sample at each step to the corresponding equilibrium volume in cm^3/g (S.T.P.) as a function of relative equilibrium pressure (P/P_0). Isotherm plots were then obtained directly from the MicroActive software.

In the case of MCM-41 desiccant materials (MCM-41@150, 165 and 180), nitrogen physisorption was performed by PhD student Wantana Sangchoom, under the supervision of Dr Robert Mokaya, at the School of Chemistry, Faculty of Science, University of Nottingham, using a Micromeritics ASAP 2020 analyser. Same procedure was adopted as previously depicted, where a first dried was carried out at 130 °C and then outgassed under high vacuum at 200 °C for 12 h in order to ensure that all moisture and volatiles were properly evacuated prior the test. For the two pre-existing mesoporous solids (MS-3.3 and 8.3) used

on this research, methodology of nitrogen physisorption and textural characterization can be found in Dr Sean Casey's thesis and in previous publication (Hall *et al.*, 2012).

3.4.1.1 Pore volume and pore size distribution

The description of the estimation of pore size distribution (PSD) and total pore volume (V_p) provided can be also found in Thomann *et al*., (2015a; 2015b). Total pore volume is determined when all pores are filled with liquid adsorbate, and that the amount of vapour adsorbed at a relative pressure, P/P_0 is associated with the progressive pore filling by the process of capillary condensation. This condition may be applied, when an identifiable part of the isotherm remains nearly horizontal (*e.g.* plateau showed in a Type IV isotherm) over a range of P/P_0. This implies that capillary saturation has been reached, hence the average pore size distribution can be estimated from it. Pore size distribution derives from the distribution of pore volume (amount of adsorbed gas) with respect to pore size. In some cases, when adsorption/ desorption does not exhibit full reversibility (*e.g.* Type H2 hysteresis loop), the adsorption branch of the isotherm can be used for PSD determinations. For this research (refer to Section 4.2), the adsorption branch of the isotherm has been selected, where $P/P_0 = 0.99$. For the determination of the PSD and V_p, the Barrett–Joyner–Halenda (BJH) method was used by applying a cylindrical pore model assuming the Kelvin equation where:

$$r_K = \frac{-2\gamma V_m}{RT\ln(P/P_0)}$$

Equation 3.1 – The Kelvin radius, r_K equation for mesoporous size calculations when assuming cylindrical pore geometry. (Rouquerol *et al.*, 1994)

γ = the surface tension of nitrogen at its boiling point.

V_m = the molar volume of liquid nitrogen (34.7 cm^3/mol).

R = gas constant (8.314 J/(mol K)).

T = boiling point of nitrogen.

P/P_0 = partial pressure of nitrogen.

r_K = the Kelvin radius of the pore.

Even before capillary condensation begins, some nitrogen is adsorbed in the walls of the adsorbent, leading to a statistical thickness, t of an adsorbed layer. In the same logic, the actual pore radius becomes: $r_p = r_K + t$. In this 'ideal scenario', the BJH model assumes that (1) the pores are cylindrical, (2) the adsorbed amount of gas in equilibrium is retained by a) physical adsorption (pore walls) and b) capillary condensation (in the inner capillary volume), (3) all pores are independent and not interconnected, and (4) hemispherical menisci formation is assumed with large contact angle (*i.e.* > 90°).

3.4.1.2 Specific surface area determination

According to the Brunauer–Emmett–Teller (BET) method, the specific surface area (SSA) can be estimated from the physisorbed gas attached on the pore surface, when assuming the formation of a uniform monolayer capacity, n_m. The SSA was automatically carried out by computing the multipoint BET analysis method. The linear region selected for the BET analysis was within P/P_0 = 0.05 to 0.30 range. The SSA expressed in m^2/g can be calculated from:

$$SSA = n_m^a a_m L$$

Equation 3.2 – Specific surface area. (Rouquerol *et al.*, 1994)

Where, the average area a_m (molecular cross-sectional area calculated from the liquid density of the adsorbate) occupied by a single nitrogen molecule in the completed monolayer, a_m = 0.162 nm^2 at 77 K. n^a_m is the monolayer capacity, where n^a is the amount adsorbed at relative pressure P/P_0, and L is the number of entities per mole, also called 'Avogadro's number' normally accepted as 6.022 x 10^{23} mol^{-1} (Atkins and De Paula, 2010; Rouquerol *et al.*, 1994).

3.4.2 Water vapour isotherms using dynamic vapour sorption

Dynamic vapour sorption (DVS), is a gravimetric method for determination of vapour interactions with surfaces. This is performed by varying the vapour concentration that surrounds a sample within a closed chamber. Through measuring of the mass changes the amount of vapour adsorbed can be obtained. The EMC occurs at a static value of φ (at constant temperature), when mass change ≈ 0, whilst a series of step changes in mass are recorded as a function of time. In this research, a DVS Advantage-2 series (Surface Measurements Systems Ltd., London, UK – refer to Figure 3.10b), was used for the determination of water vapour adsorption/ desorption isotherms for the MCM-41 and SBA-15 desiccant materials. As Figure 3.10a schematically shows, the microbalance (5) measures the changes in weight through the mass flow controllers (2) and the dual reservoir vapour generator module (3). A constant stream of 'dry gas carrier' (nitrogen – (1)) is saturated with different solvents (water for this research – (11)) at the desired water vapour pressure. This is performed by the electronic mass flow controller (2) that mixes both the dry gas and water, in order to provide an accurate and controlled vapour pressure through the Advantage Control Software (15).

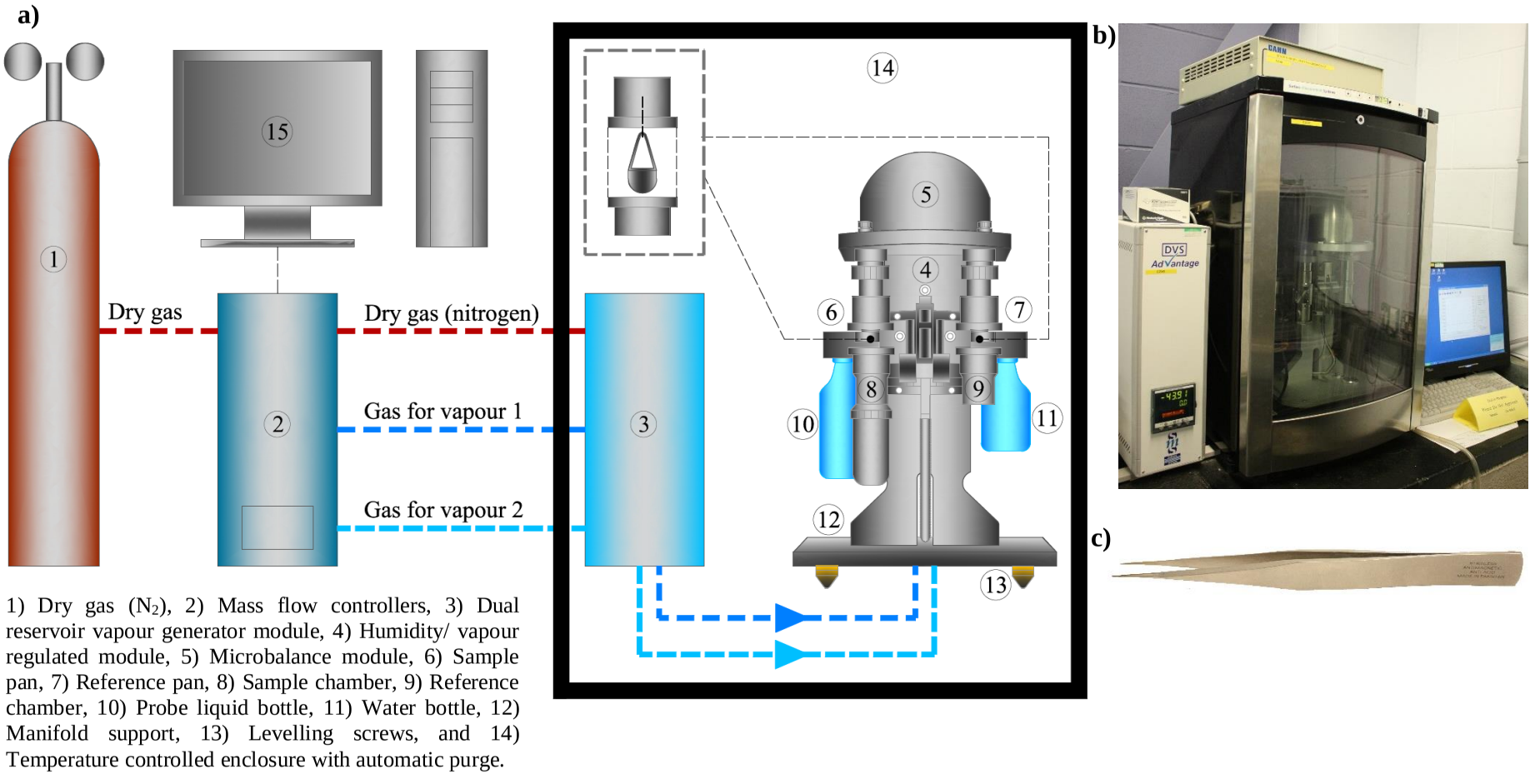


Figure 3.10 – a) Schematic representation of the DVS Advantage Advantage-2 series. Adapted images are under authorization from Surface Measurements Systems Ltd., London, UK. b) The DVS unit inside the Laboratory within the Nottingham Transportation Engineering Centre, Faculty of Civil Engineering, University of Nottingham. c) Special forceps used for hanging samples within the sample chamber.

The DVS, as Figure 3.10 shows, incorporates an ultra-microbalance (1µg sensitivity) with fully automated weighing/ purging which is capable to independently control T_{db} and relative humidity to an accuracy of ± 0.5 K and ± 1.5%, respectively. All the data was automatically recorded and measured in 1 min time-step intervals using the Advantage Control Software. All desiccant materials (MCM-41 and SBA-15) were outgassed as previously depicted in Section 3.3.1.1. In order to ensure stability for baseline measurements accuracy, the chamber (8) (refer to Figure 3.10a) was left to fully equilibrate at 23 °C (± 0.5 °C) and at constant nitrogen flow (10 sccm) for 1 h, prior to the test and taring of the ultra-microbalance. Subsequently, the samples (~ 0.02 g) were rapidly placed in the glass sample pan (6), and then hung inside the chamber using the forceps (Figure 3.10c). A counter weight was set to zero in the glass reference pan (7) and the initial mass (M_0) was set in the Advantage Control Software.

Immediately after that, a pre-heating sequence (heating ramp rate of 2 °C/ min, from 23 °C) at 150 °C for 1 h was activated in the Advantage Control Software prior to the test, to ensure the condition $w = w_0$ was maintained. Then, the pre-set sequence of 21 steps (full cycle adsorption/ desorption) was initiated to increase with a targeted relative vapour pressure from φ = 0.05 to 1 (φ = 0.05 intervals) along with the change in mass step (0.001%/ min) until EMC was reached. All tests were performed at T_{db} 23 °C (± 0.5 °C) and to a constant water vapour flow rate of 100 sccm (0.1 L/ min). Once the test was finished, the adsorption/ desorption isotherms were obtained from the Advantage Control Software, where each φ set point at EMC was automatically recorded and plotted.

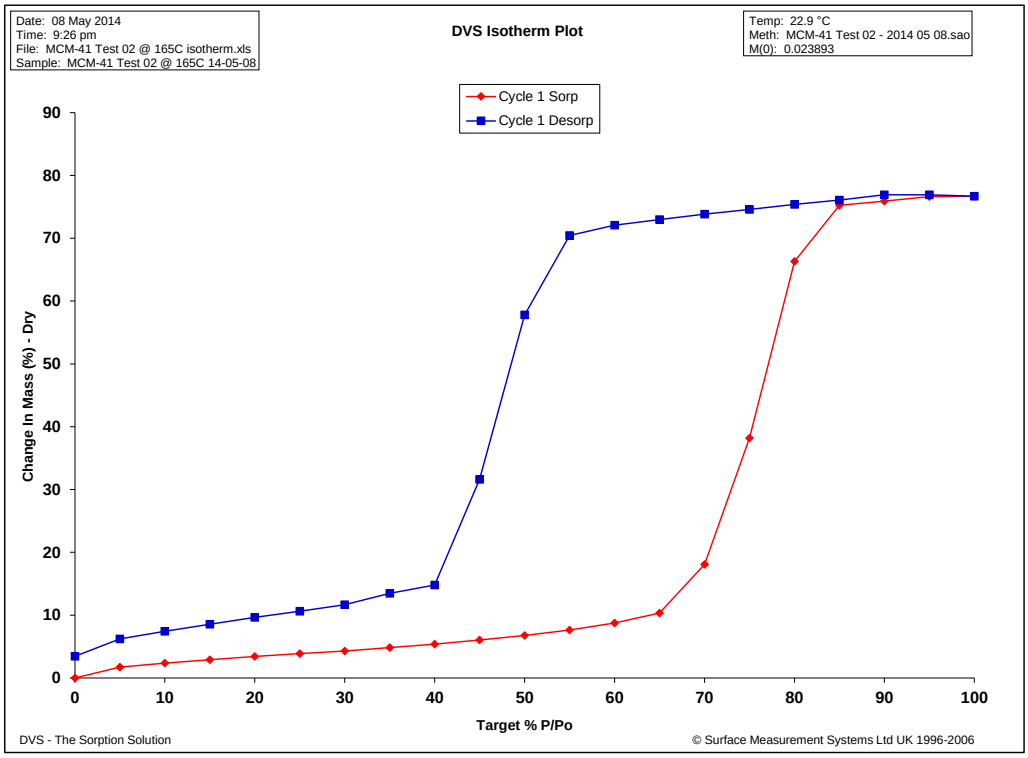


Figure 3.11 – Water vapour isotherm example from the ACS, using the gravimetric DVS from Surface Measurements Systems Ltd, UK. The example corresponds to the MCM-41@165 desiccant.

Figure 3.11 shows an example of the produced water vapour isotherm gathered from the ACS. All protocols were conducted according to the BS EN ISO 12571:2000.

3.5 Physical modelling for water vapour adsorption/ desorption kinetics comparison

This section describes the physical modelling conducted for the determination of the kinetics of water vapour adsorption/ desorption for all desiccants made (SBA-15 and MCM-41). This provided important information regarding the time-response for water vapour adsorption/ desorption under specific operational $\Delta\varphi$ ranges, with the aim to understand:

1. The desiccant's behaviour under specific operational $\Delta\varphi$ ranges.
2. How the isotherm shape and corresponding moisture storage (Δw) influence the time-response in changes of water vapour adsorption, and
3. The pore-blocking effect (theoretical insight) within the hysteresis loops.

For this, a set of four experiments to assess the kinetics of water vapour adsorption/ desorption among all desiccants were performed. The description of the methodology is presented below. The physical simulations were carried out using two different instruments: (1) the climatic chamber and (2) the DVS Advantage-2 series. This work was intended to meet objective 4 (from Stage 2) as outlined in Section 1.3 – also refer to Figure 1.2.

3.5.1 Climatic chamber

A climatic chamber (TAS Series 3 LTCL – 600) was used, as previously described in Section 3.2.1, to fluctuate between the pre-defined $\Delta\varphi$ cycles ($\Delta\varphi$ = 0.2 – 0.3; 0.3 – 0.5, 0.5 – 0.7; and 0.7 – 0.95). This apparatus was used for the desiccant materials MS-3.3, 8.3, and Silica gel in order to compare and validate the results against previous work using the same samples and equipment. As Figure 3.12 shows, each cycle (t = 4 h) comprised 2 h of water vapour adsorption (*e.g.* $\Delta\varphi$ = 0.2 → 0.3), followed by 2 h of water vapour desorption (*e.g.* $\Delta\varphi$ = 0.3 → 0.2), where two complete cycles (t = 8 h in total) were performed. Prior to the test, all samples were outgassed under high-vacuum at 120 °C for 12 h to ensure that all moisture and volatiles were properly evacuated. The climate chamber was left to fully equilibrate at 23 °C (± 0.5 °C) and at the corresponding φ (*e.g.* φ = 0.2) for 1 h prior to the test. Then, the samples (~ 2 g) were transferred and

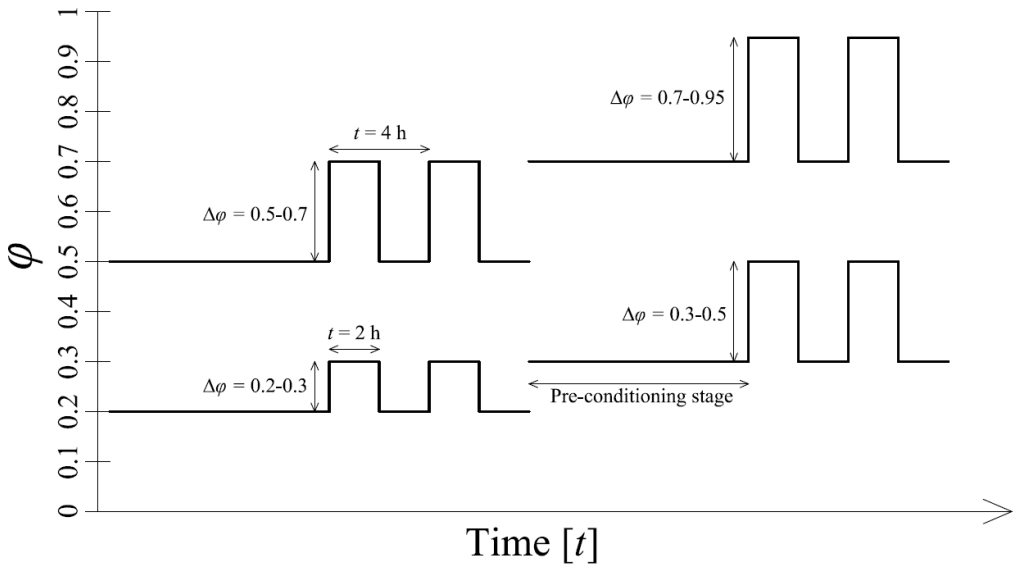


Figure 3.12 – Schematic diagram of adsorption/ desorption between pre-defined $\Delta\varphi$ cycles ($\Delta\varphi$ = 0.2 – 0.3; 0.3 – 0.5, 0.5 – 0.7; and 0.7 – 0.95), where t = 2 h.

placed inside the chamber within the petri dish in a uniform ~ 2 mm layer for a pre-conditioning stage (refer to Figure 3.1a). The pre-conditioning was meant to establish constant mass within the desiccant, and to ensure that EMC was reached before the cycles started at the different initial moisture content, *w*; *i.e*. w_{20}, w_{30}, w_{50} and w_{70}. Following the pre-conditioning sequence, the pre-set targeted adsorption/ desorption cycles were performed, and all data was automatically recorded using the weighing balance (VIBRA HT Series), as previously described (refer to Section 3.2.1 and Figure 3.1). In this occasion, EMC was not intended to be fully achieved, since more important was to understand the kinetics for water vapour adsorption/ desorption. The recording of mass changes data for each cycle was then transferred to Excel for plotting.

3.5.2 Dynamic vapour sorption (DVS)

A second set of experiment were conducted to study the kinetics of water vapour adsorption/ desorption in rapid-response desiccant materials; MCM-41 and

SBA-15. The DVS Advantage-2 series was used due to its ability to rapidly fluctuate between the pre-defined $\Delta\varphi$ cycles previously described (refer to Figure 3.12). In this case, three complete cycles (t = 12 h in total) were performed. All MCM-41 and SBA-15 samples were outgassed prior to the test under high-vacuum at 120 °C for 12 h as with previous experiments. Once again, the DVS was left to fully equilibrate at 23 °C (± 0.5 °C) before taring of the ultra-microbalance. Same procedure was adopted for placing the sample (~ 0.02 g) and pre-heating sequence (refer to Section 3.4.2) to ensure that EMC was reached before the cycles started at the different initial moisture content, w; *i.e*. w_{20}, w_{30}, w_{50} and w_{70}. After that, the sequence for the targeted adsorption/ desorption cycles was activated from the Advantage Control Software. EMC was not intended to be fully achieved, where all data was recorded and automatically plotted by the Advantage Control Software as with previous experiments.

3.5.3 Hygrothermal model validation

A series of hygrothermal simulations were carried out aimed to replicate the experimental testing for the kinetics of water vapour adsorption/ desorption (refer to Section 3.5.2). This was performed under the same specific operational $\Delta\varphi$ ranges, and aimed to address objective 4 (from Stage 2) as outlined in Section 1.3. The numerical data was then validated against the physical modelling results performed in the DVS Advantage-2 series. This was primarily selected because of the electronic mass flow controller, which allows accurate representation of the vapour pressure within the sample chamber. Detailed information of the parameters used for the setup of the hygrothermal model is presented below. The

setup of the numerical modelling was designed to simulate the kinetics of the water vapour uptake, aimed to sequentially fluctuate between the adsorption/ desorption cycles within specific operational $\Delta\varphi$ limits across an arbitrary sixty-cycles (N = 60). The desiccant materials used in this model were the new synthesised (previously described in Section 3.4) and correspond to the MCM-41 and SBA-15. Each desiccant was assessed using the same pre-defined operational $\Delta\varphi$ cycles ($\Delta\varphi$ = 0.2 – 0.3; 0.3 – 0.5, 0.5 – 0.7; and 0.7 – 0.95) as for the DVS experiments seen in Section 3.5.2. The initial w was set at EMC according to the lower φ value for each operational $\Delta\varphi$ pair; *i.e.*, EMC at w_{20}, w_{30}, w_{50} and w_{70}. Each adsorption/ desorption test was carried out under isothermal conditions, where T_{db} = 23 °C. In order to proportionally set the infiltration rate of 100 sccm (0.006 m^3 h^{-1}) and the material quantity (0.02 g), scaling of the volume from the DVS sample chamber (V_{ch} = 0.0002945 m^3) – refer to Figure 3.10 – respect to the physical model (V = 1 m^3) was estimated. This resulted in a constant ACH = 20.37 and an exposed surface area of 0.01 m^2 of the non-visualized component, which enabled validation of the numerical model against the DVS experiments. The description of the closed environment (refer to Figure 3.2) as well as the parameters of the numerical model can be found along Section 3.3.

3.6 3D Numerical simulations for optimized water vapour isotherms

A series of hygrothermal numerical simulations were performed using the hygrothermal technique developed (refer to Section 3.3), to inform the design of 'ideal' water vapour isotherms. This was followed by an energy consumption case scenario, aimed to assess their suitability for specific humidity buffering

applications. This was done with the aim to address objective 5 (from Stage 3) as outlined in Section 1.3 – also refer to Figure 1.2.

3.6.1 Sensitivity analysis for continuous moisture loads

Sensitivity analysis was conducted between selected desiccants gathered from literature and the created ones (SBA-15 and MCM-41). Figure 3.13 shows the water vapour sorption isotherms of five desiccant candidates which were selected, defined by the IUPAC (Rouquerol *et al.*, 1998), as a representative group of mesoporous materials. This was done in order to assess their kinetics of continuous moisture loads and their performance for water vapour exchange. Particular interest was given to analysing their behaviour with respect to the portion of the isotherm corresponding to the steep Δw gradient between the upper ($\varphi_{i,U}$) and lower ($\varphi_{i,L}$) limits; *e.g.* represented as $\Delta w_{40\text{-}50}$ in Table 3.4.

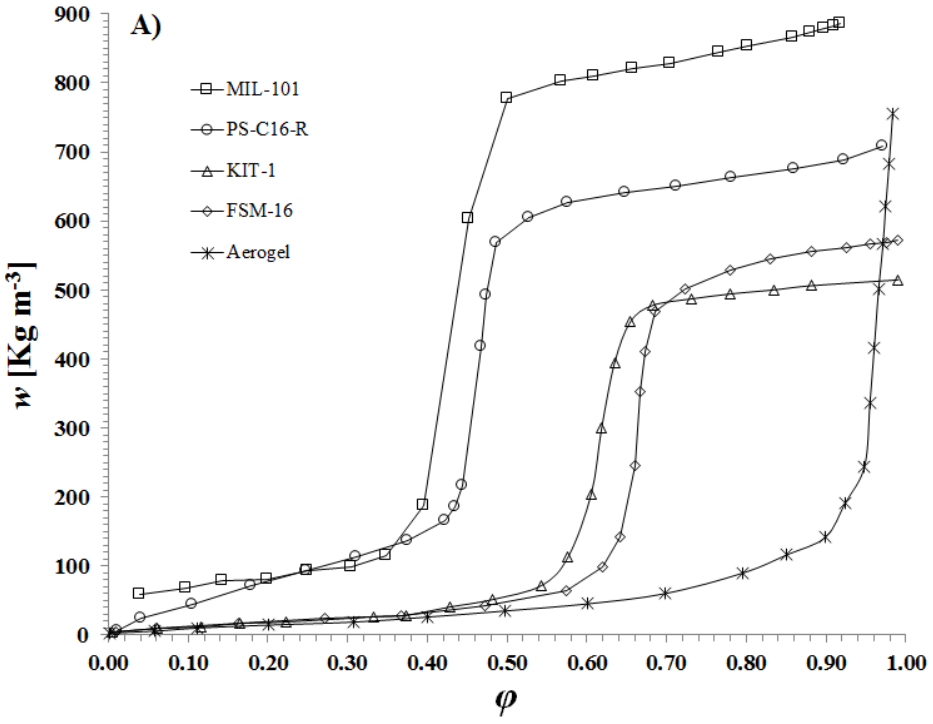


Figure 3.13 – Water vapour sorption isotherms for all desiccant candidates. References are provided for the following desiccants candidates: MIL-101(Henninger *et al.*, 2012), PS-C16-R (Naono *et al.*, 2000), KIT-1 and FSM-16 (Wang *et al.*, 2013), Aerogel (Knez and Novak, 2001).

Material	Moisture storage at Δw					
	$\Delta w_{40\text{-}50}$	$\Delta w_{50\text{-}60}$	$\Delta w_{60\text{-}70}$	$\Delta w_{70\text{-}80}$	$\Delta w_{80\text{-}90}$	W_f
	(kg/m^3)					
MIL-101	589.4	32.9	18.6	24.3	25.8	886.9
PS-C16-R	403.8	56.8	25.2	11.4	26.5	709.1
KIT-1	42.9	153.2	272.9	7.2	12.0	514.8
FSM-16	14.4	55.9	370.2	44.0	16.7	572.9
Aerogel	8.8	10.3	14.8	29.7	52.1	754.8

Table 3.4 – Moisture storage function for all desiccant materials. References are provided for the following materials: MIL-101 (Henninger *et al.*, 2012), PS-C16-R (Naono *et al.*, 2000), KIT-1 and FSM-16 (Wang *et al.*, 2013), and Aerogel (Knez and Novak, 2001).

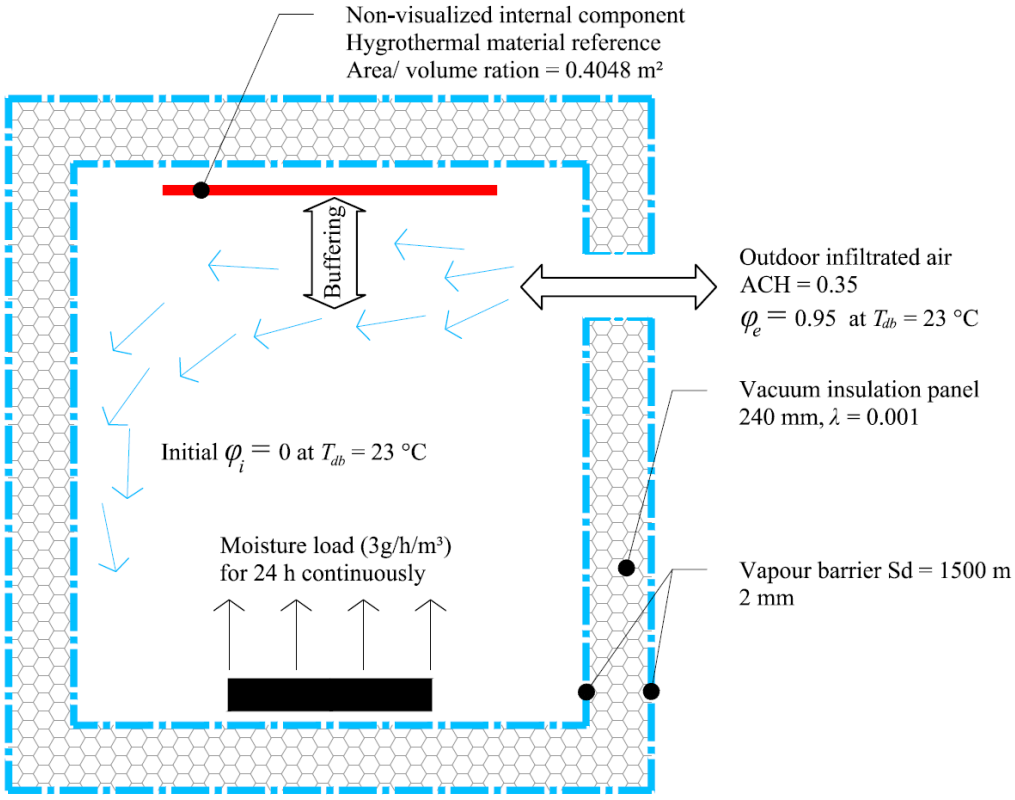


Figure 3.14 – Close environment representation for the numerical simulations. Adapted from (Thomann *et al.*, 2015b).

Additionally, in order to assess the continuous moisture uptake throughout the water vapour isotherm, all desiccants were deemed to have a totally outgassed condition; *i.e*. initial moisture content, w = 0. Figure 3.14 shows the closed environment used where the initial indoor air humidity was set as φ_i = 0, under isothermal conditions at T_{db} = 23 °C. The numerical model was programmed to perform the adsorption of water vapour between the operating limits φ_{min} = 0 and φ_{max} = 0.95. For the latter, a constant 24 h moisture load (3 g/h) and an outdoor air humidity, φ_e = 0.95 were set at an air infiltrated rate of 0.35 ACH. This was intentionally created, in order to represent a 'continuous overloading moisture scenario' with respect to the isolated box of volume, V = 1 m^3. As shown in Figure 3.14, the closed environment fabric (V = 1 m^3) comprised 2 mm thick water vapour barrier (S_d = 1500 m) and 240 mm thick vacuum insulation panel (λ = 0.001 W/ m K). The non-visualized internal component comprised 2 mm thickness of the desiccant with an exposed surface area of 0.4048 m^2 equivalent to ~ 500 g. As with previous numerical simulations, all hygrothermal functional properties used were those found in Table 3.1, except for moisture storage function which can be seen in Table 3.4. In order to show consistency with previous simulations, the parameters were set to have: (i) increased accuracy and adapted convergence (*i.e*. when termination criteria for each numerical iteration is finished – refer to Section 2.5.2.6), (ii) net volume = 1 m^3, (iii) time step 1 min, (iv) optional climate (φ = 0.95 / 23 °C), (v) inner climate calculated, (vi) initial boundary conditions (φ = 0 / 23 °C), (vii) 'fine' mesh grid spacing, and (viii) calculation accuracy of 0.5 % / 0.5 °C for φ and T_{db}, respectively. Further analysis was conducted aimed to determine the fraction of cumulative moisture uptake per hour. This was done according to the water vapour exchange rate of

the desiccants under continuum-level of moisture loads (refer to Section 6.2.2 for results). This would imply that the desiccant is fully capable to cope with the cumulative of moisture loads (uninterrupted increments of 3 g/h) when the condition of 100 % is satisfied. In the same logic, by assuming the initial moisture content, $w = 0$, the whole isotherm can be then analysed with respect to the decay in their performance; *i.e.* independently of the steep Δw gradient between the upper ($\varphi_{i,U}$) and lower ($\varphi_{i,L}$) limits.

3.6.2 Humidity buffering

The next numerical simulations were conducted in a series of tailored closed environments (*i.e.* specific operating φ limits) with the aim to determine the desiccant's capacity for humidity buffering. This was done by assessing the fluctuation of $\varphi(t)$ within the operational limits (φ_{min} and φ_{max}) when performing repeated loop cycling, at N number of cycles, in order to assess their suitability for specific relative humidity applications. This was conducted against five pairs of operating limits ($\varphi_{min} - \varphi_{max}$) as Table 3.5 shows; *e.g.*, 0.4 – 0.5.

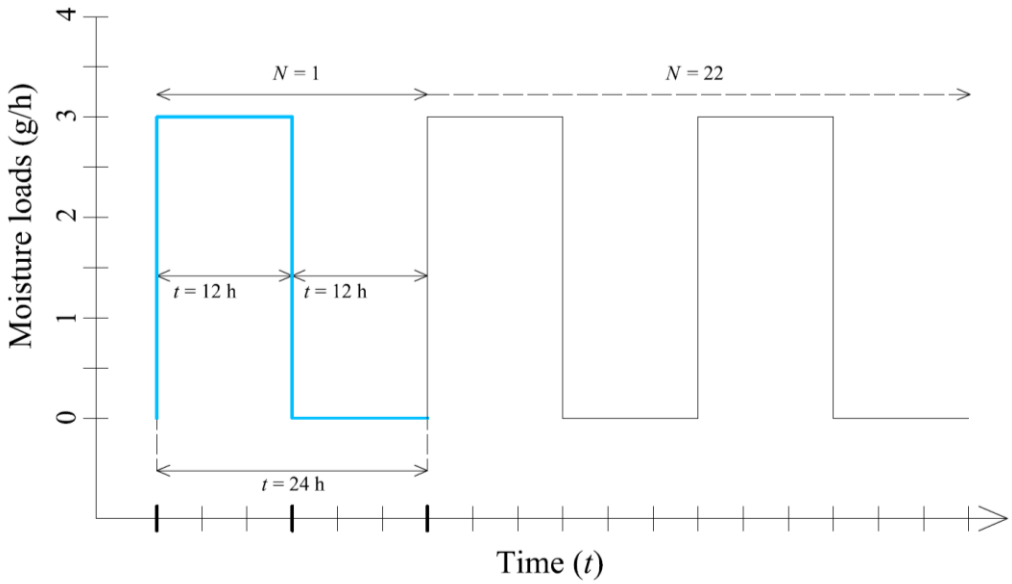


Figure 3.15– Moisture loads schedule as a function of time (t), which corresponds to the 24 h cycle for the parametric assessment (refer to Table 3.5) of all desiccant materials as depicted in Table 3.4.

Operational parameters						
Area/volume ratio	Mass	ACH	φ_{min}	φ_{max}	φ_e	EMC
(m^2)	(kg)	(-)	(-)	(-)	(-)	(-)
0.4048	0.5	0.35	0.4	0.5	0.4	w_{40}
			0.5	0.6	0.5	w_{50}
			0.6	0.7	0.6	w_{60}
			0.7	0.8	0.7	w_{70}
			0.8	0.9	0.8	w_{80}

Table 3.5 – Parameters for the numerical model setup when performing the parametric assessment for humidity buffering under five pairs of operational limits (φ_{min}–φ_{max}) 0.4 – 0.5; 0.5 – 0.6; 0.6 – 0.7; 0.7 – 0.8; and 0.8 – 0.9.

Figure 3.15 shows the total number of loading cycles, N = 22 where successive cycles of 24 h were performed. This comprised 12 h of moisture loads (3 g/h) followed by 12 h of no moisture loads. All desiccants were set at EMC according to each pair of operational limits, where the initial moisture content, w corresponded to the φ_{min} limit; *i.e.*, w_{40} for φ_{min} = 0.4 and φ_{max} = 0.5. As Table 3.5 shows, the air infiltration rate was set constant at 0.35 ACH, where φ_e was determined by the φ_{min} limit for each pair of operational limits; *i.e.*, φ_e = 0.4 for φ_{min} = 0.4 and φ_{max} = 0.5. Again, all simulations were performed at constant dry bulb temperature, T_{db} = 23 °C. The exposed surface area (refer to Table 3.5) for the non-visualized component was set similarly with previous simulations as previously described in Section 3.6.1. The fabric components of the closed environment, as well as the parameters for the numerical model were set as described in previous Section 3.6.1.

3.6.3 Dehumidification loads and energy consumption

A new series of hygrothermal simulations were conducted for all desiccants with the aim to quantify the energy used for dehumidification loads (dehumidification

performance) and cooling demand. This eventually enabled the determination of the relative effect on energy efficiency of the desiccant, by the quantification of dehumidification loads (kg/h) removed when assisting a mixed mode air conditioning system. This was conducted against the same operational limits ($\varphi_{min} - \varphi_{max}$), as previously depicted in Section 3.6.2 and in Table 3.5; *i.e.*, 0.4 – 0.5; 0.5 – 0.6; 0.6 – 0.7; 0.7 – 0.8; 0.8 – 0.9. For this, it was defined in the numerical model an HVAC device, comprising a cooling system where the upper indoor dry bulb temperature set point, ($T_{dbi,U}$) was set as $T_{dbi} \geq 25$ °C, with an oversized total cooling capacity of 50 kW. Additionally, the HVAC system included a dehumidification unit, which was capable to simulate instantaneous control response of 50 kg/h of dehumidification capacity when the upper indoor air humidity set point (φ_{max}) was exceed. This set point was defined for each pair of operating limits as previously mentioned; *i.e.*, $\varphi_i \geq 0.5, 0.6, 0.7, 0.8, 0.9$. If any of the operational limits were exceeded, and once φ_{max} and $T_{dbi,U}$ set points had been reached, the ratio of dehumidification and cooling demand could therefore be estimated by the numerical model, and hence the relative effect on energy efficiency of the desiccant calculated. Commonly, this always occurred in cases where positive moisture loads were presented; *i.e.*, where infiltration of air at lower moisture content did not occur. The initial moisture content, w was set respect to the φ_{min} limit, *i.e.*, EMC at w_{40}, w_{50}, w_{60}, w_{70}, and w_{80}. The air infiltration rate was set constant at 0.35 ACH, where the derived moisture content of the exterior air (at the psychrometric conditions: $\varphi_e = 0.95$ at $T_{db} = 23$ °C) was counted as a continuum moisture load within the closed environment. The exposed surface area for the non-visualized component was set similarly as previously depicted in Section 3.6.1. The fabric components of the closed

environment, as well as the parameters for the numerical model were set as described in previous Section 3.6.1. However, for each pair of simulations the initial boundary conditions were always set according to the φ_{min} operating limit, at isothermal condition; *i.e.* T_{db} = 23 °C.

3.7 Summary

1. In order to address objective 1 (Stage 1) outlined in Section 1.3, the procedure to determine the water vapour isotherm (adsorption/ desorption) for the pre-existing MS materials (MS-3.3 and 8.3) was provided in Section 3.2. Additionally, the parameters used in the climatic chamber were also described. The resultant value of moisture content, *w* would then be used by WUFI+ as an input for the hygrothermal simulations in the following preliminary sensitivity analysis.
2. In order to address with objective 2 (Stage 1) outlined in Section 1.3, preliminary numerical modelling simulations and the design process of water vapour isotherms were described in Section 3.3. This was followed by a series of sensitivity analyses in order to: i) calibrate the hygrothermal modelling technique for water vapour isotherm design operation, ii) assess the behaviour of hypothetically designed 'ideal' isotherms for specific operational $\Delta\varphi$ ranges, and iii) provide analysis for the hypothetical isotherms.
3. In order to meet objective 3 (Stage 2) outlined in Section 1.3, synthesis and characterization of new MS desiccants (SBA-15 and MCM-41) was presented in Section 3.2. This consisted in nitrogen physisorption analysis for the desiccant materials, where pore volume and pore size

distribution were obtained from the BJH method, and SSA from the BET method. Additionally, the procedure in determining the water vapour isotherm (adsorption/ desorption) for the new MS materials (SBA-15 and MCM-41) was presented, as well as the parameters used in the dynamic vapour sorption.

4. In order to meet objective 4 (Stage 2) outlined in Section 1.3, the physical modelling was introduced in Section 3.5, where a set of experimental simulation were presented with the aim to determine the kinetics of water vapour adsorption/ desorption under specific operational $\Delta\varphi$ ranges. These were conducted by using a climatic chamber and a dynamic vapour system. A new series of hygrothermal simulations were described, with the aim to replicate the physical testing and to enable validation of the hygrothermal modelling.
5. In order to meet objective 5 (Stage 3) outlined in Section 1.3, further numerical simulations using the hygrothermal modelling technique were presented in Section 3.6. This was done with the aim to inform the design of 'ideal' water vapour isotherms and to assess their capacity for humidity buffering in a series of closed environments. Additional simulations were also described in order to assess the dehumidification performance of the desiccants, based on an energy consumption case study scenario. This, by quantifying the operational energy used when assisting a mixed mode HVAC system, would enable estimation of the relative effect on operational energy efficiency.

CHAPTER 4 Hygrothermal design approach for ideal water vapour isotherms

4.1 Overview

This chapter presents the results that correspond to Stage 1 from the methodological scheme (refer to Figure 1.2), in order to address objectives 1 and 2 as outlined (Section 1.3). The work contained in this chapter is based on work by the author in the published article Thomann *et al*. (2015).The latter was based on the development of a hygrothermal modelling technique for the design of 'ideal' water vapour sorption isotherms, as described in Section 3.3. This includes:

1. Characterization (water vapour isotherms) of the pre-existing MS materials MS-3.3 and MS-8.3, to provide material properties data for the hygrothermal modelling technique (Section 4.2).
2. Preliminary sensitivity analysis for the pre-existing MS materials, to enable calibration and operation of the hygrothermal modelling technique (Section 4.3.1).
3. Numerical simulations (Section 4.3.2 and 4.3.3) and parametric studies, to provide sensitivity analysis for the hypothetically-designed isotherms (Section 4.4).
4. Future work and the applicability of the hygrothermal modelling technique for enhanced relative humidity buffering under non-isothermal conditions (Section 4.6

4.2 Water vapour isotherm characterization for pre-existing MS materials

Figure 4.1 shows the experimental water vapour adsorption isotherms for MS-3.3 and 8.3, which were conducted according to the procedure described in Section 3.2. According to the IUPAC classification, MS-3.3 and 8.3 materials present a distinctive Type III isotherm. Similarly, both MS materials present its higher water vapour uptake above φ = 0.7, where MS-8.3 shows a significant difference within the φ = 0.7 – 0.95 range compared with MS-3.3 (refer to Table 4.1). This is perhaps due to entering into a multilayer formation (*i.e.* onset of capillary condensation). However, within the φ = 0.5 – 0.7 range, MS-3.3 shows a small but significant difference (25.6 kg/m^3) with a higher water vapour uptake compared to MS-8.3.

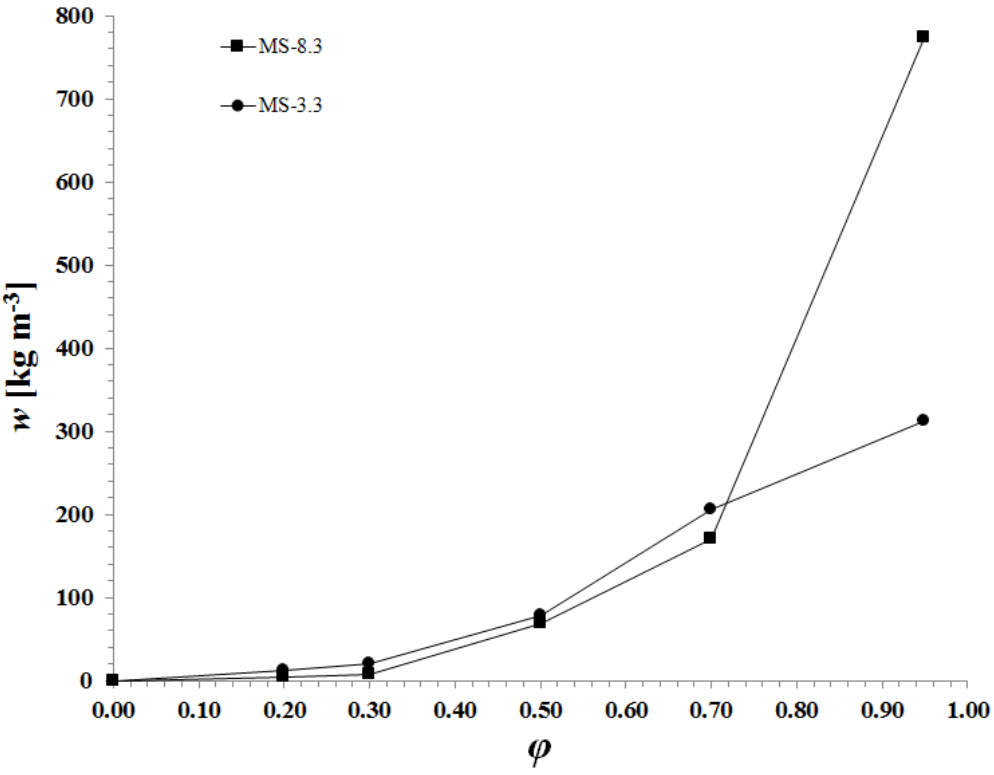


Figure 4.1 – Water vapour adsorption isotherms for MS-3.3 and 8.3.

Sample	Moisture content				
	φ = 0 – 0.3	φ = 0.3 – 0.5	φ = 0.5 – 0.7	φ = 0.7–0.95	w
	(kg/m^3)				
MS-3.3	21	58.2	126.2	106.8	312.2
MS-8.3	6.8	62.3	100.6	603.8	773.6

Table 4.1 – Water vapour adsorption with respect to the relative humidity ranges (φ = 0 – 0.3; 0.3 – 0.7; and 0.7 – ~1), and corresponding moisture content, *w*.

On the other hand, Figure 4.1 only shows equilibrium moisture content values up to φ = 0.95 for the two desiccants, where it seems there is a tendency for higher water vapour uptake (specifically for MS-8.3 material) beyond the data presented in the curves. In the same logic, this may result in underestimation of their total moisture content towards φ = ~ 1. The latter indicating that water vapour adsorption, within the mesopore/ macropore regions, can still be performed at very high relative humidity values. Similarly, the desiccant that achieved the highest moisture content, *w* was the MS-8.3 material having *w* = 773.6 kg/m^3. In terms of the calibration and operation of the hygrothermal modelling technique, these *w* values will be used as the 'reference material properties data' for the preliminary sensitivity analysis in Section 4.3.

4.3 Numerical simulations for the development of hygrothermal modelling technique

4.3.1 Preliminary sensitivity analysis for pre-existing MS materials

Figure 4.2 shows the relative humidity buffering results from the pre-existing MS materials (MS-3.3 and MS-8.3) where a number of cycles, *N* = 60 and 11 (Figure 4.3) were set, respectively (refer to Section 3.3.1).

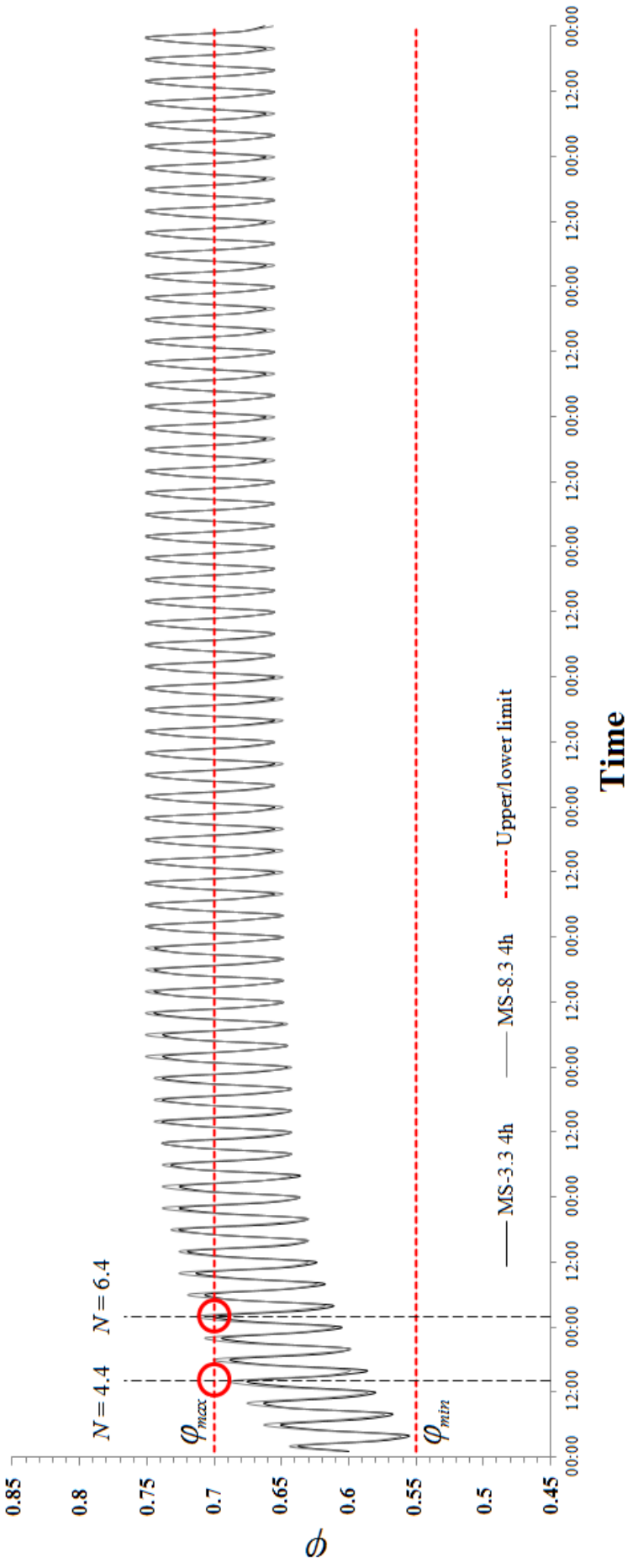


Figure 4.2 – Relative humidity buffering for the 4h cycle and number of cycles, $N = 60$.

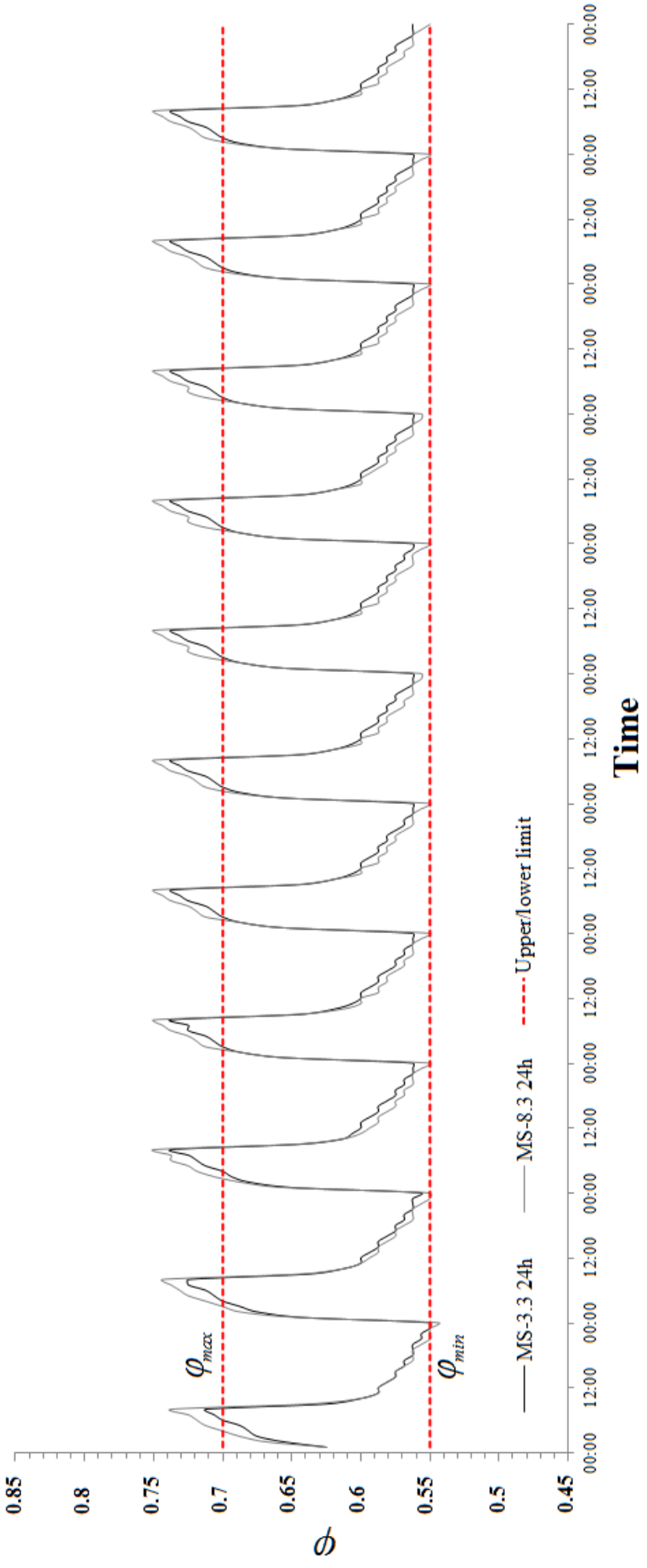


Figure 4.3 – Relative humidity buffering for the 24h cycle and number of cycles, $N = 11$.

It is evident from Figure 4.2 and Figure 4.3, that uninterrupted moisture loads affected the material's capacity for humidity buffering and resulted in progressive decay when performing repeated long-term loop cycling. This decay indicated a distinctive behaviour in terms of a material failure point, which occurred at N number of cycles, *i.e*. MS-8.3, $N = 4.4$; and MS-3.3, $N = 6.4$. This occurred when the fluctuation of $\varphi(t)$ exceeded the upper limit ($\varphi_{max} = 0.7$) by $\varphi = 0.05$, and in the case of the 'overloading moisture scenario' (Figure 4.3), before a complete cycle was finished. It seems that the small difference of water vapour uptake within the $\varphi = 0.5 – 0.7$ range (25.6 kg/m^3) clearly affected the capacity for humidity buffering for the operational limits ($\varphi_{min} = 0.55$ and $\varphi_{max} = 0.7$). In terms of the design process of an 'ideal' water vapour isotherm, the results may indicate that the capacity for humidity buffering can be related to the pore volume assigned in a specific portion of the isotherm.

4.3.2 Sensitivity analysis for new isotherm candidates

Figure 4.4 presents the relative humidity buffering results for all the new hypothetically-created isotherm candidates (A_1–A_6). The fluctuation of $\varphi(t)$ was assessed within the operating limits $\varphi_{min} = 0.55$ and $\varphi_{max} = 0.7$ (refer to Section 3.3.3 and 3.3.4), and the number of cycles, $N = 60$ (Figure 4.4) and 11 (Figure 4.5) were set, respectively. It can clearly be seen in Figure 4.4 that there was an early decay for humidity buffering, especially in materials A_1, A_5 and A_6; *i.e.* A_1, $N = 6.5$; A_5, $N = 4.4$; and for A_6, $N = 4.4$.

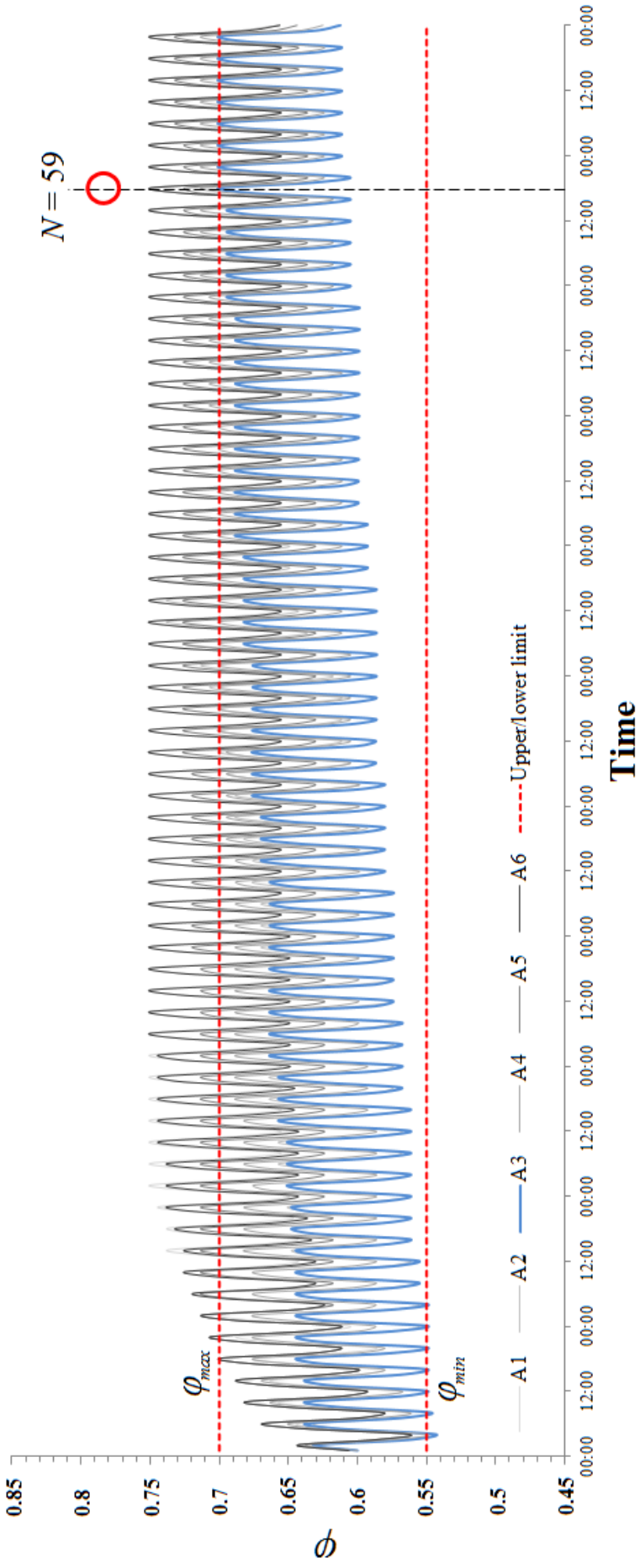


Figure 4.4 – Relative humidity buffering results for all the new hypothetically-created isotherms candidates (A_1 – A_6) for the 4h cycle and number of cycles, $N = 60$.

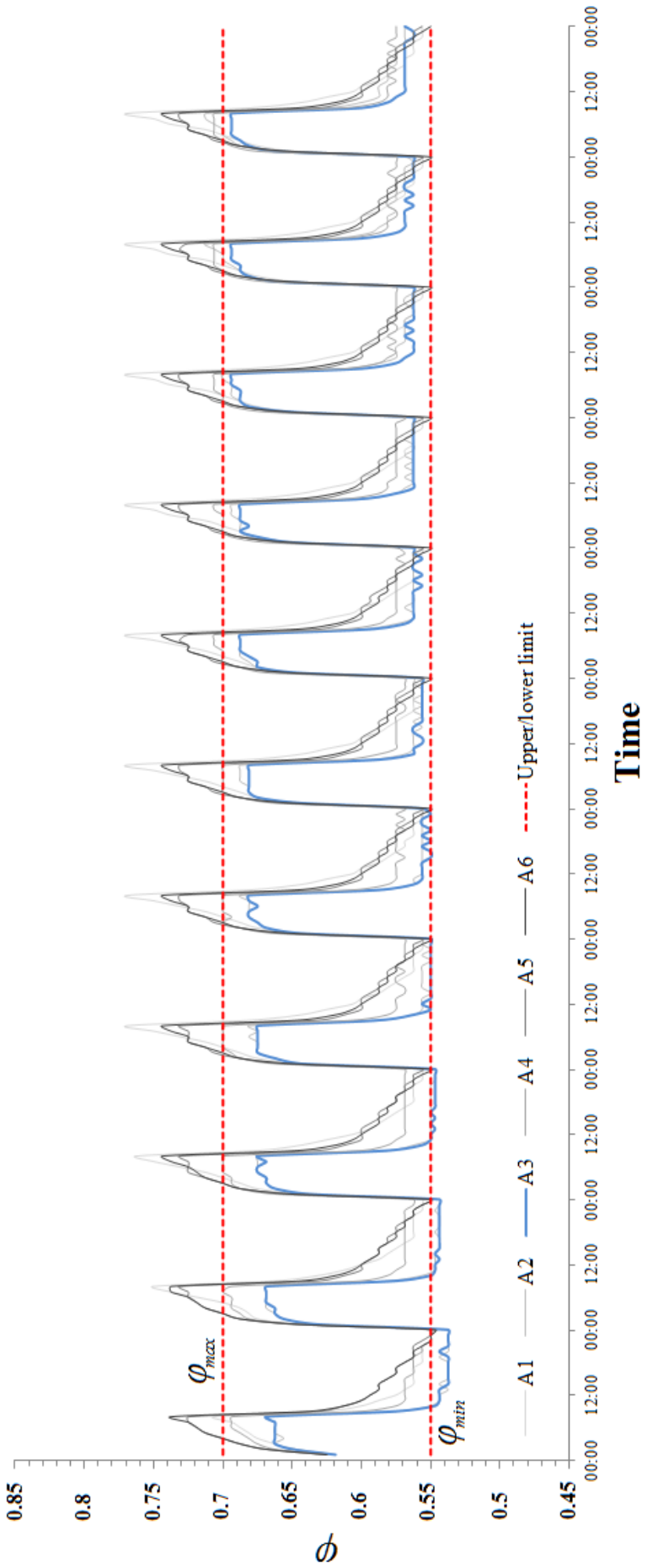


Figure 4.5 – Relative humidity buffering results for all the new hypothetically-created isotherms candidates (A_1 – A_6) for the 4h cycle and number of cycles, $N = 11$.

Conversely, it was evident that for those which present the highest Δw within the linear portion of the isotherm between $\varphi_{i,U} - \varphi_{i,L}$ (refer to Figure 3.7 in Section 3.3.3) are still performing in terms of relative humidity buffering (A_2, A_3 and A_4). Consistently, this was showed by having a higher number of cycles performed when the fluctuation of $\varphi(t)$ exceeded the upper limit ($\varphi_{max} = 0.7$); *i.e.* A_2, $N = 32.4$; A_3, $N = 59$; and for A_4, $N = 33.4$. At this stage, the 'optimum isotherm' (A_3) was identified as the one having the best performance for relative humidity buffering within the operating limits $\varphi_{min} = 0.55$ and $\varphi_{max} = 0.7$. In the same logic, it appears that for those materials that have a lower Δw within the linear portion of the isotherm between $\varphi_{i,U} - \varphi_{i,L}$ (A_1, A_5 and A_6), an early decay for relative humidity buffering was seen (see Figure 4.4 and Figure 4.5).

Further analysis showed that the early decay seen in Figure 4.4 and Figure 4.5 could be also associated with the initial moisture content, w_{55} set in the numerical model (refer to Section 3.3.4). In some cases, by reducing the instantaneous capacity to start the relative humidity buffering above φ_{min}. Evidence of this is illustrated in Figure 4.6, where the potential for humidity buffering is represented as the portion of the isotherms in bold red lines between $\varphi_{i,U} - \varphi_{i,L}$. This could be partially an indication of why these materials showed an early decay for relative humidity buffering, since they are apparently not using their maximum Δw gradient. Instead, only a portion of the isotherm with a less steep gradient between $\varphi_{i,L} = 0.55$ and $\varphi_{i,U} = 0.65$ (see materials A_1, A_5 and A_6) is used, and therefore a lower moisture storage capacity associated. Analysis of pore filling stages within the specific portion of the isotherms would be presented in more details in Section 6.2.1 as w is reaching equilibrium moisture content.

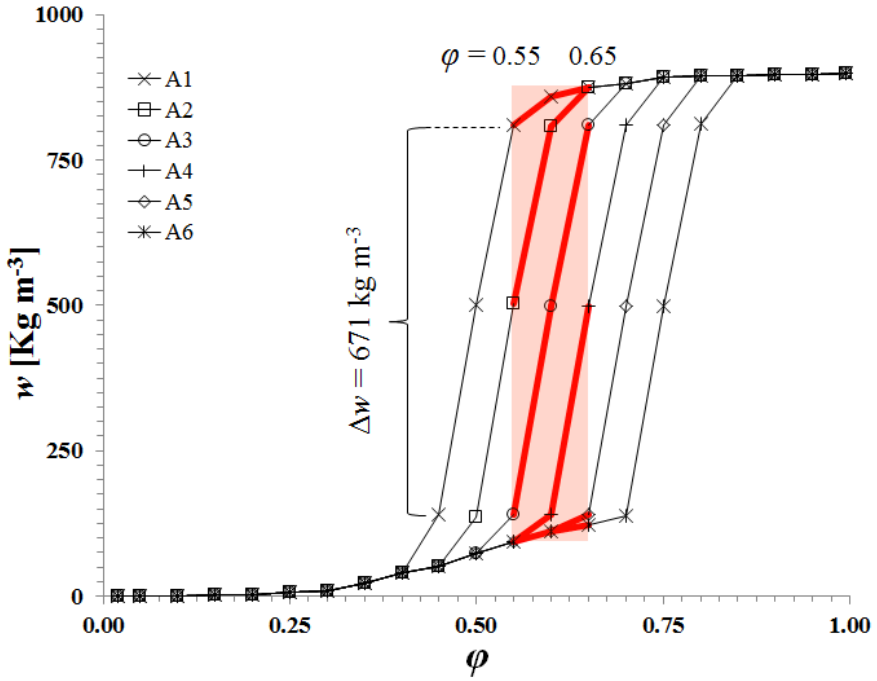


Figure 4.6 – Water vapour isotherm candidates A_1-A_6 showing the portion of the isotherm for potential relative humidity buffering between $\varphi_{i,U} - \varphi_{i,L}$. Adapted from (Thomann *et al.*, 2015b).

4.3.3 Sensitivity analysis for isotherms with pore volume reduced

Figure 4.7 and Figure 4.8 show the relative humidity buffering results for the proportionally-reduced isotherm candidates (B_1–B_4). These were assessed within the same operating limits and number of cycles; *i.e.* N = 60 (Figure 4.7) and N = 11 (Figure 4.8) as described previously (refer to Section 3.3.4). Figure 4.7 shows that there was a small indication of the reduction in pore volume (from 100% to 60% – refer to Section 3.3.3) when analysing the relative humidity amplitude between the adsorption/ desorption cycle. It appears to be that after each 'cycle regeneration' (*i.e.* desorption cycle at constant ACH and without moisture loads) there was a small but significant kind of hysteresis generated. This was possibly triggered by the cumulative moisture uptake, after which a progressive decay for humidity buffering resulted in the φ_{max} limit being reached.

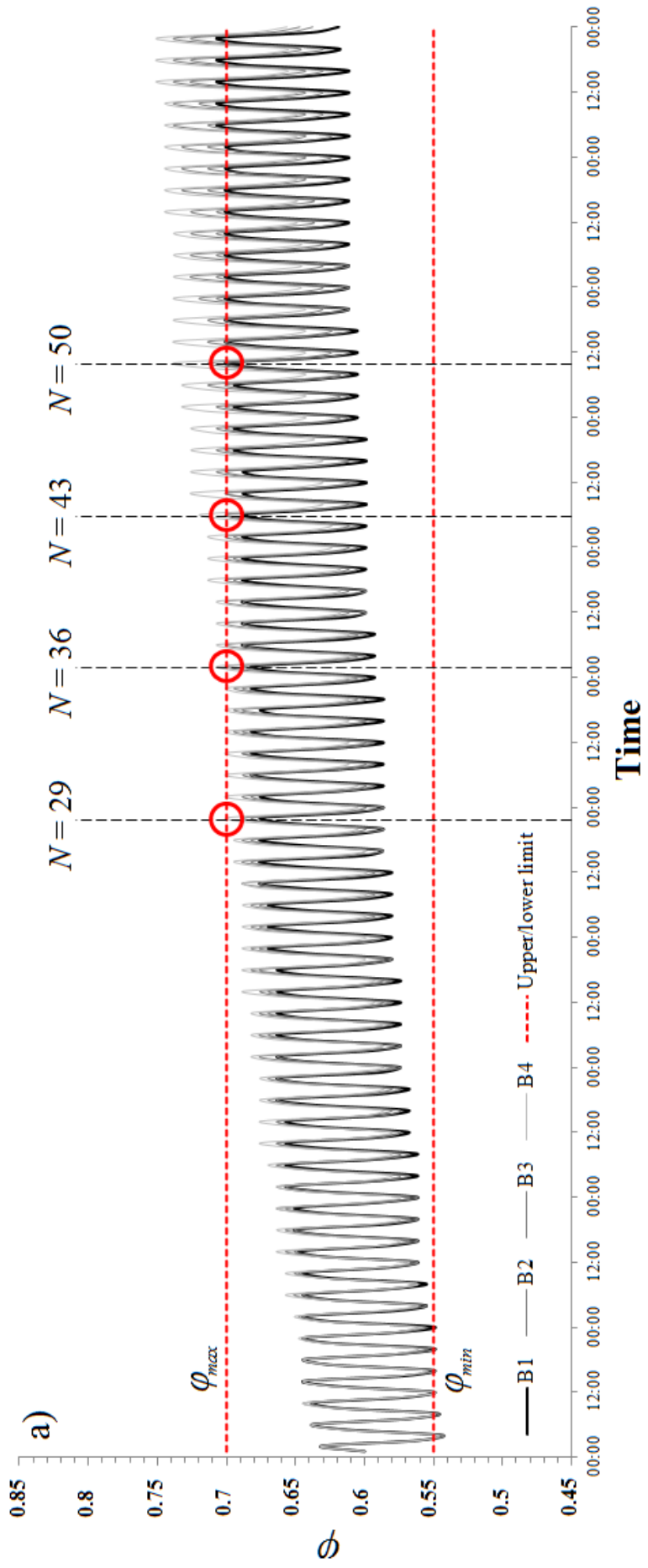


Figure 4.7 – Relative humidity buffering results from the proportionally reduced water vapour isotherms derived from candidate A_3; where the number of cycles, $N = 60$

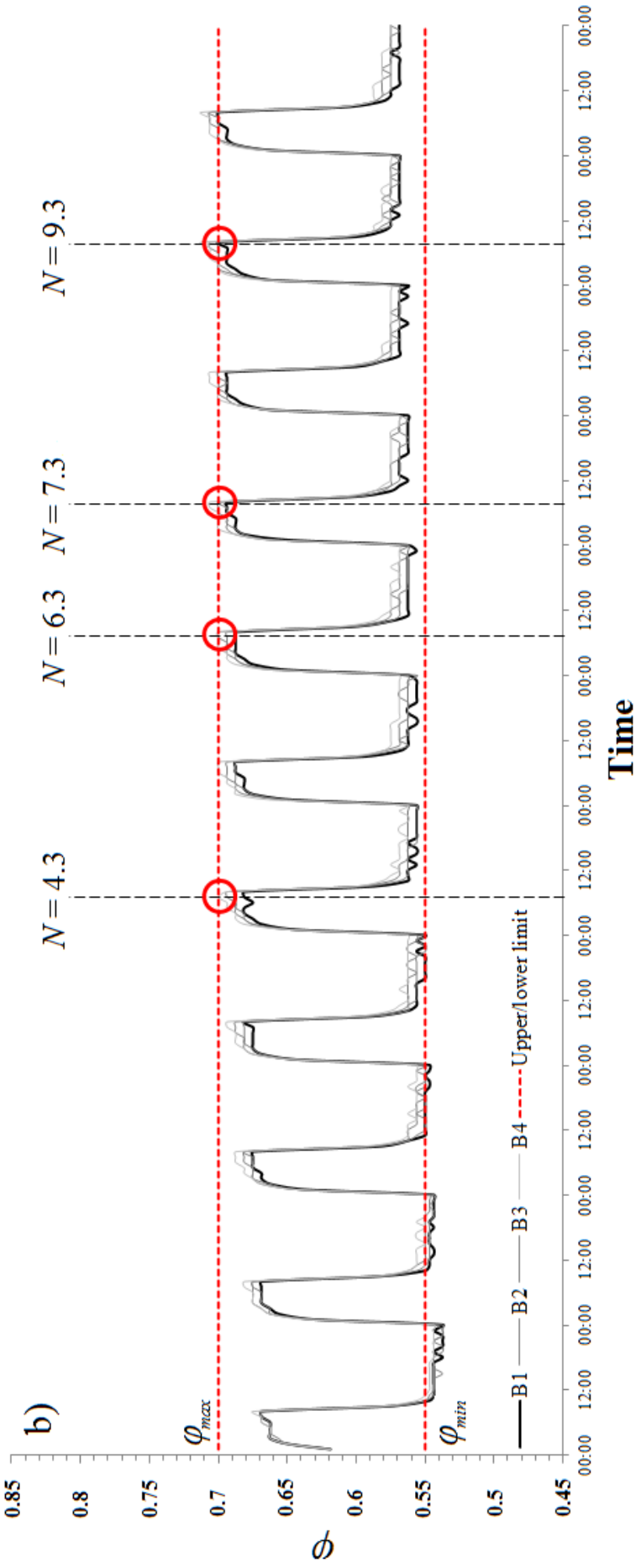


Figure 4.8 – Relative humidity buffering results from the proportionally reduced water vapour isotherms derived from candidate A_3; where the number of cycles, $N = 11$.

This can be also seen in Figure 4.8, where an initial rapid response for moisture uptake is performed for all material candidates during the first ~ 2.5 hours, but suddenly these achieved the φ_{max} limit. Further analysis may suggest that this progressive decay also seems to be strongly related to the kinetics of adsorption at a corresponding portion of the isotherm. Further discussion will be presented on Section 6.2.1.

On the other hand, lowering the pore volume of the 'optimum isotherm' (A_3) did not significantly reduce the ability of the candidate materials for relative humidity buffering. This can be seen when comparing the previous isotherms simulated (A_1–A_6, refer to Section 4.3.2) with candidates materials B_1–B_4. It was evident that by reducing up to 30% of the pore volume (as in the case of B_3), the decay for relative humidity buffering closely equalled the number of cycles, N for both scenarios (N = 36 seen in Figure 4.7, and N = 6.3 in Figure 4.8) compared with the case of A_2 (N = 32.5 and 8.3) and A_4 (N = 33.4 and 6.2, refer to Figure 4.4 and Figure 4.5, respectively); the latter ones having greater total pore volume (also refer to Figure 3.7).

From Figure 4.9a it appears that the largest proportion of total water uptake (candidate isotherm A_3) corresponded to the longest time for the material to exceed the φ_{max} limit. Furthermore, Figure 4.9b shows a positive linear correlation between the moisture storage capacity, $\Delta w_{55\text{-}65}$ within the linear portion of the isotherm (between $\varphi_{i,U} - \varphi_{i,L}$), and the time taken to exceed the φ_{max} limit. This confirms that the performance of a material for a relative humidity buffering application strongly relates to the pore volume within the critical portion of the isotherm (Δw gradient), rather than having a larger modal pore diameter.

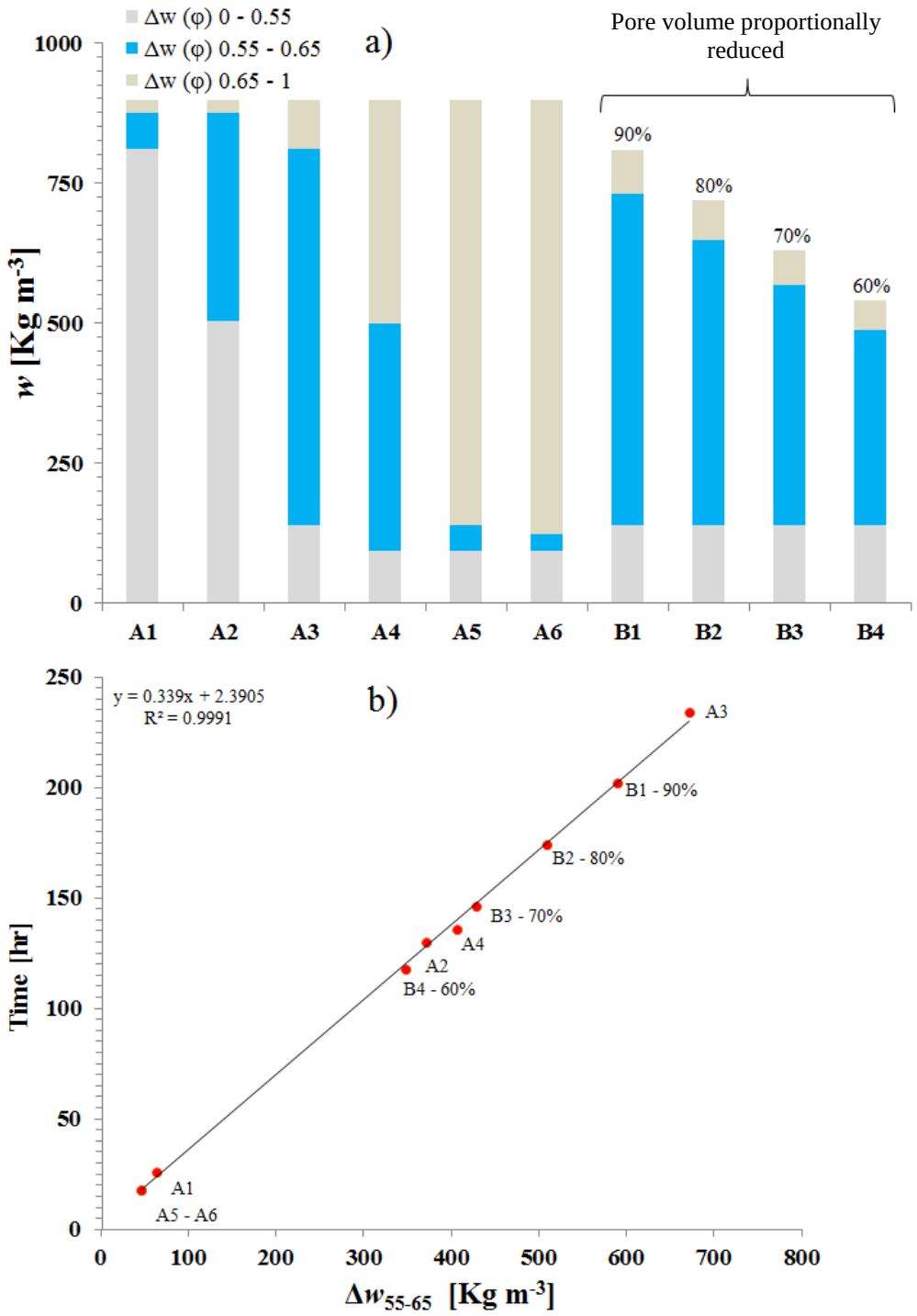


Figure 4.9 – Correlation between Δ*w* and relative humidity buffering decay. a) Water uptake at Δ*w* range. b) Δ*w*/*t* linear correlation (Thomann *et al.*, 2015b).

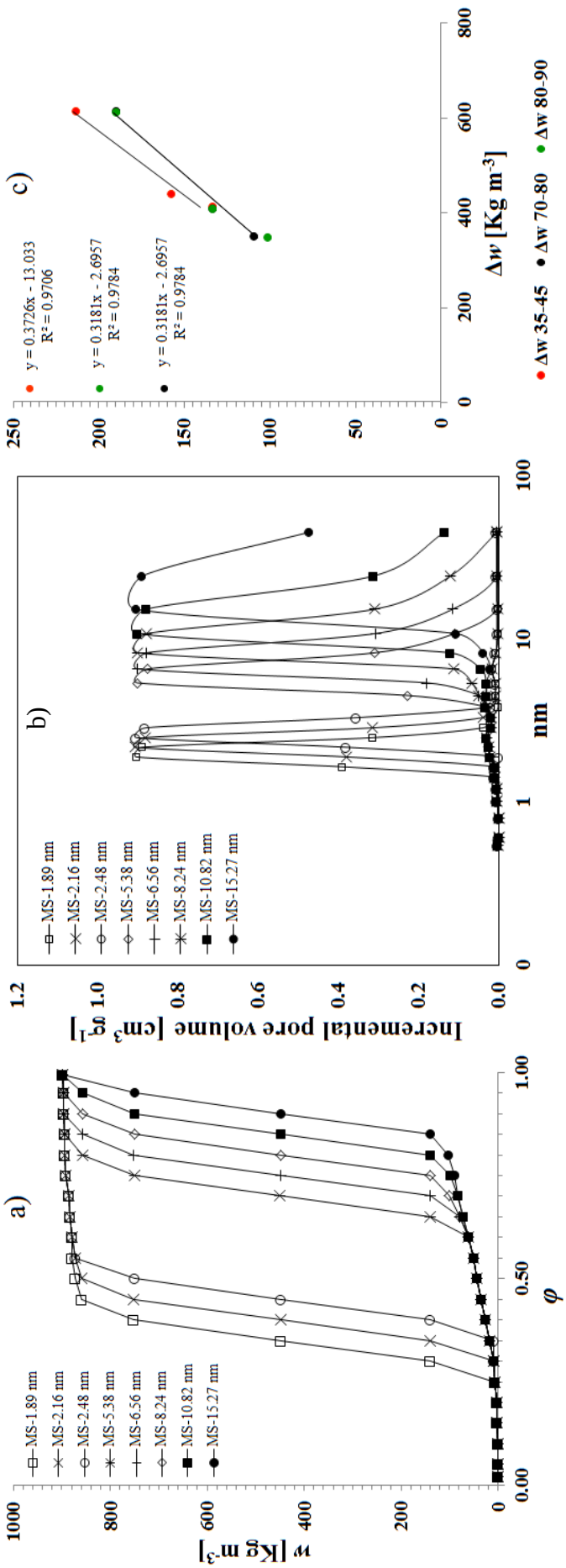


Figure 4.10 – Isotherm candidates for different $\varphi_{i,U} - \varphi_{i,L}$ limits. a) Water vapour sorption isotherms. b) Corresponding modal pore diameter derived from Kelvin's equation. c) $\Delta w/t$ linear correlation (Thomann *et al.*, 2015b).

Figure 4.9b also shows that this linear correlation persisted for B_1–B_4, where reduction in pore volume gave a proportional increase in elapsed time before buffering failure (at *N* cycles). The slope of the linear correlation $\Delta w/t$ seen in Figure 4.10c, also shows that for other candidate isotherms designed for different φ_{min} and φ_{max} limits.

4.4 Standardization process for humidity buffering

4.4.1 Volumetric moisture load analysis

Figure 4.11 shows the simulated results for candidate material A_3, according to the procedures described in Section 3.3.5. The results show a non-linear positive correlation between interior moisture load per unit volume, ω_{ml} and the minimum quantity (mass) of desiccant required to fully maintain φ buffering within the operating limits $\varphi_{min} = 0.55$ and $\varphi_{max} = 0.7$.

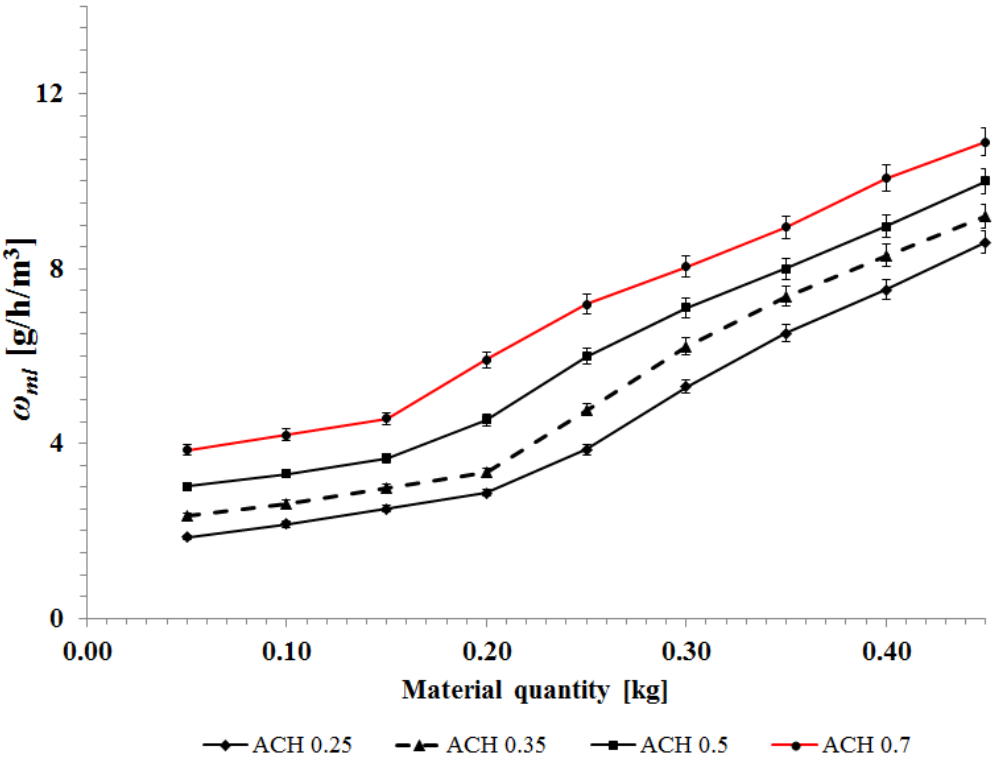


Figure 4.11 – Permissible volumetric moisture loads at constant $\varphi = 0.5$ (Thomann *et al.*, 2015b).

It was found that as the background air infiltration to the closed environment (ACH) increased, the moisture content of the infiltration air either adds or subtracts from the interior moisture loads (g/s). As a result, the minimum mass of the desiccant required could be adjusted in accordance with the trends shown in Figure 4.11. This would imply that if $\varphi_{i,L} \leq \varphi_e \leq \varphi_{i,U}$, then the exposed surface area of the desiccant required becomes highly sensitive to ACH with respect to the relative humidity buffering capacity of the desiccant.

4.4.2 Ventilation sensitivity analysis on volumetric moisture loads

From Figure 4.11 it could also be suggested that the diluting capacity of the air decays as the ACH becomes lower; unless the moisture content of φ_e is sufficiently low (see Figure 4.12).

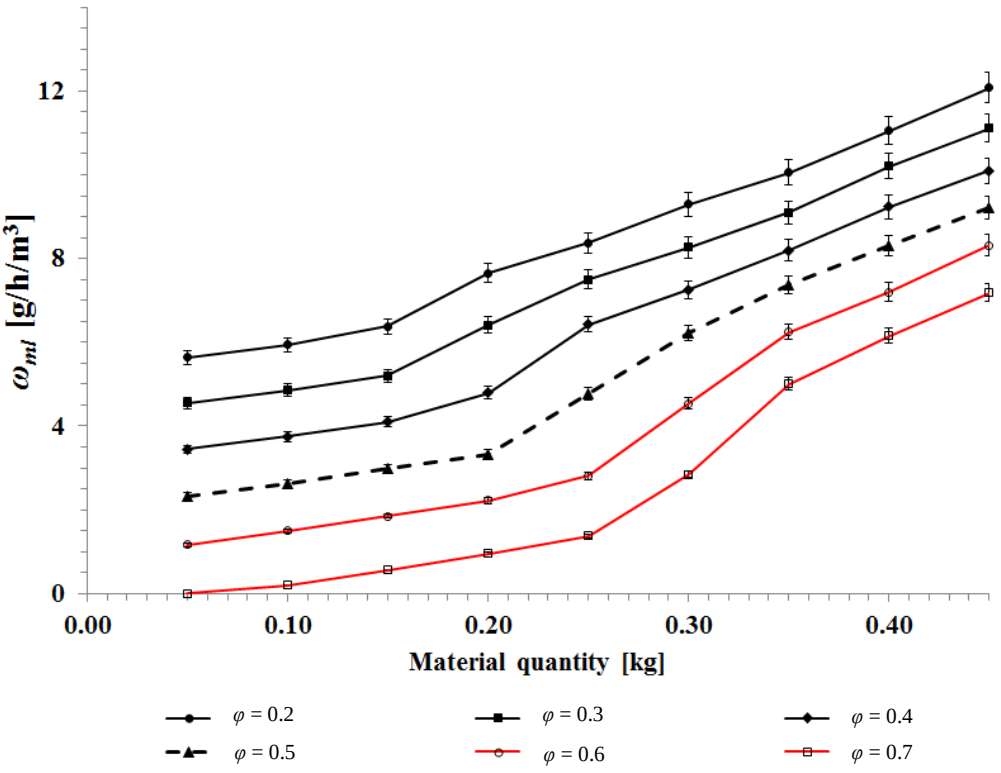


Figure 4.12 – Permissible volumetric moisture loads at constant ACH = 0.35 and different φ_e (Thomann *et al.*, 2015b).

This can be partially explained as the resultant indoor moisture content of the closed environment is increased/ reduced due to the low/ high moisture exchange (kinetics of sorption/ desorption) between the absorbent and the background air infiltrated. Figure 4.12 also shows that if $\varphi_e < \varphi_{i,L}$, the exposed surface area of desiccant reduces whilst the buffering capacity increases (and therefore *N*). This could also imply that the interior moisture loads can potentially be wholly offset by infiltration alone. Conversely, if $\varphi_e > \varphi_{i,U}$ (red lines in Figure 4.12), *N* decreases and the desiccant may not be able to buffer the closed environment unless ACH is very low.

4.5 Discussion

From the characterization (water vapour isotherm) of the pre-existing MS materials (MS-3.3 and MS-8.3), it was found that both materials displayed a low water vapour uptake in the low φ range (before the onset of capillary condensation). Presumably, this may represent weak adsorbent-adsorbate interactions, which resulted in pore filling at higher vapour pressure through capillary condensation, *i.e.* both cases above $\varphi = 0.7$.

The implications of the underestimation (specifically for MS-8.3) of total moisture content ($> \varphi = 0.95$) with respect to a fixed porosity ($n = 0.78$ refer to Table 3.1 in Section 3.3.1), is that WUFI+ may not be able to estimate *n*, unless there is a reduction of the pore wall thickness. This may also suggest that a possible 'swelling effect' could have taken place within pore network of the MS materials at higher relative humidities, and therefore allowing greater water vapour uptake.

The significance of the preliminary numerical simulations (refer to Section 4.3.1) indicated that a principle may be established within the operating limits $\varphi_{min} - \varphi_{max}$, where there appears to be an independent correlation between N and modal pore diameter from MS-3.3 and MS-8.3. The latter showed a small but significant difference in water vapour uptake (inferior in 25.6 kg/m^3) compared with MS-3.3, and where φ was within the range 0.5 – 0.7. This affected the capacity for humidity buffering and resulted in an early decay at a lower number of cycles, N; *i.e.* MS-8.3, N = 4.4; and MS-3.3, N = 6.4.

The results shown in Section 4.3.2 (refer to Figure 4.4 and Figure 4.5) provided the best relative humidity buffering performance within the operation limits (φ_{min} = 0.55 and φ_{max} = 0.7). Here, the 'ideal' isotherm was identified as candidate A_3, which maintained the fluctuation of $\varphi(t)$ over a larger number of cycles, N. This confirmed the hypothesis (refer to Section 3.1) in which the best performance for relative humidity buffering is achieved by using those materials where the maximum theoretical pore volume is assigned within the linear portion of the isotherm between the values $\varphi_{i,L}$ and $\varphi_{i,U}$.

On the other hand, the early decay for humidity buffering seen in the hypothetical isotherms (refer to Section 4.3.2) was especially noticeable in materials A_1, A_5 and A_6. Apparently, this could be an indication that the available moisture storage capacity was relatively small compared with the moisture loads being applied, finding an early equilibrium with the moisture content of the air above φ_{max}. Additionally, all these materials (A_1–A_6) exhibited a degree of hysteresis at the desorption stage below φ = 0.6. This could be explained since the material achieved a greater φ value than φ_{max}, and therefore a higher w according to the portion of the isotherm during the desorption cycle.

From Section 4.3.3, hysteresis was also presented for the new isotherms with pore volume being reduced (B_1–B_4), and as the candidates reached capillary condensation above $\varphi_{i,U}$ (*i.e.* the top knee, refer to Figure 3.5) full equilibrium moisture content was achieved. This was consistent with the time taken for buffering decay to occur as the number of cycles, *N* were sequentially completed in reverse order from lower to higher pore volume; *i.e.* B_4 to B_1.

When comparing the humidity buffering results between candidate isotherms A_1–A_6 and B_1–B_4 (within the specific operating limits $\varphi_{min} = 0.55$ and $\varphi_{max} = 0.7$) an important observation was made. The materials' suitability for relative humidity buffering appears to be highly sensitive to the Δw gradient between $\varphi_{i,L}$–$\varphi_{i,U}$ limits, rather than having higher total pore volume capacity. This was in consistent agreement with the number of decay cycles, *N*, and found to be highly sensitive to the value Δw between $\varphi_{i,L}$–$\varphi_{i,U}$ limits, *i.e.* controlled by φ (*x*–axis) adjustments to the sorption isotherm and hence independent of modal pore diameter.

Significant implications can be drawn from the positive linear correlation between the moisture storage capacity, $\Delta w_{55\text{-}65}$ and the time taken to exceed the φ_{max} limit (refer to Figure 4.9). The latter, suggested that the $\varphi_{i,U}$ limit may enable one to define a critical φ value for any relative humidity buffering application. Moreover, it seems that the onset for capillary condensation appears to be after $\varphi_{i,L}$ and up until the material reaches full equilibrium moisture content. This suggests that when designing an 'ideal' isotherm for a specific application, adjustment of the maximum Δw should be allocated between the operating limits $\varphi_{i,L}$–$\varphi_{i,U}$.

From Figure 4.11 and Figure 4.12, further applications can be identified based on the standardization process of the volumetric moisture loads, ω_{ml}. This can be explained as previously shown in Section 4.3.3, where the number of cycles, N was highly sensitive to Δw. This would imply that the prediction of total permissible moisture loads could be confidentially be estimated for any candidate isotherm.

4.6 Future work

This section summarises proposed further work for the applicability of the top-down design tool for desiccant material design. In particularly, this is discussed for the development of hypothetical desiccants for enhanced relative humidity buffering and thermal storage under non-isothermal condition within closed environments.

4.6.1 Conceptual model for adsorption/ heat transfer

As previously described in Section 4.4, the background air infiltration, φ_e (set as an ACH rate) can either add to/ subtract from the interior moisture loads. Therefore, φ_e can be substituted as a moisture load by the values of its moisture content (g H_2O/kg dry air). Given the psychrometric conditions for T_{db} and φ (orange line seen in Figure 4.13a), with respect to a fixed ACH rate, this can lead to the estimation of the volumetric mass flow rate (g/h/m^3). Consequently, the summation of ω_{ml} (black dots seen in Figure 4.13a) and the volumetric mass flow rate (g/h/m^3) can be wholly substituted as a value for the total interior moisture loads, ω_T as seen within the psychrometric chart (light-blue dots in Figure 4.13).

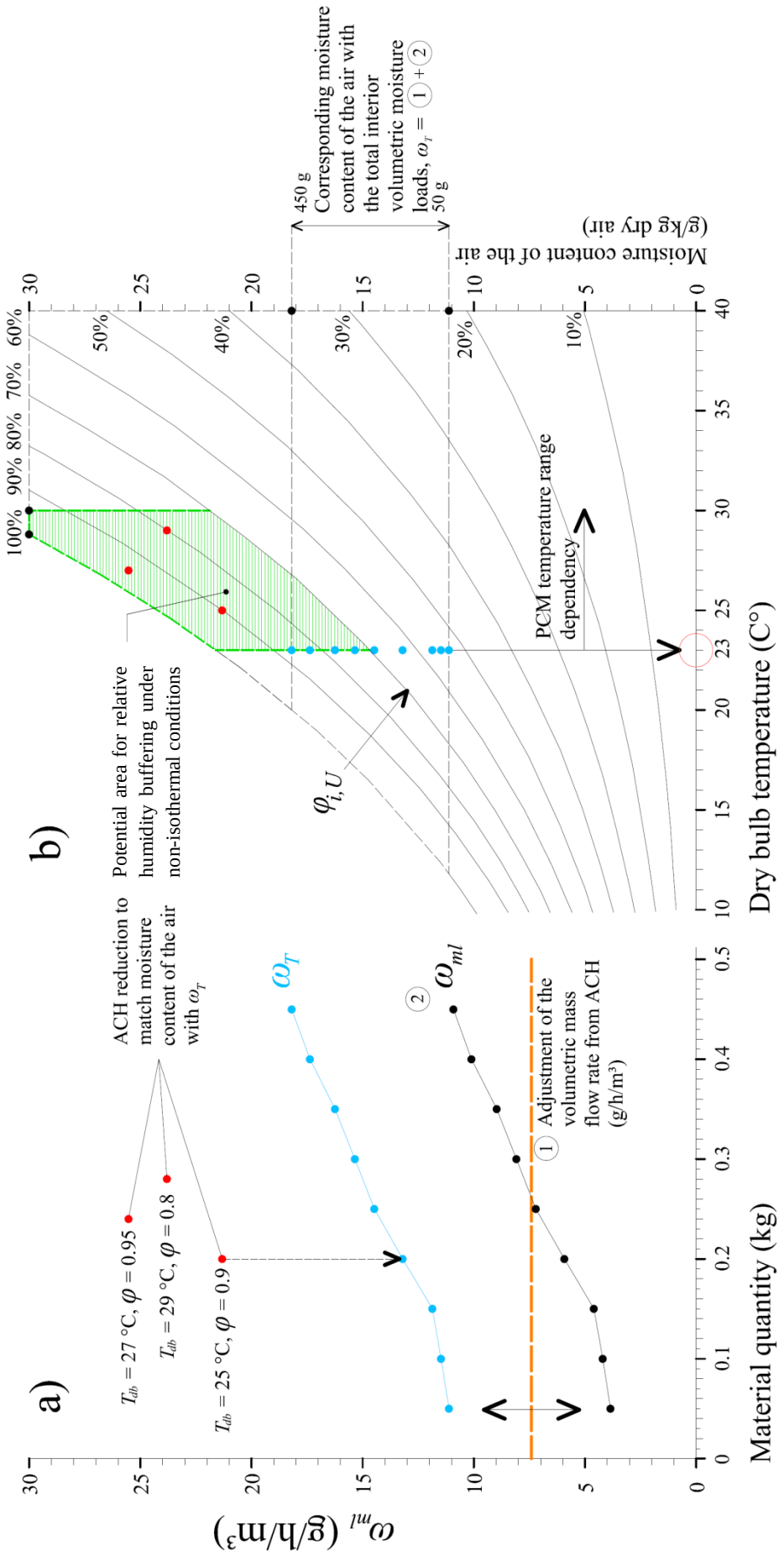


Figure 4.13 – Conceptual model for expanded hygrothermal applications within a psychrometric chart and under non-isothermal conditions.

Previously, the absorbents were deemed to perform under isothermal psychrometric conditions within the closed environment. Figure 4.14 represents a conceptual model for hygrothermal buffering through enhanced heat transfer (adsorption and vapour) and storage (sensible and latent heat) for hypothetically designed isotherms. The aim of this future study will therefore be to formulate a conceptual model that enables theoretical insight into enhanced hygrothermal functional properties for combined relative humidity and temperature buffering (including temporal thermal storage) through:

1. The adsorption of heat through the pore network (enthalpy of the air).
2. Vapour transfer (diffusion), and
3. Thermal storage (using phase change material (PCM) encapsulation) for hypothetical mesoporous desiccants.

This would eventually allow the design of tailored desiccants to buffer and store moisture under non-isothermal psychrometric conditions within closed environments. The existing data of ω_{ml} (refer to Figure 4.11 and Figure 4.12) and the volumetric mass flow rate (ACH-dependent) will be set as the limit for ω_T at this stage (red dots in Figure 4.13a–b). Selection of the new operating psychrometric parameters (that matches ω_T) within the green area from Figure 4.13b can be then freely designated, providing that the PCM would stabilize the indoor T_{db} whilst absorbing moisture. As with previous numerical simulations (refer to Section 4.3 and 4.4), this would hypothetically assess the capacity of the desiccants for relative humidity buffering within the operating limits φ_{min} = 0.55 and φ_{max} = 0.7, including both the storage of moisture and thermal energy under non-isothermal conditions.

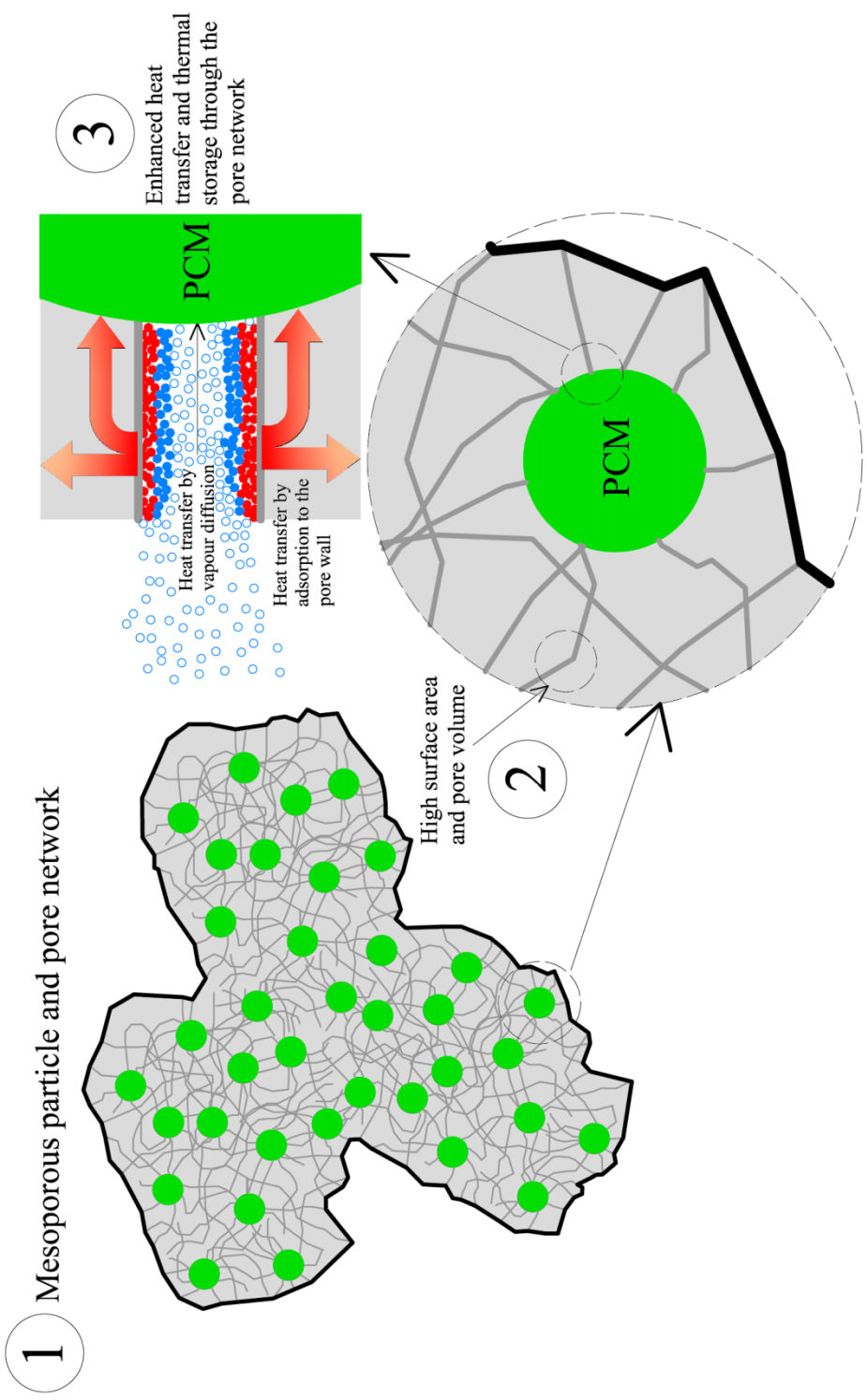


Figure 4.14 – Conceptual model for hygrothermal buffering through enhanced heat transfer and storage for hypothetically designed absorbents. (1) Design of a mesoporous pore network, (2) encapsulation of PCM within a mesoporous structure, and (3) enhanced heat transfer and thermal storage.

4.7 Summary

1. A hygrothermal modelling technique was developed that enabled a top-down predictive design of 'ideal' water vapour isotherms that are optimised to match any relative humidity buffering applications.
2. In order to enable calibration and operation of the hygrothermal modelling technique, characterization of the pre-existing materials (MS-3.3 and 8.3) and preliminary numerical simulations were conducted in order to provide material properties data and sensitivity analysis.
3. An important principle was established, in which no correlation was found between N and the modal pore diameter, when humidity buffering was performed within the operating limits φ_{min} = 0.55 and φ_{max} = 0.7.
4. Sensitivity analysis was conducted for the new set of candidate water vapour isotherms (A_1–A_6 and B_1–B_4). Significant implications were drawn from this, in which a positive linear correlation was found between the time taken for the material to exceed the φ_{max} limit (decay for relative humidity buffering) and the linear portion within the isotherm. This was found to be highly sensitive to the pore volume within the Δw gradient between $\varphi_{i,U}$ and $\varphi_{i,L}$ limits, independent of modal pore diameter and total pore volume capacity. The latter confirmed the hypothesis set in Section 3.1 for achieving optimum relative humidity buffering performance within the specified operation limits, *i.e.* in this case φ_{min} = 0.55 and φ_{max} = 0.70.
5. A non-linear positive correlation was found between the volumetric moisture loads, ω_{ml} and the mass of desiccant required to fully maintain relative humidity buffering within the specified operational limits, φ_{min} =

0.55 and φ_{max} = 0.70. The relative humidity buffering capacity and the exposed surface area of the material were strongly affected both by φ_e and ACH.

6. Further applications from the standardization process could be found, suggesting that the prediction of total permissible moisture loads can be confidently be estimated. This could be achieved by assuming that the permissible volumetric moisture loads, ω_{ml} changed proportionally with the gradient, Δw of an optimised isotherm.
7. Expanded theoretical work was proposed, which can be conducted by utilizing this design method for further relative humidity buffering applications, and for sensitivity analysis when assessing closed environments. This was hypothesised by the development of a conceptual model for hygrothermal functional properties that enables enhancement in the heat transfer and thermal storage whilst buffering moisture loads under non-isothermal conditions.

CHAPTER 5 Mesoporous desiccant characterization and water vapour adsorption/ desorption kinetics

5.1 Overview

This chapter presents the results that correspond to Stage 2, from the methodological scheme (refer to Figure 1.2), in order to address objectives 3 and 4 as outlined in Section 1.3. This includes:

1. Volumetric nitrogen physisorption characterization for the new MS desiccants (SBA-15 and MCM-41), including: 1) nitrogen adsorption/ desorption isotherms, 2) pore volume, 3) pore size distribution, and 4) specific surface area (Section 5.2).
2. Gravimetric determination of water vapour adsorption/ desorption isotherms for the new MS desiccants, using dynamic vapour sorption (Section 5.3).
3. Physical modelling comparison for the new MS desiccant, with respect to the time-response for water vapour adsorption/ desorption, using a climate chamber and dynamic vapour sorption (DVS) techniques (Section 5.4).
4. Hygrothermal model validation by comparing the results gathered from experimental testing (Section 5.4) with the hygrothermal simulation data. The latter applied when assessing the time-response for water vapour adsorption/ desorption for the new MS desiccants (Section 5.5).

5.2 Nitrogen Physisorption

5.2.1 Nitrogen adsorption/ desorption isotherms

Figure 5.1 shows the nitrogen adsorption/ desorption isotherms for the MS desiccants (SBA-15 and MCM-41) according to the procedure described in Section 3.4.1. In the case of SBA-15 and MCM-41 materials, a characteristic Type IV isotherm (IUPAC classification) was found where the monolayer and multilayer formation appears to occur within the mesopore range before the onset of capillary condensation (pore filling). In the case of MS-3.3 and 8.3 desiccants a reversible Type I isotherm was found. It can be suggested that both materials showed an enhanced concentration (adsorbent-adsorbate interactions) of adsorbed nitrogen molecules at low P/P_0 featuring an almost horizontal plateau, which is well-known to be related to the micropore filling region. This indicates a relative small multilayer adsorption in this region.

As opposed to MCM-41 and SBA-15 desiccants, MS-3.3 and 8.3 presented no evidence of a steep step over a narrow P/P_0 range, but rather a sudden nitrogen adsorption was found at higher P/P_0 (> 0.95) suggesting that wider mesopores were entering into a capillary condensation pore filling stage. Additionally, Figure 5.1 also shows well-defined Type H1 hysteresis loops in most desiccants, indicating overall reversibility for nitrogen adsorption and desorption. This was more evidenced in MCM-41@150–165; as expected in this kind of tubular-structured materials (Sing, 1998; Rouquerol *et al.*, 1998).

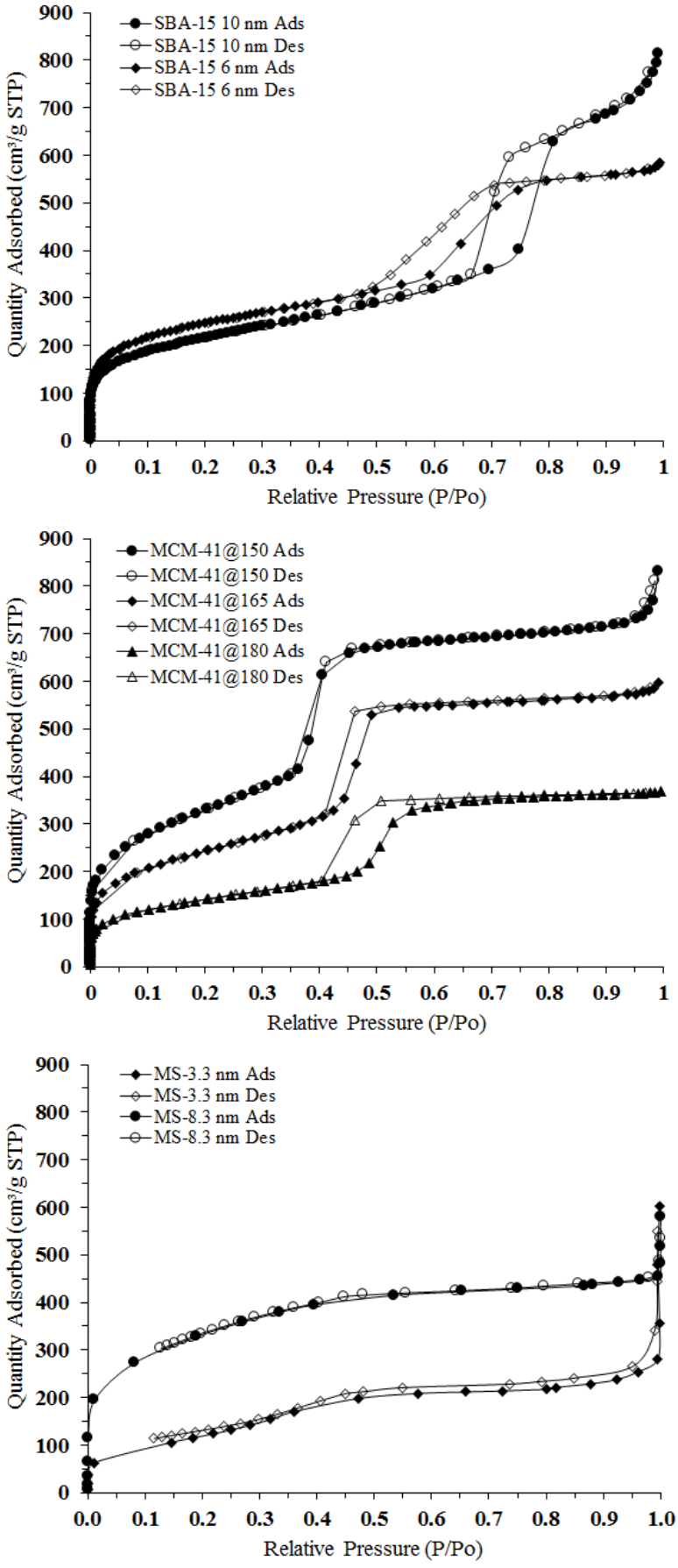


Figure 5.1 – Nitrogen adsorption isotherms. Filled symbols denote adsorption.

Sample	Adsorption		Desorption	
	Lower limit	Upper limit	Percolation threshold	[a] Lower closer point
	$P/P_{0(L)}$	$P/P_{0(U)}$	P/P_0	P/P_0
SBA-15 6 nm	0.59	0.74	0.73	0.46
SBA-15 10 nm	0.74	0.8	0.79	0.66
MCM-41@150	0.36	0.4	0.4	0.35
MCM-41@165	0.44	0.5	0.46	0.4
MCM-41@180	0.44	0.56	0.5	0.4

Table 5.1 – Adsorption/ desorption lower and upper P/P_0 ranges for SBA-15 and MCM-41 materials, when using nitrogen as an adsorbate. [a] Where adsorption and desorption branches coincide with respect to a limiting partial pressure; *i.e.* P/P_0 = ~ 0.42 in the case of nitrogen.

Additionally, this type of hysteresis loop is often associated with pores that exhibit a narrow distribution of relatively uniform cylindrical pores (Branton *et al.*, 1995). In the case of wider hysteresis loops, such as for SBA-15 and MCM-41@180 materials, a delayed condensation stage may be the cause; *i.e*. there is not a stable condensed state of nitrogen (liquid-gas metastable state). The latter may be removed by increasing the operational temperature (Branton *et al.*, 1997; Ravikovitch *et al.*, 1995); *i.e*. by triggering nitrogen evaporation during the desorption process. This technique is widely found in literature, and it cannot be solely attributed to the pore-blocking effect (refer to Section 2.7.2 and 2.7.3) as in the case of a Type H2 hysteresis loop. This is because there is no defined percolation threshold (knee) together with the characteristic steep desorption (Seaton, 1991), but rather the desorption branch of the isotherm is parallel to the adsorption branch (also refer to Table 5.1).

5.2.2 Specific surface area and pore size distribution

As Table 5.2 shows, high specific surface areas (SSA) were found amongst the desiccants that achieved greater micropore volume, V_m; *e.g.* MCM-41@150 (1190 m^2/g) and MS-8.3 (1084 m^2/g), both having larger V_m among all desiccants; 0.37 and 0.29 cm^3/g, respectively. These were obtained from the monolayer capacity according to the procedure depicted in Section 3.4.1.1. The micropore volume, V_m (MCM-41 desiccants) was in consistent agreement with the anticipated reduction in pore volume resulting from alteration of the pore wall thickness during synthesis (crystallisation) (Thomann *et al.*, 2015b). As Table 5.2 shows, the increased pore wall thickness affected total pore volume (V_p) and SSA, which decreased from 1.29 cm^3/g and 1190 m^2/g for MCM-41@150, to 0.54 cm^3/g and 455 m^2/g for MCM-41@180. This is also presented in Figure 5.1, where a gradual decrease in the height (V_p) and sharpness of the mesopore filling step (steepness of the adsorption portion of the isotherm where the onset of capillary condensation stage begins) is shifted to a higher P/P_0 range, due to the increased pore size.

Sample	S_{BET} m^2/g	V_m cm^3/g	V_p cm^3/g	D_p nm
MCM-41@150 [a]	1190	0.37	1.28	2.78
MCM-41@165 [a]	879	0.27	0.92	3.4
MCM-41@180 [a]	455	0.12	0.54	3.77
SBA-15 6 nm [b]	876	0.17	0.91	5.7
SBA-15 10 nm [b]	757	0.12	1.26	10.2
MS-3.3 [c]	748	0.25	0.65	3.3
MS-8.3 [c]	1084	0.29	1.31	8.3

Table 5.2 – Textural properties summary for MCM-41, SBA-15 and MS desiccant materials. Values [a] were taking from Ref. (Thomann *et al.*, 2015b). Values [b] and [c] were taking from Ref. (Thomann *et al.*, 2015a) and (Hall *et al.*, 2012), respectively.

Figure 5.2 shows the pore size distribution by means of incremental pore volume (Figure 5.2a – for MCM-41 and SBA-15) and relative volumetric distribution (Figure 5.2b for MS-3.3 and 8.3), both determined by the BJH method as depicted in Section 3.4.1.1. Figure 5.2a clearly shows that for MCM-41 desiccants, the incremental pore volume reduction corresponds to the pore size distribution, which is gradually shifted toward higher P/P_0 ranges (refer to Table 5.2).This was previously confirmed by the author (Thomann *et al.*, 2015b), when controlling temperature variation during the synthesis process for MCM-41, and was found to be highly sensitive to the increase in pore wall thickness.

On the other hand, Figure 5.2b shows that the volumetric distribution for the MS desiccants is clearly defined by micropore/ mesopore filling. The latter can be clearly seen for MS-8.3 at the lower range of pore size distribution, due to a higher nitrogen adsorption in that range; *i.e*. small shoulder between 2 – 3 nm. In the case of MS-3.3, a distinctive narrow pore size distribution was observed within the mesopore structure. However, at higher P/P_0 (above P/P_0 = ~ 0.98), there was some indication of pore filling within the macropore region. Evidence of this is found when analysing larger pore size (> 20 nm), where an increased volume is gradually adsorbed as the pore size increases. This can also be found in desiccants SBA-15 10 nm and MCM-41@150 from Figure 5.2a.

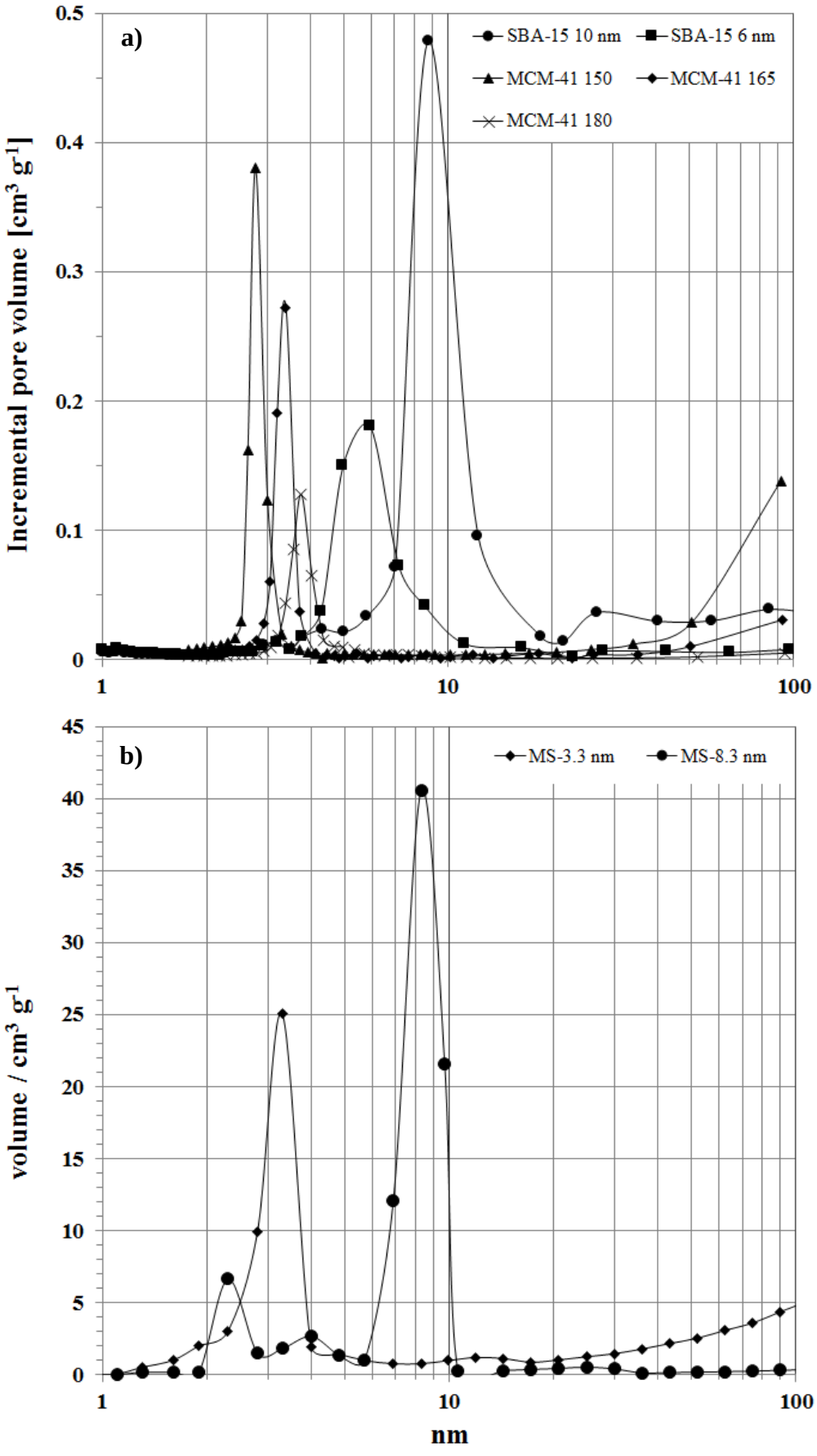


Figure 5.2 – PSD for all materials. a) Incremental pore volume BJH from the adsorption branch. b) Relative volume (%) BJH from the adsorption branch. Values taken from (Hall *et al.*, 2012).

5.3 Hygrothermal functional properties characterization

5.3.1 Water adsorption isotherm

Figure 5.3 shows the experimental water vapour adsorption/ desorption isotherms for all MCM-41 and SBA-15 desiccants, performed in accordance with the procedure described in Section 3.4.2. Almost all of the water vapour adsorption isotherm seen in Figure 5.3 presented a characteristic 'S-shaped' Type V isotherm following the IUPAC classification (except SBA-15 10 nm with a Type III isotherm). As previously shown in Section 4.2, both types (*i.e.* V and III) may present weak adsorbent-adsorbate interactions, resulting in pore filling at higher vapour pressure through capillary condensation.

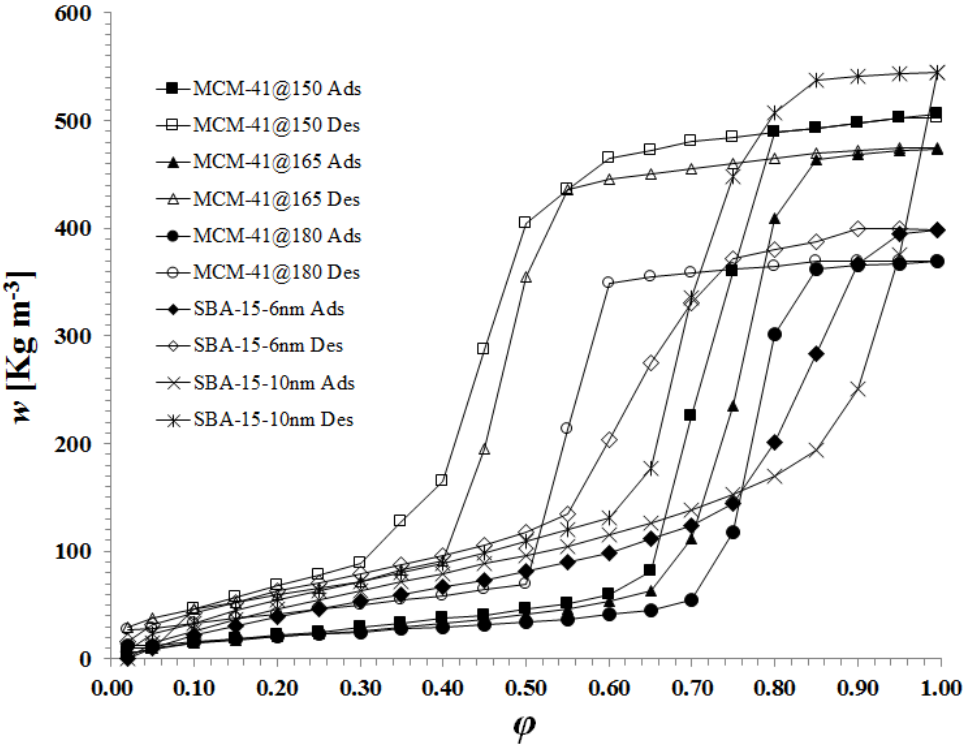


Figure 5.3 – Water vapour adsorption/ desorption isotherms. Adsorption is denote with filled symbols. MCM-41@150–180 are provided from Ref. (Thomann *et al.*, 2015b); MCM-41@165 and SBA-15 6–10 nm from Ref. (Thomann *et al.*, 2015a).

However, this phenomenon occurs at different relative humidity ranges for both types of isotherm. Evidence of this is presented in Table 5.3, where in the case of a Type V isotherm (after the steep gradient over a narrow φ range) a sub-plateau indicates that the material has nearly reached a capillary saturation. Conversely, this stage is not shown for Type III materials, which indicates continuous water vapour adsorption towards the mesopore/ macropore region at very high relative humidity values; *e.g*. the case of SBA-15 10 nm. This is also plausible when analysing the N_2 adsorption isotherms (Type I), where it can be clearly seen that there is a sudden increase in nitrogen adsorption ($P/P_0 > 0.95$). Within the steep gradient over the $\varphi_{b\text{-}c}$ range, the change in moisture content, Δw is found for each category of desiccant (Table 5.3) as follow: MCM-41@150, $\varphi_{b\text{-}c}$ = 0.65 – 0.8 and $\Delta w_{b\text{-}c}$ = 411.8 kg/m^3; SBA-15 10 nm, $\varphi_{b\text{-}c}$ = 0.8 – 1 and $\Delta w_{b\text{-}c}$ = 268.1 kg/m^3; and MS-8.3, $\varphi_{b\text{-}c}$ = 0.7 – 1 and $\Delta w_{b\text{-}c}$ = 545 kg/m^3.

Sample	Adsorption			Moisture storage			
	$\varphi_{a\text{-}b}$	$\varphi_{b\text{-}c}$	$\varphi_{c\text{-}d}$	$\Delta w_{a\text{-}b}$	$\Delta w_{b\text{-}c}$	$\Delta w_{c\text{-}d}$	w
	(-)			(kg/m^3)			
MCM-41@150	0 - 0.65	0.65 - 0.8	0.8 - 1	81.2	411.8	13.5	506.5
MCM-41@165	0 - 0.65	0.65 - 0.8	0.8 - 1	111.5	298.1	63.8	473.4
MCM-41@180	0 - 0.7	0.7 - 0.85	0.85 - 1	54.7	246.9	7.7	309.3
SBA-15-6nm	0 - 0.75	0.75 - 0.9	0.9 - 1	144.3	222.1	32.6	398
SBA-15-10nm	0 - 0.85	0.85 - 1	-	251.4	268.1	-	519.5
MS-3.3	0 - 0.7	0.7 - 1	-	40.5	169.5	-	210
MS-8.3	0 - 0.7	0.7 - 1	-	228.6	545	-	773.6
Silica Gel	-	-	-	-	-	-	310.1

Table 5.3 – Stages for water vapour adsorption in the ranges $\varphi_{a\text{-}b}$, $\varphi_{b\text{-}c}$, and $\varphi_{c\text{-}d}$ and the corresponding moisture storage, Δw for same φ ranges. Refer to the conceptual model shown in Figure 2.19 and Section 2.7.1.

Figure 5.3 also shows a distinctive Type H2 hysteresis loop for almost all desiccant materials, which may indicate that a pore-blocking effect has taken place in the desorption branch of the water isotherm. As explained before, this

is perhaps due to significant differences in interconnected pore sizes within a complex structure. This may also indicate, for example, that a critical pressure is needed to overcome the pore-blocking effect at the percolation threshold; *i.e*. at the pore neck at point 'c' from Figure 2.19, where the pore network empties. In other words, the critical water vapour pressure should be sufficiently enough to enable full desorption and reversibility of the isotherm; also refer to Section 2.7.3.

It can then be hypothesised that, there could be some degree of correlation between the water vapour and nitrogen isotherm. This follows when the 'lower closer point', $\varphi_{,L}$ (where the water phases gas-liquid-like and condensate enter metastable equilibrium) of the water vapour desorption isotherm coincides with the onset of capillary condensation in the nitrogen desorption isotherm ($P/P_{0(L)}$). This hypothesis assumes total reversibility for the nitrogen adsorption/ desorption isotherm. The implications of this are that the narrow pore size distribution from the water vapour desorption isotherm would eventually match the one from the nitrogen adsorption isotherm. Some preliminary analysis of this is presented in Table 5.4 (columns b and c), where a good agreement has been found when matching both points of the isotherms ($\varphi_{,L}$ and $P/P_{0(L)}$); *e.g*. for SBA-15 6 nm, $\varphi_{,L}$ = 0.5 and $P/P_{0(L)}$ = 0.46; for MCM-41@150, $\varphi_{,L}$ = 0.3 – 0.4 and $P/P_{0(L)}$ = 0.35; and MCM-41@165, $\varphi_{,L}$ = 0.4 and $P/P_{0(L)}$ = 0.4. Further preliminary evidence shows a positive agreement when comparing the values for the percolation threshold ($\varphi_{,P}$) from the water vapour isotherm with the upper ($P/P_{0(U)}$) limit from the nitrogen adsorption isotherm (refer to Table 5.4 in columns a and d).

Sample	Desorption (H_2O)		Adsorption (N_2)	
	$(\varphi,_P)$	$(\varphi,_L)$	$(P/P_{0(L)})$	$(P/P_{0(U)})$
	a	b	c	d
SBA-15 6 nm	0.75	0.5	0.46	0.74
SBA-15 10 nm	0.8	0.6	0.66	0.8
MCM-41@150	0.5	0.3–0.4	0.35	0.4
MCM-41@165	0.55	0.4	0.4	0.5
MCM-41@180	0.6	0.5	0.4	0.56

Table 5.4 – a) Desorption percolation threshold ($\varphi,_P$) and b) lower closer point ($\varphi,_L$) for SBA-15 and MCM-41 materials using water vapour as an adsorbate. c) Onset of capillary condensation ($P/P_{0(L)}$) for SBA-15 and MCM-41 materials, when using nitrogen as an adsorbate.

5.4 Kinetics of water adsorption/ desorption comparison

Figure 5.4 shows the kinetics of water vapour adsorption/ desorption comparison among all desiccant materials and the corresponding moisture content, *w* achieved for the three-cycle time-response test. The operational $\Delta\varphi$ ranges for each cycle were according to the procedure depicted in Section 3.5.2; where a) $\Delta\varphi$ = 0.2 – 0.3; b) 0.3 – 0.5, c) 0.5 – 0.7; and d) 0.7 – 0.95, respectively. The results presented in Figure 5.4a–b may show weak adsorbent-adsorbate interactions, which is characteristic in Type III and V isotherms as previously described in Section 5.3.1; low moisture content are achieved by almost all desiccants. Nevertheless, it can be seen that SBA-15, MS-3.3 and MS-8.3 materials show a significant increase in *w* at $\Delta\varphi_{0.2\text{-}0.3;\ 0.3\text{-}0.5}$ cycles. This is mainly attributed to the higher Δw that those desiccants present compared with MCM-41 in that particular $\Delta\varphi$ range of the adsorption isotherm (refer to Figure 5.3 and Table 5.5); *e.g.* MCM-41@150 $\Delta w_{20\text{-}30}$ = 7.1 kg/m^3 and SBA-15 10nm $\Delta w_{20\text{-}30}$ = 16.9 kg/m^3.

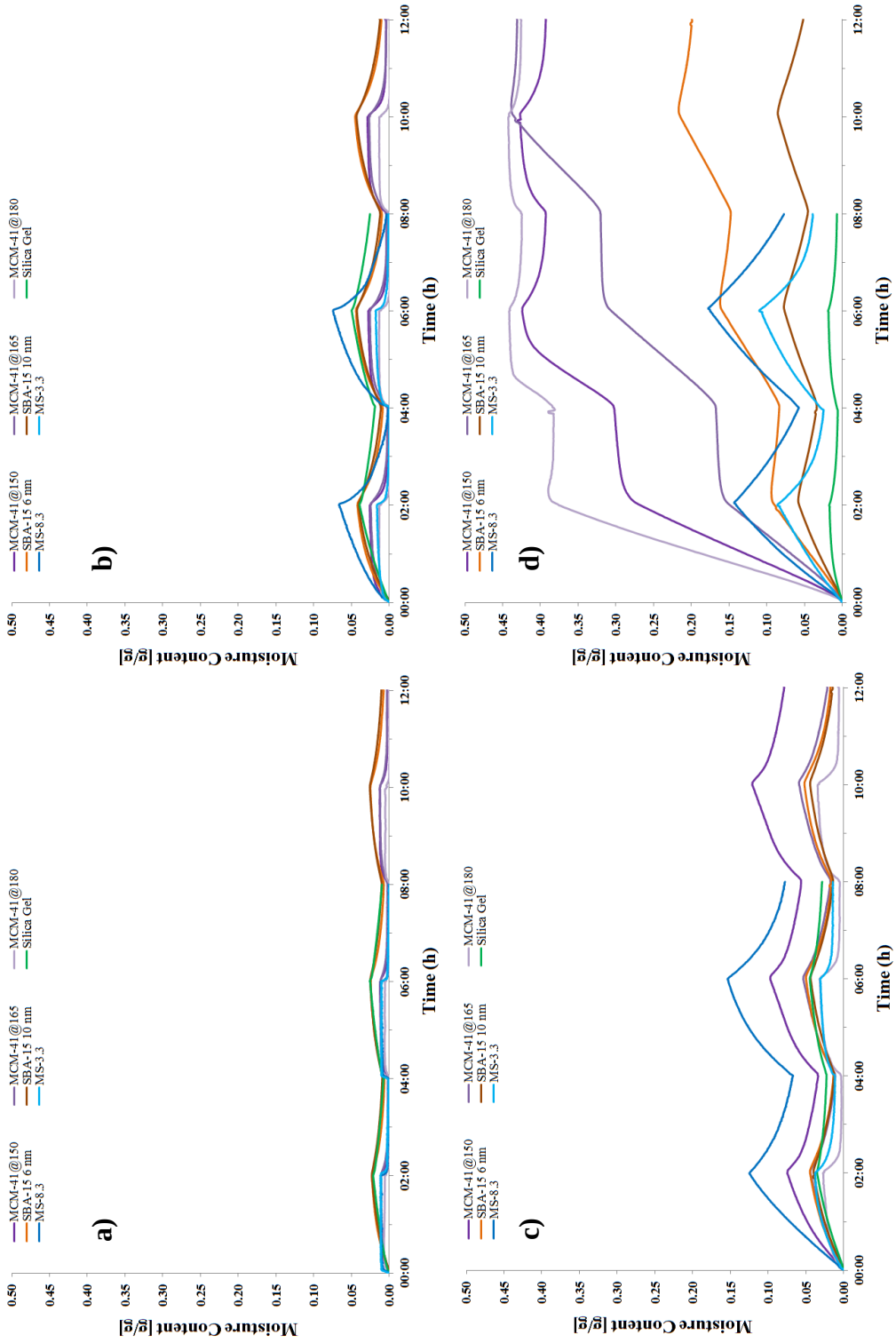


Figure 5.4– Comparison between moisture content (g/g) at different φ ranges, for the kinetics of water vapour adsorption/ desorption for a three-cycle time-response DVS test. Where a) φ = 0.2 – 0.3; b) 0.3 – 0.5, c) 0.5 – 0.7; and d) 0.7 – 0.95, respectively.

Conversely, Table 5.5 shows that MS-8.3 has greater moisture content, $\Delta w_{50\text{-}70}$ = 129.5 kg/m^3, resulting in approximately five times more capacity for moisture adsorption compared with all other desiccants, as shown in Figure 5.4c. On the other hand, it can be seen in Figure 5.4c that MCM-41@150 and MS-8.3 consistently started to show hysteresis phenomena (also refer to Figure 2.20 in Section 2.7.2). In the case of MCM-41@150, this can be attributed to entering into some kind of scanning curve (unknown at this stage) within the hysteresis loop by the increased resultant moisture storage capacity at the $\Delta w_{65\text{-}95}$ range, and to the onset of capillary condensation. Notice that in Figure 5.4d, all MCM-41 present an outstanding capacity and also a rapid-response for moisture adsorption; *e.g.* MCM-41@180 has around eight times more moisture adsorption capacity in the first two hours of the first cycle, compared with SBA-15 10 nm. As Table 5.5 shows, MCM-41 materials possess a higher moisture content capacity at the $\Delta w_{70\text{-}95}$ range (excepting MS-8.3).

Sample	Moisture storage at Δw			
	$\Delta w_{20\text{-}30}$	$\Delta w_{30\text{-}50}$	$\Delta w_{50\text{-}70}$	$\Delta w_{70\text{-}95}$
	(kg/m^3)			
MCM-41@150	7.1	16.0	179.5	276.6
MCM-41@165	5.4	15.1	69.8	361.1
MCM-41@180	3.9	9.3	20.2	312.8
SBA-15-6nm	14.2	28.3	42.6	270.0
SBA-15-10nm	16.9	33.1	41.8	236.8
MS-3.3	6.2	6.6	15.8	169.5
MS-8.3	7.1	87.0	129.5	545.0
Silica Gel	42.5	88.1	57.4	35.0

Table 5.5 – Moisture storage capacity at different Δw (kg/m^3) for all desiccant materials.

Excluding SBA-15 10 nm and Silica gel, all other desiccants clearly present hysteresis phenomena (also refer to points 1c–2b–3c in Figure 2.20). The progressive increase of their moisture content, w (each time commencing at

different initial w) may be related to the presence of scanning curves within the hysteresis loop, which helped those materials to nearly reach EMC_{95}. From another perspective, this can also be explained as their steep Δw gradient at the linear portion of the isotherm is located in a lower $\Delta\varphi$ range than $\Delta\varphi_{0.7\text{-}0.95}$ (refer to Table 5.3). This suggests that these materials (MCM-41, MS, and SBA-15 6 nm) are entering into a capillary saturation stage whilst performing the $\Delta\varphi_{0.7\text{-}0.95}$ cycle. Therefore other pore widths (larger size) are also absorbing moisture, leading to a significant pore-blocking effect during the desorption cycles. Apparently, this would not be the case for SBA-15 10 nm, since the capillary condensation stage has not been fully reached; *i.e*. its greatest performance is found at values $\varphi = 0.9$. This is where the $\Delta\varphi$ range contributes to its maximum moisture content within the Δw gradient.

On the other hand, the premise presented in Chapter 4 and Section 4.5 can be confirmed for those desiccants having the best performance for moisture adsorption capacity. The latter appeared to be highly sensitive to the Δw gradient in the relative humidity operating ranges where the onset of capillary condensation began (steep gradient over $\varphi_{b\text{-}c}$ range – refer to Table 5.3). This may also suggest that it strongly relates to the pore volume allocated within the specific portion of the isotherm (the steep Δw gradient before capillary saturation), rather than simply having a bigger modal pore diameter (refer to Table 5.2).

5.5 Experimental results and model validation

5.5.1 Dynamic vapour sorption (DVS)

Figure 5.5 and Figure 5.6 show the experimental and numerical simulations for the kinetics of water vapour adsorption/ desorption according to the procedure describe in Section 3.5.3. A representative group from the MCM-41 and SBA-15 results (MCM-41@150–180 and SBA-15 6 nm) was selected, and the comparison between the corresponding moisture content, w achieved for the three-cycle time-response test was assessed using same operational $\Delta\varphi$ ranges for each cycle according to Section 5.4. There appears to be some degree of water vapour adsorption/ desorption reversibility, especially in Figure 5.5b and e, where in both experimental and numerical, $N = 3$ was achieved. This could be an indication that the Δw gradient was sufficiently small with respect to the relevant portion of the adsorption isotherm (refer to Figure 5.3 and Table 5.5); *e.g.* MCM-41@180 $\Delta w_{20\text{-}30} = 3.9$ kg/m^3 and $\Delta w_{30\text{-}50} = 9.3$ kg/m^3. Additionally, the relationship between Δw gradient and the rapid-response for water vapour adsorption/ desorption (experimental data) was also confirmed, in cases where a steep adsorption/ desorption curve (Figure 5.5a, b, d and e) was presented. In the case of those materials that possess higher Δw gradient for the specific operational $\Delta\varphi$ ranges, both experimental and numerical data were found that their capacity for water vapour adsorption was significantly beyond the required time period for achieving EMC. Evidence of this is shown in Figure 5.7, where the segmented red line indicates moisture adsorption towards achieving EMC (EMC_{70} and EMC_{95}). Notice that only in cases a and b, EMC has been achieved (only experimental data) in the number of cycles, $N = 3$.

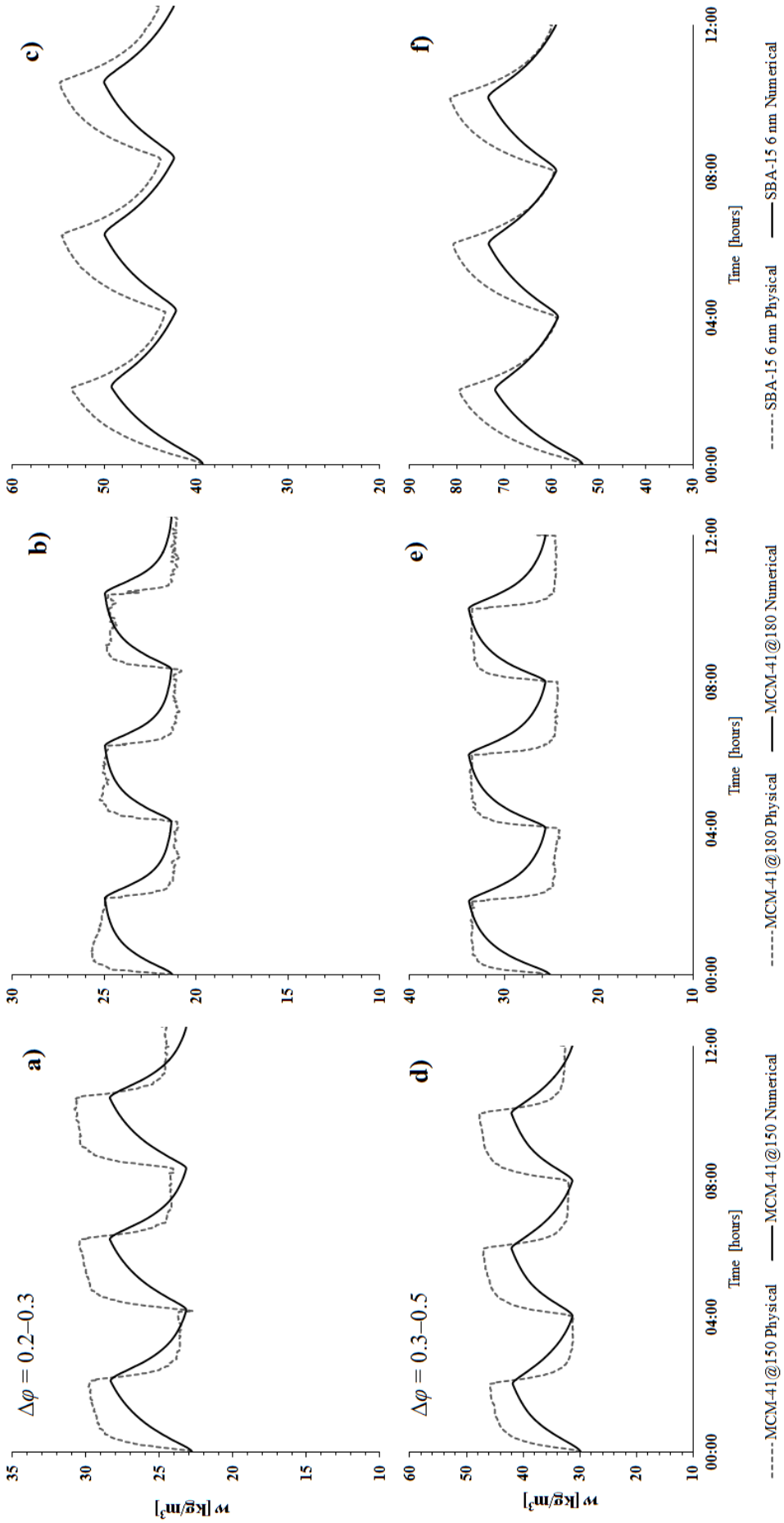


Figure 5.5 – Water vapour sorption/desorption kinetics comparison between experimental DVS and numerical simulations for MCM-41@150–180, and SBA-15 6 nm. The results are deemed to be read horizontally for each operating range ($\Delta\varphi$ = 0.2–0.3 and $\Delta\varphi$ = 0.3–0.5).

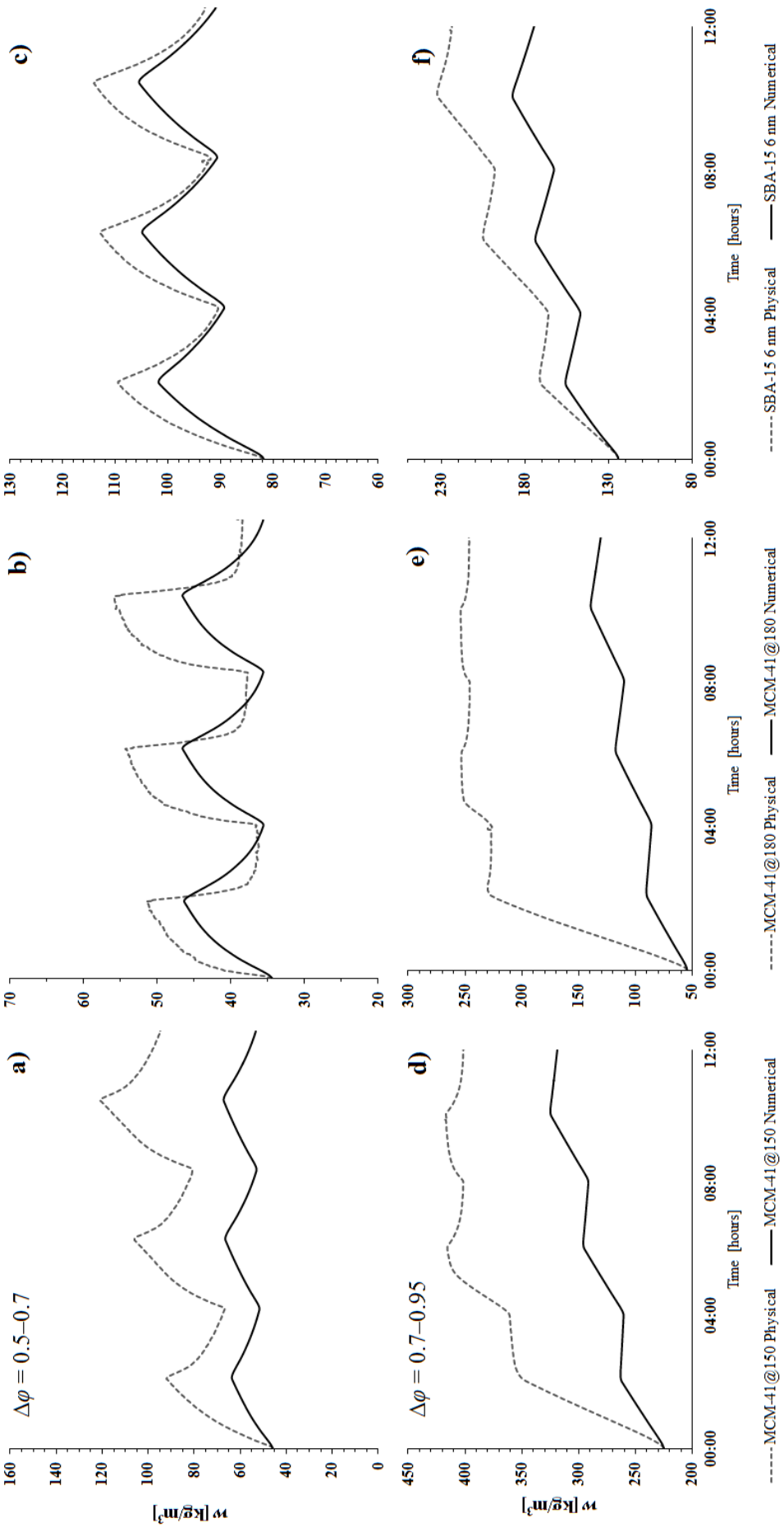


Figure 5.6 – Water vapour adsorption/ desorption kinetics comparison between experimental DVS and numerical simulations for MCM-41@150–180, and SBA-15 6 nm. The results are deemed to be read horizontally for each operating range ($\Delta\varphi$ = 0.5 – 0.7 and $\Delta\varphi$ = 0.7 – 0.95).

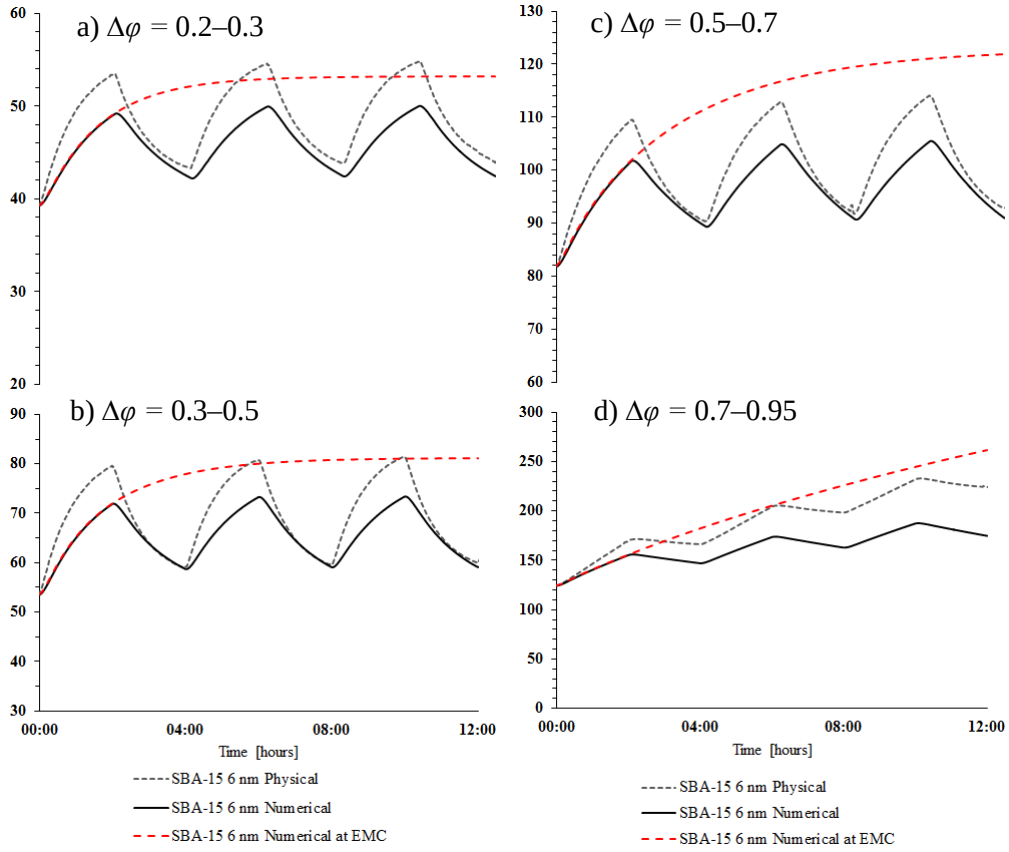


Figure 5.7 – Water vapour adsorption/ desorption kinetics comparison between experimental DVS and numerical simulations for SBA-15 6 nm, where the operating ranges are a) $\Delta\varphi$ = 0.2 – 0.3; b) $\Delta\varphi$ = 0.3 – 0.5); c) $\Delta\varphi$ = 0.5 – 0.7; and d) $\Delta\varphi$ = 0.7 – 0.95). The segmented red line correspond to EMC at the higher operational range (*i.e.* φ = 0.3, 0.5, 0.7 and 0.95) for each cycle.

It was evident that the numerical predictions appears to be underestimated (solid black line seen in Figure 5.5 a, c, d and f – and Figure 5.6) when analysing the time in achieving EMC. This may be attributed due to the lack of a dynamic input for *w*, within numerical models with respect to the time-response for water vapour adsorption at partial EMC; *i.e.*, *w* inputs are assumed to be at full EMC for single sorption isotherms. As previously mentioned in Section 5.4, the hysteresis phenomena through the pore-blocking effect may be an 'additional' cause for these divergences, with an important contribution from the activation of capillary condensation stages; *e.g.* Figure 5.6a, d, e and f. Further analysis

confirmed the above mentioned, where the average difference (%) between experimental and numerical *w* data for all adsorption/ desorption cycles was calculated. Notice in Table 5.6 that there are significant differences (%) when analysing MCM-41@150 and 180 at high Δ*w* ranges ($\Delta w_{50\text{-}70}$ and $\Delta w_{70\text{-}95}$ cycles respectively); *e.g.*, MCM-41@150 with 53.4% (adsorption) and 53.8% (desorption), MCM-41@180 with 88.1% (adsorption) and 84.4% (desorption). The lowest difference values were obtained in those materials that have a lower Δ*w* value in the appropriate operational range; *e.g.* SBA-15 10 nm and Silica Gel, suggesting some degree of water vapour adsorption/ desorption reversibility (refer to Section 5.4).

	MCM-41@150				MCM-41@165				MCM-41@180			
	$\Delta w_{20\text{-}30}$	$\Delta w_{30\text{-}50}$	$\Delta w_{50\text{-}70}$	$\Delta w_{70\text{-}95}$	$\Delta w_{20\text{-}30}$	$\Delta w_{30\text{-}50}$	$\Delta w_{50\text{-}70}$	$\Delta w_{70\text{-}95}$	$\Delta w_{20\text{-}30}$	$\Delta w_{30\text{-}50}$	$\Delta w_{50\text{-}70}$	$\Delta w_{70\text{-}95}$
Ads. cycle 1	9.3%	14.7%	26.5%	14.5%	8.8%	12.4%	12.8%	6.3%	5.3%	6.3%	12.0%	56.5%
Des. cycle 1	3.7%	7.6%	27.5%	30.8%	2.2%	5.6%	7.6%	16.1%	4.5%	11.4%	5.5%	88.1%
Ads. cycle 2	11.0%	15.8%	40.8%	35.1%	10.7%	13.6%	17.1%	20.5%	3.7%	5.6%	17.1%	84.4%
Des. cycle 2	3.3%	6.1%	40.4%	32.0%	2.8%	4.3%	13.8%	25.9%	4.6%	11.5%	4.5%	73.7%
Ads. cycle 3	12.5%	17.5%	53.4%	29.4%	12.0%	14.9%	21.8%	28.0%	3.2%	5.4%	20.4%	68.5%
Des. cycle 3	3.3%	5.2%	53.8%	23.1%	3.8%	3.8%	18.3%	29.0%	4.6%	11.2%	4.7%	58.6%
	SBA-15-6nm				**SBA-15-10nm**				**Silica Gel**			
Ads. cycle 1	7.4%	9.1%	5.8%	4.0%	5.4%	5.8%	3.2%	0.2%	2.0%	1.2%	1.5%	2.0%
Des. cycle 1	2.7%	2.0%	2.4%	10.1%	3.9%	1.3%	1.1%	0.4%	3.3%	3.1%	1.4%	1.5%
Ads. cycle 2	8.4%	8.7%	6.1%	13.0%	6.4%	4.3%	2.1%	0.3%	1.0%	1.5%	2.0%	2.6%
Des. cycle 2	3.7%	2.0%	2.4%	16.4%	3.9%	1.4%	1.1%	0.3%	5.4%	5.1%	1.5%	1.6%
Ads. cycle 3	8.5%	9.1%	6.5%	18.5%	6.6%	4.1%	1.7%	0.9%	-	-	-	-
Des. cycle 3	4.2%	2.6%	3.0%	20.5%	4.2%	1.4%	1.1%	0.6%	-	-	-	-
	MS-8.3				**MS-3.3**							
Ads. cycle 1	16.0%	36.4%	29.3%	15.1%	3.8%	6.7%	16.1%	12.1%				
Des. cycle 1	17.7%	68.3%	17.3%	4.1%	1.8%	1.3%	10.3%	21.8%				
Ads. cycle 2	11.2%	12.4%	30.2%	10.8%	2.4%	9.8%	8.7%	0.8%				
Des. cycle 2	19.1%	77.4%	11.2%	2.4%	4.7%	2.3%	13.3%	31.7%				

Table 5.6 – Average difference (%) between experimental and numerical *w* data for all desiccants materials, when modelling the kinetics of water vapour adsorption/ desorption for the three-cycle time-response test. The operational $\Delta\varphi$ ranges are those seen in Figure 5.5 and Figure 5.6.

5.6 Discussion

The results presented in Section 5.2 showed that the steepest gradient (within the adsorption branch of the isotherm) found in SBA-15 10 nm and MCM-41@150 – 165, occurred within a specific P/P_0 range; *e.g.*, P/P_0 = 0.74 – 0.80; 0.36 – 0.40; and 0.44 – 0.50, respectively. This suggests a well-defined pore structure in which the highest quantity of nitrogen adsorbed corresponds to the incremental pore volume (also refer to Figure 5.2). There appears to be that, in the case of SBA-15 6 nm and MCM-41@180, a wider pore size distribution, in contrast to a narrow distribution found in SBA-15 10 nm. This suggests that the steepness seen on the linear part of the adsorption isotherm may be related to the pore volume that corresponds to a particular range of pore diameters (refer to Figure 5.1). This is perhaps due to some slight pore size variation within the mesopore structure.

A low-pressure hysteresis phenomenon was observed in MS-3.3 when performing nitrogen adsorption/ desorption analysis (refer to Figure 5.1). This can be observed because the desorption branch did not coincide with the adsorption branch; *i.e.* the lower closing point for nitrogen (P/P_0 = ~ 0.42) was not achieved. This phenomenon was suggested by Silvestre-Albero *et al.*, (2012), and may have its origin in a technical issue with respect to the lack of equilibrium in the adsorption branch. The latter, due to restricted accessibility for nitrogen molecules at low pressures and temperatures, which disappear when adsorption equilibration times are increased.

In Section 5.3, some preliminary analyses were found when correlating water vapour desorption and nitrogen adsorption isotherms. These results suggested that the percolation threshold from water vapour isotherm (desorption branch) would eventually correlate with the upper limit of the nitrogen adsorption isotherm. The implications of this correlation would potentially enable determination of the pore size distribution using the water vapour desorption branch where the maximum incremental pore volume is found. This is particularly the case for those materials that possess a steep gradient over a narrow P/P_0 range in the N_2 adsorption branch; *i.e*. Type IV nitrogen adsorption isotherms, and where the pore-blocking effect corresponds with a Type V water vapour isotherm.

The results in Section 5.4 showed that, even though the $\Delta w_{50\text{-}70}$ range was higher for MCM-41@150 ($\Delta w_{50\text{-}70}$ = 179.5 kg/m^3) compared to MS-8.3 ($\Delta w_{50\text{-}70}$ = 129.5 kg/m^3), it can be suggested that the rapid-response observed for MS-8.3 was due to greater surface affinity with water molecules. This can be confirmed in the steeper gradient ($\Delta w_{50\text{-}65}$) for MS-8.3 compared with MCM-41@150, as seen in Figure 5.3 and Figure 4.1 (the latter, refer to Section 4.2), *i.e*. the onset of capillary condensation begins at φ = 0.65 and hence lowering the time-response for adsorption. It can be suggested that the 'phenomena' related to the lowering in response time for MS-8.3 (within the higher operational cycle, $\Delta\varphi$ = 0.7 – 0.95) would be necessarily due to the isotherm type (Type III). As presented in Section, 2.7.1, the maximum capillary potential, ψ occurs at the onset of capillary condensation, where clusters of water molecules begin to spontaneously aggregate each other to generate a condensed phase.

In Section 5.5 some indications of hysteresis were observed at higher operational $\Delta\varphi$ ranges in all desiccant materials. However, the scanning curves remain unidentified at this stage. Following the same logic, this may imply that a combination of both time-response (at lower operational $\Delta\varphi$ ranges) together with a hysteresis phenomenon and scanning curves (at higher operational $\Delta\varphi$ ranges) can operate independently and simultaneously. This may indicate that water vapour diffusion and liquid transport (capillary condensation and surface diffusion) may be independently controlled at both low and high operational $\Delta\varphi$ ranges.

5.7 Summary

1. Nitrogen physisorption was carried out in order to characterize the textural properties for the new MS desiccants (SBA-15 and MCM-41). Nitrogen adsorption/ desorption isotherms as well as specific surface area and incremental pore volume were obtained from BJH method.
2. The incremental pore volume for all MCM-41 materials clearly correlated with the pore size distribution shifting toward higher P/P_0 ranges, which was gradually reduced as pore wall thickness was increased (Thomann *et al.*, 2015b).
3. Preliminary analysis was conducted with the aim of determining a correlation between water vapour and nitrogen isotherms based on the assumptions of a pore-blocking effect. A good fitting agreement was found between the point that corresponded to the 'lower closing point', $\varphi_{,L}$ of the water vapour desorption isotherm and the point that corresponded to the onset of capillary condensation, $P/P_{0(L)}$ from the

nitrogen adsorption isotherm. This was also confirmed when matching both the percolation threshold, $\varphi_{,P}$ from the water isotherm and the upper limit, $P/P_{0(U)}$ from the nitrogen adsorption isotherm. The implications are that pore size distribution analysis from the Type V water vapour desorption branch could be enabled, when the pore-blocking effect is known to correspond to a reversible Type IV nitrogen adsorption isotherm.

4. It was found that a possible pore-blocking effect took place when analysing the time-response test, resulting in a significant increase in moisture content, w over the three-cycles. The accumulation effect of w, was preliminarily attributed to the presence of scanning curves within the hysteresis loop, which suggests that there is a dependency upon the pore size within an interconnected pore structure.
5. It was found that at higher operational φ ranges ($\Delta\varphi_{0.7\text{-}0.95}$), some materials (MCM-41) experienced high water vapour adsorption response, but also a high degree of hysteresis. This was attributed to the onset of capillary condensation together with the presence of scanning curves through the pore-blocking effect during the desorption cycles.
6. Some degree of water vapour adsorption/ desorption reversibility was found when comparing experimental and numerical simulation data, especially in those materials having Δw gradients that are sufficiently small; *e.g.* MCM-41@180 $\Delta w_{20\text{-}30} = 3.9$ kg/m^3 and $\Delta w_{30\text{-}50} = 9.3$ kg/m^3. This also suggested a rapid-response for adsorption/ desorption from the experimental data with a characteristic steep curve over the numerical data.

7. The underestimations from the numerical prediction were found to be mainly attributed to the lack of a dynamic input for *w*, but largely as a combined contribution from time-response together with a hysteresis phenomenon and scanning curves. This was evident, when analysing the significant differences (%) between experimental and numerical *w* data for all adsorption/ desorption cycles; *e.g.*, MCM-41@180 with 88.1% (adsorption) and 84.4% (desorption) in the $\Delta w_{70\text{-}95}$ range.

CHAPTER 6 Mesoporous desiccant optimization for energy efficiency of mixed mode HVAC systems

6.1 Overview

This Chapter presents the results that correspond to Stage 3, from the methodological scheme (refer to Figure 1.2), in order to address objective 5 (Section 1.3). This relates to the optimization and application of the hygrothermal modelling technique and includes:

1. Sensitivity analysis based on a series of relative humidity buffering simulations, in order to provide specification for the 'ideal' water vapour isotherm. A selection of desiccant materials gathered from literature and the ones synthesised in this study were assessed with respect to the kinetics of continuous moisture loads (Section 6.2.1) and their performance for water vapour exchange (Section 6.2.2).
2. Numerical simulations within a series of closed environments (*i.e.* specific operating limits), with the purpose to assess the desiccant's suitability for specific relative humidity buffering scenarios (Section 6.2.3).
3. Numerical simulations within a series of closed environments (Section 6.2.3), with the aim to assess the dehumidification performance of the desiccants based on an energy consumption case scenario. This was followed by the quantification of energy used for dehumidification loads and cooling demand in order to estimate the relative effect on energy efficiency when assisting a mixed mode HVAC system (Section 6.3)

6.2 Sensitivity analysis

6.2.1 Continuous moisture loads

Figure 6.1 shows the simulated results for all desiccant materials (refer to Figure 3.13 from Section 3.6.1), where three stages (related to the kinetics of water adsorption) were seen to occur as w reached EMC_{100}. The latter, indicated a connection with the specific portion of the water vapour isotherm and is represented in Figure 6.2 and Table 6.1. The first stage (sketched as a box with segmented lines in Figure 6.2b) was identified as an early saturation stage which was dependent on the corresponding φ values between points *a* and *b* and the Δw gradient from the schematic isotherm seen on Figure 6.2a. It was evident that having a small Δw gradient between points *a* and *b*, (where $w < 50$ kg/m^3 at different φ values at point *b*; *e.g*. MCM-41, Aerogel, KIT-1, and FSM-16), meant that a steep gradient was observed during the first 24 hrs. Conversely, those materials that possess a higher Δw gradient (between φ values *of* 0 and 0.5) during adsorption, as in the case of MIL-101, PS-C16-R, and SBA-15, resulted in a less steep curve and doubled the time taken to reach the 1st inflection point, denoted as *b* in Figure 6.2b. The second stage (sketched box in Figure 6.2b) was identified by having a particular sub-plateau portion of the adsorption curve between points *b* and *c*. This was characterized by stabilizing the indoor relative humidity, φ_i which was associated with the Δw gradient at the 2nd inflection point *c*, *i.e*. the top knee seen on Figure 6.2a. In other words, the slope of the sub-plateau was clearly related with the highest Δw gradient of the water vapour isotherm between points *b* and *c*. This meant that the indoor relative humidity was stabilised for a longer period of time.

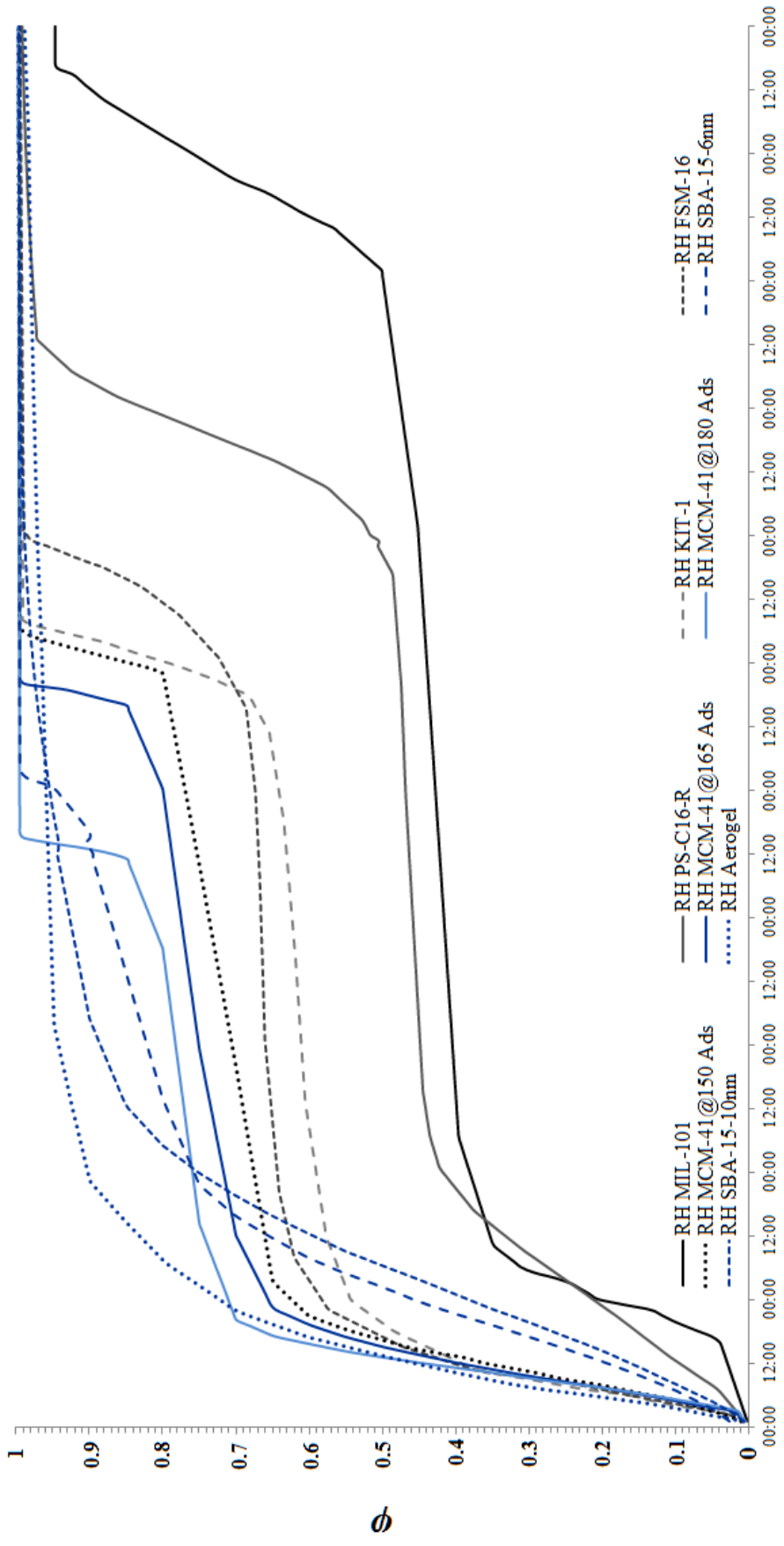


Figure 6.1 – Kinetics of continuous water vapour adsorption (against time) at the corresponding three stages (refer to Figure 6.2) for all desiccant candidates when achieving EMC_{100} (Thomann *et al.*, 2015a).

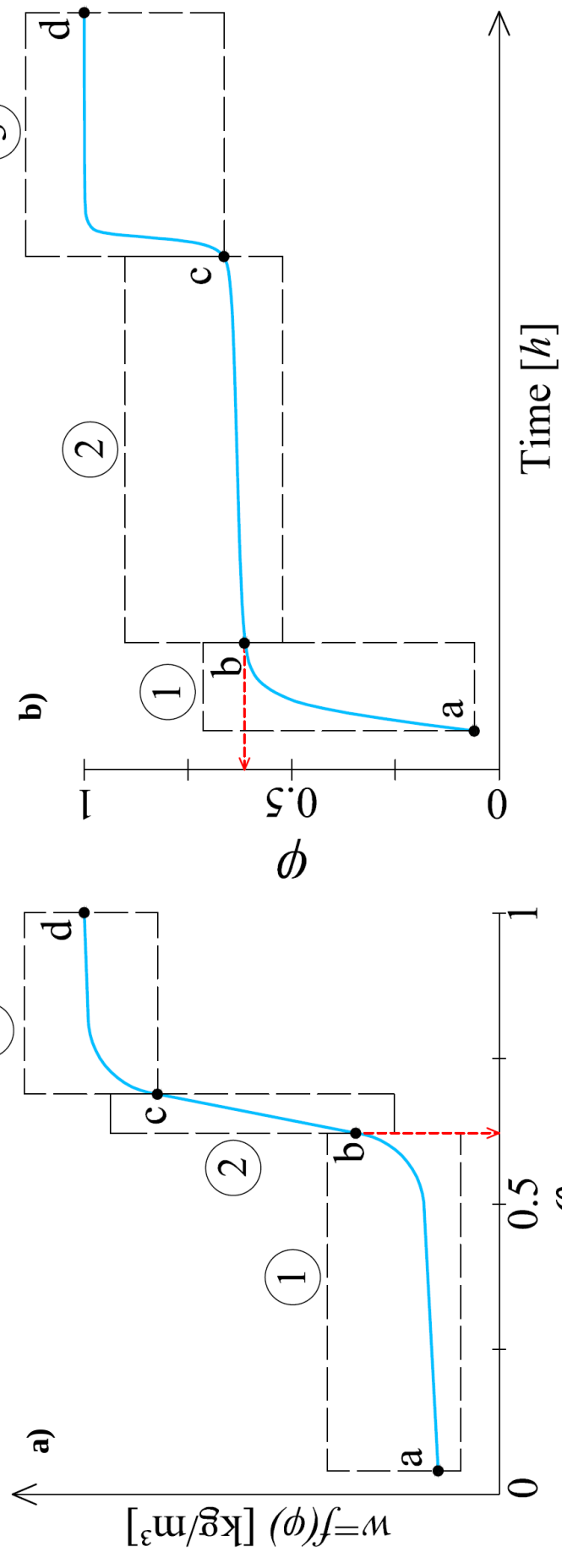


Figure 6.2 – a) Water vapour sorption isotherm portions within the three stages *a-b*, *b-c*, and *c-d*. b) Corresponding kinetics of water adsorption at different EMC stages *a-b*, *b-c*, and *c-d* that shows EMC in the segments 1, 2 and 3. From (Thomann *et al.*, 2015a).

Material	Moisture storage at Δw				Time
	φ_c	$\Delta w_{a\text{-}b}$	$\Delta w_{b\text{-}c}$	$\Delta w_{c\text{-}d}$	EMC_{100}
	(-)		(kg/m^3)		(hrs)
MIL-101	0.5	187.4	589.4	110.1	264+
PS-C16-R	0.52	217	403.8	140.1	264+
KIT-1	0.65	113.4	340.5	60.9	152
FSM-16	0.72	98	370.2	104	168
MCM-41@150	0.8	81.2	411.8	13.5	150
MCM-41@165	0.8	111.5	298.1	63.8	141
MCM-41@180	0.85	54.7	246.9	7.7	112
SBA-15-6nm	0.9	144.3	222.1	32.6	123
SBA-15-10nm	0.85	251.4	268.1	-	-
Aerogel	0.9	244.7	510.1	-	-

Table 6.1 – Moisture storage (Δw gradient) for the specific portions of the isotherm *a*-*b*, *b*-*c*, and *c*-*d*. Critical φ, (φ_c) where an inflection and a steep gradient after the sub-plateau before reaching EMC_{100}.

For most desiccant materials, this sub-plateau may be an indication of entering into a capillary condensation stage at point *b* from Figure 6.2a; *i.e*. onset of multilayer physisorption between (φ = ~ 0.35 – 0.90 – refer to Figure 3.13). The latter presents a prolonged stage for water vapour adsorption within a specific portion of the isotherm, which is associated with a steep moisture content gradient, Δw. This means that at some point an inflection in the curve must occur (point *c*), if not, this would imply that a prolonged capillary condensation (pore filling) stage is governed by liquid transport through capillary condensation at higher relative humidities (above $\varphi > 0.9$); *e.g*. as in the case of Type III isotherm materials Aerogel and SBA-15 10 nm.

The third stage between points *c* and *d* (sketched box in Figure 6.2b) was found to be followed by a rapid increase in the indoor relative humidity, φ_i towards EMC_{100}. This was especially seen in all Type V isotherm, where a critical φ value (φ_c) – refer to Table 6.1 – was described by an inflection and a steep gradient after the sub-plateau (point *c*). This perhaps, could be an indication that the

desiccants are nearly reaching capillary saturation within a critical pore radius (r_c), but in this case below $\varphi < 0.9$; *e.g*. MCM-41@150, $\varphi_c = 0.8$; MCM-41@165 and 180, $\varphi_c = 0.85$; FSM-16 and KIT-1, $\varphi_c = \sim 0.7$; MIL-101 and PS-C16-R, $\varphi_c = \sim 0.5$.

On the other hand, it was found that the time taken to reach the inflection point *d* towards EMC_{100}, not only depended on the progressive reduction in the Δw gradient between points *c* and *d*, but also was partially related to the previous Δw gradient between points *b* and *c*. Evidence of this is found when comparing MCM-41@150 and 165 ($\Delta w_{c\text{-}d}$ = 13.5 and 63.8 kg/m^3, respectively), as the time taken to reach point *d* is longer for MCM-41@150 (9 hours). A larger difference in the region $\Delta w_{b\text{-}c}$ (MCM-41@165, 113.7 kg/m^3) could be the reason, and would suggest that ultimately the final time taken to reach EMC_{100} would be associated with total pore volume. However in some cases, where isotherms resembled each other (*e.g*. KIT-1 and FSM-16), it was apparent that by having a greater value in the region $\Delta w_{c\text{-}d}$ the elapsed time before reaching EMC_{100} was significantly increased. This can be seen when comparing materials KIT-1 (152 hrs) and FSM-16 (168 hrs), both having similar Δw at $\varphi = 0.7$ (460 kg/m^3 – refer to Figure 3.13), but with the latter having a steeper *w* gradient which resulted in a higher Δw above $\varphi = 0.7$ (~ 44 kg/m^3).

6.2.2 Water vapour adsorption kinetics

Figure 6.3 shows the kinetics of the cumulative water vapour uptake for all desiccant candidates within the closed environment as described in Section 3.6.1. As with previous results (Section 6.2.1), the same correlations were observed between the three stages of the kinetics of water vapour adsorption

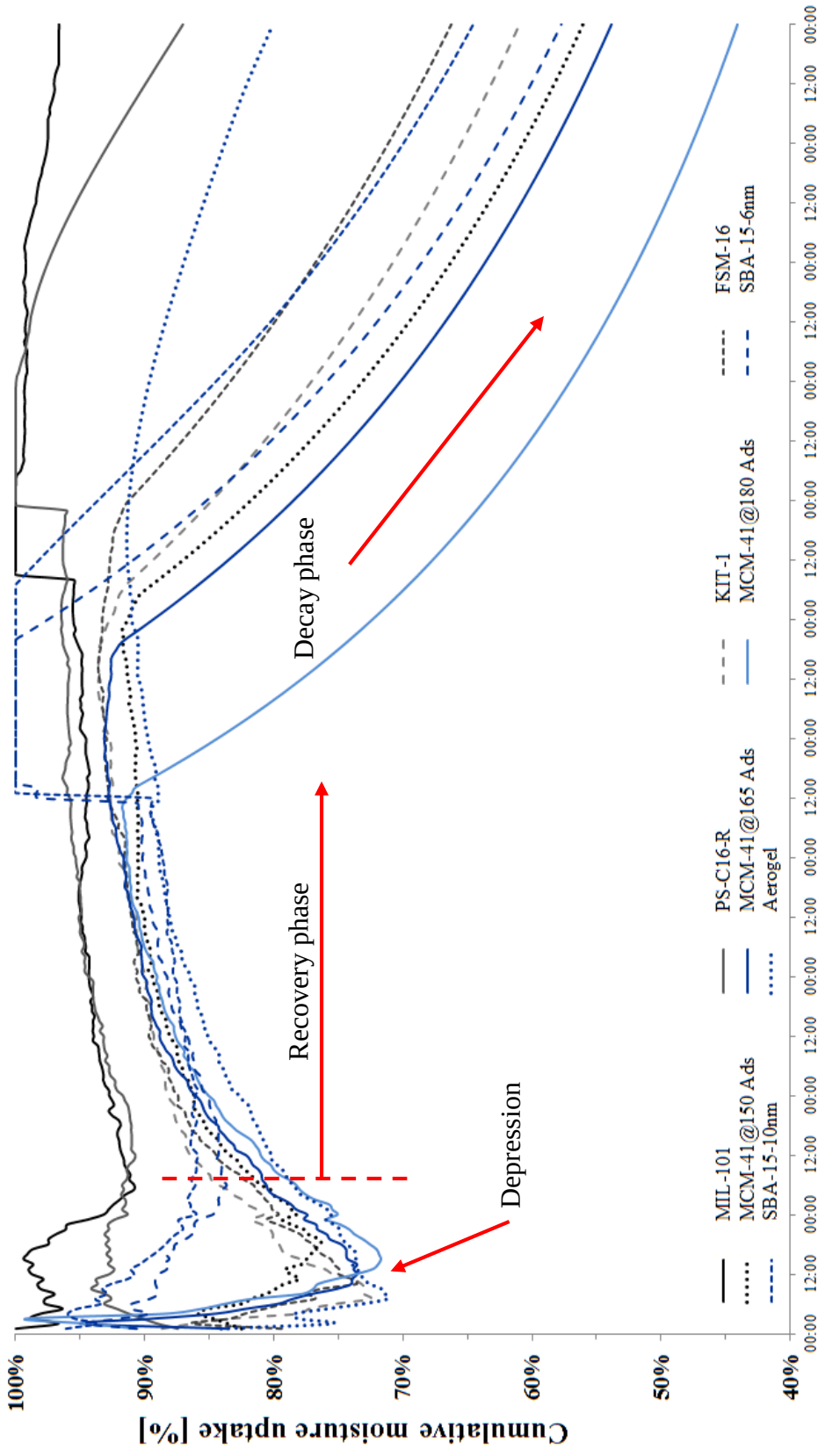


Figure 6.3 – Cumulative water vapour uptake for all desiccant candidates. Initial $w = 0$ for all desiccant materials and the moisture load applied is the moisture content of the infiltrated air at ACH = 0.35, where $\varphi_e = 0.95$ (Thomann *et al.*, 2015a).

and the corresponding portions of the isotherms (see Figure 6.2a). Considering the moisture loads applied, there appears to be a high initial water vapour uptake (relative to $w = 0$), which was followed by a reduction in the water vapour uptake performance (depression); *e.g*. MCM-41, KIT-1, FSM-16, and Aerogel.

Conversely, in those materials with higher initial Δw gradient between points *a* and *b* (*e.g*. MIL-101, PS-C16-R and SBA-15), the water vapour uptake performance was clearly enhanced (between 84% to 99%) within the first 24 h. Figure 6.3 also shows that the time taken to recover their performance (after the depression) was totally independent for each isotherm according to their Δw gradient between points *b* and *c*, as they reached point *c* at different times. At the recovery phase, it was observed for all materials that the gradual increment in their performance for water vapour uptake clearly correlated with the indoor relative humidity, φ_i stabilization in the sub-plateau seen on Figure 6.1. In the case of Type III materials (SBA-15 10 nm and Aerogel) this was not clearly associated as previously discussed in Section 6.2.1. It is then logical to assume that the highest Δw gradient between points *b* and *c* of the portion of the isotherm clearly corresponded to the optimum water vapour uptake performance. This latter point can be better understood following the results shown in Table 6.2. It can be suggested that once point *c* of the isotherm has been reached (especially Type V isotherms), so the maximum capillary potential for suction as well. Evidence of this can be seen when correlating the corresponding relative humidity ranges with the capillary transport coefficient of suction (D_{ws}) contribution at each portion of the isotherm (*i.e. a-b, b-c, c-d*).

Material	Contribution from the portion of the isotherm to D_{ws}			Corresponding operating φ range		
	$D_{ws(a\text{-}b)}$	$D_{ws(b\text{-}c)}$	$D_{ws(c\text{-}d)}$	$\varphi_{a\text{-}b}$	$\varphi_{b\text{-}c}$	$\varphi_{c\text{-}d}$
	(%)			(-)		
MIL-101	21.1%	**66.5%**	12.4%	0 - 0.39	**0.39 - 0.5**	0.5 - 1
PS-C16-R	30.6%	**54.8%**	14.6%	0 - 0.44	**0.44 - 0.52**	0.52 - 1
KIT-1	22.0%	**66.1%**	11.8%	0 - 0.58	**0.58 - 0.65**	0.65 - 1
FSM-16	24.8%	**62.8%**	12.5%	0 - 0.64	**0.64 - 0.72**	0.72 - 1
MCM-41@150	16.0%	**80.4%**	3.5%	0 - 0.65	**0.65 - 0.8**	0.8 - 1
MCM-41@165	13.5%	**73.0%**	13.5%	0 - 0.65	**0.65 - 0.8**	0.8 - 1
MCM-41@180	14.8%	**83.1%**	2.1%	0 - 0.7	**0.7 - 0.85**	0.85 - 1
SBA-15-6nm	36.2%	**55.7%**	8.2%	0 - 0.75	**0.75 - 0.9**	0.9 - 1
SBA-15-10nm	37.4%	**62.6%**	0.0%	0 - 0.85	**0.85 - 1**	-
Aerogel	18.8%	**81.2%**	0.0%	0 - 0.9	**0.9 - 1**	-

Table 6.2 – Capillary transport coefficient of suction (D_{ws}) contribution at each portion of the isotherm; where the operating ranges are associated with the specific portion of the isotherm seen in Figure 6.2.

Notice that for all materials (refer to column $D_{ws(b\text{-}c)}$), the greatest liquid transport within the capillary condensation stage corresponds as with the highest moisture content gradient, $\Delta w_{b\text{-}c}$ (refer to Table 6.1) between $\varphi_{b\text{-}c}$; *e.g.* MCM-41@150 and 180, 80.4% and 83.1%. It is interesting to notice that in the case of MIL-101, PS-C16-R and SBA-15, the $D_{ws(a\text{-}b)}$ contribution was substantially higher compared with the rest of the Type V materials (KIT-1, FSM-16 and MCM-41). This confirms that by having higher initial moisture content gradient, Δw between points *a* and *b* would eventually reduce the $D_{ws(b\text{-}c)}$ contribution; *e.g.* PS-C16-R, $D_{ws(b\text{-}c)}$ = 54.8%, also refer to Figure 6.1 and Table 6.1.

On the other hand, by comparing Figure 6.1 and Figure 6.3, and once point *c* has been reached, the moisture content associated was sufficiently high that the performance for water vapour uptake begin to decay. This also relates to the decline for $D_{ws(c\text{-}d)}$, which is clearly reduced in all Type V isotherm materials as seen in Table 6.2. Perhaps, this may be an indication of moisture content dependency at this stage, suggesting that at some point within the $\Delta w_{c\text{-}d}$ gradient,

this would lead to a capillary saturation stage towards $\psi = 0$, and therefore reducing the performance significantly for water vapour uptake (decay phase seen in Figure 6.3).

Figure 6.4a shows a positive linear correlation between total *w* and the water vapour being exchanged (against time) for all desiccant candidates. The results show that the linear correlation corresponds with the capability to exchange water vapour as *w* ascends (*i.e.* from MCM-41@180 to MIL-101). However, Figure 6.4b shows that no correlation was found between the moisture content, *w* and the time taken to exceed the upper indoor relative humidity limit, $\varphi_{i,U}$ ($\varphi = \sim 1$). It can be seen that for Type V isotherms this correlation is positive ($R^2 = 0.99$). Figure 6.4b also shows that when including the Type III isotherm (SBA-15 10 nm and Aerogel) a significant deviation from the linear trend line A was found, which resulted in $R^2 = 0.77$. This could be partially explained as the early stage of saturation (points *a* and *b*) causes an acceleration process for capillary condensation towards capillary saturation (above $\varphi > 0.9$), and therefore, reducing the elapsed time whilst reaching the total water vapour exchanged capacity.

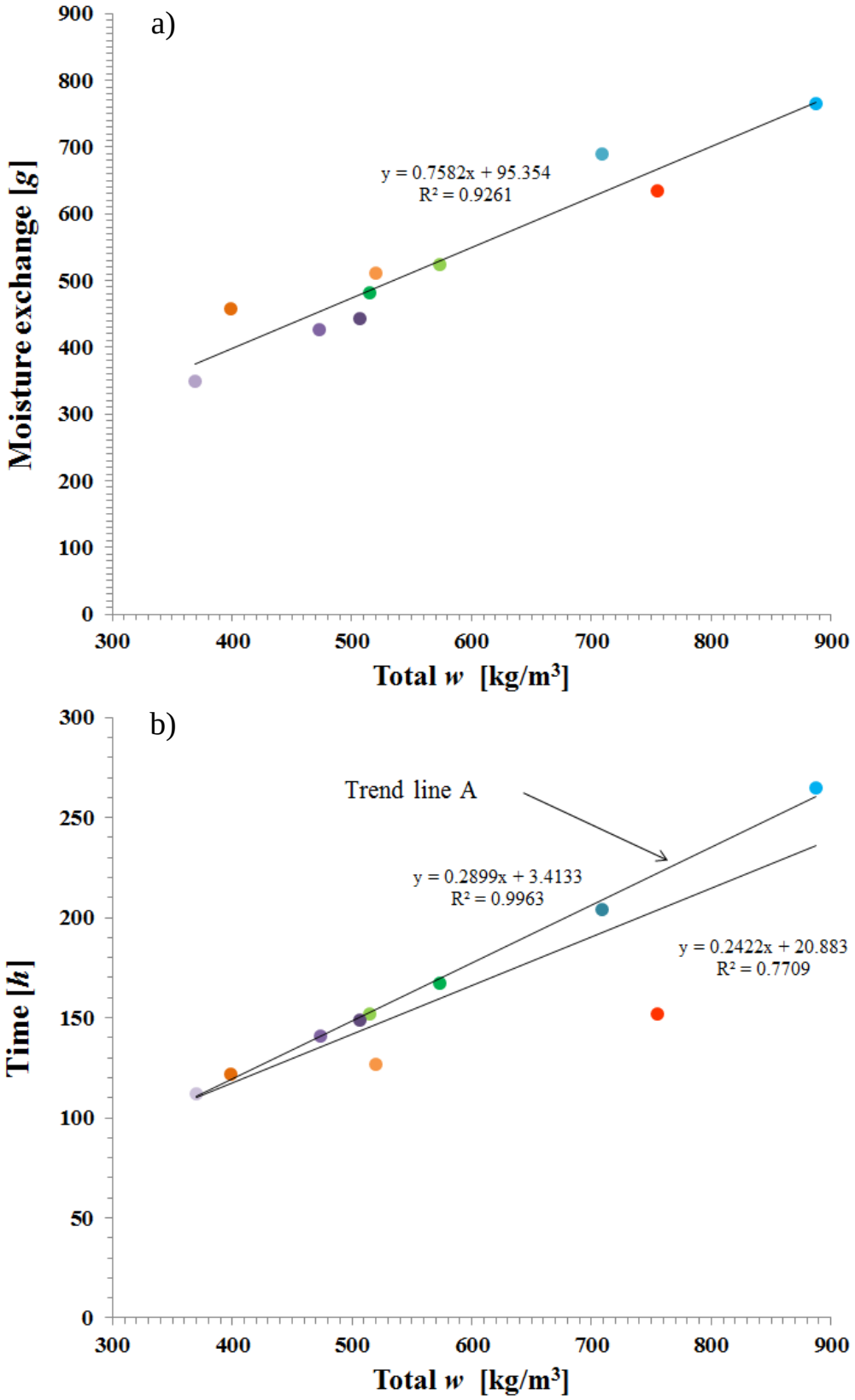


Figure 6.4 – a) Linear correlation between *w* and the and the water vapour being exchanged (against time). b) Relationship between total *w* and the time taken to achieve EMC_{100} (Thomann *et al.*, 2015a).

6.2.3 Sensitivity analysis for specific relative humidity buffering scenarios

Figure 6.5a–d shows the relative humidity buffering results for all desiccant candidates within the specific operating limits ($\varphi_{min} - \varphi_{max}$) in a repeated long-term loop cycling (at N = 12) as described in Section 3.6.2. In Section 4.5, an important premise was found regarding to the materials' suitability for specific relative humidity buffering applications and the corresponding Δw gradient between $\varphi_{i,L} - \varphi_{i,U}$ limits. It is then logical to assume that the early decay shown in most materials seen in Figure 6.5a–d correlates with the smaller Δw gradient within the operating range (refer to Figure 6.1 and Table 6.1) for that particular relative humidity buffering scenario. This sudden decay is consistent with the material's failure after N number of cycles when the fluctuation of $\varphi(t)$ exceeds the φ_{max} limit, and with the performance of water vapour uptake decay shown in Figure 6.3.

On the other hand, the most suitable desiccant can be clearly identified for each set of operating limits, *e.g.* MIL-101 and PS-C16-R, φ = 0.4 – 0.5; KIT-1 and FSM-16, φ = 0.6 – 0.7; MCM-41@150, 165 and 180, φ = 0.7 – 0.8. The criteria for suitability of the desiccants is also in agreement with the progressive decay for humidity buffering, as shown in Figure 6.6b, which is the time taken to exceed the upper limit (φ_{max}), when N = 12. Figure 6.6b also shows that for desiccants that last longer during decay, it was strongly related to the largest proportion of water vapour uptake capacity (Figure 6.6a). For example, MIL-101 and PS-C16-R desiccants showed the greatest water vapour uptake within the portion of the isotherm that correspond to φ = 0.4 – 0.5, which matches with the longest time taken to exceed the upper limit (φ_{max}) in 265 and 250 hours, respectively.

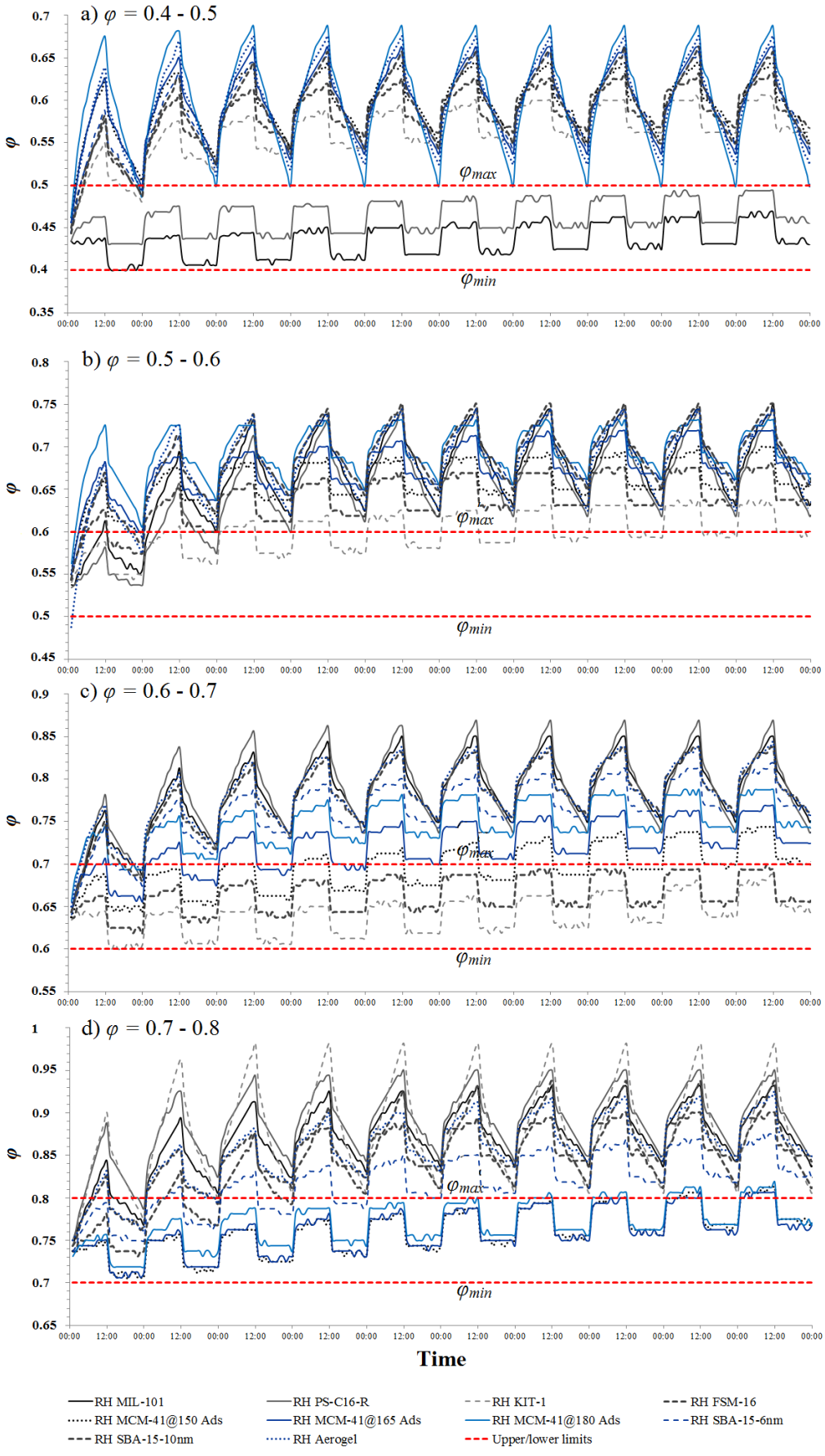


Figure 6.5 – Relative humidity buffering results for all desiccant candidates within the following operating ranges: a) φ = 0.4 – 0.5; b) φ = 0.5 – 0.6; c) φ = 0.6 – 0.7; d) φ = 0.7 – 0.8. The red-dotted lines correspond to the maximum and minimum relative humidity limits (Thomann *et al.*, 2015a).

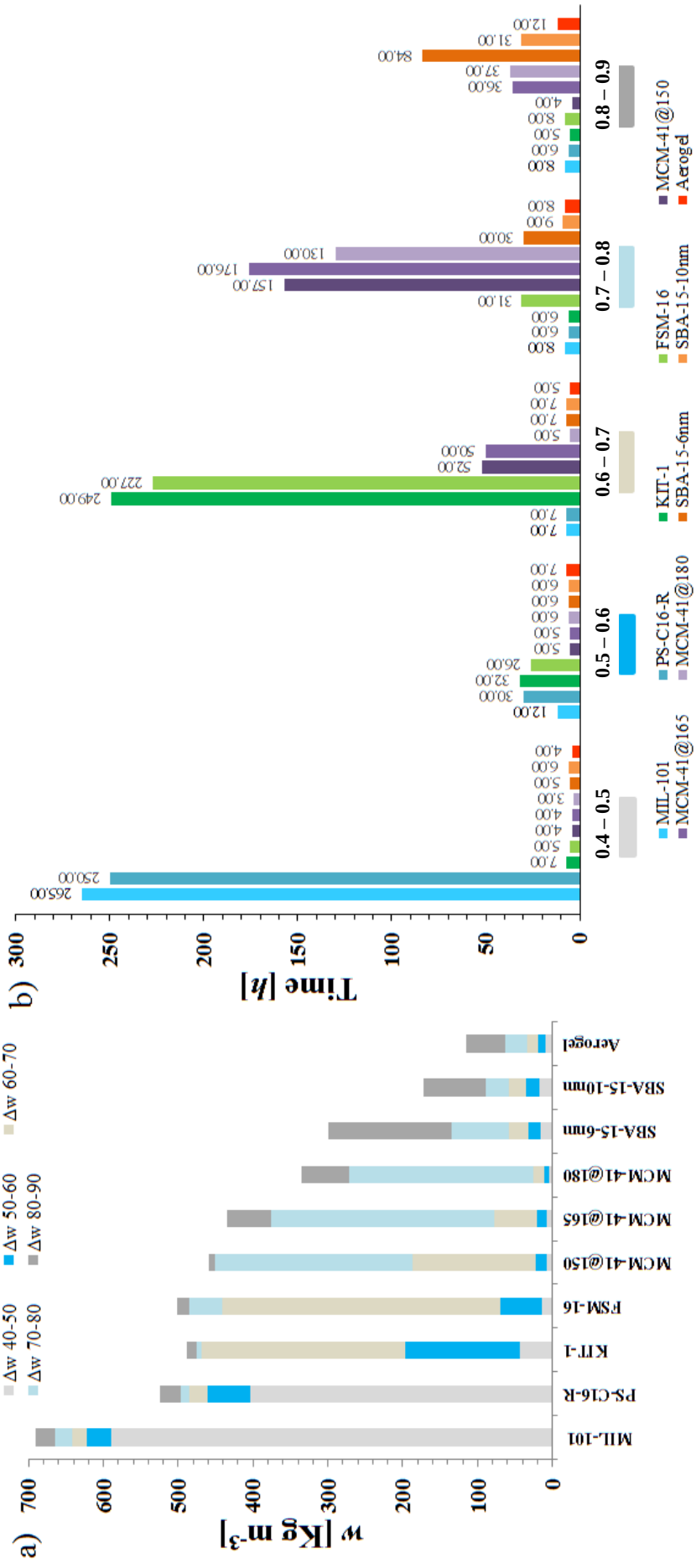


Figure 6.6 – a) Water vapour uptake capacity at different Δw for all desiccant candidates. b) Time taken for desiccant failure when the fluctuation of $\varphi(t)$ exceeds the φ_{max} limit; where Δw = 40 – 50; 50 – 60; 60 – 70; 70 – 80; and 80 – 90. This also correspond to the threshold when the materials reaches failure at the number of cycles, N = 12 (Thomann *et al.*, 2015a).

6.3 Air dehumidification and energy consumption

6.3.1 Dehumidification loads

Figure 6.7 shows the ratio between the moisture loads removed by the desiccants and the HVAC system (dehumidification), as described in Section 3.6.3. These were estimated once the upper set point, φ_{max} on the HVAC system was reached; *i.e.* the upper limit defined between the operating ranges: φ = 0.4 – 0.5; 0.6 – 0.7; and 0.7 – 0.8. In all cases this was found when analysing the steepness of the curve as it reached EMC. As previously described in Section 6.2.2, this could be an indication of (1) a small Δw gradient within a specific part of the isotherm (refer to Figure 6.6a), and (2) for the reduction in the water vapour uptake performance (refer to Figure 6.5). This also supports the assumption that all moisture loads were fully controlled (100%) by the HVAC system.

Conversely, the plateau seen along the *x*-axis in Figure 6.7a (at 0 %), means that all moisture loads were passively regulated by the desiccants, and dehumidification from the HVAC system was not needed. For most desiccants, once reaching the inflection point (*e.g.* red circles seen in Figure 6.7), the steepness of the curve clearly showed the moisture content, *w* dependency (Δw gradient) with respect to the operating range ($\varphi_{min} - \varphi_{max}$), and the desiccant's ability to cope with moisture loads. Hereafter, a gradual contribution from the HVAC system for air dehumidification began to operate, and therefore working in true mixed mode. This was consistent with the results shown previously in Figure 6.5, as point *c* of the isotherm was reached.

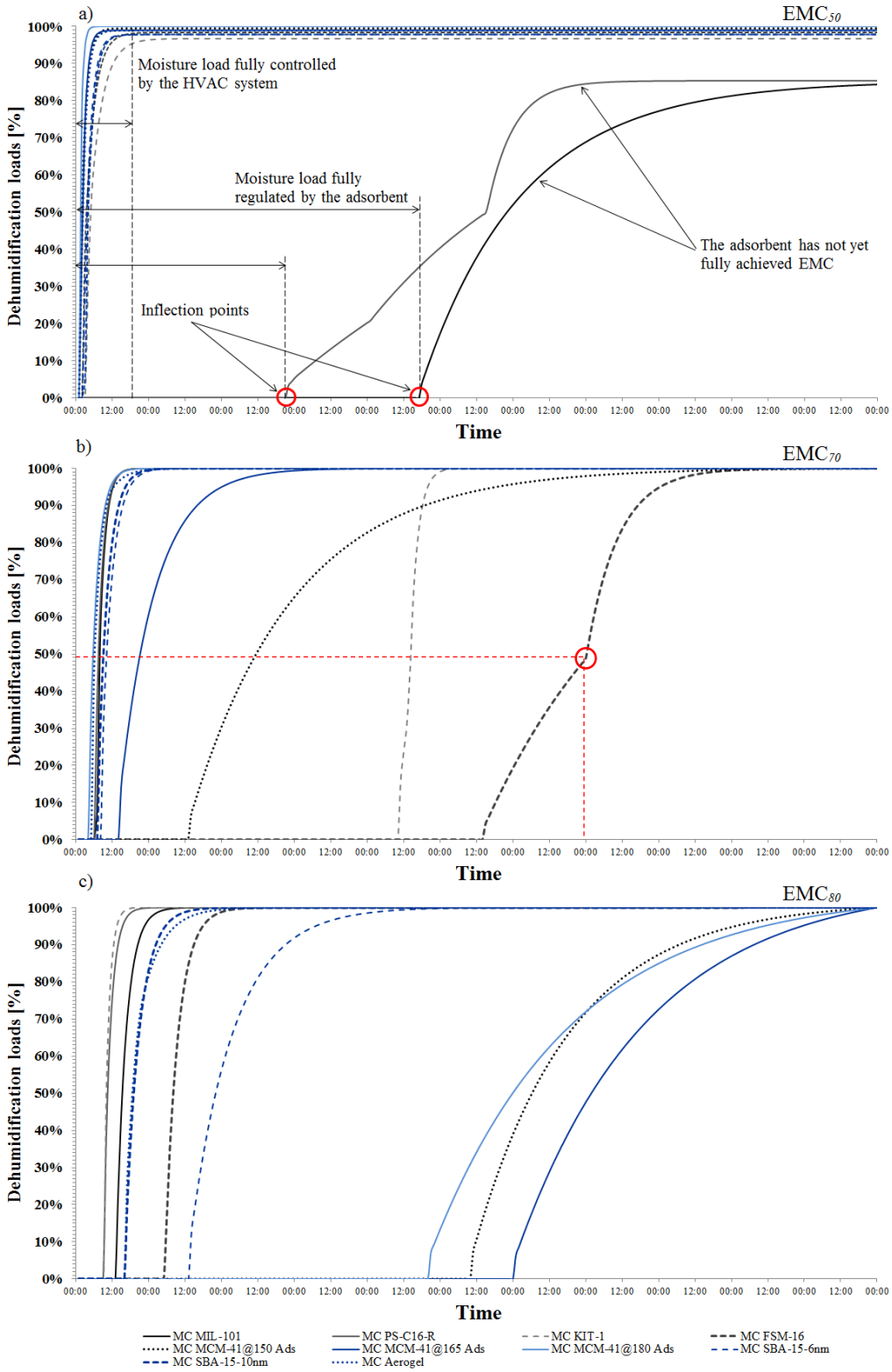


Figure 6.7 – Dehumidification ratio performed by the HVAC system and the desiccant candidates according to the operating φ ranges a) 0.4 – 0.5; b) 0.6 – 0.7; and c) 0.7 – 0.8. Here, 0% indicates that the desiccant candidate is fully regulating indoor relative humidity. Above 0% indicates that the HVAC system start to working in truly mixed mode. From (Thomann *et al.*, 2015a).

The efficiency of the mixed mode HVAC system is exemplified in Figure 6.7b, where FSM-16 desiccant presents a second inflection point (red circle at ~ 50% of efficiency) and a steeper portion of the curve towards EMC_{70}. This perhaps suggests that the slight change in the water vapour sorption isotherm (refer to Figure 6.1) between φ = ~ 0.66 – 0.7, triggered a sudden decay in moisture removal. In practical terms, this could also be an indicator for re-setting the system into a degassing stage of the desiccant for re-use. Notice that in Figure 6.7c, all MCM-41 desiccants showed similar performance curves. This may also suggests that the steepness of their water vapour isotherm (within the maximum theoretical pore volume between $\varphi_{i,U}$ and $\varphi_{i,L}$ limits) is strongly related to it, as the adsorbed water vapour is continuously building-up (also refer to PS-C16-R in Figure 6.7a). Conversely, it seems that the steep curve showed in Figure 6.7b (KIT-1) followed a rapid increase in the indoor relative humidity, φ_i towards EMC_{70}. This is in agreement with kinetics of water vapour adsorption seen at the third stage between points *c* and *d* of the isotherms, as described in Section 6.2.1; *i.e.* the desiccant is entering into a capillary saturation stage. This same principle was followed by all desiccants in which the operating range was not optimized for their Δw gradient. In all cases, it was recognized that the higher elapsed time before starting the inflection of the curve corresponded to the desiccant's best performance that fits within their optimum operating ranges as described in Section 6.2.2; *e.g.* MIL-101 and PS-C16-R (φ = 0.4 – 0.5), MCM-41@150, KIT-1, and FSM-16 (φ = 0.6 – 0.7), and all MCM-41 types (φ = 0.7 – 0.8) – compare with Figure 6.6a.

Figure 6.8 shows the comparison between the resultant indoor $\varphi(t)$ and the material's $\varphi(t)$ at different operating ranges for desiccant materials MIL-101,

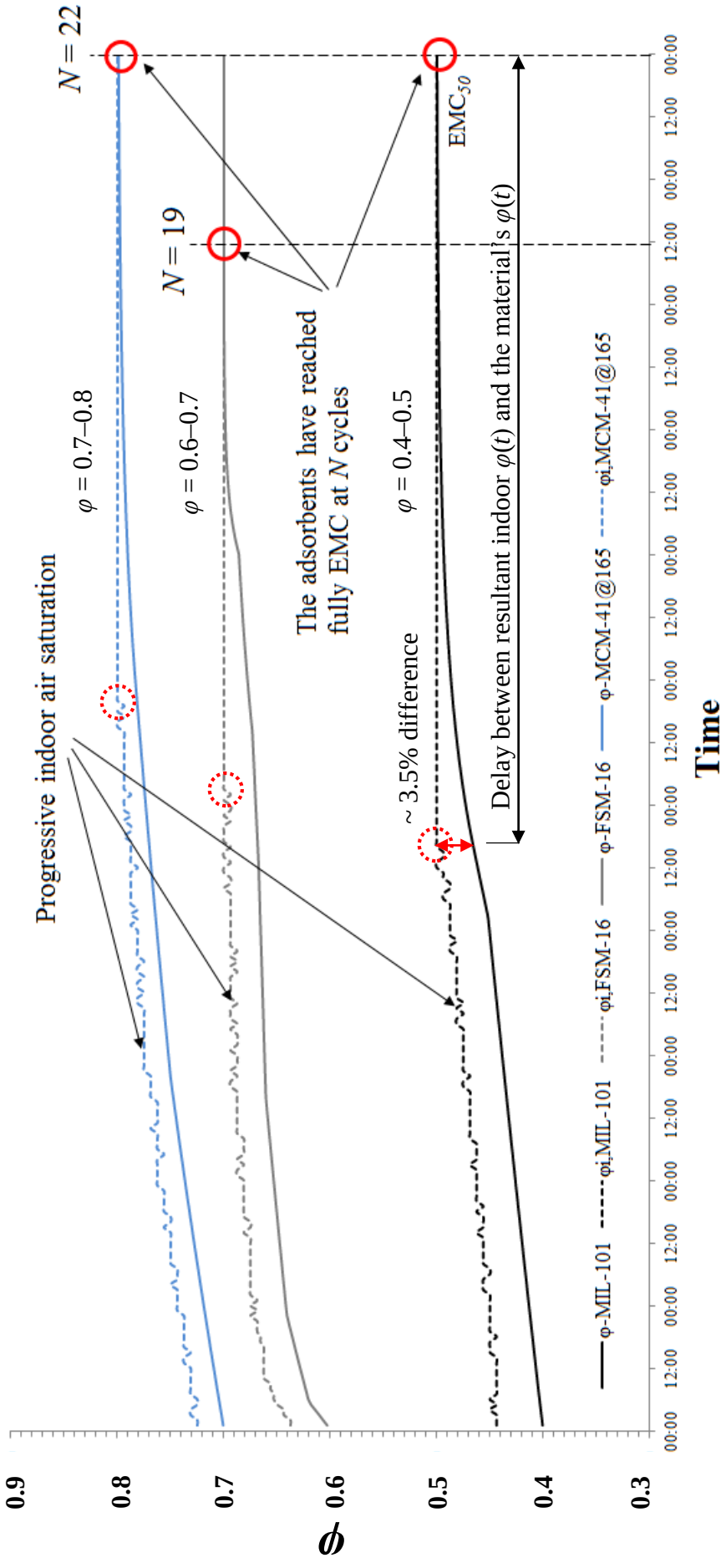


Figure 6.8 – Comparison between the resultant indoor $\varphi(t)$ and the material's $\varphi(t)$ at different operating ranges for desiccant materials MIL-101, FSM-16 and MCM-41@165. The offset dotted-lines represent the progressive indoor air saturation towards equilibrium with the desiccant at the respective ACH. The total number of cycles, N = 22 and the red circles represents when the desiccants have been reached EMC at the corresponding operating $\boldsymbol{\varphi}$ ranges.

FSM-16 and MCM-41@165. A significant difference in the resultant (buffered) indoor relative humidity, φ_i was found in all simulations, suggesting that the desiccant appears not to have achieved EMC (*i.e.* $EMC_{50;70;80}$). As a result, a distinctive offset (delay) between both curves was observed, where it can be suggested that: (1) there is a strong influence from the water vapour adsorption rates (time-response), perhaps derived by *A* and the vapour diffusion resistance coefficient $\mu(\varphi)$ within the numerical model, and hence, (2) causing the delay time in achieving EMC. In other words, the desiccant may continue adsorbing water vapour whilst the HVAC system is dehumidifying the indoor air as the φ_{max} set point had not been reached; and hence started to operate in mixed mode at an early stage. This small relative humidity variance was sufficient in the case of PS-C16-R (~ 3.5%) and resulted in lowering the time taken to remove moisture for more than 50% (compare the dashed and continuous red circles from Figure 6.8, and the red circles from Figure 6.7a).

6.3.2 Energy consumption for air dehumidification

Figure 6.9 shows a positive linear correlation between the latent heat used for air dehumidification and the moisture content gradient, Δw capacity, for each pair of operational φ limits; *e.g.*, the light blue box corresponding to φ = 0.5 – 0.6 (refer to Section 3.6.3). It can be seen that each trend line corresponds to the aggrupation of all desiccants when air dehumidification was performed by the HVAC system. It was found that this satisfactorily proves that full control of the relative humidity fluctuations within a specific closed environment can be passively regulated by desiccants with high Δw gradients at the appropriate range.

Consistent agreement between the latent heat of air dehumidification and the decay up to material failure was also found, which confirmed the desiccant's suitability for specific operating ranges. Evidence of this is presented in further results for each specific operating range shown in Figure 6.10. This revealed that the energy consumption for removing the excess in dehumidification loads by the HVAC system were strongly related to those desiccants with higher Δw gradients, and hence corresponding to those that fit within the optimum operating ranges as previously identified in Figure 6.6b.

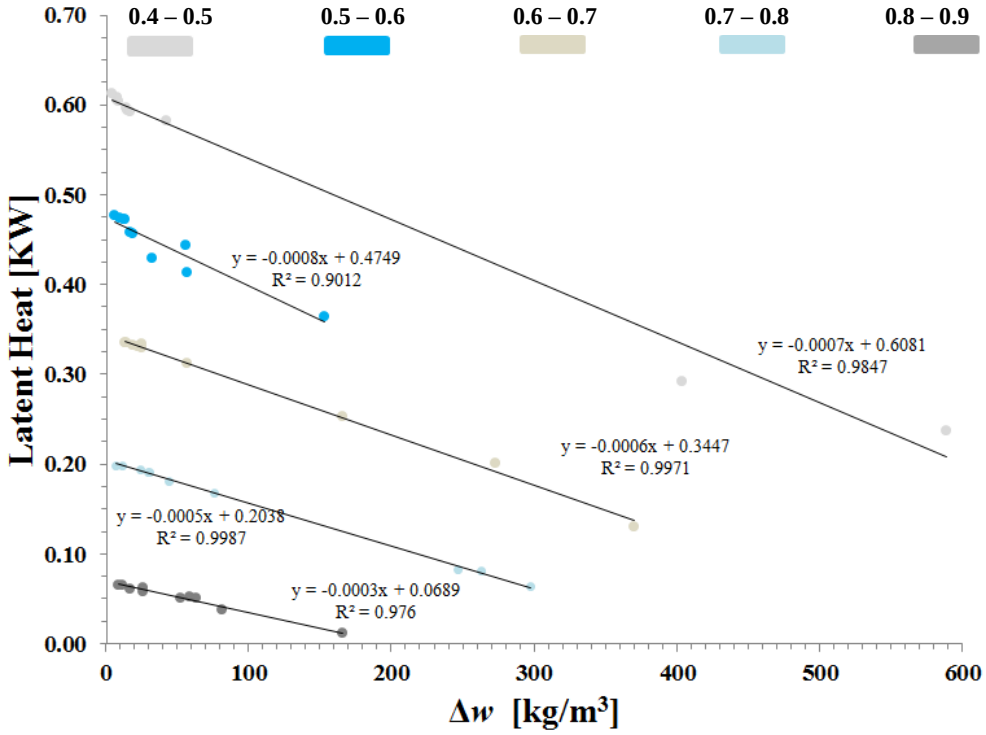


Figure 6.9 – Correlation between moisture sorption capacity and the latent heat used for air dehumidification from the HVAC system at the corresponding operating ranges (φ = 0.4 – 0.5; 0.5 – 0.6; 0.6 – 0.7; 0.7 – 0.8; 0.8 – 0.9). Each trend line correspond to the aggrupation of all desiccant candidates when performing the air dehumidification through the HVAC system. (Thomann *et al.*, 2015a).

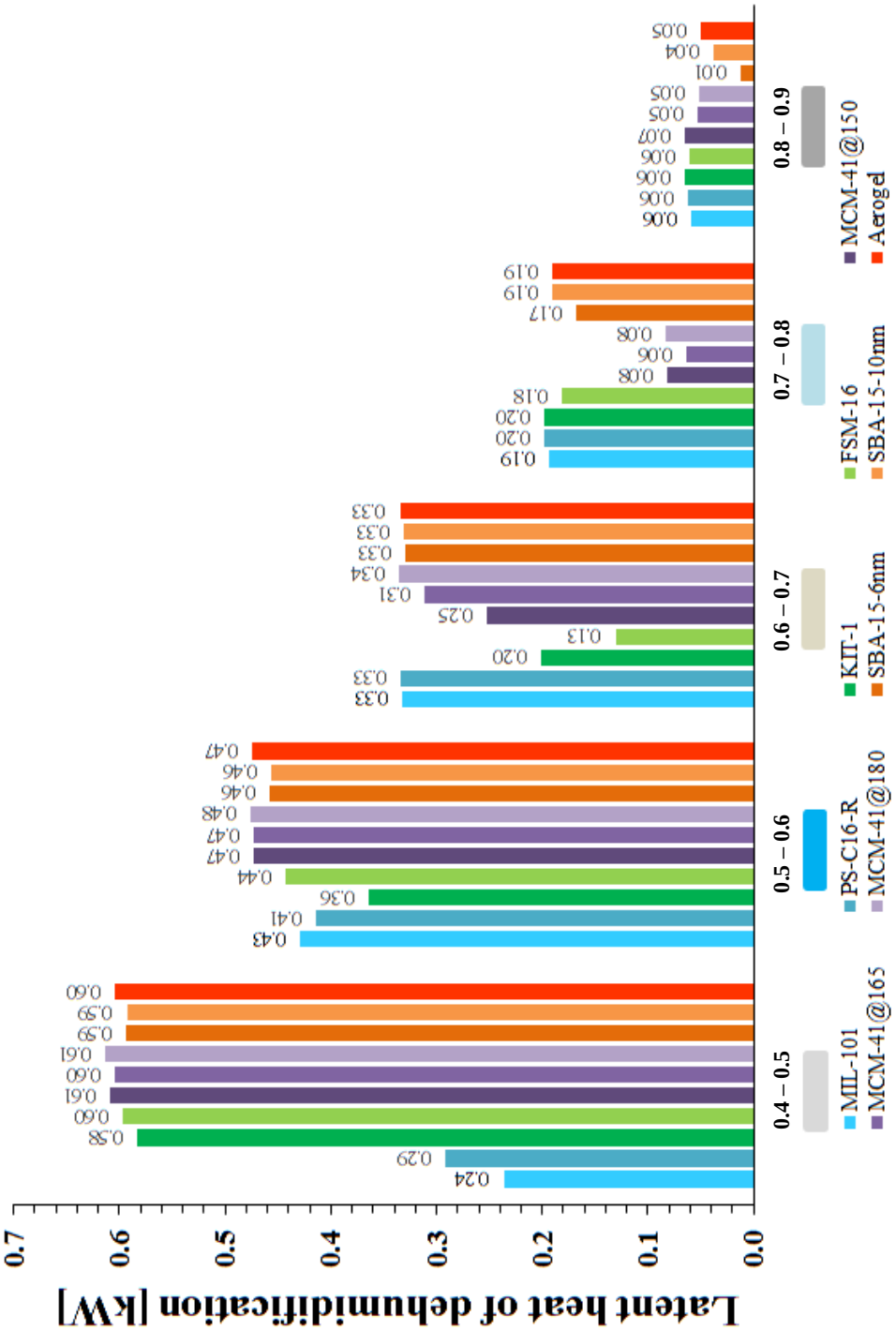


Figure 6.10 – Latent heat of dehumidification comparison among all desiccant from the HVAC system at the corresponding operating ranges (φ = 0.4 – 0.5; 0.5 – 0.6; 0.6 – 0.7; 0.7 – 0.8; 0.8 – 0.9).

Although the desiccant's suitability for specific operating ranges was previously confirmed, when it comes to analyse the desiccant's overall energy consumption performance, there appear to be some limitations. Figure 6.11 shows the total energy used for air dehumidification (latent heat) including the energy used for cooling purposes (see light-blue hatched boxes in Figure 6.11a). It seems that in order to maintain isothermal conditions (T_{dbi} = 23 °C), some desiccants (MIL-101 and PS-C16-R) exhibited a significant contribution to total energy consumption by using the cooling mode in the HVAC system (0.22 and 0.16 kW respectively – light-blue hatched boxes seen in Figure 6.11a). This was attributed to a slight increment in the resultant air temperature when performing relative humidity buffering for the operating range, φ = 0.4 – 0.6; most likely due to heat of adsorption effects.

In most operating ranges (refer to Figure 6.10, *e.g.* 0.4 – 0.5) for Type III isotherms (SBA-15 10 nm and Aerogel), there is a slight but significant increment in the overall energy consumption. As presented in Section 6.2.2, this may be affected by the accelerated process of capillary condensation towards capillary saturation, which showed an early saturation stage within the portions of the isotherm (refer to points *a–c* from Figure 6.1), and thus lowering their performance for air dehumidification. This can be seen in Figure 6.11b, where no correlation trend (R^2 = 0.2706) was found between total moisture storage, *w* and total latent heat for air dehumidification.

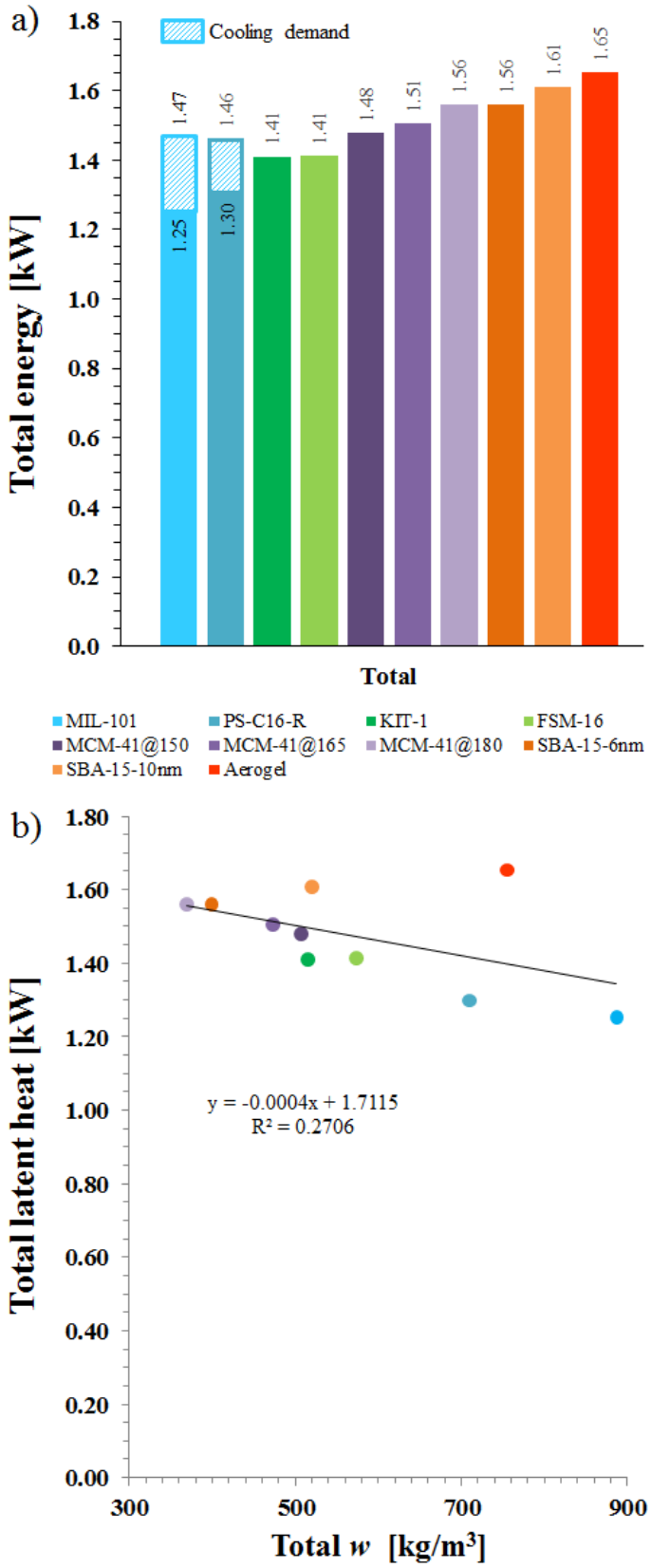


Figure 6.11 – a) Total energy used for air dehumidification for all desiccant candidates. In the case of materials MIL-101 and PS-C16-R, a cooling demand is represented by the hatched box above the values. b) Non-linear correlation between total moisture storage, *w* and total latent heat for air dehumidification. Type III isotherms can clearly be recognized as the precursors of this non-linear trend as their total moisture content, *w* do not correlate with the total energy used for air dehumidification and cooling loads, resulting in $R^2 = 0.2706$. From (Thomann *et al.*, 2015a).

The latter may indicate that having higher w does not result in lowering the energy used for dehumidification purposes when assuming total pore volume capacity. This was evident when comparing the total energy used for desiccant having Type III and V isotherms; *e.g.* MCM-41@180 (1.51 kW and w = 369.4 kg/m^3) and Aerogel (1.65 kW and w = 754.8 kg/m^3), the latter one having $w \sim 2$ times higher compared with MCM-41@180.

6.4 Future work

6.4.1 Material's regeneration for re-use within specific operating ranges

Figure 6.12 shows the applicability of the model, when the desiccant is desired to be re-used through a regeneration process by degassing it at certain temperature. In this scenario, it has been assumed that the portion of the water vapour isotherm to be degassed is the one that corresponds to the maximum theoretical pore volume between $\varphi_{i,U}$ and $\varphi_{i,L}$. In the same logic, this would also represent the highest Δw gradient (maximum moisture storage capacity). As indicated in Figure 6.12, this accounts for 61% of this hypothetical water vapour isotherm with Δw = 385 kg/m^3. This also suggests that a positive offset in energy used at the degassing stage (material's regeneration for re-use), could be significantly increased if considering the defined steepness of the Δw gradient in which the maximum pore volume is found (light-blue line between points *b* and *c*). For example, if considering the description from the previous energy consumption analysis seen in Section 6.3, where the ratio between the moisture loads removed by the desiccants and the HVAC system were estimated.

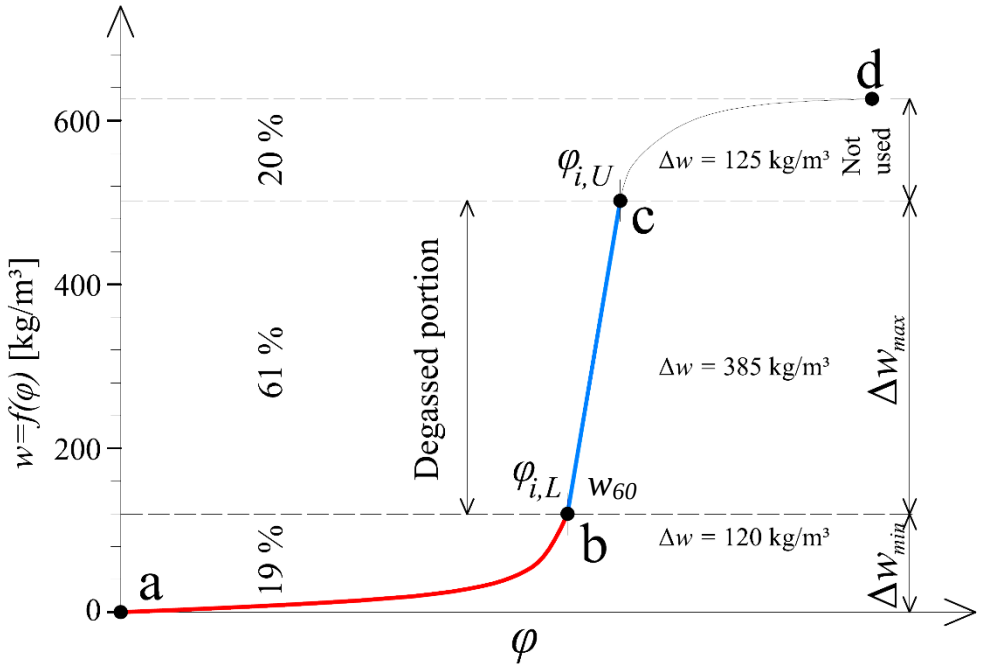


Figure 6.12 – Schematic representation of desiccant's regeneration. Water vapour isotherm degassing process for re-use between points *c* and *b*; this corresponds to the maximum theoretical pore volume between $\varphi_{i,U}$ and $\varphi_{i,L}$. The red portion line between points *a* and *b* is not degassed, and the portion above point *c* (percolation threshold) not used.

The same set point (φ_{max}) on the HVAC can be used as a reference for the desiccant's regeneration for specific applications within closed environment scenarios. In order to assimilate the real benefit, the operational (desiccant's degassing at certain temperature) and saving (moisture loads fully regulated by the desiccant, and not by using an HVAC system) costs need to be compared. This may imply, for example, that if w_{60} is required (see light-blue line in Figure 6.12) as the lower moisture content limit (rather than full desorption at $w = 0$: see red line in Figure 6.12) for the degassing process, the operational cost could eventually be reduced. This can only be beneficial if the operational costs by partial degassing from the desiccant are lower (or a fraction) than the benefits generated by the passive moisture loads regulation. At this stage, further research is needed in order to establish the water adsorption/ desorption affinity with surfaces at their different water vapour adsorption stages (points 1 to 3 in Figure

6.2) and its relationship with the energy used (regeneration temperature) at different operating φ ranges.

6.5 Discussion

From Figure 6.1, some implications were drawn from the continuous water vapour adsorption with respect to a small Δw gradient between points *a* and *b* of the water vapour isotherm; *i.e*. the φ values. The latter implying that some desiccant materials would be unsuitable for relative humidity buffering applications below specific points of their isotherm; *e.g*. MCM-41@180, φ = ~ 0.7; MCM-41@165, φ = ~ 0.6; and KIT-1, φ = ~ 0.48. On the other hand, the greater amount of physisorbed water vapour for MIL-101 and PS-C16-R may be partially attributed due to high surface areas and increased adsorbate/ adsorbent site interactions, and hence the increase of adsorbed water monolayers.

When analysing the results provided in Figure 6.1, it also confirmed the hypothesis (refer to Section 3.1) that the best performance for water vapour adsorption is related to the maximum allocation of pore volume within the linear portion of the isotherm between $\varphi_{i,L}$ and $\varphi_{i,U}$. In the same logic, it was found that the slope of the sub-plateau seen on Figure 6.1 may define the steepness (between $\varphi_{i,L}$ and $\varphi_{i,U}$) of the Δw gradient within the sorption isotherm. The latter, resulted in the stabilization of the indoor relative humidity, φ_i for a longer period of time, before reaching the onset for rapid increase in the indoor relative humidity towards EMC_{100}.

On the other hand, it was found that for those materials having Type III isotherms (Aerogel and SBA-15 10), the kinetics of water adsorption at the third stage and the inflection towards point *d* (EMC_{100}) were not clearly associated. This could

be explained as *w* is gradually increasing and is sufficiently high that the transition between capillary condensation towards a state of pore saturation or critical moisture content (w_c) becomes unnoticed; after this stage losing its capillary potential (ψ) for liquid transport (Künzel, 1995; Hall, 2010).

From Section 6.2.2, the reduction of the water vapour uptake performance corresponded to those desiccant materials with the smallest Δw gradient between points *a* and *b*. This may indicate that an early saturation stage between points *a* and *b* can be also related to a lower affinity for water vapour adsorption or the presence of weak adsorbent-adsorbate interactions, which results in pore filling at higher vapour pressure. This could suggest that the enhanced process for the kinetics of water vapour exchange can be attributable to the efficient use of their maximum capillary potential for suction, combined with strong adsorbate-adsorbate interactions; *i.e.* capillary condensation through large self-stabilized water cluster formation (also refer to Section 2.7.1). Therefore, indicating the use of their maximum pore volume capacity within the highest Δw gradient (specifically between points *b* and *c* – refer to Figure 6.1) whilst performing a capillary condensation stage driven by their maximum capillary transport potential, D_{ws} before reaching capillary saturation.

From Section 6.3.1, it was found that the efficiency of the mixed mode HVAC system was clearly related to the desiccant's performance for moisture removal, and found a strong dependency with the Δw gradient with respect to the operating limits ($\varphi_{min} - \varphi_{max}$). Conversely, for those having a smaller Δw gradient, a distinctive early decay for removing the moisture loads was shown, and hence all moisture loads were controlled by the HVAC system.

In the same logic, the results provided in Section 6.3.2 clearly showed that the suitability of the desiccants to operate within specific operating ranges ($\varphi_{min} - \varphi_{max}$) was strongly related to the Δw gradient between those ranges. The latter was found to have a positive linear correlation between the latent heat used for air dehumidification and the decay of their performance, with respect to the Δw gradient. However, this was not seen when analysing the total energy consumption (latent heat for air dehumidification and energy used for cooling demand) for all types of desiccants, specifically for those having Type III isotherms. This could be explained as those desiccants have their maximum theoretical pore volume at higher φ limits (above $\varphi = 0.9$), which also means that they would not use all the available moisture storage capacity, Δw for relative humidity buffering. Therefore, no correlation was found (*e.g.* $R^2 = 0.2706$ in Figure 6.11b) between total moisture storage, w and total latent heat for air dehumidification.

6.6 Summary

1. A series of numerical simulations (refer to Section 3.6) were conducted with the aim of assessing desiccant suitability for regulating specific indoor relative humidity conditions, and to provide specification of the 'ideal' water vapour isotherm.
2. It was found that the three stages of the kinetics of water adsorption corresponded to a specific portion of the isotherm (points *a* to *d*, seen in Figure 6.2). The prolonged time for stabilizing the indoor relative humidity, φ_i was particularly seen in those desiccants that possessed a higher Δw gradient between $\varphi_{i,L} - \varphi_{i,U}$ limits and also points *b* and *c* from

Figure 6.2; most likely due to the beginning of a capillary condensation stage. After point *c*, a rapid increase in the indoor relative humidity was found. This can be related to liquid transport leading to a capillary saturation stage. This behaviour was particularly prominent in Type V isotherms, and in some cases below $\varphi < 0.9$ (*e.g.* FSM-16 and KIT-1, $\varphi_c = \sim 0.7$), which may indicate that most of the total pore volume has been filled with water vapour with respect to a critical pore radius (r_c).

3. The water vapour uptake performance was clearly enhanced in desiccants with higher Δw gradients between $\varphi_{i,L} - \varphi_{i,U}$ limits, partially contributed to by a greater capillary potential. After reaching point *c*, the desiccant's performance for water vapour uptake decayed, perhaps, due to entering into a capillary saturation stage and towards $\psi = 0$.
4. It was found that the ratio between the moisture loads removed by the desiccants and the HVAC system was strongly related to the three stages of the kinetics of water adsorption, which are referred in Figure 6.7. The desiccant's suitability for removing the indoor moisture loads was found to correlate with those that possess the highest Δw gradient within specific operating ranges (between φ_{max} and φ_{max}). In most cases, this meant passive regulation of the moisture loads before the dehumidification from the HVAC system took place; *i.e.* working in true mixed mode.
5. A distinctive offset (delay) was found between the resultant (buffered) indoor humidity variation over time, $\varphi(t)$ and that of the material, which resulted in early operation during mixed mode operation with an HVAC system. It was suggested that this may originate from the assumptions

within the numerical model for the water vapour adsorption rates (time-response) derived by A and the diffusion coefficient $\mu(\varphi)$ values.

6. A positive linear correlation was found between the latent heat used for air dehumidification and the Δw gradient, confirming the desiccant's suitability for specific operating ranges, whilst passive regulation of the moisture loads were controlled by consuming less energy.
7. No correlation was found between total moisture storage, w and total latent heat for air dehumidification, and found that Type III isotherms were affected by a significant increment in the overall energy consumption. This can be explained, since their maximum theoretical pore volume between $\varphi_{i,U}$ and $\varphi_{i,L}$ was not used, showing an early saturation stage. The latter was confirmed by the lower performance for air dehumidification, which may be attributed to an accelerated process of capillary condensation towards capillary saturation ($\varphi > 0.9$). Therefore, having a greater total pore volume (higher capacity for moisture storage) does not always imply lowering the energy consumption for dehumidification purposes, particularly when analysing total energy consumption between Type III and V isotherms.
8. Some desiccants presented a significant energy consumption contribution using the cooling mode from the HVAC system, which was mainly due to a slight increase in the resultant air temperature whilst performing relative humidity buffering. This was probably due to the heat of adsorption, and found to be within the operating ranges $\varphi = 0.4 – 0.6$ for desiccants MIL-101 and PS-C16-R.

9. Expanded theoretical application of the model can be conducted when desiccant's regeneration for re-use is desired. Some advantages may suggest further energy consumption reductions when considering: (1) the energy consumed when performing a partial degassing stage (rather than full desorption), and (2) the expected energy consumption savings when fully regulation of moisture loads is performed by the desiccants; whilst the HVAC system is not being used. The true benefit would be the comparison of the operational costs from the above mentioned points.

CHAPTER 7 Discussion

A hygrothermal modelling technique that enables top-down predictive design of ideal water vapour sorption isotherms has successfully been developed, based on the hypothesis described in Section 3.1. The results provided in Chapter 4 enabled the calibration and operation of the hygrothermal modelling technique. This meant that a principle could be established for designing ideal water vapour isotherms for humidity buffering applications within defined operating limits, $\varphi_{min} - \varphi_{max}$. In terms of the decay in humidity buffering behaviour during fluctuation of the function, $\varphi(t)$ it was found no correlation between the number of cycles, N and the modal pore diameter from MS-3.3 and MS-8.3. This confirmed the first hypothesis in Section 3.1, where optimum performance in relative humidity buffering was found to be related to maximum theoretical pore volume within the linear portion of the isotherm that exists between points $\varphi_{i,L}$ and $\varphi_{i,U}$. The second hypothesis set in Section 3.1 was also confirmed. A positive linear correlation was found between the range in moisture storage capacity, Δw within the linear portion (between $\varphi_{i,U} - \varphi_{i,L}$) of all candidate isotherms (A_1–A_6 and B_1–B_4) and the time taken to exceed the φ_{max} limit. Again, in terms of the design process of an 'ideal' water vapour isotherm, this implies that adjustments of the Δw gradient should be restricted to points (and corresponding pore diameters) between the operating limits $\varphi_{i,L}$–$\varphi_{i,U}$.

However, there are still some limitations from the top-down design tool in terms of predicting water vapour adsorption/ desorption kinetics (*i.e.* time-response), especially for those rapid-response desiccants that have a steep Δw gradient over a narrow $\Delta\varphi$ range. As presented in Chapter 5, there were some significant

underestimations, when comparing experimental and numerical data. The latter may result from a coupled phenomenon between the water vapour adsorption/ desorption kinetics and the possible presence of scanning curves within the hysteresis loop, particularly Type H2. These divergences may be reduced (*i.e.* full reversibility), by the implementation of dynamic inputs for moisture content, *w* within the numerical code. In terms of future research this would provide a greater understanding of the hysteresis and pore-blocking effects observed in this study, which probably relate to the behaviour of water vapour under confinement, *i.e.* adsorbate-adsorbate interactions.

Some of the issues that have emerged from the preliminary analysis of the correlation between water vapour desorption and nitrogen adsorption isotherms are related to the accuracy of gas adsorption measurements. As presented in Section 5.2, there was a low-pressure hysteresis observed in MS-3.3 desiccants when performing nitrogen adsorption/ desorption, which was also seen in most MCM-41 and SBA-15 desiccants for water vapour adsorption/ desorption (refer to Section 5.3.1). Nitrogen and water vapour isotherm correlation (for pore size distribution analysis) requires a more rigorous methodology in order to determine:

1. Adsorption/ desorption isotherm characterisation (nitrogen and water), particularly below the onset for capillary condensation and an increased time for equilibration of the adsorbate at low pressure.
2. Statistical significance of both nitrogen and water vapour isotherm correlation, by assessing the occurrence between the point, $\varphi,_L$ of the water vapour desorption isotherm and the point where capillary condensation occurs in the nitrogen desorption isotherm ($P/P_{0(L)}$).

From the numerical simulation results provided in Chapter 6, a strong correlation was found between the water vapour isotherm and the kinetics for water vapour adsorption/ desorption. This was with respect to the time taken to reach each of the three stages shown in Figure 6.2. This was particularly visible in the case of Type V water vapour isotherms. Ultimately these correlations would enable:

1. Prediction of the time taken to desiccant failure (within continuous moisture loads scenarios) with respect to the indoor relative humidity stabilization.
2. Selection of the most suitable desiccant for regulating specific relative humidity conditions, according to the moisture content gradient, Δw.

However, such correlations were not evident when analysing the results and performance of Type III isotherms. In terms of the kinetics of water vapour adsorption/ desorption, there was not a defined sub-plateau portion of the adsorption curve between points *b* and *c* (refer to Figure 6.1). This implied that prolonged capillary condensation occurred at higher relative humidities (above $\varphi > 0.9$), and that the inflection towards point *d* (EMC_{100}) was not clearly associated. This was also seen in Figure 6.4b, where the linear correlation between total water content, *w* and the water vapour being exchanged was not found for Type III isotherms. The latter was also confirmed when analysing the desiccant's overall energy consumption for dehumidification purposes. No correlation was found between the total moisture storage, *w* and total latent heat for air dehumidification (*e.g.* $R^2 = 0.2706$ in Figure 6.11b). Therefore, for the purpose of informing the design of optimized hygrothermal functional properties (*i.e.* 'ideal' water vapour isotherm), the maximum pore volume should occur at

pore diameters that relate to the linear portion of the isotherm (between $\varphi_{i,L}$ and $\varphi_{i,U}$). This suggested that having a larger moisture storage capacity alone was not an indication of the desiccant's suitability for regulating relative humidity in specific applications, nor an indication of lowering the energy consumption for air dehumidification when assisting an HVAC system.

In general terms, the major contribution of this hygrothermal modelling technique is a theoretical insight that enables predictive design of new desiccants as well as a screening of existing desiccants. This technique could be confidently used for desiccants where the water vapour isotherms are fully reversible, and can also be used for broader applications than the passive regulations of indoor relative humidity in buildings, *e.g.* automotive and aerospace.

CHAPTER 8 Conclusions

8.1 Concluding remarks

This section presents the main conclusions of this thesis according to the overall aim and objectives outlined in Chapter 1. This was with respect to the implementation of a hygrothermal modelling technique that enables top-down predictive design of mesoporous desiccants. The general interest in which desiccants have been considered in the industry (*e.g.* heating & cooling) normally relates to the improvement of water vapour adsorption/ desorption for targeted applications. In particular when considering their full adsorption capacity (*i.e.* large pore volumes), one may disregard other significant correlations between the hygrothermal properties and the structure of the pore network, *i.e.* pore morphology and hysteresis.

In this study, the concept of a top-down approach was explored where ideal material properties were first determined, and then new materials were synthesised in order to experimentally achieve these properties. In other words, this technique was meant to assist the predictive design of 'ideal' water vapour isotherms by determining the optimum hygrothermal properties needed to achieve regulation of indoor relative humidity in closed environments. In the same logic, this research has also sought to determine the desirable behaviour of mesoporous desiccants when assisting a HVAC system (in mixed mode) with the aim of determining the relative effects on total energy efficiency.

Chapter 4 provided the results from the characterization of the pre-existing materials (MS-3.3 and MS-8.3) which in turn served as realistic input data to feed the hygrothermal modelling technique. This data was initially used to enable the calibration and operation of the technique based on the preliminary sensitivity analysis (Section 4.3.1). As presented in Section 4.3.2 and 4.3.3, the hygrothermal functional properties gathered from the pre-existing materials were used as a template to assist the design process of 'ideal' water vapour isotherms. Consequently, objectives 1 and 2 from Section 1.3 were fulfilled at the first stage of the top-down design as shown in Figure 1.2. The major implication from these results was that a principle could be established that would enable the prediction of ideal water vapour isotherms using a hygrothermal model. In terms of the progressive decay in humidity buffering, this was strongly related to the pore volume within the linear portion of the isotherm that exists between points $\varphi_{i,L}$ and $\varphi_{i,U}$. This confirmed the first hypothesis in Section 3.1, and candidate isotherm A_3 was identified as the ideal. This meant that the fluctuation of the function, $\varphi(t)$ could be maintained within the operating limits $\varphi_{min} = 0.55$ and $\varphi_{max} = 0.70$ for a finite number of cycles, N, after which the desiccant would need to be fully desorbed (*i.e.* recharged).

The positive linear correlation found between the moisture storage capacity, $\Delta w_{55\text{-}65}$ and the time taken to exceed the φ_{max} limit, confirmed the second hypothesis in Section 3.1. This correlation was found to be highly sensitive to the Δw gradient between points $\varphi_{i,L}$ and $\varphi_{i,U}$, which can be controlled by φ (x-axis) adjustments to the sorption isotherm. These results proved that the top-down technique can inform the design of optimized hygrothermal functional properties with respect to specific relative humidity buffering scenarios. The

latter implied that for enhanced moisture buffering performance, the maximum fraction of total pore volume possible should occur within the linear portion of the isotherm that exists between the operating limits $\varphi_{i,L}$ and $\varphi_{i,U}$.

The pore structure for the newly created MCM-41 and SBA-15 desiccants was characterised using both nitrogen and water vapour physisorption analysis. As presented in Chapter 5, the desiccants offered a wide range of candidate isotherms with tuneable pore geometry that could be optimized (during synthesis) to match the predicted 'ideal' isotherms. This satisfied objective 3 at the second stage of the top-down design tool presented (Section 1.3). It was found that for both nitrogen and water vapour physisorption a steep adsorption gradient within a specific portion of the isotherm corresponded with the maximum incremental pore volume, which may indicate a well-defined modal pore diameter (refer to Figure 5.2).

In most of the desiccants, a Type H2 hysteresis loop occurred. It was hypothesised that a possible correlation between the water vapour desorption isotherm (lower closing point, $\varphi,_L$) and the nitrogen desorption isotherm, (onset for capillary condensation, $P/P_{0(L)}$) may be established. However, in both nitrogen and water vapour isotherms a low-pressure hysteresis phenomenon was observed in most desiccants, which may limit the scope of this hypothesis. It was suggested that the gas adsorption measurements would require a more accurate determination at low pressure, and particularly below the onset for capillary condensation allowing an increased time for equilibration of the adsorbate. Together with statistical analysis, this hypothesis could eventually enable a deeper understanding of the pore network and particularly the pore-blocking

effects. Further analysis suggested that the pore-blocking effect could also significantly affect the time-response during adsorption/ desorption cycles. The latter may be attributed to the presence of scanning curves within the hysteresis loop, which at the stage of this study are uncharacterised.

In terms of validation of the hygrothermal modelling technique (objective 4 from Section 1.3), there are still some issues that restrict the full prediction of the water vapour adsorption/ desorption kinetics (*i.e*. time-response). Although, there were some cases where full water vapour adsorption/ desorption reversibility was found, there are still some significant underestimations between the experimental and numerical data. Preliminary analysis showed that these underestimations may be attributed to the lack of a dynamic input in the model for moisture content, *w*.

However, it was suggested that this may be a combined effect between the time-response for water vapour adsorption/ desorption, and the presence of scanning curves within hysteresis loops. The theoretical implication of these results is to provide further insight that will inform the development of hygrothermal models and include scanning curve predictions. Future research could focus on accurate numerical prediction of the water vapour adsorption/ desorption kinetics for rapid-response desiccants.

As presented in Chapter 6, a series of numerical simulations were conducted using a selection of well-known existing commercial desiccants with the aim of classifying their applicability in different humidity buffering scenarios. This was done by assessing the relative humidity buffering capacity and the kinetics of water vapour adsorption/ desorption, and then measuring their effect on total

energy efficiency when used in mixed mode with an HVAC system. This satisfied objective 5 and relates to the third stage of the top-down design tool (Section 1.3). It was evident that the kinetics of water vapour adsorption strongly related to the fractional pore volume between the limits $\varphi_{i,L}$ and $\varphi_{i,U}$. This was most pronounced in Type V isotherms due to the presence of a steep adsorption gradient within a narrow portion of the isotherm. This related to the onset of capillary condensation and the maximum incremental pore volume, *i.e*. defined mean pore diameter.

The implication for these results is that existing commercial desiccants can be assigned to applications in which the mixed mode operating limits are ideal for optimum performance. Desiccants with Type V isotherms, for example, have exceptional performance for humidity buffering under narrow operating limits (φ_{max} and φ_{max}). A positive linear correlation was found between the latent heat used for air dehumidification and the Δw gradient for passive regulation of the moisture loads at a lower rate of energy consumption. However, this was not true when total moisture content, w was compared against total latent heat for air dehumidification (no correlation, $R^2 = 0.2706$). This was especially significant those Type III isotherms where the maximum theoretical pore volume between $\varphi_{i,U}$ and $\varphi_{i,L}$ was not used; *e.g*. SBA-15 10 nm and Aerogel.

Overall, the main implication of this research is that it provides theoretical insight that enables top-down predictive design of advanced mesoporous desiccants using a numerical hygrothermal model. This has successfully been used for identifying optimised water vapour isotherms and then enabling experimental synthesis of mesoporous desiccants with ideal geometry. This

work serves as a framework for several broader practical applications beyond the improvement of passively regulating relative humidity buffering in buildings, *e.g*. aircraft cabins, automotive interiors, archives and storage of biological samples.

8.2 Recommendations for further research

Based on the experimental and numerical modelling data presented in this research, it is recommended that further experimental investigations be undertaken as presented below:

- There is still significant underestimations from numerical predictions of water vapour adsorption/ desorption (*i.e*. time-response) which may result from the coupled phenomenon of both water vapour adsorption kinetics and scanning curves within the hysteresis loop (non-reversibility). This especially applies to those rapid-response materials having a steep Δw gradient over a narrow $\Delta \varphi$ range. These divergences may be reduced (*i.e*. full reversibility), by the implementation of dynamic inputs for moisture content, w within the numerical code packages that considers together the hysteresis phenomena and the pore-blocking effect. Additionally, it was suggested that accurate gas adsorption measurements are required, specifically for desiccants that presented low-pressure hysteresis in both nitrogen and water vapour isotherms.
- There is a potential area for further investigation in the design of tailored desiccants which considers relative humidity buffering and thermal storage within closed environments. This, would eventually enable the

formulation of theoretical insights (*i.e*. conceptual modelling) for enhanced hygrothermal functional properties under non-isothermal psychrometric conditions. Further investigations are suggested, in order to estimate the relative effect of enhanced heat transfer (physisorption/ vapour diffusion) and thermal storage (sensible and latent heat) for hypothetically-created desiccants.

- Whilst some good initial agreement (*i.e*. curve-fitting) was found between water vapour (*e.g*. Type V) and nitrogen isotherms (*e.g*. Type IV), there is still a need for an accurate methodology, conducting statistical studies. Therefore, further experimental investigations are required to enable the correlation between water and nitrogen adsorption/ desorption data, and to determine the implications from the pore filling/ empting mechanisms; *e.g*. adsorbent-adsorbate interactions, and pore-blocking effect. This would ultimately allow pore size distribution analysis or prediction from experimental and hypothetically-created water vapour isotherms.

REFERENCES

ABUKU, M., JANSSEN, H. & ROELS, S. 2009. Impact of wind-driven rain on historic brick wall buildings in a moderately cold and humid climate: Numerical analyses of mould growth risk, indoor climate and energy consumption. *Energy and Buildings,* 41**,** 101-110.

AKIYAMA, G., MATSUDA, R., SATO, H., HORI, A., TAKATA, M. & KITAGAWA, S. 2012. Effect of functional groups in MIL-101 on water sorption behavior. *Microporous and Mesoporous Materials,* 157**,** 89-93.

ALLINSON, D. & HALL, M. 2010. Hygrothermal analysis of a stabilised rammed earth test building in the UK. *Energy and Buildings,* 42**,** 845-852.

ANTRETTER, F., SAUER, F., SCHÖPFER, T. & HOLM, A. Validation of a hygrothermal whole building simulation software. Proceedings of Building Simulation 2011: 12th Conference of International Building Performance Simulation Association, Sydney, Australia, 2011.

ATKINS, P. & DE PAULA, J. 2010. Atkins' physical chemistry. *Oxford University Press, Oxford, UK.*

BAZANT, M. Z. & BAŽANT, Z. P. 2012. Theory of sorption hysteresis in nanoporous solids: Part II Molecular condensation. *Journal of the Mechanics and Physics of Solids,* 60**,** 1660-1675.

BAŽANT, Z. P. & BAZANT, M. Z. 2012. Theory of sorption hysteresis in nanoporous solids: Part I: Snap-through instabilities. *Journal of the Mechanics and Physics of Solids,* 60**,** 1644-1659.

BELDING, W. A., DELMAS, M. P. F. & HOLEMAN, W. D. 1996. Desiccant aging and its effects on desiccant cooling system performance. *Applied Thermal Engineering,* 16**,** 447-459.

BERKOWITZ, B. & EWING, R. P. 1998. Percolation theory and network modeling applications in soil physics. *Surveys in Geophysics,* 19**,** 23-72.

BLASCO, T., CORMA, A., NAVARRO, M. & PARIENTE, J. P. 1995. Synthesis, characterization, and catalytic activity of Ti-MCM-41 structures. *Journal of Catalysis,* 156**,** 65-74.

BONNAUD, P. A., COASNE, B. & PELLENQ, R. J. M. 2010. Molecular simulation of water confined in nanoporous silica. *Journal of Physics: Condensed Matter,* 22**,** 284110.

BRANTON, P. J., HALL, P. G. & SING, K. S. 1995. Physisorption of alcohols and water vapour by MCM-41, a model mesoporous adsorbent. *Adsorption,* 1**,** 77-82.

BRANTON, P. J., SING, K. S. & WHITE, J. W. 1997. Adsorption of carbon tetrachloride and nitrogen by 3.4 nm pore diameter siliceous MCM-41. *Journal of the Chemical Society, Faraday Transactions,* 93**,** 2337-2340.

BROADBENT, S. R. & HAMMERSLEY, J. M. Percolation processes. Mathematical Proceedings of the Cambridge Philosophical Society, 1957. Cambridge Univ Press, 629-641.

BSI. BS EN 15026 2007: Hygrothermal performance of building components and building elements. . *Assessment of moisture transfer by numerical simulation* London; 2007

CANIVET, J., FATEEVA, A., GUO, Y., COASNE, B. & FARRUSSENG, D. 2014. Water adsorption in MOFs: fundamentals and applications. *Chemical Society Reviews*.

CARRASCO-MARÍN, F., MUEDEN, A., CENTENO, T. A., STOECKLI, F. & MORENO-CASTILLA, C. 1997. Water adsorption on activated carbons with different degrees of oxidation. *Journal of the Chemical Society, Faraday Transactions,* 93**,** 2211-2215.

CASEY, S. P., HALL, M. R., TSANG, S. C. E. & KHAN, M. A. 2012. Nanocomposite materials for rapid-response interior air humidity buffering in closed environments.

CASEY, S. P., HALL, M. R., TSANG, S. C. E. & KHAN, M. A. 2013a. Energetic and hygrothermal analysis of a nano-structured material for rapid-response humidity buffering in closed environments. *Building and Environment,* 60**,** 24-36.

CASEY, S. P., HALL, M. R., TSANG, S. E. & KHAN, M. A. 2013b. Nanocomposite materials for rapid-response interior air humidity buffering in closed environments. *Journal of Building Performance Simulation,* 6**,** 354-366.

CEROLINI, S., D'ORAZIO, M., DI PERNA, C. & STAZI, A. 2009. Moisture buffering capacity of highly absorbing materials. *Energy and Buildings,* 41**,** 164-168.

CHANG, R. & OVERBY, J. 2003. *General chemistry: the essential concepts*, McGraw-Hill New York.

CHUNG, J. D. & LEE, D.-Y. 2009. Effect of desiccant isotherm on the performance of desiccant wheel. *International journal of refrigeration,* 32**,** 720-726.

CIMINO, R., CYCHOSZ, K. A., THOMMES, M. & NEIMARK, A. V. 2013. Experimental and theoretical studies of scanning adsorption–desorption isotherms. *Colloids and Surfaces A: Physicochemical and Engineering Aspects,* 437**,** 76-89.

COASNE, B., DI RENZO, F., GALARNEAU, A. & PELLENQ, R. J. M. 2008a. Adsorption of Simple Fluid on Silica Surface and Nanopore: Effect of Surface Chemistry and Pore Shape. *Langmuir,* 24**,** 7285-7293.

COASNE, B., GALARNEAU, A., RENZO, F. & PELLENQ, R. M. 2008b. Molecular simulation of adsorption and intrusion in nanopores. *Adsorption,* 14**,** 215-221.

COHAN, L. H. 1938. Sorption hysteresis and the vapor pressure of concave surfaces. *Journal of the American Chemical Society,* 60**,** 433-435.

COLLIER, R., CALE, T. & LAVAN, Z. 1986. Advanced desiccant materials assessment. Enerscope, Inc., Glendale, AZ (USA).

CORMA, A., KAN, Q., NAVARRO, M. T., PÉREZ-PARIENTE, J. & REY, F. 1997. Synthesis of MCM-41 with different pore diameters without addition of auxiliary organics. *Chemistry of materials,* 9**,** 2123-2126.

DAI, Y. J., WANG, R. Z., ZHANG, H. F. & YU, J. D. 2001. Use of liquid desiccant cooling to improve the performance of vapor compression air conditioning. *Applied Thermal Engineering,* 21**,** 1185-1202.

DAOU, K., WANG, R. & XIA, Z. 2006. Desiccant cooling air conditioning: a review. *Renewable and Sustainable Energy Reviews,* 10**,** 55-77.

DAVIS, S. J. & CALDEIRA, K. 2010. Consumption-based accounting of CO2 emissions. *Proceedings of the National Academy of Sciences,* 107**,** 5687-5692.

DESTA, T. Z., LANGMANS, J. & ROELS, S. 2011. Experimental data set for validation of heat, air and moisture transport models of building envelopes. *Building and Environment,* 46**,** 1038-1046.

DO, D. & DO, H. 2000. A model for water adsorption in activated carbon. *Carbon,* 38**,** 767-773.

DO, D., JUNPIROM, S. & DO, H. 2009. A new adsorption–desorption model for water adsorption in activated carbon. *Carbon,* 47**,** 1466-1473.

DO, D. D. 1998. *Adsorption analysis: equilibria and kinetics,* Imperial College Press.

DOS SANTOS, G. H., MENDES, N. & PHILIPPI, P. C. 2009. A building corner model for hygrothermal performance and mould growth risk analyses. *International Journal of Heat and Mass Transfer,* 52**,** 4862-4872.

EHRENMANN, J., HENNINGER, S. K. & JANIAK, C. 2011. Water Adsorption Characteristics of MIL-101 for Heat-Transformation Applications of MOFs. *European Journal of Inorganic Chemistry,* 2011**,** 471-474.

EVERETT, D., GREGG, S., SING, K. & STOECKLI, H. 1979. Characterization of porous solids. *Society of Chemical Industry London***,** 229.

FARHA, O. K., YAZAYDıN, A. Ö., ERYAZICI, I., MALLIAKAS, C. D., HAUSER, B. G., KANATZIDIS, M. G., NGUYEN, S. T., SNURR, R. Q. & HUPP, J. T. 2010. De novo synthesis of a metal–organic framework material featuring ultrahigh surface area and gas storage capacities. *Nature chemistry,* 2**,** 944-948.

FERREIRO-RANGEL, C. A., LOZINSKA, M. M., WRIGHT, P. A., SEATON, N. A. & DÜREN, T. 2012. Kinetic Monte Carlo Simulation of the Synthesis of Periodic Mesoporous Silicas SBA-2 and STAC-1: Generation of Realistic Atomistic Models. *The Journal of Physical Chemistry C,* 116**,** 20966-20974.

FOSTER, A. G. 1932. The sorption of condensible vapours by porous solids. Part I. The applicability of the capillary theory. *Transactions of the Faraday Society,* 28**,** 645-657.

FRAUNHOFER. *WUFI Pro & Plus®: PC-Program for coupled heat and mass transfer in building components* [Online]. Available: http://www.wufi.de/index_e.html [Accessed 17/09/2013.

FREIRE, R. Z., OLIVEIRA, G. H. C. & MENDES, N. 2008. Predictive controllers for thermal comfort optimization and energy savings. *Energy and Buildings,* 40**,** 1353-1365.

FURUKAWA, H., GÁNDARA, F., ZHANG, Y.-B., JIANG, J., QUEEN, W. L., HUDSON, M. R. & YAGHI, O. M. 2014. Water Adsorption in Porous Metal–Organic Frameworks and Related Materials. *Journal of the American Chemical Society,* 136**,** 4369-4381.

GIOVAMBATTISTA, N., ROSSKY, P. & DEBENEDETTI, P. 2012. Computational Studies of Pressure, Temperature, and Surface Effects on the Structure and Thermodynamics of Confined Water. *Annual Review of Physical Chemistry,* 63**,** 179-200.

GRÜN, M., UNGER, K. K., MATSUMOTO, A. & TSUTSUMI, K. 1999. Novel pathways for the preparation of mesoporous MCM-41 materials: control

of porosity and morphology. *Microporous and Mesoporous Materials,* 27**,** 207-216.

GUYER, R. & MCCALL, K. 1996. Capillary condensation, invasion percolation, hysteresis, and discrete memory. *Physical Review B,* 54**,** 18.

HALL, C. & HOFF, W. D. 2012. *Water transport in brick, stone, and concrete,* Spon Press London.

HALL, M. & ALLINSON, D. 2009a. Analysis of the hygrothermal functional properties of stabilised rammed earth materials. *Building and Environment,* 44**,** 1935-1942.

HALL, M. & ALLINSON, D. 2009b. Assessing the effects of soil grading on the moisture content-dependent thermal conductivity of stabilised rammed earth materials. *Applied Thermal Engineering,* 29**,** 740-747.

HALL, M. R. 2010. *Materials for energy efficiency and thermal comfort in buildings,* CRC Press.

HALL, M. R., CASEY, S. P., LOVEDAY, D. L. & GILLOTT, M. 2013. Analysis of UK domestic building retrofit scenarios based on the E. ON Retrofit Research house using energetic hygrothermics simulation-energy efficiency, indoor air quality, occupant comfort, and mould growth potential. *Building and Environment*.

HALL, M. R., TSANG, S. C. E., CASEY, S. P., KHAN, M. A. & YANG, H. 2012. Synthesis, characterization and hygrothermal behaviour of mesoporous silica high-performance desiccants for relative humidity buffering in closed environments. *Acta Materialia,* 60**,** 89-101.

HANDBOOK, A. F. 2009. American society of heating, refrigerating and air-conditioning engineers. *Inc.: Atlanta, GA, USA*.

HENNINGER, S. K., HABIB, H. A. & JANIAK, C. 2009. MOFs as adsorbents for low temperature heating and cooling applications. *Journal of the American Chemical Society,* 131**,** 2776-2777.

HENNINGER, S. K., JEREMIAS, F., KUMMER, H. & JANIAK, C. 2012. MOFs for use in adsorption heat pump processes. *European Journal of Inorganic Chemistry,* 2012**,** 2625-2634.

HENS, H. S. L. C. 2012. *Building Physics--Heat, Air and Moisture: Fundamentals and Engineering Methods with Examples and Exercises,* Ernst & Sohn.

HOLM, A., KUENZEL, H. M. & SEDLBAUER, K. The hygrothermal behaviour of rooms: combining thermal building simulation and hygrothermal envelope calculation. Proceedings of the 8th International IBPSA Conference, 2003. 499-505.

HOLM, A. H. & KUENZEL, H. M. 2002. Practical application of an uncertainty approach for hygrothermal building simulations—drying of an AAC flat roof. *Building and Environment,* 37**,** 883-889.

HORCAJADA, P., RAMILA, A., PEREZ-PARIENTE, J. & VALLET-REGı, M. 2004. Influence of pore size of MCM-41 matrices on drug delivery rate. *Microporous and Mesoporous Materials,* 68**,** 105-109.

HORIKAWA, T., SAKAO, N. & DO, D. 2013. Effects of temperature on water adsorption on controlled microporous and mesoporous carbonaceous solids. *Carbon,* 56**,** 183-192.

HORIKAWA, T., SEKIDA, T., HAYASHI, J. I., KATOH, M. & DO, D. D. 2011. A new adsorption–desorption model for water adsorption in porous carbons. *Carbon,* 49**,** 416-424.

HUTSON, N. D. & YANG, R. T. 1997. Theoretical basis for the Dubinin-Radushkevitch (DR) adsorption isotherm equation. *Adsorption,* 3**,** 189-195.

IEA. 2016. *Energy-efficient Buildings: Heating and Cooling Equipment* [Online]. International Energy Agency. Available: http://www.iea.org/ [Accessed 06/04/2016 2016].

INAGAKI, S., FUKUSHIMA, Y., KURODA, K. & KURODA, K. 1996. Adsorption isotherm of water vapor and its large hysteresis on highly ordered mesoporous silica. *Journal of Colloid and Interface Science,* 180**,** 623-624.

INCROPERA, F. P., DEWITT, D. P., BERGMAN, T. L. & LAVINE, A. S. 2007. *Fundamentals of Heat and Mass Transfer*, John Wiley & Sons.

ISO, E. 2001. 12572: 2001. *Hygrothermal performance of building materials and products. Determination of water vapor transmission properties," AFNOR.*

JARONIEC, M., KRUK, M. & OLIVIER, J. P. 1999. Standard nitrogen adsorption data for characterization of nanoporous silicas. *Langmuir,* 15**,** 5410-5413.

JASUJA, H., ZANG, J., SHOLL, D. S. & WALTON, K. S. 2012. Rational tuning of water vapor and CO2 adsorption in highly stable Zr-based MOFs. *The Journal of Physical Chemistry C,* 116**,** 23526-23532.

KALAMEES, T. & VINHA, J. 2003. Hygrothermal calculations and laboratory tests on timber-framed wall structures. *Building and Environment,* 38**,** 689-697.

KARAGIOZIS, A. 2001. WUFI-ORNL/IBP Hygrothermal Model.

KARAGIOZIS, A., KÜNZEL, H. & HOLM, A. 2001. WUFI-ORNL/IBP—a North American hygrothermal model. *Performance of Exterior Envelopes of Whole Buildings VIII***,** 2-7.

KARAGIOZIS, A. N., SALONVAARA, M., HOLM, A. & KUENZEL, H. Influence of wind-driven rain data on hygrothermal performance. Proceedings of the Eighth International IBPSA Conference. Eindhoven, Netherlands, 2003.

KHADEMI, M. & SAHIMI, M. 2011. Molecular dynamics simulation of pressure-driven water flow in silicon-carbide nanotubes. *The Journal of Chemical Physics,* 135**,** 204509-204509-7.

KHUTIA, A., RAMMELBERG, H. U., SCHMIDT, T., HENNINGER, S. & JANIAK, C. 2013. Water sorption cycle measurements on functionalized MIL-101Cr for heat transformation application. *Chemistry of Materials,* 25**,** 790-798.

KIKKINIDES, E., KAINOURGIAKIS, M. & STUBOS, A. 2003. Origin of hysteresis of gas adsorption in disordered porous media: Lattice gas model versus percolation theory. *Langmuir,* 19**,** 3338-3344.

KINSARA, A. A., ELSAYED, M. M. & AL-RABGHI, O. M. 1996. Proposed energy-efficient air-conditioning system using liquid desiccant. *Applied Thermal Engineering,* 16**,** 791-806.

KNEZ, Z. & NOVAK, Z. 2001. Adsorption of water vapor on silica, alumina, and their mixed oxide aerogels. *Journal of Chemical & Engineering Data,* 46**,** 858-860.

KORJENIC, A. & BEDNAR, T. 2012. An analytical solution of a moisture transfer problem for coupled room and building component. *Energy and Buildings,* 47**,** 254-259.

KRUK, M., JARONIEC, M. & SAYARI, A. 1997a. Adsorption study of surface and structural properties of MCM-41 materials of different pore sizes. *The Journal of Physical Chemistry B,* 101**,** 583-589.

KRUK, M., JARONIEC, M. & SAYARI, A. 1997b. Application of large pore MCM-41 molecular sieves to improve pore size analysis using nitrogen adsorption measurements. *Langmuir,* 13**,** 6267-6273.

KRUS, M. 1996. *Moisture transport and storage coefficients of porous mineral building materials: Theoretical principles and new test methods*, Fraunhofer IRB Verlag.

KRUS, M., FITZ, C. & SEDLBAUER, K. 2013. Reducing the Risk of Microbial Growth on Insulated Walls by Improving the Properties of the Surface Materials. *Hygrothermal Behavior, Building Pathology and Durability.* Springer.

KRUS, M. & SEDLBAUER, K. Mould growth prediction by computational simulation. Annex41 Report "A1-T4-D-5-1. pdf" in Trondheim Meeting, Trondheim, Norway, 2005.

KUENZEL, H., KARAGIOZIS, A. & HOLM, A. 2001. *A hygrothermal design tool for architects and engineers*, ASTM International West Conshohocken, PA.

KÜNZEL, H. M. 1995. *Simultaneous heat and moisture transport in building components*, IRB-Verlag Stuttgart.

KÜNZEL, H. M., HOLM, A., ZIRKELBACH, D. & KARAGIOZIS, A. N. 2005. Simulation of indoor temperature and humidity conditions including hygrothermal interactions with the building envelope. *Solar Energy,* 78**,** 554-561.

KÜNZEL, H. M., KRUS, M., FITZ, C., HOFBAUER, W., SCHERER, C. & BREUER, K. Accelerated Test Procedure to Assess the Microbial Growth Resistance of Exterior Finishes. 12th International Conference on Durability of Building Materials and Components, Porto, Portugal.

KÜSGENS, P., ROSE, M., SENKOVSKA, I., FRÖDE, H., HENSCHEL, A., SIEGLE, S. & KASKEL, S. 2009. Characterization of metal-organic frameworks by water adsorption. *Microporous and Mesoporous Materials,* 120**,** 325-330.

KWIATKOWSKI, J., WOLOSZYN, M. & ROUX, J.-J. 2009. Modelling of hysteresis influence on mass transfer in building materials. *Building and Environment,* 44**,** 633-642.

KWIATKOWSKI, J., WOLOSZYN, M. & ROUX, J.-J. 2011. Influence of sorption isotherm hysteresis effect on indoor climate and energy demand for heating. *Applied Thermal Engineering,* 31**,** 1050-1057.

LA, D., DAI, Y., LI, Y., WANG, R. & GE, T. 2010. Technical development of rotary desiccant dehumidification and air conditioning: a review. *Renewable and Sustainable Energy Reviews,* 14**,** 130-147.

LERBRET, A., LELONG, G., MASON, P. E., SABOUNGI, M. L. & BRADY, J. W. 2011. Water Confined in Cylindrical Pores: A Molecular Dynamics Study. *Food biophysics,* 6**,** 233-240.

LIMMER, D. T. & CHANDLER, D. 2012. Phase diagram of supercooled water confined to hydrophilic nanopores. *arXiv preprint arXiv:1205.2157*.

LIU, H., ZHANG, L. & SEATON, N. A. 1992. Determination of the connectivity of porous solids from nitrogen sorption measurements — II. Generalisation. *Chemical Engineering Science,* 47**,** 4393-4404.

LIU, H., ZHANG, L. & SEATON, N. A. 1993. Analysis of Sorption Hysteresis in Mesoporous Solids Using a Pore Network Model. *Journal of Colloid and Interface Science,* 156**,** 285-293.

MANZANO, H., MOEINI, S., MARINELLI, F., VAN DUIN, A. C. T., ULM, F. J. & PELLENQ, R. J. M. 2012. Confined Water Dissociation in Microporous Defective Silicates: Mechanism, Dipole Distribution, and Impact on Substrate Properties. *Journal of the American Chemical Society,* 134**,** 2208-2215.

MASCHMEYER, T., REY, F., SANKAR, G. & THOMAS, J. M. 1995. Heterogeneous catalysts obtained by grafting metallocene complexes onto mesoporous silica. *Nature,* 378**,** 159-162.

MASON, G. 1988. Determination of the pore-size distributions and pore-space interconnectivity of Vycor porous glass from adsorption-desorption hysteresis capillary condensation isotherms. *Proceedings of the Royal Society of London. Series A, Mathematical and Physical Sciences***,** 453-486.

MCBAIN, J. W. 1935. An explanation of hysteresis in the hydration and dehydration of gels. *Journal of the American Chemical Society,* 57**,** 699-700.

MICROMERITICS. 2015. *Gas adsorption theory* [Online]. Available: http://www.micromeritics.com/Library/Scientific-Posters.aspx [Accessed 28/10/2015 2015].

MILISCHUK, A. A. & LADANYI, B. M. 2011. Structure and dynamics of water confined in silica nanopores. *The Journal of Chemical Physics,* 135**,** 174709-174709-11.

MITCHELL, J. K. & SOGA, K. 2005. Fundamentals of soil behavior. *Wiley, New York.*

MUNOZ, B., RAMILA, A., PEREZ-PARIENTE, J., DIAZ, I. & VALLET-REGI, M. 2003. MCM-41 organic modification as drug delivery rate regulator. *Chemistry of materials,* 15**,** 500-503.

NALAPARAJU, A., ZHAO, X. & JIANG, J. 2010. Molecular understanding for the adsorption of water and alcohols in hydrophilic and hydrophobic zeolitic metal− organic frameworks. *The Journal of Physical Chemistry C,* 114**,** 11542-11550.

NAONO, H., HAKUMAN, M., TANAKA, T., TAMURA, N. & NAKAI, K. 2000. Porous Texture and Surface Character of Dehydroxylated and Rehydroxylated MCM-41 Mesoporous Silicas—Analysis of Adsorption Isotherms of Nitrogen Gas and Water Vapor. *Journal of Colloid and Interface Science,* 225**,** 411-420.

NGUYEN, T. X. & BHATIA, S. K. 2011. How water adsorbs in hydrophobic nanospaces. *The Journal of Physical Chemistry C,* 115**,** 16606-16612.

NIK, V. M., SASIC KALAGASIDIS, A. & KJELLSTRÖM, E. 2012. Assessment of hygrothermal performance and mould growth risk in ventilated attics in respect to possible climate changes in Sweden. *Building and Environment,* 55**,** 96-109.

OHBA, T., KANOH, H. & KANEKO, K. 2004. Cluster-growth-induced water adsorption in hydrophobic carbon nanopores. *The Journal of Physical Chemistry B,* 108**,** 14964-14969.

OSANYINTOLA, O. F. & SIMONSON, C. J. 2006. Moisture buffering capacity of hygroscopic building materials: Experimental facilities and energy impact. *Energy and Buildings,* 38**,** 1270-1282.

PAVLÍK, Z. & ČERNÝ, R. 2008. Experimental assessment of hygrothermal performance of an interior thermal insulation system using a laboratory technique simulating on-site conditions. *Energy and Buildings,* 40**,** 673-678.

PÉREZ-LOMBARD, L., ORTIZ, J. & POUT, C. 2008. A review on buildings energy consumption information. *Energy and Buildings,* 40**,** 394-398.

PIEROTTI, R. & ROUQUEROL, J. 1985. Reporting physisorption data for gas/solid systems with special reference to the determination of surface area and porosity. *Pure Appl Chem,* 57**,** 603-619.

RAMOS, N. M. M., DELGADO, J. M. P. Q. & DE FREITAS, V. P. 2010. Influence of finishing coatings on hygroscopic moisture buffering in building elements. *Construction and Building Materials,* 24**,** 2590-2597.

RAVIKOVITCH, P., DOMHNAILL, S. Ó., NEIMARK, A., SCHÜTH, F. & UNGER, K. 1995. Capillary hysteresis in nanopores: theoretical and experimental studies of nitrogen adsorption on MCM-41. *Langmuir,* 11**,** 4765-4772.

RAVIKOVITCH, P., WEI, D., CHUEH, W., HALLER, G. & NEIMARK, A. 1997. Evaluation of pore structure parameters of MCM-41 catalyst supports and catalysts by means of nitrogen and argon adsorption. *The Journal of Physical Chemistry B,* 101**,** 3671-3679.

REGALADO, C. M. 2006. A geometrical model of bound water permittivity based on weighted averages: the allophane analogue. *Journal of Hydrology,* 316**,** 98-107.

RODE, C., PEUHKURI, R., HANSEN, K. K., TIME, B., SVENNBERG, K., ARFVIDSSON, J. & OJANEN, T. Moisture buffer value of materials in buildings. Proceedings of the 7th Symposium on Building Physics in the Nordic Countries, 2005. 108-115.

ROUQUEROL, J., AVNIR, D., FAIRBRIDGE, C., EVERETT, D., HAYNES, J., PERNICONE, N., RAMSAY, J., SING, K. & UNGER, K. 1994. Recommendations for the Characterisation of Porous Solids (Recommendations 1994). *Pure Appl. Chem,* 66**,** 1739-1758.

ROUQUEROL, J., ROUQUEROL, F. & SING, K. S. W. 1998. *Absorption by powders and porous solids,* Academic press.

RUTHVEN, D. M. 1984. *Principles of adsorption and adsorption processes,* John Wiley & Sons.

SAAM, W. & COLE, M. W. 1975. Excitations and thermodynamics for liquid-helium films. *Physical Review B,* 11**,** 1086.

SAARENKETO, T. 1998. Electrical properties of water in clay and silty soils. *Journal of Applied Geophysics,* 40**,** 73-88.

SARCE THOMANN, F., HALL, M. R., SANGCHOOM, W. & MOKAYA, R. 2015. A hygrothermal modelling approach to water vapour sorption isotherm design for mesoporous humidity buffers. *Microporous and Mesoporous Materials,* 211**,** 113-123.

SEATON, N. A. 1991. Determination of the connectivity of porous solids from nitrogen sorption measurements. *Chemical Engineering Science,* 46**,** 1895-1909.

SEDLBAUER, K. 2001. Prediction of mould fungus formation on the surface of and inside building components. *Fraunhofer Institute for Building Physics*.

SEDLBAUER, K. 2002. Prediction of mould growth by hygrothermal calculation. *Journal of Building Physics,* 25**,** 321-336.

SEDLBAUER, K., KRUS, M., ZILLIG, W. & KUNZEL, H. 2001. Mold growth prediction by computational simulation. *Fraunhofer Institute for Building Physics*.

SELVAM, P., BHATIA, S. K. & SONWANE, C. G. 2001. Recent advances in processing and characterization of periodic mesoporous MCM-41 silicate molecular sieves. *Industrial & Engineering Chemistry Research,* 40**,** 3237-3261.

SEO, Y. K., YOON, J. W., LEE, J. S., HWANG, Y. K., JUN, C. H., CHANG, J. S., WUTTKE, S., BAZIN, P., VIMONT, A. & DATURI, M. 2012. Energy-Efficient Dehumidification over Hierachically Porous Metal–Organic Frameworks as Advanced Water Adsorbents. *Advanced Materials,* 24**,** 806-810.

SHAHSAVARI, R., PELLENQ, R. J. M. & ULM, F. J. 2010. Empirical force fields for complex hydrated calcio-silicate layered materials. *Phys. Chem. Chem. Phys.,* 13**,** 1002-1011.

SHIRONO, K. & DAIGUJI, H. 2007. Molecular simulation of the phase behavior of water confined in silica nanopores. *The Journal of Physical Chemistry C,* 111**,** 7938-7946.

SILVESTRE-ALBERO, A. M., JUÁREZ-GALÁN, J. M., SILVESTRE-ALBERO, J. & RODRÍGUEZ-REINOSO, F. 2012. Low-pressure hysteresis in adsorption: an artifact? *The Journal of Physical Chemistry C,* 116**,** 16652-16655.

SING, K. S., EVERETT, D., HAUL, R. A., MOSCOU, L., PIEROTTI, R., ROUQUEROL, J. & SIEMIENIEWSKA, T. 1985. Reporting physisorption data for gas/solid systems with special reference to the determination of surface area and porosity (Recommendations 1984). *Pure and applied chemistry,* 57**,** 603-619.

SING, K. S. W. 1998. Adsorption methods for the characterization of porous materials. *Advances in Colloid and Interface Science,* 76–77**,** 3-11.

SING, K. S. W. 2004. Characterization of porous materials: past, present and future. *Colloids and Surfaces A: Physicochemical and Engineering Aspects,* 241**,** 3-7.

SOLER-ILLIA, G. J. A. A. & AZZARONI, O. 2011. Multifunctional hybrids by combining ordered mesoporous materials and macromolecular building blocks. *Chemical Society Reviews,* 40**,** 1107-1150.

SPANGLER, M. G. & HANDY, R. L. 1982. *Soil engineering,* Harper & Row.

SRIVASTAVA, N. & EAMES, I. 1998. A review of adsorbents and adsorbates in solid–vapour adsorption heat pump systems. *Applied Thermal Engineering,* 18**,** 707-714.

STEEMAN, H. J., JANSSENS, A., CARMELIET, J. & DE PAEPE, M. 2009a. Modelling indoor air and hygrothermal wall interaction in building

simulation: Comparison between CFD and a well-mixed zonal model. *Building and Environment,* 44**,** 572-583.

STEEMAN, H. J., VAN BELLEGHEM, M., JANSSENS, A. & DE PAEPE, M. 2009b. Coupled simulation of heat and moisture transport in air and porous materials for the assessment of moisture related damage. *Building and Environment,* 44**,** 2176-2184.

STEEMAN, M., DE PAEPE, M. & JANSSENS, A. 2010a. Impact of whole-building hygrothermal modelling on the assessment of indoor climate in a library building. *Building and Environment,* 45**,** 1641-1652.

STEEMAN, M., VAN BELLEGHEM, M., DE PAEPE, M. & JANSSENS, A. 2010b. Experimental validation and sensitivity analysis of a coupled BES–HAM model. *Building and Environment,* 45**,** 2202-2217.

STORCK, S., BRETINGER, H. & MAIER, W. F. 1998. Characterization of micro- and mesoporous solids by physisorption methods and pore-size analysis. *Applied Catalysis A: General,* 174**,** 137-146.

STRIOLO, A., CHIALVO, A., GUBBINS, K. & CUMMINGS, P. 2005. Water in carbon nanotubes: Adsorption isotherms and thermodynamic properties from molecular simulation. *The Journal of Chemical Physics,* 122**,** 234712.

THOMANN, F. S., HALL, M. R., MOKAYA, R. & STEVENS, L. A. 2015a. Hygrothermal simulation-informed design of mesoporous desiccants for optimised energy efficiency of mixed mode air conditioning systems. *Journal of Materials Chemistry A,* 3**,** 17290-17303.

THOMANN, F. S., HALL, M. R., SANGCHOOM, W. & MOKAYA, R. 2015b. A hygrothermal modelling approach to water vapour sorption isotherm design for mesoporous humidity buffers. *Microporous and Mesoporous Materials,* 211**,** 113-123.

TRECHSEL, H. R. Moisture analysis and condensation control in building envelopes. 2001. ASTM.

VALLET-REGI, M., RAMILA, A., DEL REAL, R. & PÉREZ-PARIENTE, J. 2001. A new property of MCM-41: drug delivery system. *Chemistry of materials,* 13**,** 308-311.

VAN BELLEGHEM, M., STEEMAN, M., WILLOCKX, A., JANSSENS, A. & DE PAEPE, M. 2011. Benchmark experiments for moisture transfer modelling in air and porous materials. *Building and Environment,* 46**,** 884-898.

WALL, G. & BROWN, R. 1981. The determination of pore-size distributions from sorption isotherms and mercury penetration in interconnected pores: The application of percolation theory. *Journal of Colloid and Interface Science,* 82**,** 141-149.

WANG, W., WU, L., LI, Z., FANG, Y., DING, J. & XIAO, J. 2013. An overview of adsorbents in the rotary desiccant dehumidifier for air dehumidification. *Drying Technology,* 31**,** 1334-1345.

WOLOSZYN, M., KALAMEES, T., OLIVIER ABADIE, M., STEEMAN, M. & SASIC KALAGASIDIS, A. 2009. The effect of combining a relative-humidity-sensitive ventilation system with the moisture-buffering capacity of materials on indoor climate and energy efficiency of buildings. *Building and Environment,* 44**,** 515-524.

WOLOSZYN, M. & RODE, C. Tools for performance simulation of heat, air and moisture conditions of whole buildings. Building Simulation, 2008. Springer, 5-24.

YANG, K., LIN, Y., LU, X. & NEIMARK, A. V. 2011. Solvation forces between molecularly rough surfaces. *Journal of Colloid and Interface Science,* 362**,** 382-388.

YANG, X., FAZIO, P., GE, H. & RAO, J. 2012. Evaluation of moisture buffering capacity of interior surface materials and furniture in a full-scale experimental investigation. *Building and Environment,* 47**,** 188-196.

YANUKA, M. 1989. Percolation processes and porous media: III. Prediction of the capillary hysteresis loop from geometrical and topological information of pore space. *Journal of Colloid and Interface Science,* 127**,** 48-58.

YU, S. & ZHANG, X. 2012a. Hygrothermal Characterization of Porous Building Materials-Experiment Research on Isothermal Sorption and Capillary Problem. *Advanced Materials Research,* 418**,** 944-949.

YU, S. & ZHANG, X. 2012b. Hygrothermal Characterization of Porous Building Materials-New Research Method on Water Vapor Transmission. *Advanced Materials Research,* 418**,** 903-907.

ZHANG, H., YOSHINO, H. & HASEGAWA, K. 2012. Assessing the moisture buffering performance of hygroscopic material by using experimental method. *Building and Environment,* 48**,** 27-34.

ZHANG, L. & NIU, J. 2002. Performance comparisons of desiccant wheels for air dehumidification and enthalpy recovery. *Applied Thermal Engineering,* 22**,** 1347-1367.

ZHDANOV, V., FENELONOV, V. & EFREMOV, D. 1987. Determination of pore-size distribution from sorption isotherms: application of percolation theory. *Journal of Colloid and Interface Science,* 120**,** 218-223.

ZHENG, X., GE, T. & WANG, R. 2014. Recent progress on desiccant materials for solid desiccant cooling systems. *Energy,* 74**,** 280-294.